Probing the interstellar medium and massive star formation using submillimeter dust emission

by

Arabindo Roy

A thesis submitted in conformity with the requirements
for the degree of Doctor of Philosophy
Graduate Department of Astronomy and Astrophysics
University of Toronto

Copyright © 2011 by Arabindo Roy

Abstract

Probing the interstellar medium and massive star formation using submillimeter dust emission

Arabindo Roy
Doctor of Philosophy
Graduate Department of Astronomy and Astrophysics
University of Toronto
2011

This thesis aims to improve our understanding of the early stages of massive star formation and of the physical properties of interstellar clouds. To achieve this, I have used submillimeter continuum dust emission data obtained by the Balloon-borne Large Aperture submillimeter Telescope (BLAST) in the first science flight in 2005, with a 2-m telescope operating simultaneously at 250, 350, and 500 μm. Unfortunately, BLAST produced images of about $3\farcm3$ resolution due to an uncharacterized optical problem.

In Chapter 2, I discuss implementation of the Lucy-Richardson (L-R) method of deconvolution to restore BLAST images to near diffraction limited resolution. Its performance and convergence have been extensively analyzed through simulations and comparison of deconvolved images with available high-resolution maps.

In Chapter 3, I study diverse phenomena in the Cygnus X region associated with high mass star-formation. To interpret the BLAST emission more fully and place the compact sources in context, archival data cubes of ^{13}CO line emission from KOSMA, MIPS images from the *Spitzer* Legacy Survey of this region, and 21-cm radio continuum emission from the Canadian Galactic Plane Survey have been used. Utilizing available ancillary multi-wavelength observations, the influence of OB stars and stellar clusters on Cygnus X has been studied, revisiting the well-known DR H II regions and their surroundings in the light of submillimeter continuum dust emission and CO line emission. An effort has been made to assess the evolutionary sequence of the compact sources (spatial extent of

about 1 pc) on the basis of L-M diagram and subsequently to relate this sequence to independent empirical evidence and theory. Using multi-resolution observations, evidence for hierarchical substructures within molecular clouds has been examined.

Finally, in Chapter 4, a multi-wavelength power spectrum analysis of the large scale brightness fluctuations in the Galactic plane is presented. This analysis has been used to assess the level of cirrus noise which limits the detection of faint sources. A characteristic power law exponent of about -2.7 has been obtained for sub-regions of Aquila and Cygnus X. The observed relative amplitudes of power spectra at different wavelengths have been related through a spectral energy distribution, thereby determining a characteristic temperature for the Galactic diffuse emission.

Dedication

To my beloved *ma* and *baba*

To my grandparents

To my elder brother, Manik-da

Acknowledgements

It is a pleasure to acknowledge various people who directly or indirectly have extended their help intellectually, emotionally, and mentally for the completion of this thesis. Today I feel indebted to each and everyone of you.

First, I want to thank my advisor Peter Martin without whose guidance and support this thesis would not have been completed. I must admit that it is he who has taught me and raised love for observational Astrophysics. Those long discussions in your office which often lasted till mid-night were very fruitful. Thanks for editing papers and correcting my English. I really feel fortunate to have you as my mentor.

I owe thanks for my beloved parents who have struggled throughout their life, have made sacrifices for providing me with education, and have always been a source of inspiration and strength in my life. Another person who is very important in my life – Manik-da, who has supported me both financially and morally. Without his support possibly I would not have found me in this position today. My little sister Anushree for extending her love and care. I thank my uncle and aunty who are always happy on my success.

I am very thankful to Apratim da, Moja-da, and Urmila-di who helped me in multiple of ways – discussing physics with Apratim da on Thursday nights, Moja-da helping me preparing my slides at his house, and Urmila-di serving us with good meals.

I also want to thank Pat McDonald for mentoring me first year projects. I also thank Howard Yee for helping me out in the first years of my graduate studies.

My committee members Norm and Barth for setting higher goals in every committee meeting.

Thank you Kaitlin, Fernando, Andrew, Daniela, Santiago, Sherry, Mubdi, Marco, Juan, and others for helping me in various of ways.

Lastly, I thank my wife Nayan for her trust and love.

Contents

List of Tables

List of Figures

Chapter 1

Introduction

Galaxies are the visible structural units of the universe. We study the dynamics of galaxies to help determine the cosmological parameters for understanding the creation history of the cosmos. Without stars, galaxies would be massive but dark bodies. Star formation makes galaxies luminous objects.

Light from the distant galaxies travels a vast span in space and time carrying information about conditions in the early universe. Thus, they are one of the most important tracers of the structural evolution of the universe and cosmic history. Distant supernovae in galaxies have made it possible to determine the cosmic scale factor of the universe. Last but not least, the cold and neutral universe during the 'dark-ages' became again observable because of reionization due to energetic photons emitted by newly-born massive stars.

Figure 1.1 (Franceschini et al., 2008) shows that a large fraction of the background radiation in the universe generated by stars is in the infrared and submillimeter. The majority of these photons originated as reprocessed radiation from dust surrounding heavily enshrouded young massive stars. In this thesis I have used continuum dust emission maps obtained by the Balloon-borne Large Aperture Submillimeter Telescope (BLAST) which records radiation in the range 250 to 500 μm (Pascale et al., 2008). In order to understand the galactic evolution it is necessary to study massive star formation inside our local Galaxy. Massive stars are responsible for altering the dynamics and enriching the chemistry of the interstellar medium (ISM) (Bergin et al., 2001; di Francesco et al., 2007; Beuther et al., 2007a) through a combination of vigorous outflows (Matzner, 2002), expansion of H II regions (Krumholz & Matzner, 2009), stellar winds, and the production of heavy elements during supernova explosions. OB stars (M $>$ 8 $M_{\odot}$) are

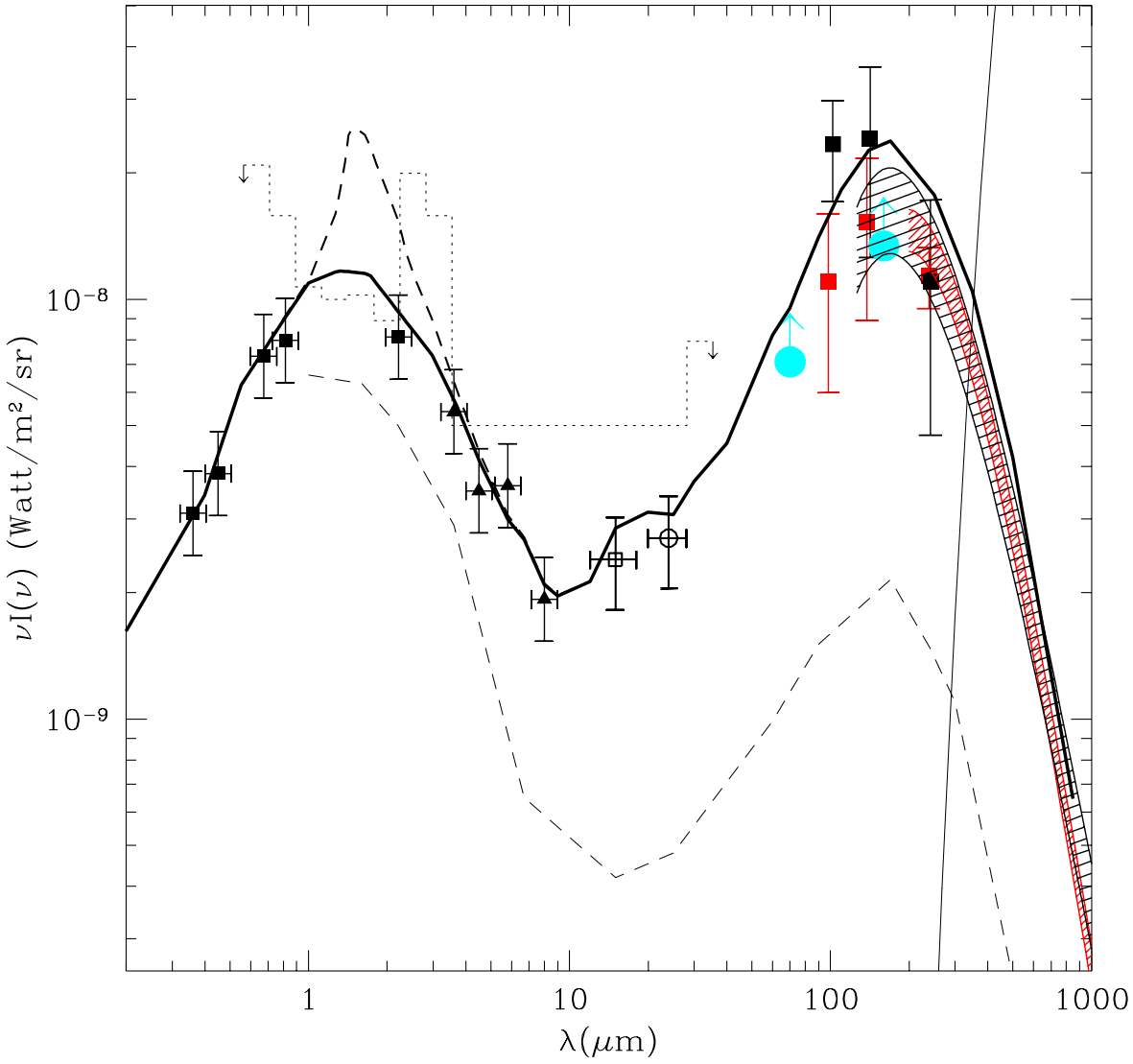

Figure 1.1 The CIB spectrum measured by COBE and the optical extragalactic background obtained by integrating ultradeep HST images. The thick line tracks the background spectrum over the wide wavelength range. This plot is taken from Franceschini et al. (2008), who provide references for the details. The main point to appreciate here is the significant amount of energy that has been absorbed from the optical and re-radiated in the far-infrared.

emitters of copious UV photons which are ultimately responsible for the dissociation of molecules and ionization of atoms in molecular clouds. Moreover, a considerable fraction of the Galactic energy budget both in the form of radiative and kinetic energy is due to the massive stars. They power the far-infrared luminosity through the heating of dust and provide large scale energy input for sustaining turbulence in the ISM, forming self-similar structures on all observable scales. Matzner (2002) has shown that expanding H II regions and protostellar outflows from the stellar clusters can inject energy at the scale of Giant Molecular Clouds (GMCs). Despite the crucial astrophysical consequences, very little is known about the early stages of the evolution of massive stars due to their short evolution period, their birth within highly obscured regions of distant cold dusty molecular clouds, their multiplicity, and complexities involved in the clumpy local ambient environment.

On the other hand, studying low-mass star formation is relatively "easy" because of their reduced complexity during formation. Moreover, they are formed in nearby molecular clouds, facilitating the gathering of observational evidence for confronting theoretical predictions. There is a well-supported paradigm (see § 1.2.3) that low-mass stars form in comparative isolation by accreting mass in an environment where the gravity overpowers thermal and non-thermal pressure gradients. An average temperature of about 10-20 K is generally found in a low-mass star forming cloud resulting in an accretion rate of about 10^{-6} to 10^{-5} $M_{\odot}$ yr^{-1} (McKee & Tan, 2003; Zinnecker & Yorke, 2007; McKee & Ostriker, 2007). Unfortunately, a scaled up version of low-mass star formation cannot explain the massive counterparts as different physical processes are associated with their formation. For example, most massive stars also form in a cold ambient medium (10-20 K), and will have a low accretion rate in the initial stage of formation which is unable to explain the final accumulation of stellar mass within such a short span of time. For recent reviews of star formation see Larson (2003), Mac Low & Klessen (2004), McKee & Ostriker (2007), Zinnecker & Yorke (2007), di Francesco et al. (2007), and Bergin & Tafalla (2007).

1.1 Low-mass vs. High-mass Star Formation

For low mass stars, the paradigm is that stars are formed inside gravitationally bound substructures within molecular clouds (Shu et al., 1987; Chabrier & Baraffe, 1997; Chabrier et al., 2005; Baraffe et al., 2003; McKee & Ostriker, 2007). However, before the onset of any star forming activity, the core is dynamically balanced against the gravitational field by the mechanical support provided by the thermal pressure gradient. Under this

circumstance, subsonic evolution of underlying gas will tend to form a $1/r^2$ density distribution (Bodenheimer & Sweigart, 1968). The collapse of the quasi-stable core is initiated within the critically supported region. Finally, a protostar accreting at a rate proportional to c_s^3/G (c_s is the isothermal sound speed) is formed via gravitational collapse. This newly-born protostellar core is surrounded by an envelope of dust and gas from which the central object continues to accrete material through the accretion disk. The gravitational energy of the accreted material is partly converted into rotational energy of the core and disk (which can power bi-polar jets) and partially converted to heat which is radiated away. Luminosities of the protostars at this stage (class 0) will be mainly dominated by accretion.

The scenario of star formation changes when the mass of protostars is approximately greater than 8 $M_\odot$ (Zinnecker & Yorke, 2007; McKee & Ostriker, 2007). The high-mass protostars initiate nuclear burning while still accreting because the characteristic Kelvin-Helmoltz time scale is smaller than the accretion time. Unlike low-mass stars, massive stars are not optically visible in their pre-main sequence stage, being still embedded inside the dusty molecular envelope. A main difficulty with massive star formation is that the disruptive effect of intense radiation pressure and ionizing photons produced by the star eventually halts the accretion. This feedback process is so strong that it seems impossible to build increasingly massive cores, and on this basis Larson and Starrfield (1971) and Khan (1974) prescribed an upper limit on stellar mass. However, in reality the observed upper limit is higher than the theoretical prediction (25 $M_\odot$; Larson & Starrfield, 1971). There is much to be learned. Furthermore, massive stars generally form in dense clusters, and interaction among the forming stars and their influence on the environment become necessary factors to be taken into account in explaining their evolution.

1.2 The Turbulent ISM

1.2.1 Seeds for Massive Star Formation

The largest molecular structures (radii $\sim$ 10 to 100 pc) formed out of the turbulent ISM are known as Giant molecular clouds (GMCs; 10^4 to 10^6 $M_\odot$, Solomon et al., 1985). Overdense regions inside these gigantic structures at relatively smaller scales (1 to 10 pc) are designated as clumps. Moreover, the (magnetic) turbulent motions can also sweep up material in the form of elongated substructures known as filaments. Finally, at the

sub-parsec scale of the hierarchical structure, called cores, the interior is less turbulent, or possibly dominated by subsonic (Kolmogorov) turbulence. If these core structures, often in filaments, are massive enough (empirically, above some threshold column density), then they should be efficient in forming stars (André et al., 2010; Krumholz & McKee, 2008). However, the overall star formation efficiency at the scale of the embedding molecular cloud is low, ~ 10 %, because only a small fraction of the molecular cloud is at sufficiently high-density

One of the important discoveries about the physical properties of molecular clouds was made by Larson (1981), later to be known as Larson's laws. Observations of molecular clouds reveal scale-invariant correlations between velocity dispersion, size, and mass: $\sigma \propto R^{\alpha}$, and $\sigma \propto M^{\beta}$, where α and β are the scaling indices. In the range of 0.1 $\leq R \leq$ 100 pc, Larson (1981) obtained a power-law correlation index α of 0.38. This characteristic scaling is similar to subsonic turbulent flows whose hierarchy in velocity distribution is determined by the Kolmogorov scaling law, $\sigma \propto L^{0.33}$. Subsequent studies have shown that α ranges between 0.4 - 0.5 (Myers & Goodman, 1988; Falgarone et al., 1992; Caselli & Myers, 1995) which is steeper than the Kolmogorov spectrum. The linewidth-size scaling $\sigma \propto R^{0.5}$ is more suggestive of supersonic turbulence than Kolmogorov turbulence. Discontinuities in the velocities due to supersonic shock flows naturally give rise to an energy spectrum $E(k) \propto k^{-2}$, which can be recast to explain $\sigma \propto R^{0.5}$ (Padoan, 1995; Ballesteros-Paredes & Mac Low, 2002; Boldyrev et al., 2002; Padoan et al., 2002; Padoan & Nordlund, 2002).

Thus the picture of the ISM, based on observational evidence, is that interiors of molecular cloud are in great commotion, a situation often described by a hierarchy of velocity distributions present over a wide dynamical range, very similar to any complex hydrodynamical turbulent motion. At the larger scale, supersonic turbulent motions can generate shocks that compress gas, and ultimately produce inhomogeneous density structures on all observable scales inside the parent molecular cloud (Larson, 1981; Falgarone et al., 1992; Padoan, 1995; Mac Low & Klessen, 2004). Occasionally, substructures become large and dense enough to undergo gravitational instability, but the supersonic velocity field in the interior provides sufficient support to counter gravity (McKee & Tan, 2003). Statistically, only the clumps with intermittent turbulence will collapse to form protostars. Furthermore, smaller-sized clumps, where the velocity dispersion is more similar to the subsonic Kolmogorov spectrum, are more prone to gravitational collapse (Padoan, 1995). Sometimes, external-triggers such as shocks from stellar winds can in-

duce a large fraction of a molecular cloud to collapse.

Turbulence regulates the star formation rate at least in two ways. First, it resists global collapse of the molecular cloud under gravity, reducing the effective accretion rate. Second, it breaks the clump material into a large number of smaller fragments, which leads to the formation of clusters. Different star forming regions might show somewhat different level of turbulence. For example, the Orion region, where star formation is taking place at all scales including massive stars, is sustained by a higher level of turbulence than the Taurus clouds which is forming only low-mass stars (Larson, 1981).

1.2.2 Role of the Magnetic Field

Magnetic fields are ubiquitous in the Galactic plane (Mestel & Spitzer, 1956; Crutcher, 1999). In addition to turbulence, the magnetic field plays a crucial role in the evolution of interstellar clouds and the formation of (massive) stars. Moreover, waves generated due to perturbation inside a magnetized medium dissipate more slowly than turbulent motions, providing support for a longer time against collapse. Massive stars are believed to form in magnetically supercritical cloud cores via dynamical contraction (Shu et al., 1987).

Low-mass stars are formed out of magnetically subcritical cores via ambipolar diffusion (Shu et al., 1987; Nakano, 1998). The evolution of a centrally condensed magnetized cloud should proceed quasi-statically until self-gravity becomes dominating (Basu & Mouschovias, 1994, 1995b,a; Ciolek & Basu, 2000).

The interstellar magnetic field has been probed indirectly through optical, infrared, submillimeter, and radio observations. Measurements of the polarization of the submillimeter dust emission would provide a large-scale picture of the Galactic magnetic field in the molecular cloud. This is being investigated for example by the recently launched BLAST-pol experiment (Marsden et al., 2008; Fissel et al., 2010). Data will also be available at lower resolution from Planck[1] and at higher resolution from the SCUBA-2 polarimeter (Bastien et al., 2005; Crutcher et al., 2004).

[1] http://www.rssd.esa.int/index.php-project=planck

1.2.3 Theoretical Models

To capture the complex dynamics involved in the formation of massive stars and the dominant physical processes involved in the formation of structures within giant molecular complexes, a number of theoretical and phenomenological models have been proposed.

One view of massive star formation is the turbulent core model proposed by McKee & Tan (2003), where massive stars are thought to form in gravitationally bound turbulent cores. In this model, a non-thermal velocity field due to turbulence provides a global support against gravitational collapse, thereby reducing the rate of infall of gas into over-dense regions. Thus, evolution of cores procedes in a quasi static way. These cores are part of self-similar density fluctuations inside bigger structures known as clumps which have been created by supersonic turbulent motion linked with shock dissipation and gravity. Possibly not all of these density substructures will produce massive stars, but the final stellar destiny will depend upon the mass, density and internal dynamics of the core. For example, if a massive core is undergoing rapid density fluctuations which are themselves gravitationally bound, then the core would most probably form a low-mass star cluster. However, turbulence-regulated massive star formation has been criticized by Dobbs et al. (2005) on the grounds that turbulence should promote fragmentation of molecular clouds into low-mass stars, and so is not an efficient means of forming a single massive star. Latter, Krumholz (2006) took up this issue, showing that radiative feedback from the accretion luminosity of newly born low-mass protostars may provide thermal support against fragmentation even in a turbulent medium. In this case, formation of a massive star from a core can be summarized in the following chronological order: a cold turbulent core fragments into many low-mass stars; their accretion luminosity heats up the ambient medium; this enhanced thermal support halts further fragmentation of the cloud material; a massive star forms by gravitational instability in the warmer gas. Indeed, thermal stability feedback from the low-mass stars is not sufficient to ensure formation of a massive star; in addition the core must have sufficient mass concentrated in a small volume area. Krumholz & McKee (2008) predicted that a critical surface density (Σ) of 1 g cm^{-2} is essential for turning gas into a massive star. Hence, the regions of high density $\sim$ 1 g cm^{-2} are the markers of potential massive star forming sites. Empirically, Plume et al. (1997) found surface densities of $\sim$ 1 g cm^{-2} associated with massive star forming regions, and similarly as pointed out in Chapter 3, Le Duigou & Knödlseder (2002) found a similar surface density for the embedded OB star clusters

in the Cyg X region. On the other hand, low-mass star forming regions have a lower surface density of ~ 0.03 g cm^{-2} (André et al., 2010).

Bonnell et al. (1997) developed an alternative competitive accretion model. In this model gas accretion is one of the dominant physical processes which determines the observed mass function. Prior to the massive star formation, the initially static molecular cloud undergoes collapse locally at random multiple sites due to Jeans' instability. The initial stellar density may reach $\sim 10^8$ cores pc^{-3} ($\sim$ number of Jeans' masses within the cloud) for a very brief period of time; however, gravitational interaction among the siblings plays an important role in merging (Bonnell et al., 1998). An individual stellar core gains mass by accreting gas from its surrounding through the Bondi-Hoyle accretion mechanism, allowing for the possibility that tidal effects can reduce the accretion radius. Moreover, in this model, a core that begins with slightly more initial mass or is favored by the reservoir of gas in its proximity has a greater ability to accrete due to an increased gravitational potential. This results in higher-mass stars toward the denser center of the cluster, and as the potential keeps on growing, gas continues to be funnelled down to the center of the cluster. Although this model is successful in reproducing the observed IMF, it does not take account of any feedback mechanisms that might counter accretion and star formation.

Very recently, Wang et al. (2010) have concluded from their simulations that neither the turbulent model nor the competitive accretion mechanism completely controls the formation of massive stars; the 'clump dynamics' in which a collective outflow feedback from accreting low-mass stars play an important role too.

1.3 Observation of Massive Star Forming Sites

1.3.1 Molecular Line Tracers

It is important to know under what physical and chemical conditions of the parent molecular cloud stars are born. Dust continuum emission surveys trace column density along the line of sight (see § 1.3.2), but are not an adequate means to reveal a complete picture of the dynamical, morphological, and chemical aspects involved with the evolution. Different molecular tracers, which might survive or alternatively deplete at different physical and chemical conditions, can be utilized as probes of the density profile, temperature distribution, outflows, stability of the fragments, and kinematics of local regions associated

with the star forming site.

Molecular line emission from high density tracers such as ^{13}CO, $C^{17}O$,$C^{18}O$, NH_3, CS, provides a three dimensional picture in position-velocity coordinates of the substructures inside the molecular cloud (Plume et al., 1992, 1997; Dame et al., 2001; Beuther et al., 2002b). However, usage of these molecular tracers is limited by their relative abundances in different density conditions, optical depth properties, and ability to survive in cold temperature conditions (di Francesco et al., 2007). For example, Ohashi et al. (1999), Bergin et al. (2001), and Young et al. (2004) found observational evidence for depletion of CCS, CS, H_2CO molecules, respectively, toward dense cores.

The measured line width (FWHM of velocity profiles) is dominated by non-thermal turbulent motion inside molecular clouds. Line-width correlates with spatial dimension of cloud: $\Delta v \sim R^{\alpha}$ (see § 1.2.1). Fuller & Myers (1992) obtained $\alpha \sim 0.44$ after studying line widths of NH_3, CS, and $C^{18}O$ molecules; however, Caselli & Myers (1995) found α of about 0.22 associated with massive cores in the Orion molecular cloud.

1.3.2 Continuum Dust Emission

Stars are formed inside dense molecular clouds. It is a natural expectation that more stars will be formed where there is high concentration of interstellar material, but of course it is the details that are interesting. Generally, gas is traced by dust emission. In the context of star formation, dust plays a dual role. Firstly, it helps in the gravitational collapse of the molecular cloud by acting as a cooling agent. When a cloud collapses, the gravitational energy is converted into thermal energy. If the thermal pressure is not released, then material is prevented from collapsing. The molecular medium is optically thick but the dust is not. Secondly, dust absorbs radiation at higher frequencies where it can be optically thick, and reprocesses the energy, emitting at longer wavelengths where it is optically thin. This reveals the presence of (massive) stars which are deeply embedded in the molecular cloud.

Compact (Mezger et al., 1967) and ultracompact H II regions (UCH II) are the brightest and most luminous objects in the Galaxy, emitting most of their radiation at infrared wavelengths peaking at ~ 100 μm (Mezger & Henderson, 1967; Kurtz et al., 1994, 2000; Churchwell, 2002). They contain at least one ionizing star which creates an H II region in the surrounding material. Apart from the warm dust emission, H II regions are also detected in radio continuum emission. One of the classic papers on H II regions is the

(DR) survey of the Cyg X region in 5-GHz continuum emission by Downes & Rinehart (1966). In an annual review, Habing & Israel (1979) summarized the then contemporary discoveries of H II regions and investigations of their formation. However, not much was known about their structural morphologies until Wood & Churchwell (1989b) and Kurtz et al. (1994) discovered the existence of UCH II regions at subarcsecond resolution.

High mass protostellar objects (HMPOs; Beuther et al., 2007b) are the precursors of UCH II regions, still accreting material from the reservoir. Massive molecular outflows are one of the phenomena associated with the early stages of massive star formation and HMPOs are no exception (Beuther et al., 2002b). In transition to the UCH II stage, they are generally weak or not detected in radio free-free emission. However, they are detectable in the far infrared bands of *IRAS* due to warm dust emission. Much research has been conducted to study their physical properties (Wood & Churchwell, 1989a; Plume et al., 1997; Molinari et al., 1998; Beuther et al., 2002a). Van der Tak & Menten (2005) found that HMPOs might be associated with hot molecular cores. *IRAS* continuum images at far-infrared wavelengths were widely used in constraining their physical properties. However, at a resolution of $\sim 4'$ or even $1'$ with HIRES (Cao et al., 1997), and at the kpc or larger distances, the flux density is integrated over the area of an entire star-forming cluster, rather than constraining an individual member (though a single star might dominate due to the sharp dependence of luminosity and ionizing flux on mass). One of the observational challenges of studying massive stars is that they remain undetected at near-infrared wavelengths because their earliest stages are deeply embedded inside the molecular cloud.

Though many surveys have been conducted to study HMPOs and UCH II regions, little is known about their precursors. Following Beuther et al. (2007b), formation of high mass starless cores (HMSCs) and high mass cores with embedded low/intermediate mass objects should precede HMPOs. Thus, in the earliest stages of massive star formation, prior to any major embedded energy source, the dust emission is dominated by a cold component passively heated by the interstellar radiation field and not detected by *IRAS*. This stage of massive dense pre-stellar cores, analogous to the precursors of low-mass class 0 protostars, should be detected through (sub)millimeter dust continuum and molecular line tracers. Studying submillimeter and centimeter continuum emission, Molinari et al. (1998), Molinari et al. (2000), and Beuther et al. (2002b) characterized sources as precursors of UCH II regions. Searching for sources of similar youth, Motte et al. (2007) made an unbiased census of massive young stellar objects (MYSOs) in the

massive star forming Cygnus X region, using 1.2 mm continuum images produced by MAMBO-2 on the IRAM 30 m telescope. A significant fraction of their sample appeared to be in a mid-infrared-quiet phase, excellent candidates for early evolutionary stage. A complementary molecular line survey showed that the massive infrared-quiet dense cores of the Cygnus X region are associated with high-velocity SiO emission, clearly indicating powerful outflows as a consequence of accretion.

With the advent of mid-infrared space observations ISO (Perault et al., 1996) and MSX (Price et al., 2001) came the discovery of a new marker of potential star forming sites, observed in silhouette against the diffuse near infrared background and termed infrared dark cloud (IRDC) (Egan et al., 1998; Carey et al., 2000; Simon et al., 2006). An extensive review on this class of objects is presented in Bergin & Tafalla (2007). The IRDCs harbor objects at different evolutionary stages, including precursors to the HMPOs. They are touted as laboratories for testing whether massive stars are formed by competitive accretion or evolve in a quasi static equilibrium embedded in a turbulent medium. From molecular line observations Sridharan et al. (2005) found a mean velocity dispersion of $\sim$ 1.6 km s^{-1} for IRDCs which is lower by a factor of two than HMPOs, suggesting a quiescent prestellar stage. With submillimeter surveys like those from BLAST and *Herschel*, IRDC-like clouds can be detected directly by their cold dust emission (Roy et al., 2011b; Peretto & Fuller, 2010; Wilcock et al., 2011). A three-color image of dust emission obtained by the BLAST survey of 2006 is shown in Figure 1.2 from Netterfield et al. (2009). The map highlights the relatively cold (red) and warm (blue) dust distribution toward the nearby ($\sim$ 700 pc) molecular region called Vela.

1.4 Surveys

Large scale mapping of the whole sky by *IRAS* has captured the far-infrared and mid-infrared component of the Galactic dust emission. A wide range of structures in a hierarchy became visible both in the Galactic plane as well as at high latitude. The broad spectral coverage of *IRAS* filters gave a comprehensive view of dust components in the Galaxy and probed the spatial distribution of dust with an angular resolution of $4'$ (Cao et al., 1997). Though low resolution compared to modern astronomical instruments, *IRAS* had sufficient sensitivity to detect emission from a column density as low as 10^{20} H atoms cm^2 (Boulanger et al., 1996; Miville-Deschênes et al., 2007a). The FIR dust temperature has been estimated on the basis of *COBE* observations (Dwek et al., 1997;

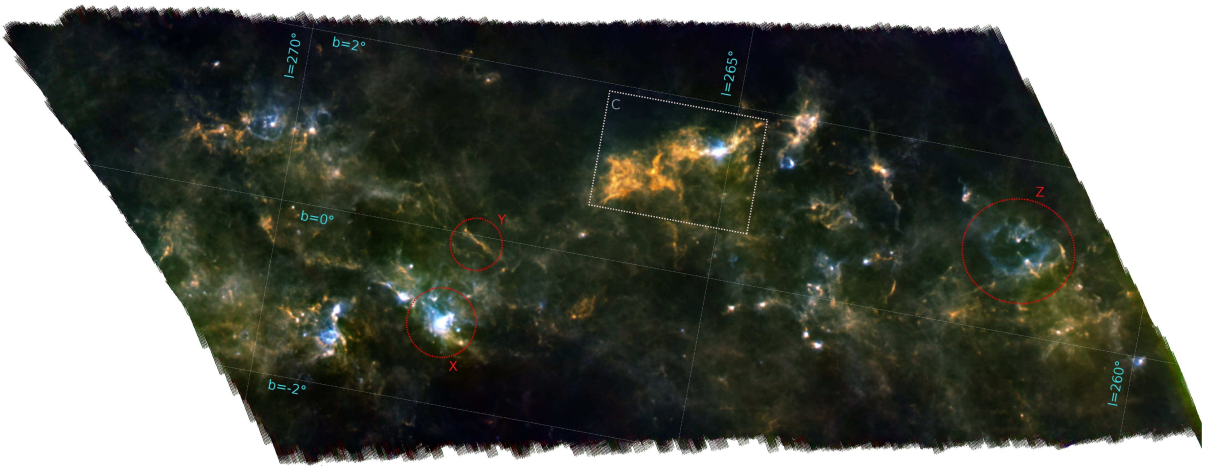

Figure 1.2 False-color image of 50 deg^2 BLAST map of the Galactic plane toward Vela using the 250 μm channel for blue, the 350 μm channel for green, and the 500 μm channel for red. Color in this image is an indicator of temperature, with blue regions being warmer and red being colder.

Schlegel et al., 1998). However, due to low sensitivity and comparatively lower spatial resolution, an average dust spectrum was computed over a large field of observation. Schlegel et al. (1998) used DIRBE and *IRAS* to make an all sky temperature map. With the better sensitivity and angular resolution of ISOPHOT (on ISO; Kessler et al., 1996), cirrus cloud temperatures of 17 K have been computed on the basis of intensity variations even on the fainter patches of the sky (Juvela et al., 2000). The submillimeter and millimeter emission of diffuse Galactic dust is dominated by the thermal radiation of large dust grains which are in equilibrium with local interstellar radiation field; these large particles, with dimension about 0.1 μm, account for the majority of the dust mass in the ISM (Compiègne et al., 2011).

The emission from this large dust component is dominant in the 100 μm band of *IRAS*. On the other hand 12, 25, and 60 μm bands are sensitive to the small grain distribution. The smaller sized grains undergo non-equilibrium stochastic heating, emitting most of the energy at shorter wavelengths. Hence, this has an effect of broadening the energy spectrum towards mid-infrared wavelengths. A spectral energy distribution (SED) for the dust emission at high Galactic latitude is shown in Figure 1.3.

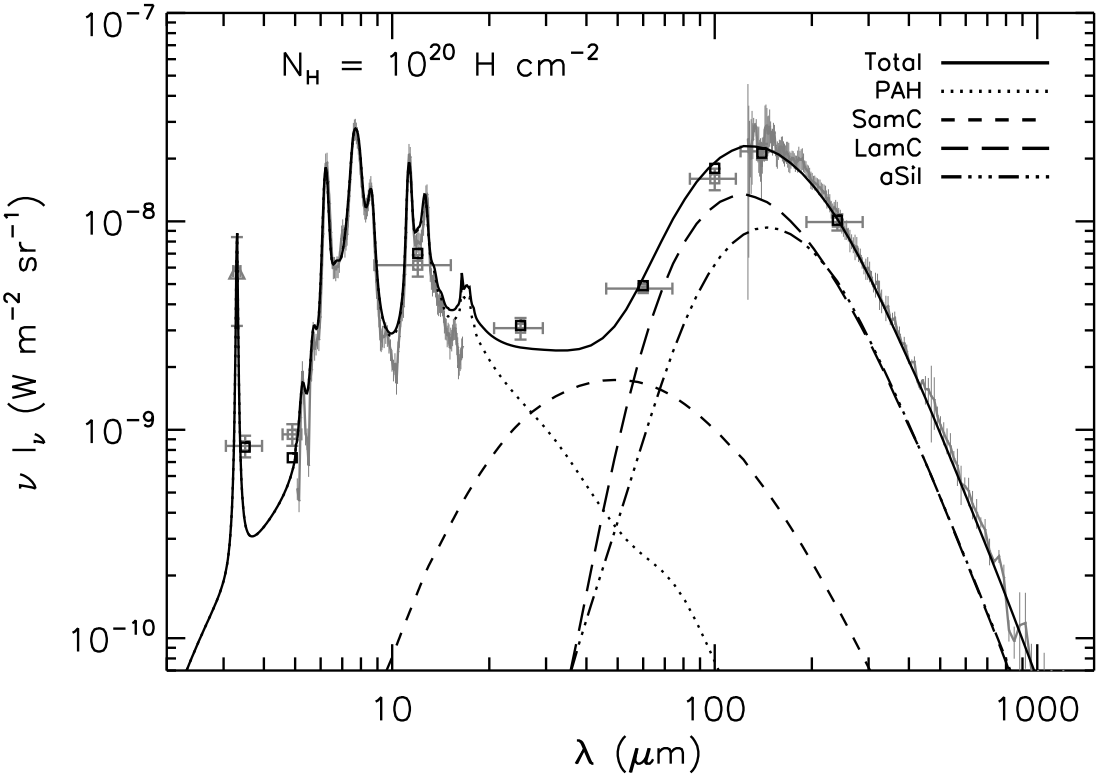

Figure 1.3 Dust emission spectrum for the diffuse high Galactic latitude ISM. The triangle at 3.3 μm is a measurment from the AROME balloon experiment and grey squares are the photometric measurments from DIRBE. The lines are the model output and black squares are the modeled DIRBE points after taking into account instrumental transmission and color corrections (Compiègne et al., 2011). The far-infrared (100 – 1000 μm) part of the SED is dominated by thermal emission from large grains of size ~ 0.1 μm. Energy in the mid-infrared part (< 60 μm) is due to smaller grains and PAHs.

1.5 Cirrus

1.5.1 Background

In the Galactic plane, as well as at high latitude, the ISM is comprised of large scale structures such as filaments along the line of sight and superimposed in the two-dimensional image. In the plane, complex dynamical processes such as violent outflows, stellar winds, expanding H II regions, shock fronts, and early condensations due to gravity give rise to the typical elongated spatial structures ranging from a few parsec to tens of parsecs. Compared to the Galactic plane ISM, high latitude clouds are not gravitationally bound and cloud structures are simpler in origin because there is no star formation activity. The dust mixed in the density structures is radiatively heated due to the local interstellar radiation field and ultimately re-emits in the far-infrared. The distribution of brightness fluctuations in the emission map results from column density variations along and across the line of sight, and reveals a self similarity in the underlying density field at all observable scales. The emission from the nearby ISM at high Galactic latitude is known as Galactic cirrus, and the brighter emission from the Galactic plane has been called "interstellar froth". However both cases are also called "cirrus" as adopted here. As discussed next, the cirrus emission is a predominant source of confusion noise at far-infrared wavelengths and its precise characterization is necessary for both Galactic and extragalactic astronomy. For example, the emission from irregularly shaped interstellar clouds limits the detectability of pre-stellar cores in molecular clouds, whose complete characterization is urgent to bring a consensus about the early stages of (massive) star formation.

A fraction of radiation in infrared wavelengths come from starlight reprocessed by dust in distant star-forming galaxies, whose combined light at low resolution is known as the Cosmic Infrared Background (CIB) radiation (see Fig. 1.1). The Galactic cirrus emission also acts as foreground noise to the CIB radiation. The importance of studying the CIB and its anisotropies is enormous, as it has imprints of earlier phases of galaxy formation (Viero et al., 2009; Planck Collaboration, 2011).

1.5.2 Source of Confusion Noise

Irrespective of observing strategy, the sensitivity of infrared and submillimeter imaging suffers primarily from four noise sources: detector noise, photon background noise, con-

fusion noise from crowded compact sources, and the noise due to spatial variations of the brightness distribution of cirrus emission. The thermal background noise is minimized by cooling the detectors. The noise analysis on four ISOPHOT images by Herbstmeier et al. (1998) has suggested that the sensitivity at far-infrared wavelengths is affected more by sky confusion noise from cirrus than by the instrumental uncertainties. In faint regions, the confusion noise at long wavelength ($\lambda > 60$ μm) comes additionally from extragalactic sources. The exact description of this noise from the CIB requires a statistical quantification of source counts based on a model characterizing the luminosity function and spectral distribution of the sources (Helou & Beichman, 1990), and for lower spatial frequencies, the clustering (Viero et al., 2009). Kiss et al. (2001) investigated the properties of cirrus confusion noise over a range of wavelengths from 90 to 200 μm using ISOPHOT maps. They have found that the confusion noise scaled with the average surface brightness as $\langle I \rangle^{1.5}$. Lagache & Puget (2000) and Matsuhara et al. (2000) separated extragalactic components and cirrus noise in ISOPHOT maps, and thereby detected the power in CIB fluctuations at the level of $5 - 12{\times}10^3$ Jy^{2}sr^{-1} at 170 and 180 μm. The CIB anisotropy is represented by a roughly Poissonian spatial distribution, with a flatter power spectrum than the cirrus noise.

1.5.3 Statistical Analysis

The cirrus is a turbulent ensemble of intricate structures present everywhere in the ISM. The physical properties of the underlying distributed field can be extracted through statistical tools. A variety of statistical methods such as correlation functions, structure functions, power spectra, and delta variance are used for the analysis. However, for the cirrus confusion noise analysis relevant to detecting compact sources, a second order structure function of the sky background convolved with the telescope beam is often used to estimate the mean squared fluctuation. For a randomly distributed Gaussian field, one-point statistics completely describes the physical properties of the field. Following the notation of Gautier et al. (1992), the second order structure function is defined as

$$S(\mathbf{r}) = \langle |\mathbf{F}(\mathbf{x} - \mathbf{r}) - \mathbf{F}(\mathbf{x})|^{\mathbf{2}} \rangle_{\mathbf{x}}, \tag{1.1}$$

where $F(x)$ is a measurement of the sky brightness at location x, and r is the separation between the two measurements, and the average is computed over the ensemble x. The result of the operation is an estimate of the average error produced by the fluctuating

field when a single reference aperture is placed at a distance of r in order to subtract the sky background from a measurement of a compact structure. In general, an estimate of the photometric error N, due to sky brightness fluctuations is obtained from the second order structure function appropriate to the measuring strategy and is given by:

$$N(r) = \sqrt{S(r)} \times \Omega, \tag{1.2}$$

where Ω is the solid angle subtended by the measuring aperture.

Equation 1.1 is connected to an auto-correlation function, $\xi(r)$, through $S(r)/2 = \langle\delta^2(x)\rangle - \xi(r)$. Mathematically, the auto-correlation function is an ensemble average involving fluctuations at two different locations, expressed as as:

$$\xi(r) = \langle\delta(\mathbf{x})\delta(\mathbf{x}+\mathbf{r})\rangle, \tag{1.3}$$

where $\delta(x)$ is expressed as $(\rho(x) - \bar{\rho}(x))/\bar{\rho}(x)$, representing the density contrast of the field. Due to (assumed) isotropy and homogeneity, the scalar quantity $\xi(r)$ only depends upon the norm of $\mathbf{r}$. The correlation is given in Fourier space by

$$\begin{aligned} \langle\delta(\mathbf{k})\delta(\mathbf{k}')\rangle &= \delta_D(\mathbf{k}+\mathbf{k}') \int \frac{d^2\mathbf{r}}{(2\pi)^2} \xi(r) \exp(i\mathbf{k}.\mathbf{r}) & (1.4)\\ &= \delta_D(\mathbf{k}+\mathbf{k}')P(k), & (1.5) \end{aligned}$$

with $P(k)$ by definition the power spectrum. The inverse relation between the power spectrum and the correlation function is

$$\xi(r) = \int d^2\mathbf{k} P(k) \exp(i\mathbf{k}.\mathbf{r}). \tag{1.6}$$

For a Gaussian field, the power spectrum completely describes the probability distribution of $\delta(\mathbf{k})$ and its statistical properties are determined by the shape and normalization of $P(k)$. One of the important statistical quantities is the variance, the correlation with a zero lag, expressed as

$$\begin{aligned} \sigma^2 &= \langle\delta^2(\mathbf{x})\rangle \\ &= \int 2\pi P(k) k^2 dk. & (1.7) \end{aligned}$$

It is clear that the cirrus confusion noise is related fundamentally to the spatial properties of the cirrus distribution. However, for practical purposes the effect of convolution by the instrument beam cannot be removed from the image, and so the noise estimation also directly depends upon the telescope configuration and the observing wavelength. Telescopes are designed to operate at the diffraction limit resolution of $1.22\lambda/D$, at each wavelength λ with a primary mirror of diameter D.

1.6 Statistical Properties of Cirrus Noise

Various observations (Gautier et al., 1992; Kiss et al., 2001; Miville-Deschênes et al., 2002) have suggested that the cirrus power spectrum follows a power law over a large dynamical range. It is generally approximated as

$$P(k) = P_0(k/k_0)^{\alpha}, \tag{1.8}$$

where P_0 is the normalization constant defined as the power at the scale $k = k_0$, and α is the exponent of the power law fit. The spatial distribution of cirrus brightness fluctuations exhibits an exponent of about -3 which is similar to the 2-dimensional power spectrum of a field with a distribution of Kolomogorov-type energy spectrum. A weak dependence of α on the mean surface brightness has also been noted by Miville-Deschênes et al. (2007b). At a given wavelength (100 μm) P_0 directly is found to vary with the mean brightness as $\langle I \rangle^3$.

1.7 Outline of Thesis

This thesis aims to improve our understanding of the early stages of massive star formation and physical properties of interstellar clouds. It is based on submillimeter observations of dust emission. Regarding massive star formation, the quest has been toward answering several puzzles involved with their formation such as what are the initial physical and environmental conditions in which massive stars are formed and is there any observable evolutionary sequence which can relate early condensation to dense molecular cores. Properties of prestellar clumps and evidence for hierarchical substructures within molecular clouds are examined. Observations are discussed in the context of present theoretical understanding.

To achieve this, I have used submillimeter data obtained by BLAST in the first science flight in 2005. BLAST recorded continuum dust emission from both Galactic and extragalactic sources with a 2-m telescope operating at 250, 350, and 500 μm (Pascale et al., 2008). Unfortunately, this first flight of BLAST produced images with about $3\farcm3$ resolution from a corrupted beam due to an uncharacterized optical problem (Truch et al., 2008). For optimal identification and characterization of prestellar clumps and cores a high resolution image is required. Hence, achieving the science goals became a more challenging task. Fortunately, BLAST images have high signal to noise, which

encouraged exploration of the Lucy-Richardson (L-R) scheme of deconvolution. This deconvolution scheme has been particularly useful in restoring BLAST images to near diffraction limited resolution, facilitating many studies: the star forming regions in Aquila (Rivera-Ingraham et al., 2010), Cygnus X (Roy et al., 2011b), IC 5146 and K3-50 (Roy et al., 2011a), and diffuse structure in the direction of the Cas A supernova remnant (Sibthorpe et al., 2010).

In Chapter 2, I first discuss how the L-R operation has restored images with better-controlled background noise and increased source detectability. The L-R method of deconvolution is efficient in resolving compact sources in crowded regions while simultaneously conserving their respective flux densities. Its performance and convergence have been extensively analyzed through simulations and cross-correlations of the deconvolved images with available high-resolution maps. New science results from two BLAST surveys in the Galactic regions K3-50 and IC 5146 are presented, further demonstrating the benefits of performing this deconvolution. Three clumps have been resolved within a radius of $4\farcm5$ inside the star-forming molecular cloud containing K3-50. Combining the better-resolved dust emission map with available multi-wavelength data, the SEDs for five clumps have been constrained to obtain masses (M), bolometric luminosities (L), and dust temperatures (T). The L-M diagram has been used as a diagnostic tool to estimate the evolutionary stages of the clumps. There are close relationships between dust continuum emission and both 21-cm radio continuum and ^{12}CO molecular line emission. In the IC 5146 field, the restored extended large scale structures in the Northern Streamer have a strong spatial correlation with both SCUBA and high resolution extinction images. A dust temperature of 12 K has been obtained for the central filament. Physical properties of ten compact sources, including six associated protostars have been obtained by fitting SEDs to multi-wavelength data. All of these compact sources are still quite cold (typical temperature below $\sim$ 16 K) and are above the critical Bonner-Ebert mass. They have associated low-power Young Stellar Objects (YSOs). Further evidence for starless clumps has also been found in the IC 5146 region. Chapter 2 has been accepted for publication in the Astrophysical Journal (Roy et al., 2011a).

In Chapter 3, the Cygnus X field is presented in a new multi-wavelength perspective based on an unbiased BLAST survey at 250, 350, and 500 μm, combined with rich datasets for this well-studied region with MAMBO, SCUBA, *IRAS*, MIPS and *MSX* data. To interpret the BLAST emission more fully and place the compact sources in context, I make use of archival data cubes of ^{13}CO line emission from KOSMA, MIPS

images from the *Spitzer* Legacy Survey of this region, and 21-cm radio continuum maps from the Canadian Galactic Plane Survey (CGPS). The primary goal is to investigate the early stages of high mass star formation. I have detected 184 compact sources in various stages of evolution across all three BLAST bands. From SEDs, now well constrained by the broad spectral coverage, the physical properties mass, surface density, bolometric luminosity, and dust temperature are obtained. Some of the bright sources with T reaching 40 K contain well-known compact H II regions, like W75N, DR21, and AFGL2591. I relate these to other sources at earlier stages of evolution via the energetics as deduced from their position in the L-M diagram. The submillimeter spectral coverage of the BLAST bands, near the peak of the SED of the dust, reveals fainter sources too cool (down to $T \sim 10$ K) to be seen by earlier shorter-wavelength surveys like *IRAS*. BLAST detects thermal emission from infrared dark clouds enabling the investigation of the phenomenon of cold "starless cores" more generally. When examined in *Spitzer* 24 or 8 μm images, these cold sources often show stellar nurseries. Although they are potential sites for massive star formation, they are "starless" in the sense that to date there is no massive protostar in a vigorous accretion phase. I discuss evolution in the context of the L-M diagram. Theory raises some interesting possibilities: some cold massive compact sources might never form a cluster containing massive stars; and clusters with massive stars might not have an identifiable compact cold massive precursor. Chapter 3 has been published in the Astrophysical Journal (Roy et al., 2011b).

In Chapter 4, I have studied multi-wavelength power spectra of diffuse Galactic dust emission from BLAST observations at 250, 350, and 500 μm in two Galactic plane fields in Cygnus X and Aquila. These submillimeter power spectra statistically quantify the self-similar structure observable over a broad range of scales and can be used to assess the cirrus noise which limits the detection of faint point sources. The advent of submillimeter surveys with the *Herschel Space Observatory* makes the wavelength dependence a matter of interest. I show that the observed relative amplitudes of the power spectra can be related through an SED for the dust. Fitting a simple modified black body to this SED, the dust temperature in Cygnus X is 19.9 ± 1.3 K and in the Aquila region 16.9 ± 0.7 K. The empirical estimates provide important new insight into the substantial cirrus noise that will be encountered in forthcoming observations. Chapter 4 has been published in the Astrophysical Journal (Roy et al., 2010). Follow-on work with initial data from *Herschel* is described in Martin et al. (2010).

Chapter 2

Deconvolution of images from BLAST 2005: Insight into the K3-50 and IC 5146 star-forming regions

2.1 Introduction

The BLAST flight of 2005 (BLAST05; Pascale et al., 2008; Chapin et al., 2008) conducted both targeted and unbiased surveys in some of the important star forming regions of the Galactic Plane. These were conducted simultaneously at the submillimeter wavelengths of 250, 350, and 500 μm. BLAST was a precursor to *Herschel* observations with SPIRE (Griffin et al., 2010). One of the science goals of BLAST surveys was to study the early stages of massive star formation and identify their precursors in order to describe a complete sequence of evolution. In order to realize this ambition, a deep survey complemented by high spatial resolution is required. With a 2-m telescope, BLAST05 optics were designed to produce dust emission maps at a diffraction-limited resolution of full width at half maximum (FWHM) 40, 58, and 75$''$ at 250, 350, and 500 μm, respectively (Pascale et al., 2008). Unfortunately, due to some uncharacterized optical problem, the BLAST05 Point Spread Function (PSF) was anomalous, producing images at a resolution of about 3$'$.3 (Truch et al., 2008; Roy et al., 2010).

Most of the resulting maps contained clear imprints of the corrupted PSF (hexagonal geometry), indicating the presence of compact sources with angular sizes comparable to the diffraction limit. Measurements of the flux density of a few isolated bright sources

can be carried out by aperture photometry or by fitting the PSF. However, because of the large beam area of the corrupted PSF, the sensitivity to compact point sources in the presence of cirrus noise suffers, and the detection of crowded sources is challenging. This leads to an underestimate of the source density and produces an incomplete source list.

In order to improve the image resolution to near the diffraction limit, a direct Fourier transform method of deconvolution was performed in analyzing the Vulpecula region (Chapin et al., 2008). In this method of deconvolution, compact sources in the processed map were enhanced to 1.′3, 1.′6, and 1.′8 at 250, 350, and 500 μm, respectively. However, the deconvolved maps were contaminated by ripples which propagated across the entire map. The generation of ripples is an intrinsic consequence of the direct Fourier inversion method when the PSF varies across the field and is not perfectly known. The amplitude of the ripples is particularly high near bright sources. Strong interference patterns are also observed in the vicinity of multiple bright sources. This makes fainter compact sources hard to detect; furthermore, artificial spatial features are introduced in diffuse structures.

To get the best science return from the BLAST maps, we consider implementation of the L-R method of deconvolution (Richardson, 1972; Lucy, 1974). The L-R deconvolution method is an iterative way of estimating the sky brightness distribution, conserving flux at every successive step. Fortunately, maps from the BLAST 2005 flight have a high signal-to-noise ratio and are well sampled with 15$''$ pixels, which is particularly important for the performance of L-R deconvolution.

Implementation of L-R deconvolution on the BLAST maps, for example Cas A (Sibthorpe et al., 2010), Aquila (Rivera-Ingraham et al., 2010), and Cygnus X (Roy et al., 2011b), has remarkably enhanced the compactness of point sources to about 1$'$ effective resolution. The other benefits of the L-R scheme are: 1) preservation of spatially diffuse structures; 2) suppression of background noise; and 3) resolving blended sources. As an example, in the Cygnus X region the L-R map led to a source catalog containing 184 sources, significantly greater than the 130 produced using the direct Fourier inversion method.

A basic goal of this chapter is to demonstrate the performance of the L-R algorithm in deconvolving BLAST05 maps. We do this via simulations and using "ground truth," i.e., comparing the details in BLAST deconvolved images with available high-resolution maps, thereby establishing the reliability of detected structures, both compact (§ 2.3.2)

and more diffuse (§ 2.3.3). In those subsections we focus primarily on the operational consequences of deconvolution for identifying compact sources and defining diffuse structures. We subsequently present new science results made possible by this deconvolution, for the star-forming regions K3-50 (§ 2.4) and IC 5146 (§ 2.5). We identify protostellar clumps and characterize their physical properties such as temperature, mass, and luminosity, by constraining SEDs using multi-wavelength data. We have also investigated the properties in the "Northern Streamer," a cold molecular ridge in the IC 5146 field.

2.2 Overview of Deconvolution

Deconvolution is a common technique used by the astronomical community for enhancing image quality. In the imaging process, various factors are responsible for the distortion of the observed sky map. In the traditional way, the data recorded represent the sky convolved with a point spread function (PSF). The PSF shape depends not only on the mirror and aperture (window) of the telescope, but also often on the atmosphere. Even in an ideal instrumental setup, images are blurred due to secondary peaks of Rayleigh diffraction. In modern astronomy, spatial resolution plays a pivotal role in deciphering morphology and obtaining accurate photometry and hence it is important to try to deblur images.

Meinel (1986) has shown a wide variety of both linear and nonlinear restoration algorithms, based on maximum likelihood and recursive improvement of images in successive iterations, taking account of the Gaussian and Poisson noise processes. Moreover, the additional *a priori* information about the positivity of the true image helps to improve resolution. One of the most frequently-used methods is the above-mentioned L-R deconvolution scheme, which conserves flux. A key property of this algorithm is that it converges toward the most likely solution of the PSF and image intensity distribution. In the literature, there exist several other techniques for image restoration. A detailed description of the Maximum Entropy Method (MEM) of deconvolution is given in Narayan & Nityananda (1986) and Bryan & Skilling (1980). A Maximum Correlation Method (MCM), which maximizes the correlation between adjacent pixels, and simultaneously improves image resolution has been been prescribed by Aumann et al. (1990) for improving *IRAS* survey maps. This algorithm is also an extension of the L-R solution as described in Meinel (1986) and Velusamy et al. (2008). The latter authors adopted the MCM technique for deconvolution of *Spitzer* images, improving the resolution by a factor

of about three.

These techniques generally require that the PSF be previously determined to high accuracy. When the PSF is only poorly known, an iterative blind deconvolution technique can be used for image restoration, where both the data and the PSF are estimated simultaneously in the successive steps (Fish et al., 1995; Tsumuraya et al., 1994).

2.2.1 Two Deconvolution Algorithms

In the classical approach to the imaging process, the data image D is expressed by

$$D(x,y) = I(x,y) * P(x,y) + N(x,y), \tag{2.1}$$

where $P(x,y)$ is the PSF of the telescope, $I(x,y)$ is the (unknown) unblurred sky image, the symbol $*$ denotes the convolution operator, and $N(x,y)$ is the noise added to the data while imaging. Recursive formulae can be obtained from the maximum likelihood solution for two different classes of noise distribution, namely the Poisson and the Gaussian noise processes (Meinel, 1986; Varosi & Landsman, 1993). From equations (31) and (64) of Meinel (1986) we write directly the solution for the Poisson noise case in the form (Varosi & Landsman, 1993):

$$I_{\rm new} = I_{\rm old}\left[\left(\frac{D}{I_{\rm old} * P}\right) * \tilde{P}\right]^q, \tag{2.2}$$

and that for Gaussian noise as:

$$I_{\rm new} = I_{\rm old} + \Big([D - (I_{\rm old} * P)] * \tilde{P}\Big)^q. \tag{2.3}$$

Here $\tilde{P}$ is the reflected PSF, $\tilde{P}(x) = P(-x)$. For $q = 1$, equation (2.2) reduces to the L-R algorithm obtained independently from Bayesian statistics (Richardson, 1972; Lucy, 1974). The Poisson noise process, by its nature, excludes any negative solutions whereas the Gaussian noise process allows negative solutions, subject to the choice of q in equation (2.3).

Ideally, after an infinite number of iterations, the output map should converge to the maximum-likelihood solution. However, in practice, after a finite number of iterations in which a close to maximum-likelihood solution has been achieved, the smoothness of the map starts deteriorating (Velusamy et al., 2008). There are no definite and generalized stopping criteria for avoiding this (Prasad, 2002). Lucy (1974) recommended a stopping criterion based on a goodness-of-fit test. However, subsequently Lucy (1992) noted that a higher number of iterations might be needed for images with a large number of pixels, and he discouraged the use of the former method.

2.2.2 Implementation on BLAST maps

BLAST05 raster-scanned targeted regions in the Galactic Plane, having different areas ranging from 3 deg^2 to 10 deg^2. From the time-ordered data, maps were produced using the optimal map-maker SANEPIC (Patanchon et al., 2008a). The combination of high scan speed and low $1/f$ knee, cross-linking where available, together with common-mode removal in SANEPIC, produces maps retaining diffuse low spatial frequency emission. However, preprocessing of the time-ordered data to remove very low frequency drifts, plus using a low pass cutoff, makes the SANEPIC map average zero – the DC level is not known. The iterative L-R deconvolution algorithm for Poisson noise (eq. [2.2]) converges only for true positive images. In order to satisfy the positivity of the initial data image $D(x, y)$, we add a constant level to the whole map (a deconvolution operation on a flat map preserves the initial map in its output). The value of the constant is estimated by pixel-pixel correlation of the BLAST images (smoothed to $4'$) with the corresponding 100 μm IRIS image, *IRAS* data reprocessed by Miville-Deschênes & Lagache (2005). We carried out deconvolutions with different values of the constant, finding the solution to be robust. After the deconvolution operation we subtracted the constant from the resulting images.

Special care has been taken to deal with the edges of the scanned region, padding the external area at a value equal to the average around the edge of the map. The convolution operations in the iterative updates were carried out by fast Fourier transform (FFT), and so to maintain a periodic boundary condition and smoothness we apodized the entire map edge with a sine function.

The maps can be produced at various pixelizations, usually $15''$, but also $10''$ or $20''$. This is sufficient to sample the degraded PSF and to sample and recover diffraction-limited information even in the 250 μm channel. Our experiments showed that the deconvolution is robust to different pixelizations in this range. Note that the corrupted PSF is not azimuthally symmetric. Therefore, at each passband a synthetic PSF appropriate to the particular scan pattern and coverage of a field is constructed from the well-sampled ($10''$ grid) telescope-frame PSFs of each bolometer (Chapin et al., 2008). In order to avoid artifacts at large angular scales we have apodized the boundaries of the PSFs with a cos^2 taper from a radius of $4\farcm5$ to $5\farcm7$.

For the actual processing we have used the IDL-implemented 'Max_likelihood.pro' routine by Varosi & Landsman (1993), which includes both methods of iterative update,

appropriate to Gaussian or Poisson noise. Probably neither is an accurate noise model for the BLAST Galactic maps, which incorporate a fluctuating cirrus background, bright cirrus structures, and strong compact sources. Empirically, the largest errors in the maps are near the bright sources, this arising from small pointing errors, the asymmetric PSF, and the particulars of the map-making process itself. Furthermore, in the reconstruction step implicit in the deconvolution (eq. [2.1]), whenever the synthetic PSF is not a perfect representation there are larger errors in predicting D where I is brighter. Thus of the two, the Poisson algorithm is expected to work better because it gives less weight where there are strong point sources, i.e., where there are larger errors in the maps. Although the noise is not actually Poisson and the solution might not be optimal, it is always consistent with the data through equation (2.1). Note that a similar situation arises in the HIRES processing of *IRAS* data, where the noise model is likely a complicated hybrid (Aumann et al., 1990). We have performed experiments with both noise models and, as anticipated, the Poisson alternative was found to perform better in enhancing the structure in the image.

As shown in Figure 2.1, L-R deconvolution progressively enhances an image, but at the expense of background noise amplification at high frequencies after a large number of iterations. This noise can be suppressed by convolving the deconvolved map with a restoring beam G of FWHM close to the diffraction limit. Mathematically this step of restoring the image might be achieved in two distinct ways: 1) convolve each side of equation (2.1) with G, and treat $I*G$ as the unknown sky map to be found by the iterative solution of this new equation; or alternatively 2) as the effective PSF use $\widehat{(\widehat{P}/\widehat{G})}(x,y)$, where $\widehat{X}$ denotes the Fourier transform of X. We have compared the results for these two alternatives with the results of the standard deconvolution subsequently smoothed by the restoring beam and have found that L-R deconvolution gives robust results for all three cases. The images shown in this chapter have not been restored.

The reason for this is that despite the complicated and asymmetric PSF and the noise in the maps, application of L-R deconvolution removed the worst effects of the corrupted beam, thus improving significantly the definition of both compact sources and diffuse structures. Compared to the results of the direct inversion, the background obtained is much smoother, although ringing around bright sources has not been completely removed. Such ringing is not seen in Figure 2.1, where there are no very bright sources, but can be seen in the maps of Aquila (Rivera-Ingraham et al., 2010), Cygnus X (Roy et al., 2011b), and K3-50 (below), each of which contain significantly brighter sources. This same effect

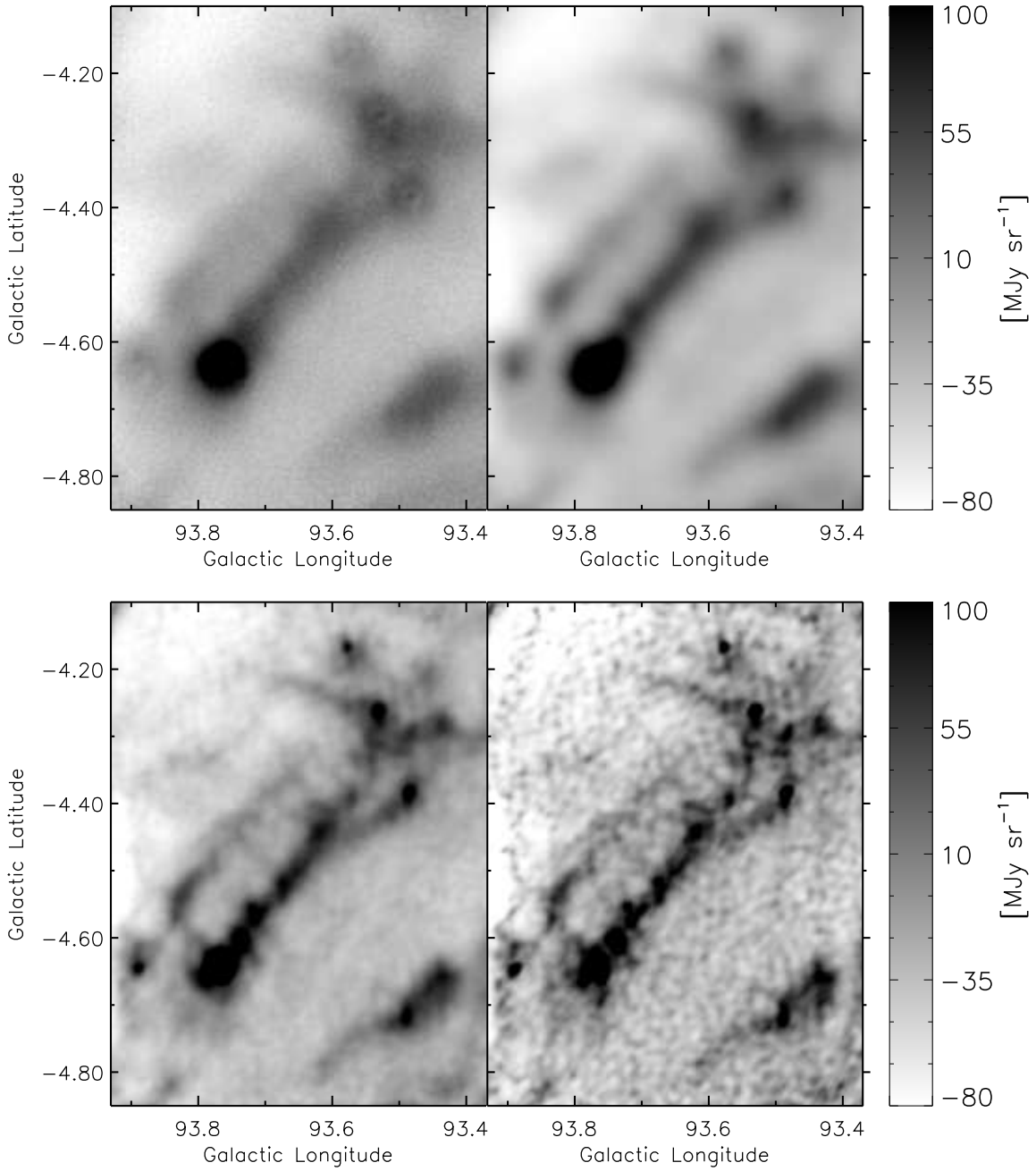

Figure 2.1 Example of BLAST image deconvolution by the L-R algorithm (Poisson noise), at 250 μm for the IC 5146 region. Upper left: unprocessed image where compact sources have the characteristic imprint of the corrupted BLAST PSF. Upper right: deconvolved image after 8 iterations. Lower left and lower right: after 64 and 256 iterations, respectively. The typical size of the compact sources in the final map is about 1′.

is shown in the simulations below.

This ringing is the principal artifact in the deconvolved images, as was also found to be the case in using the HIRES MCM algorithm to produce the Infrared Galaxy Atlas (IGA) from *IRAS* scans of the Galactic plane (Cao et al., 1997). Velusamy et al. (2008) reduced the ringing artifacts in deconvolutions of *Spitzer* data by first subtracting the background around the targeted compact sources. However, the large maps from the BLAST surveys are more complex, having large-scale structures of different brightness on which stronger sources are superimposed. Therefore, it is not practical to reduce the background everywhere to be close to zero.

These artifacts are on the scale of the corrupted PSF, and consist initially of a ring-shaped depression with an outer enhanced ridge. In successive iterative steps the artifact evolves, developing a finer series of depressions and ridges of smaller amplitude spreading from the source out into the rest of the image. The average brightness enclosed within the ringing pattern is very close to the local sky background. The intensity ratio of the brightest, smallest ring to the deconvolved central peak depends somewhat on the local background, but is typically no larger than 0.1%. Nevertheless, near very strong sources it is quite obvious, adding uncertainty in the estimation of the sky background level near bright (often crowded) sources and limiting the detectability of nearby faint sources.

2.3 Tests and Ground Truth

2.3.1 Simulations

We have performed simulations to check the robustness of the L-R deconvolution scheme. Fake sources were constructed by convolving normalized narrow Gaussians with the BLAST PSF and then multiplying them with random flux densities. Gaussians with intrinsic FWHMs ranging from $0.5'$ to $2'$ were tested. These simulated sources were inserted at different locations in the map such that the sources were well separated from each other. During the BLAST map-making process, a variance map is obtained from a combination of the noise in the time stream data and the map coverage by the bolometers in the array. We used this variance estimate to add noise to the simulated map, but in these tests we did not take into account the background structures and fluctuations from the diffuse cirrus.

We then deconvolved the simulated map using the PSF and observed the convergence

of the measured FWHMs of the sources as a function of iteration, as shown in Figure 2.2. In these tests we were able to recover the intrinsic size of the sources, convergence occurring after about 64 iterations. In Figure 2.3 we have plotted the average fractional flux densities recovered at different iterations of the L-R deconvolution. For isolated sources with various FWHMs about 98% of the input flux density is recovered. It is possible that the remaining flux density is lost due to the ringing artifact near the source, for which a Gaussian profile used in the fitting is not an accurate model.

Figure 2.4 shows the performance of L-R deconvolution in a simulation in which two compact sources with relative flux density 10 are placed only 1.′5 apart, well within the corrupted PSF. In the blurred map it is hard to discern a faint second source hidden within the brighter source. However, L-R deconvolution makes it clear. Fitting a double Gaussian to the deconvolved map, we have retrieved the initial flux densities and sizes within 96% and 99%, respectively. The positions of the recovered sources are accurate within $\sim 1''$.

2.3.2 L-R Performance on Compact Sources

Application of the L-R scheme to BLAST05 maps of the Aquila and Cygnus X regions has already shown impressive improvement in resolving confused sources in crowded regions (Rivera-Ingraham et al., 2010; Roy et al., 2011b), thereby enabling the preparation of deeper catalogs. From surveys at both longer and shorter wavelengths there was abundant ground truth for the fainter sources recovered. To demonstrate the L-R performance on a field of compact sources we have selected the region near K3-50, which is a young star-forming site containing a group of H II regions. We make use of images from *MSX* (Mill et al., 1994; Egan et al., 1998) at 8 μm, the IGA at 60 and 100 μm, and the CGPS 21-cm radio continuum survey (Taylor et al., 2003). We also make use of spectral line cubes of ^{12}CO from the Five College Radio Astronomy Observatory (FCRAO)[1] and of HI from the CGPS (Taylor et al., 2003). The science results for K3-50 are deferred to § 2.4.

Figure 2.5 shows details of the K3-50 region. The upper left panel shows how the L-R deconvolution operation has improved the resolution (cf. Fig. 6 of Truch et al., 2008). For example, the BLAST sources K4 and K5 are now well resolved compact objects in the deconvolved map with an angular resolution of $\sim 40''$, which corresponds to a

[1]http://www.astro.umass.edu/~fcrao/

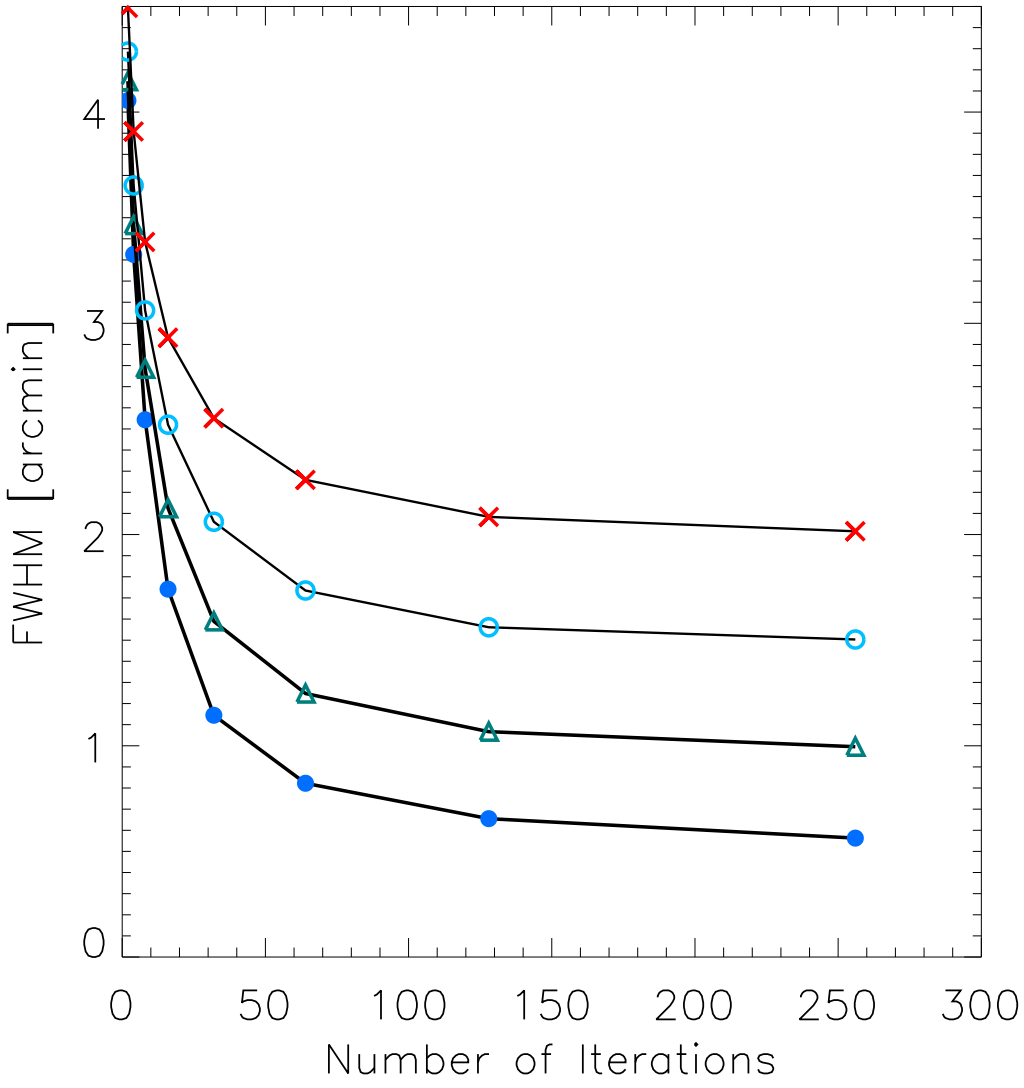

Figure 2.2 Measured FWHM of simulated sources at successive iterations of L-R deconvolution. Filled circles, triangles, open circles, and crosses represent sources of intrinsic size 0.′5, 1.′0, 1.′5, and 2.′0, respectively.

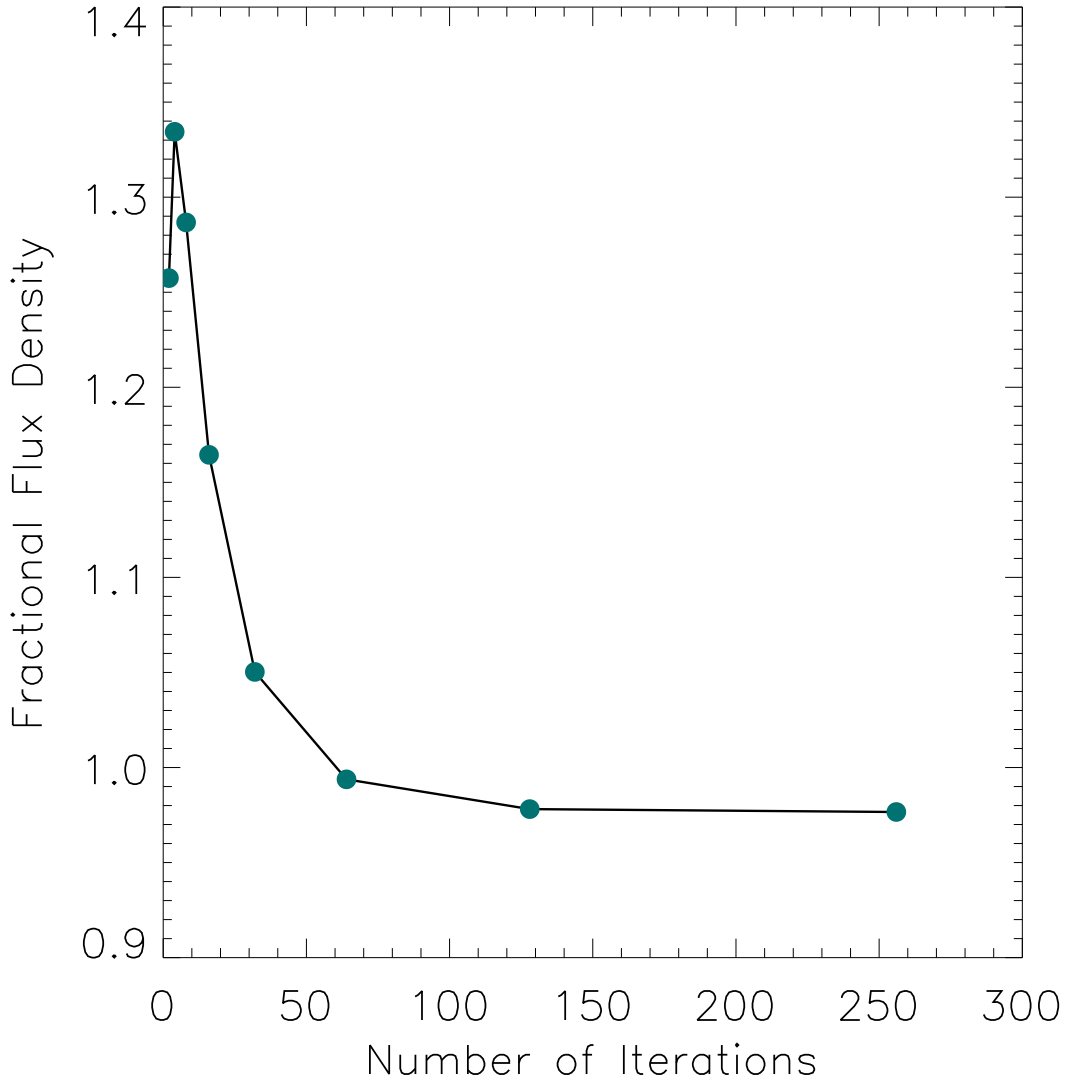

Figure 2.3 Measured fractional flux density averaged for compact sources with various FWHMs, at successive iterations of L-R deconvolution.

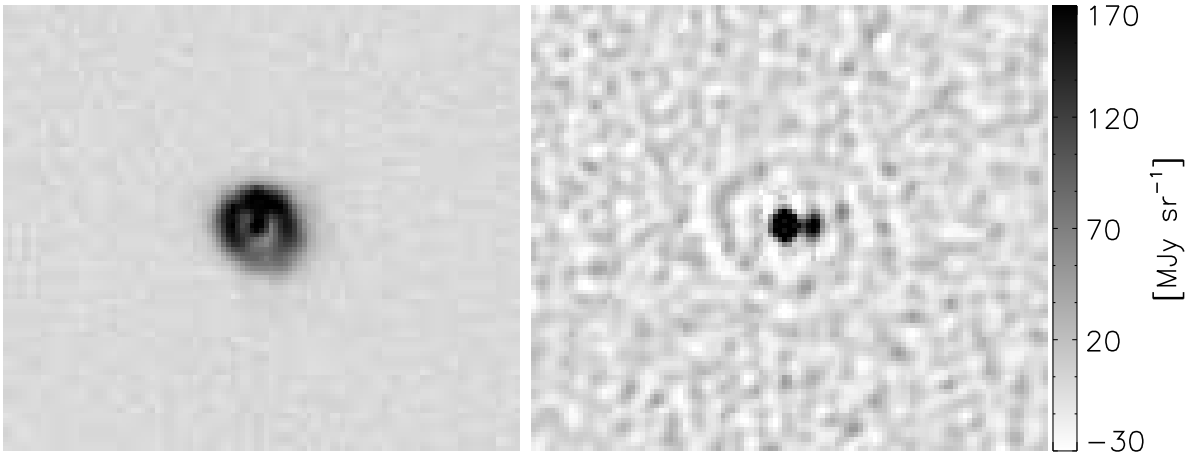

Figure 2.4 Left panel: two simulated sources of relative flux density 10 placed 1.′5 apart. Right panel: deconvolved map showing the two resolved sources. The brightness scale has been chosen to highlight the faint ring artifact.

spatial extent of about 1.7 pc at a distance of 8.7 kpc. The deconvolution also enabled the detection of faint sources which were otherwise hidden. From "by-eye" examination of the images in all three bands, we identified three sources (K1, K2, K3) as obvious detections, free of artifacts. Table 2.1 gives the flux densities and positions and the positions are indicated in all panels of Figure 2.5. The goal in this section is to find independent confirmation that these are reliable detections with good positional accuracy (we have not attempted to produce a complete source catalog for either of these small fields).

The overlaid triangles identify the radio source components obtained by Samal et al. (2010) from 1280 MHz observations, showing that there are multiple sources within the two bright BLAST sources, still unresolved at the improved BLAST resolution. Their names are indicated in the lower left panel, which also shows contours of radio emission. On the lower right panel we overlay contours of CO emission integrated over velocity ranging from -30 to -16 km s^{-1}, clearly revealing association of CO clumps with the dust emission. This applies not only to the sources K3, K4, and K5, but to more diffuse emission extending out from K4 and K5, showing that even this structure near bright sources is not an artifact. The upper right panel shows the same region imaged by *MSX* (8 μm), also at relatively high resolution. Again, there is good correspondence with BLAST.

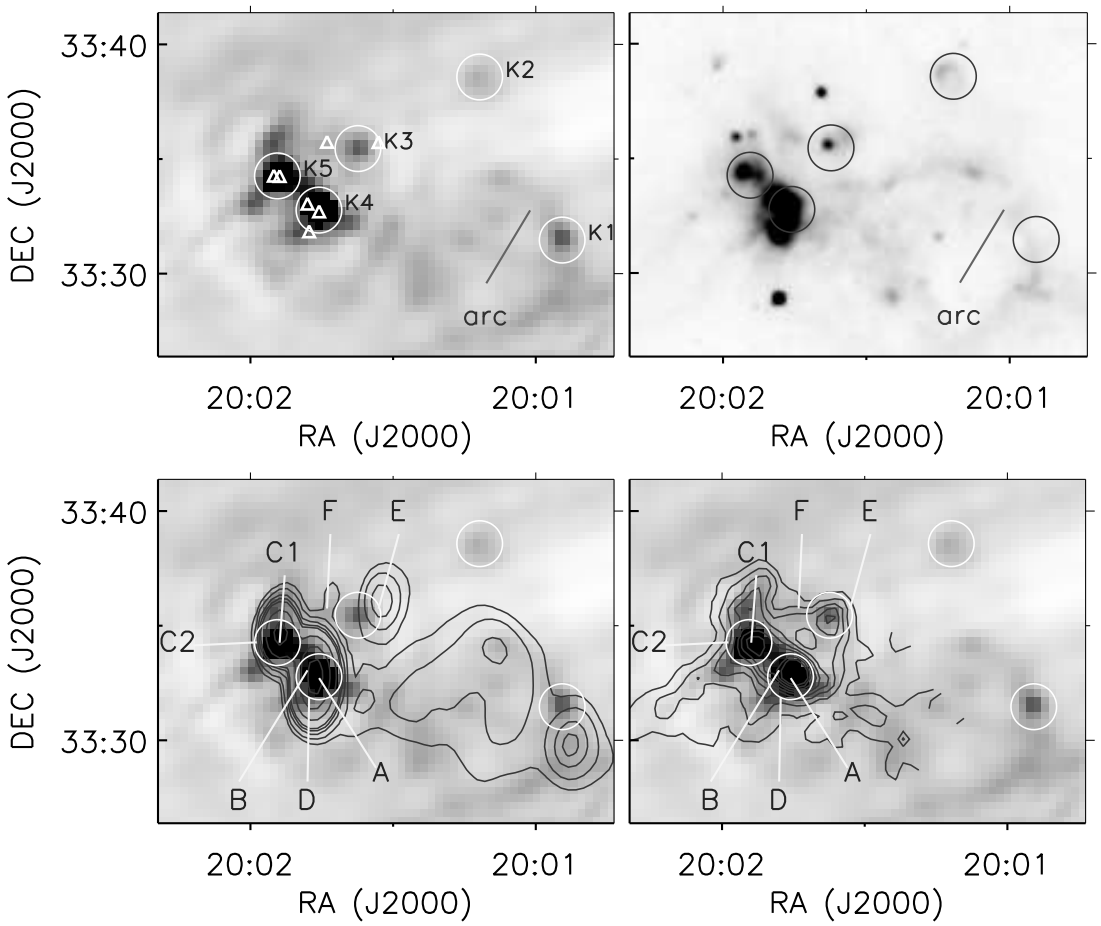

Figure 2.5 Upper left: BLAST05 map of K3-50 region at 250 μm after L-R deconvolution. BLAST compact sources are shown by the circles. The recovered FWHM of K4 (K3-50A) is 36″. Triangles show the positions of radio sources from Samal et al. (2010), with labels A to F (K3-50A to K3-50F) in the lower left panel. Lower left: contours of the 21-cm radio continuum emission (CGPS) overlaid on the deconvolved 250 μm BLAST image. Lower right: contours of the ^{12}CO line emission (FCRAO) integrated over -30 to -16 km s^{-1}. Note that the CO map coverage does not extend to K1 and K2. Upper right: 8 μm *MSX* image. The arc-like feature is also seen in the BLAST image.

K3, called IRASB by Samal et al. (2010), coincides with the cataloged point source IRAS 19597+3327A. At its position there is a CO peak at -24 km s^{-1}, the same velocity as for the much brighter K4 and K5 sources, and in the CGPS HI emission there is an absorption reversal at the same velocity. This indicates that K3 is related to this complex and is not a galaxy, as it has been alternatively classified (2MASSX J20013735+3335282). The dust emission peak identified as K2 is aligned with an asymmetric ring structure at 8 μm with no radio counterpart. K1 is on an arc of emission seen in the BLAST and *MSX* 8 μm maps, apparently related to the bubble of extended H II emission and its confinement. However, there is no prominent counterpart in either *MSX* or *IRAS* images. There is no 21-cm radio continuum counterpart either, all indicating that the source is cold and unevolved (see below). There is no confirming information from CO, since unfortunately, K1 (and also K2) is outside the area covered by that emission-line survey; the low resolution integrated CO map of Dame et al. (2001) hints at an extension in this direction.

Inspection of the deconvolved BLAST images suggests other sources as well. For example, there is a peak in dust emission along the arc, about half way between K1 and K2, which coincides with a peak in the radio continuum emission and *MSX* emission. At 500 μm this source is not prominent and so it is probably hot. As mentioned, we have not pursued the study of these fainter sources.

2.3.3 L-R Performance on Diffuse Structures

In this section we discuss the effectiveness of L-R deconvolution for recovering the morphology of extended structures. BLAST05 mapped a diffuse field toward the Cas A supernova remnant (Sibthorpe et al., 2010). The map was scanned in only one principal direction, but nevertheless the L-R deconvolution has restored numerous elongated diffuse structures. We have noted how the contrast of these structures increases with successive iterations. However, ultimately the background noise becomes amplified into non-physical small-scale structure, and so intermediate iterations produce the best compromise for studying the details of the diffuse emission. From the appearance of the maps, it was judged that 32 iterations is optimal.

Subsequently, this field has been imaged by *Herschel*[2] (Barlow et al., 2010), providing the desired ground truth to verify the efficacy of the L-R deconvolution. For comparison,

[2]http://herschel.esac.esa.int/Science_Archive.shtml

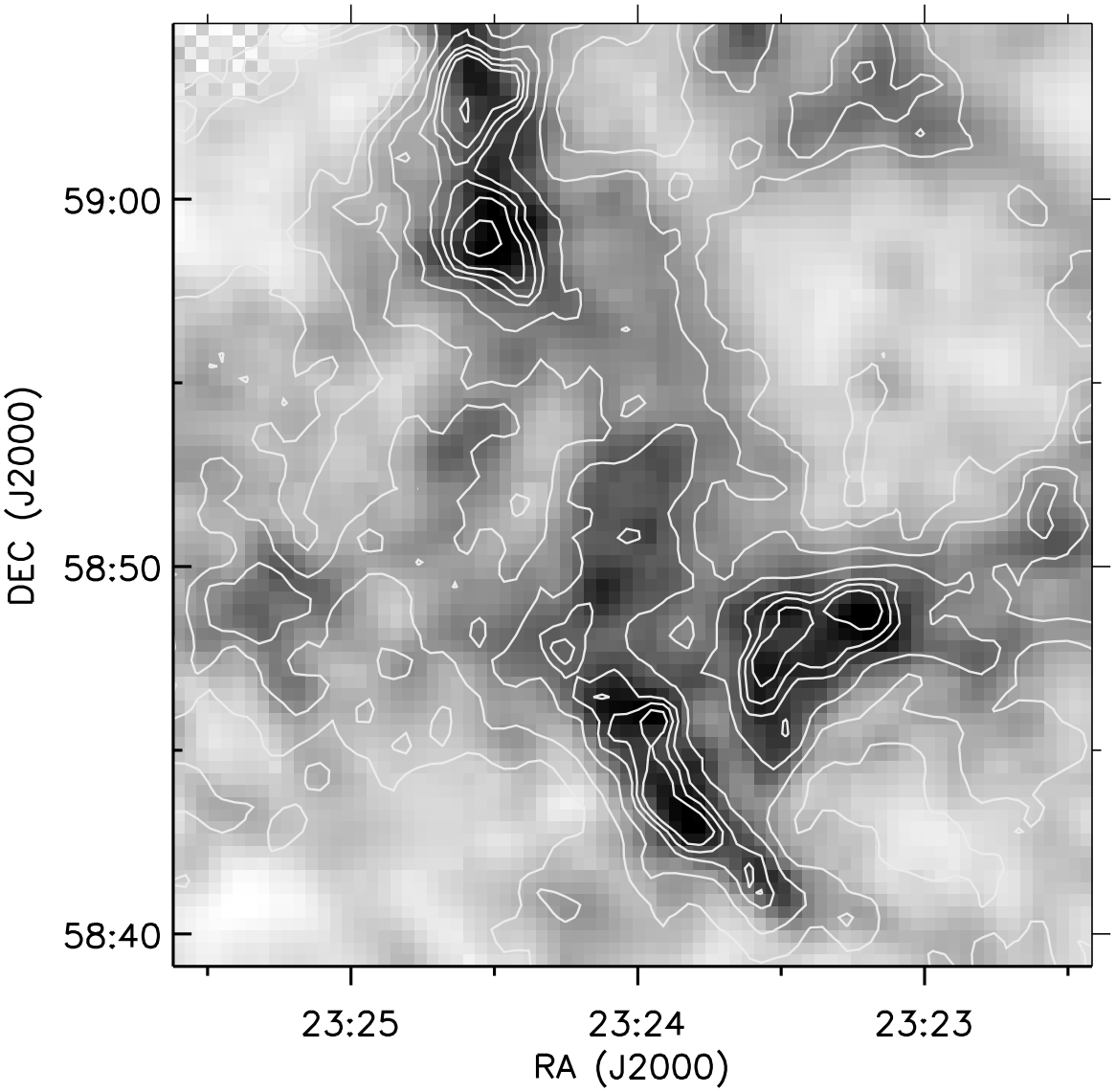

Figure 2.6 SPIRE 250 μm image of the Cas A field convolved with a 40″ Gaussian and reprojected on the 20″ BLAST grid. The contour overlay is from the corresponding BLAST deconvolved map, after 32 iterations. After deconvolution, the BLAST image faithfully reveals the morphology of the diffuse structures.

the 250 μm SPIRE image was smoothed with a 40″ Gaussian, and regridded to the 20″ pixelization of the BLAST image. Figure 2.6 shows this SPIRE image overlaid with contours from the corresponding deconvolved 250 μm BLAST map after 32 iterations. We have again examined the higher-iteration images and confirmed from this direct comparison that for the signal to noise of this BLAST survey, 32 iterations is about optimal.

There is also good evidence for recovering diffuse structures in the fields being studied here. The *MSX* 8 μm image of the K3-50 region in Figure 2.5 shows emission (probably from PAHs) along an extended shell-like structure, labelled "arc." Related structure is also seen in the radio emission, suggesting a bubble and surrounding PDR. The deconvolved BLAST05 map reveals that the same structure is also being traced by dust continuum emission, though the effect of the map edge on the lower right is apparent too. Furthermore, there is a faint ridge of submillimeter dust emission extending to the lower left of source K5 (K3-50C) which is traced by the CO contour.

Within the IC 5146 field is an elongated filamentary molecular cloud structure commonly known as the "Northern Streamer." Figure 2.7 shows a SCUBA 850 μm dust map of a targeted section in IC 5146 (Kramer et al., 2003; Di Francesco et al., 2008), overlaid with contours from the 500 μm deconvolved image. This shows that the L-R operation has preserved both large-scale structures and smaller-scale fragments along the ridge. A discussion of the astrophysics for this region is deferred to § 2.5.

2.4 Science Results for K3-50

K3-50 is a well-known group of compact H II regions, namely K3-50A–F, within the star-forming complex W58 (Israel, 1976; Howard et al., 1996; Samal et al., 2010). The warm dust surrounding the most prominent ionized region is bright in both far-infrared and submillimeter emission; the correlation with the CGPS 21-cm radio continuum emission is seen in Figure 2.5.

The radio sources K3-50A and K3-50B are well centered inside the BLAST clump K4 (spatial extent $\sim$ 1.7 pc), whereas K3-50C is within K5. Samal et al. (2010) further resolved K3-50C into two sources (C1 and C2). Moreover, this young star-forming region contains embedded infrared star clusters, namely K3-50D and K3-50B (Bica et al., 2003).

In the overlap region between the BLAST survey and the FCRAO ^{12}CO molecular line survey there is good correspondence between peaks of submillimeter and CO emission,

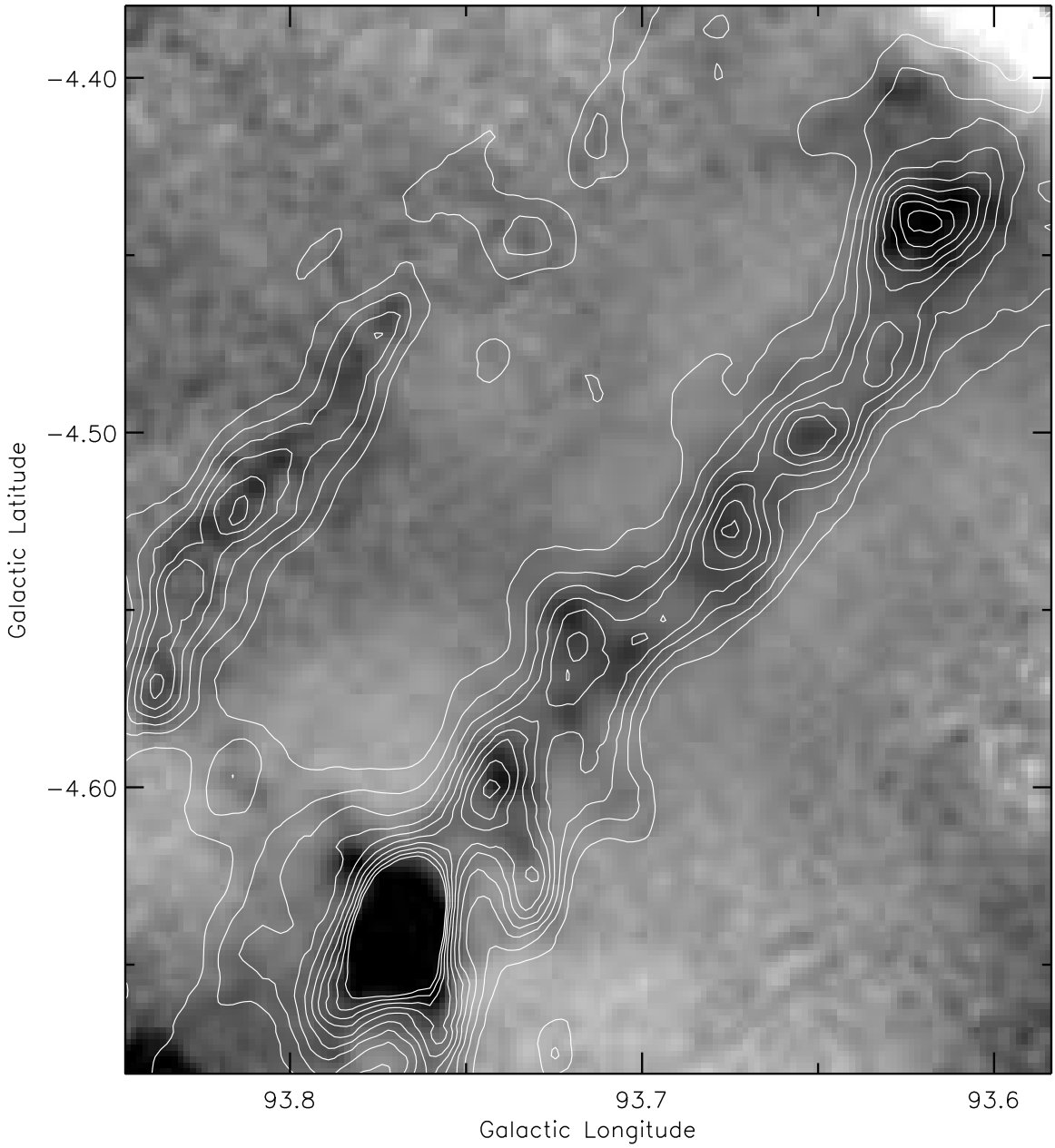

Figure 2.7 Contours from the deconvolved BLAST 500 μm image overlaid on the SCUBA 850 μm map of the "Northern Streamer" in the IC 5146 region. BLAST contours trace small-scale substructures in the SCUBA map along the filament, again showing the ability of L-R deconvolution to restore morphological detail within diffuse emission.

which provides further insight into global morphology and gas dynamics in the region. The CO contours on the lower right panel of Figure 2.5 show that K3, K4, and K5 are part of the same cloud (also see § 2.3.2). Velocity peaks associated with these sources are at -23.6, -24.6, and -22.5 km s^{-1}, respectively.

Table 2.1: SED best-fit parameters of BLAST sources in the K3-50 field

ID	BLAST Source Name	S_{250} (Jy)	S_{350} (Jy)	S_{500} (Jy)	S_{100} (Jy)	S_{60} (Jy)	T (K)	M (10^2 $M_\odot$)	L (10^4 $L_\odot$)	$L_{\rm bol}$ (10^4 $L_\odot$)
K1	J200054 + 333055	105 ± 10	61 ± 5	23 ± 3	70[a]	14[a]	20 ± 1	28 ± 5	0.7 ± 0.1	···
K2	J200112 + 333802	96 ± 9	46 ± 3	13 ± 1	277	175	33 ± 1	6 ± 1	3 ± 1	···
K3[b]	J200137 + 333454	144 ± 20	74 ± 8	20 ± 8	···	308	34 ± 1	10 ± 2	5 ± 1	···
K4	J200146 + 333214	1468 ± 19	576 ± 9	245 ± 6	11600	12000	44 ± 4	68 ± 14	152 ± 54	192
K5	J200154 + 333343	809 ± 25	357 ± 10	184 ± 6	3300	3100	35 ± 2	55 ± 14	36 ± 4	39

[a]Data used as upper limit in SED fit

[b]IRAS 19597+3327A

In our preliminary work (Truch et al., 2008) we measured flux densities for K3-50A and K3-50C (K4 and K5) by simultaneously fitting a model of two 2-dimensional Gaussians convolved with the corrupted BLAST PSF, where sizes, positions, and amplitudes were free parameters of the fit. In our present analysis, with the well-resolved deconvolved map, we fit multiple Gaussians with a linear background model to extract flux densities for individual sources. Table 2.1 summarizes the flux densities.

In order to achieve a broader multi-wavelength description of the SEDs, we have extracted flux densities at 60 and 100 μm from the IGA maps. For longer wavelength data points we have used the integrated flux densities reported by Thompson et al. (2006) at 450 and 850 μm for K4. Due to the restricted coverage of the SCUBA imaging, flux densities at 450 and 850 μm are not available for the other sources. We have also used *MSX* photometric data in deriving the bolometric luminosity; however, we have not used these data in the simple fit to the long-wavelength SED.

The SED-fitting model is a simplified single-temperature modified blackbody with a fixed dust emissivity index of $\beta = 1.5$. The mass of a compact source is related to the integrated flux density S_ν, as

$$M = \frac{S_\nu D^2}{r \kappa_\nu B_\nu(T_\mathrm{d})}. \tag{2.4}$$

Here we have adopted a 250-μm dust opacity $\kappa_0 = 10$ cm^2 g^{-1} and dust to gas ratio $r = 0.01$. We use the commonly adopted distance $D = 8.7$ kpc (Harris, 1975; Okamoto et al., 2003; Samal et al., 2010). From the HI absorption velocities and the CO emission, the sources are in a weak "Perseus arm" feature (in $l - v$ or $b - v$ diagrams) beyond the tangent point (at ~ 5.5 kpc), but not beyond the stronger emission at -60 km s^{-1}. Table 2.1 summarizes the physical properties, namely temperature (T), luminosity (L), and mass (M) for the individual BLAST sources. The reported 1-σ uncertainties of the physical parameters are obtained from Monte-Carlo simulations as described in Chapin et al. (2008).

Figure 2.8 shows an example of an SED fit, for K4. A best-fit temperature of 44 ± 4 K and total mass of $(7 \pm 1) \times 10^3$ $M_\odot$ are obtained from the parameters of the fit. Okamoto et al. (2003) have found a star cluster associated with K3-50A (the dominant radio source inside K4, also an ultra-compact H II region, Kurtz et al., 1994). Our derived luminosity is $(152 \pm 54) \times 10^4$ $L_\odot$. This clump luminosity is equivalent to a ZAMS spectral type of $\sim$O4 (Panagia, 1973), which agrees with Samal et al. (2010), who assigned a spectral type earlier than O5, based on near-infrared measurements. However the high luminosity

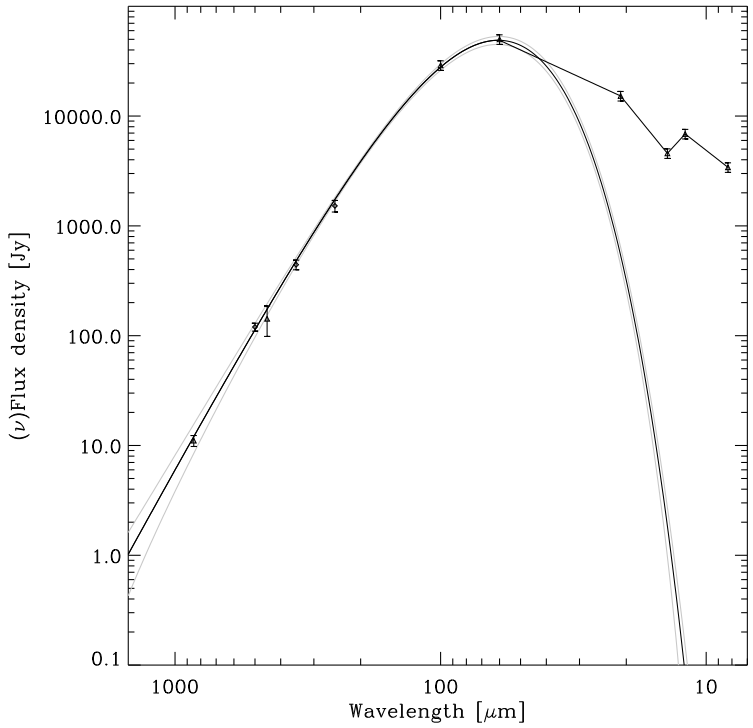

Figure 2.8 SED for K3-50A (our K4). Flux density multiplied by ν/ν_{250} plotted along the y axis. The solid line is the best fit to the modified blackbody with a fixed dust emissivity parameter of $\beta = 1.5$. The grey lines represent an envelope of 68% confidence level obtained from Monte-Carlo simulations. The best-fit parameters are given in Table 2.1. Data at wavelengths lower than 60 μm are not included in the fit but are used in estimating $L_{\rm bol}$.

supports the possibility of multiple ionizing stars in the stellar cluster. In fact, for K4 it is important to note that we measure dust emission whose energy comes collectively from K3-50A and K3-50B.

The position of a source on the L-M plane provides a rough estimate of its evolutionary stage. The relationship of the evolutionary sequence to the underlying energetics powering the dust emission is discussed in detail by Roy et al. (2011b). Naively, the evolution in the L-M diagram would be vertical (constant M) as the luminosity increases from accretion onto the massive protostar and the nuclear burning commences. In Figure 3.17, the dash (green) and dot-dash (blue) lines are the empirically-obtained loci of sources deriving the bulk of their luminosity from accretion and nuclear burning, respec-

tively (Molinari et al., 2008). Figure 3.17 also confirms that K4 contains one or more zero age main sequence stars, deriving luminosity mainly from nuclear burning, and hot enough to cause copious ionization.

In a similar fashion, for K3-50C (K5) we obtained a temperature 35 ± 2 K, which Truch et al. (2008) underestimated due to confusion in the maps combined with the uncertainties in the assumed model. The energetics of K5 are primarily influenced by the two radio sources inside the clump, namely K3-50C1 and K3-50C2 (Samal et al., 2010). Compared to K3-50A, the dust temperature is somewhat lower, suggesting that K3-50C is deeply embedded inside the molecular cloud, is less energetic, and is perhaps somewhat less evolved. Integrating the SED for K3-50C, we obtain a luminosity of (36 ± 4)×10^4 $L_\odot$ which is equivalent to ∼O6 on the ZAMS (Panagia, 1973). The clump mass is (55 ± 14)×10^2 $M_\odot$, placing it in the appropriate position in the *L*-*M* diagram.

K3 is located between the two radio sources K3-50E and K3-50F, to its West and East, respectively (see Fig. 2.5). Its luminosity is (5 ± 1)×10^4 $L_\odot$; Samal et al. (2010) underestimated the luminosity (∼ 2.5×10^3 $L_\odot$) due to the absence of FIR/submillimeter coverage. The luminosity and mass of (10 ± 2)×10^2 $M_\odot$ position K3 in the *L*-*M* plane as a "class I" object, though with possibly some power coming from accretion. Its equivalent single-star ZAMS spectral type is ∼O8.5, indicating the possibility of ionizing its surroundings. No significant radio continuum emission peak is detected either at 1420 MHz (see Fig. 2.5) or above the 5 mJy level at 1280 MHz (Samal et al., 2010). Possibly there is radio self-absorption, or the ionizing radiation is absorbed by dust in a dense envelope. Alternatively, the luminosity may come from many slightly lower mass stars, which, being cooler, would produce collectively less ionizing radiation.

A general introduction of K1 and K2 was already given in § 2.3.2. An accurate distance estimate for these sources is not available. For our present analysis we have assumed a distance of 8.7 kpc, similar to the K3-50 region. However, note that the assessment of the evolutionary stages from the *L*-*M* diagram is not affected by the distance uncertainty; the position on the *L*-*M* plane simply shifts diagonally along a line of constant L/M or temperature. The K2 clump is associated with emission in the *IRAS* 60 and 100 μm bands and has extended *MSX* 8 μm emission as well. It is relatively hot, with a temperature of 33 ± 1 K. The *L*-*M* plot suggests it is a less energetic version of K3, though the *MSX* morphology is distinctly different. K1, projected at the outskirts of the K3-50 region, with no YSO or radio counterpart, is the coldest BLAST clump in this region, at 19 ± 1 K. In the *L*-*M* diagram it is at an earlier stage of evolution, beginning

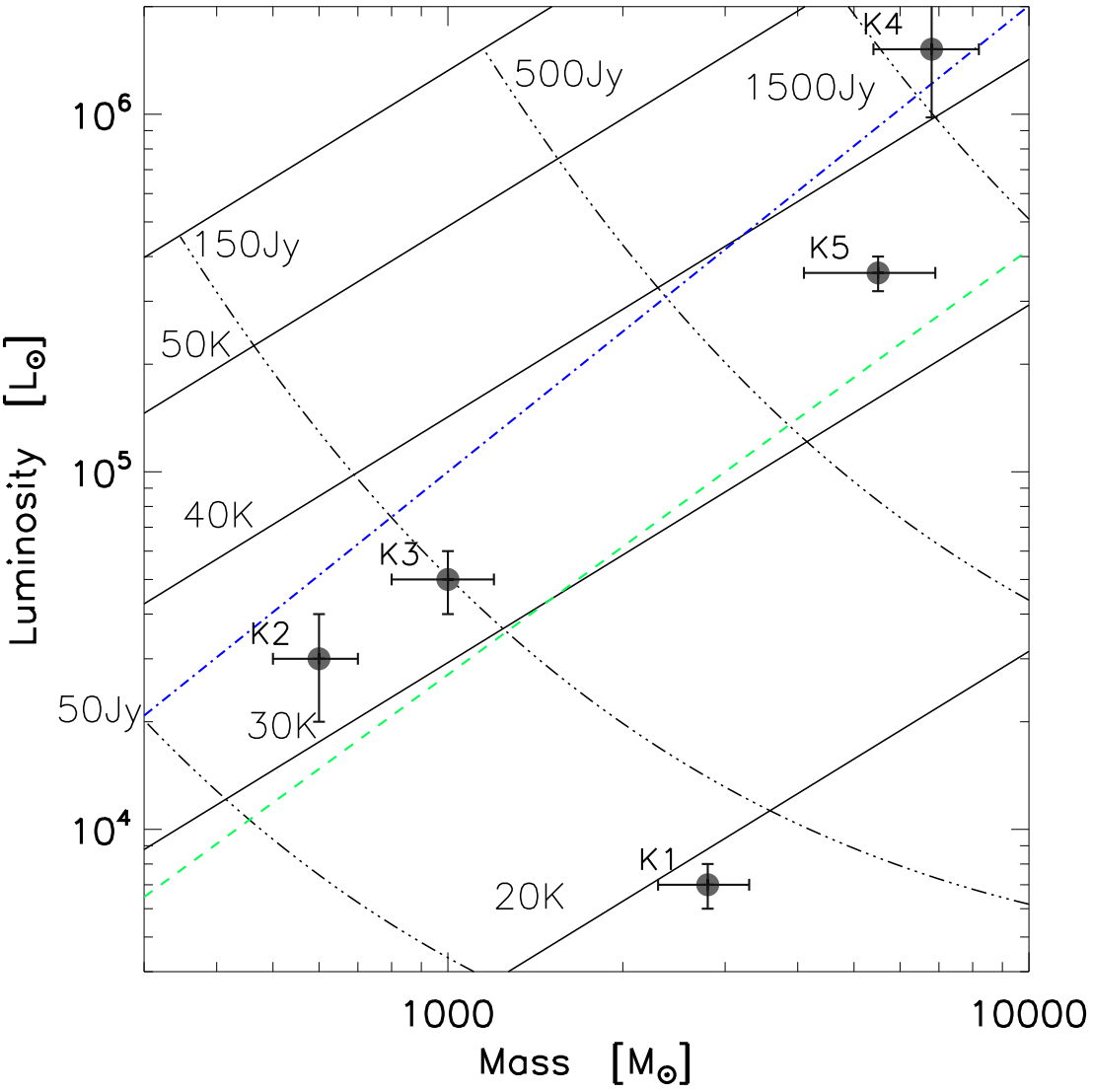

Figure 2.9 BLAST compact sources in the K3-50 region in the L-M plane. Solid diagonal lines are loci of constant T or L/M. Dot-dash curves orthogonal to these are for constant 250 μm flux density. Dash and dot-dash lines denote sources powered by accretion and nuclear burning, respectively, as derived empirically in Fig. 9 of Molinari et al. (2008).

to be powered by accretion.

2.5 Science Results for IC 5146

The IC 5146 molecular cloud complex in Cygnus has been widely studied in the optical, IR (Herbig & Dahm, 2002), submillimeter (Kramer et al., 2003) and molecular lines (Dobashi et al., 1992). Using infrared color excesses in the *JHK* bands, Lada et al. (1994) produced an extinction map, i.e., the spatial distribution for the dust column density. They also surveyed in the molecular line emission of ^{13}CO, C^{18}O, and CS. Herbig & Reipurth (2008) provide a summary of the observational progress achieved in this star-forming region. Harvey et al. (2008) have surveyed the IC 5146 region with *Spitzer* to study the properties of young stellar objects. Distance estimates range from 460 pc to 1.4 kpc (see Harvey et al., 2008 and references therein). We have adopted 1 kpc from Dobashi et al. (1992), which is close to the 950 pc used by Harvey et al. (2008). Proximity is an advantage for probing the workings of star-forming regions. At this distance, BLAST can resolve spatial structures of about 0.3 pc. Our BLAST05 observation (Fig. 2.10) targeted the filamentary structure of the "Northern Streamer," one of the densest molecular clouds in IC 5146 ("cloud C" of Dobashi et al., 1992), and reportedly the most massive ($\sim$2.2$\times$10^3 $M_\odot$). The field also contains the dark cloud L1030 and L1031 to the South-West.

Table 2.2: Flux densities of BLAST sources in the IC 5146 field

ID	BLAST Source Name	l	b	F_{250} (Jy)	F_{350} (Jy)	F_{500} (Jy)	F_{100} (Jy)	F_{60} (Jy)	F_{24} (Jy)
IC1	J214558 + 471835	93.4334	−4.6663	97.1 ± 9.0	75.1 ± 7.3	32.5 ± 2.1	···	···	···
IC2[a]	J214508 + 473305	93.4842	−4.3840	42.5 ± 1.5	39.7 ± 1.4	22.4 ± 0.8	29.0 ± 0.5	14.2 ± 0.1	0.7
IC3	J214626 + 471757	93.4844	−4.7141	60.1 ± 4.7	42.3 ± 2.3	24.0 ± 1.0	···	···	0.1
IC4[b]	J214452 + 474026	93.5297	−4.2616	38.4 ± 2.0	31.5 ± 1.5	19.9 ± 1.2	24.3 ± 0.3	13.3 ± 0.01	0.8
IC5	J214534 + 473559	93.5703	−4.3936	15.0 ± 1.0	12.1 ± 0.6	8.7 ± 0.4	···	···	0.1
IC6[c]	J214443 + 474635	93.5769	−4.1670	45.1 ± 3.4	33.5 ± 1.7	19.8 ± 1.2	10.1 ± 0.3	2.3 ± 0.1	0.2
IC7	J214558 + 473536	93.6132	−4.4397	69.1 ± 6.5	47.7 ± 2.3	30.0 ± 1.3	20.0 ± 6.2	1.7 ± 0.1	0.2
IC8	J214707 + 473242	93.7369	−4.6054	23.0 ± 2.6	20.6 ± 1.5	11.4 ± 1.5	···	···	···
IC9[d]	J214722 + 473221	93.7659	−4.6372	186.6 ± 3.4	121.8 ± 2.2	66.9 ± 1.2	97.5 ± 10.0	$36. \pm 2.2$	2.5
IC10	J214759 + 473643	93.8913	−4.6470	45.4 ± 2.7	30.8 ± 1.3	14.7 ± 0.8	12.5 ± 1.2	2.4 ± 0.2	0.3

[a]IRAS 21433+4719

[b]IRAS 21429+4726

[c]IRAS 21428+4732

[d]V1735 Cyg, Elias1-12

2.5.1 Compact Sources

Figure 2.10 shows the locations of ten BLAST compact sources in the IC 5146 region. Six of these, with *IRAS* counterparts, were identified as protostellar candidates by Dobashi et al. (1992). Among these, Elias1-12 (our IC9) is a T-Tauri star (Elias, 1978), also known to be associated with molecular outflows (Levreault, 1983). Follow-up surveys with ^{12}CO (Dobashi et al., 1993, 2001) have shown that all of these sources have molecular outflows, revealing the early stages of star formation in progress inside the embedding clumps seen by BLAST. The squares in Figure 2.10 correspond to the peak positions of the velocity-integrated ^{13}CO ($J = 1 \rightarrow 0$) molecular line emission map. There is no direct correspondence between the BLAST dust emission peaks and the ^{13}CO peaks, but the BLAST compact sources are associated with the CO clumps (see Fig. 6 of Dobashi et al., 1992).

Harvey et al. (2008) have detected 60 YSO candidates within the region surveyed by BLAST. Using the slopes across MIPS and IRAC data they classified 38 objects into Class I, flat, II, and III. These relate to progressively later stages of YSO evolution (Evans et al., 2009). Their positions and classifications are given in Figure 2.10. Along the dense "Northern Streamer" most of the sources belong to Class I and flat classifications, i.e., earlier stages of evolution. Likewise, there are *Spitzer* YSO counterparts to the ten BLAST sources, these mostly being Class I. These YSOs within the more extensive BLAST clumps (0.3 pc) are of relatively low power and so the dust is not significantly internally heated and the BLAST dust temperatures are all quite low. For example, IC9 contains several YSOs (in the 2MASS K-band image there is reflection nebulosity). At the present submillimeter sensitivity and resolution, not all YSOs have BLAST counterparts.

We have characterized the physical properties of the identified BLAST clumps by fitting SEDs as described in § 2.4. Compared to the K3-50 region (dominated by warm dust emission), the dust temperature of IC 5146 is relatively cold, which motivated us to constrain SEDs with a spectral index of $\beta = 2.0$.

Where there are separable *IRAS* sources, before performing photometry on the BLAST sources, we have convolved the respective maps to the $2'$ native beam resolution of the IGA 100 μm images (Cao et al., 1997). Otherwise we used the better BLAST resolution. Table 2.2 summarizes the flux densities. All of these sources have 250 μm flux densities greater than at 100 μm, indicating a relatively cold dust temperature. Constraining the

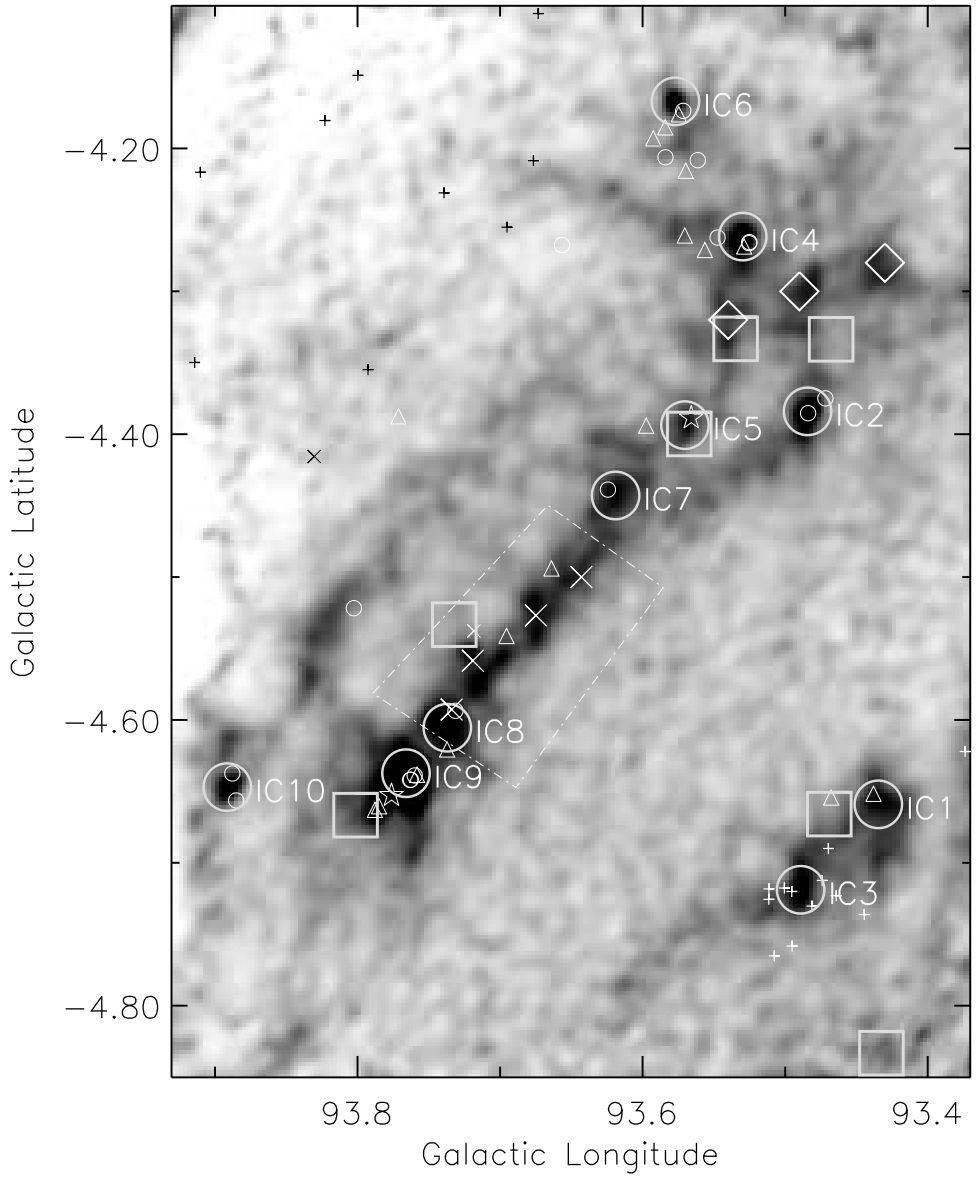

Figure 2.10 BLAST map of IC 5146 at 250 μm, showing relationships to other cataloged objects. Circles of radius 1′ locate the BLAST compact sources. Large squares correspond to the peak positions of the velocity-integrated ^{13}CO ($J = 1 \rightarrow 0$) molecular line emission map (Dobashi et al., 1992). YSOs from Harvey et al. (2008) are shown by small circles, stars, triangles, and crosses, to distinguish Class I, flat, II, and III spectra, respectively; the plus symbols represent YSO candidates for which there is no classification. The dust temperature of the cold filament within the outlined dot-dashed box is 11.7 ± 0.4 K (§ 2.5.2). Four cores characterized by Kramer et al. (2003) are marked with large crosses. Some additional cold and starless clumps identified by BLAST are marked by large diamonds.

Table 2.3: SED best-fit parameters of BLAST sources in the IC 5146 field

ID	T (K)	$M_{\rm tot}$ ($M_\odot$)	L ($L_\odot$)
IC1	12.7 ± 1.2	171 ± 50	48 ± 16
IC2	16.3 ± 0.6	35 ± 8	43 ± 4
IC3	14.9 ± 0.1	64 ± 6	47 ± 5
IC4	16.1 ± 0.7	33 ± 9	38 ± 4
IC5	14.9 ± 0.1	15 ± 2	11 ± 2
IC6	13.6 ± 0.3	73 ± 11	31 ± 2
IC7	14.0 ± 0.3	106 ± 10	53 ± 3
IC8	15.0 ± 0.1	25 ± 3	19 ± 2
IC9	15.7 ± 0.3	176 ± 18	171 ± 12
IC10	14.3 ± 0.3	55 ± 7	31 ± 2

SEDs with the longer wavelength data points is important, but unfortunately SCUBA has observed only a small part of the IC 5146 region (Fig. 2.7). This includes IC7, IC8 and IC9, for which we obtained integrated 850-μm flux densities of 10.6, 1.5, and 5.6 Jy, respectively. For the cool sources here we have used only the 100 μm flux density in the SED fits, while the 60 and 24 μm flux densities provide upper limits, as discussed in Chapin et al. (2008) and Truch et al. (2008). As an example we show the SED for the brightest clump, IC9, in Figure 2.11.

Table 2.3 summarizes the physical quantities T, M, and L obtained from the best-fit parameters of the SEDs. In this region of IC 5146 the luminosities of the identified BLAST sources range from 11 to 170 $L_\odot$ and the masses from 15 to 180 $M_\odot$. The temperatures range from 12.7 to 16.3 K, with an average of 14.8 K.

When a clump is more massive than the Bonner-Ebert critical mass, then gravity overpowers the internal (thermal, magnetic, and turbulent) supporting pressure and it undergoes collapse. Our BLAST mass estimates appear to be above the critical mass (using the simple prescription described in Kerton et al., 2001), suggesting that the compact sources are gravitationally unstable. Indeed, there are already some YSOs that are generating outflows. Dobashi et al. (2001) showed how physical processes relating to mass, momentum, and energy carried away by the outflows have direct consequences for the stability of the parent cloud and as well influence the evolutionary dynamics of the embedded stars. These outflow parameters have a correspondence with the bolometric

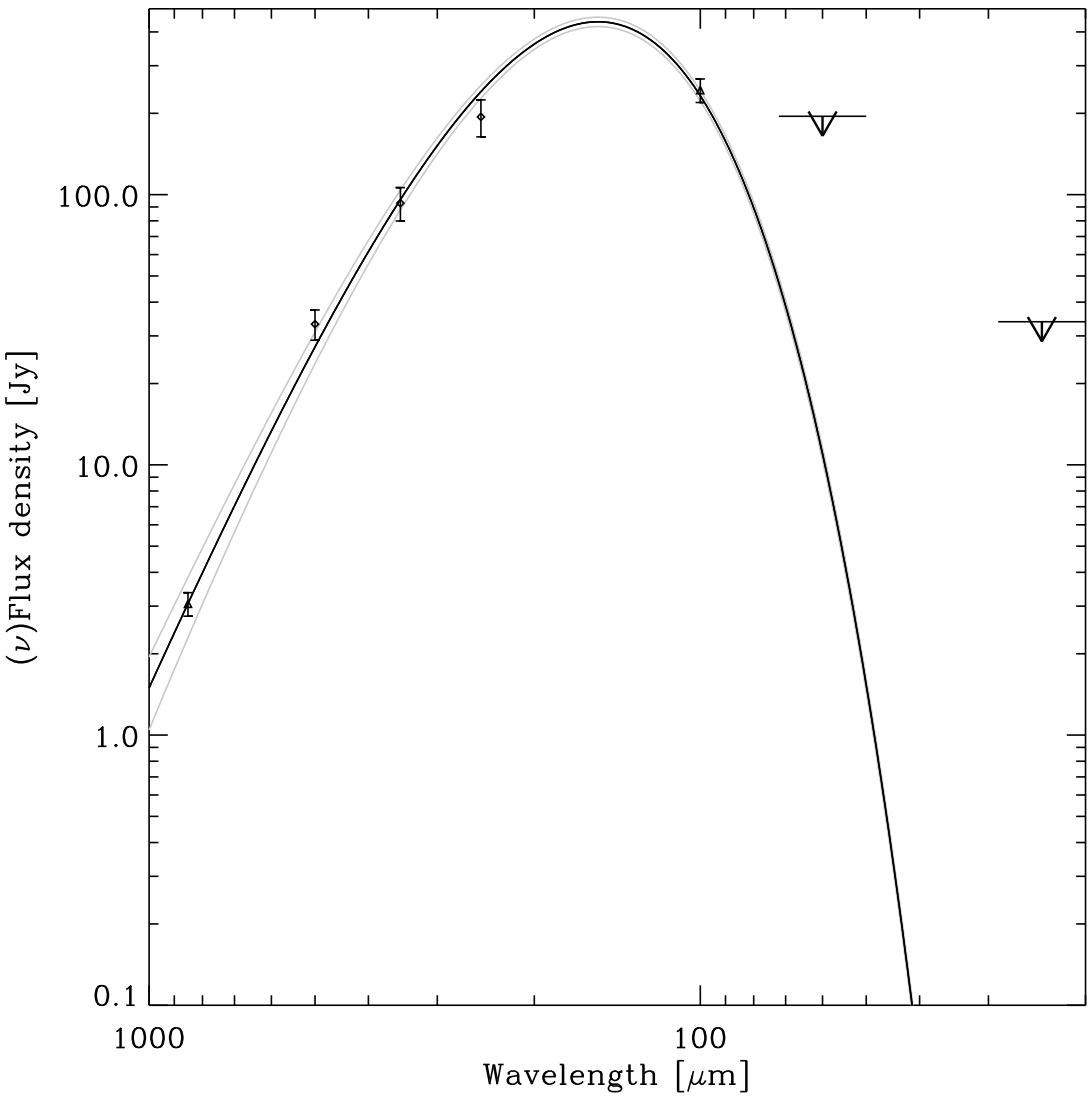

Figure 2.11 SED as in Fig. 2.8, but for IC9 (Elias1-12) in the IC 5146 region fit with $\beta = 2$. Arrows for short-wavelength data represent 3-σ upper limits above the measured flux density. The best-fit temperature for the cold envelope is 16 K.

luminosity of the accreting source (Dobashi et al., 2001). Certainly feedback processes have already begun in this molecular cloud, and Dobashi et al. (1992) have suggested that outflows have played an important role in supporting the parent cloud from collapsing.

2.5.2 Cold Central Filament

Apart from the above-mentioned compact sources, BLAST observes abundant substructure in the Northern Streamer region. The infrared extinction map by Lada et al. (1994) has also revealed a distribution of high column density clumps throughout this filament. There is a good correlation of A_V with the ^{12}CO and ^{13}CO molecular line emission maps by Dobashi et al. (1992). Not unexpectedly, our dust emission map also has a strikingly tight correlation with A_V (and CO which might not be a perfect tracer of column density at large spatial density), and with 850 μm emission, as shown in Figure 2.7.

With earlier SCUBA observations Kramer et al. (2003) studied a narrow 14′ by 2.′5 region extending from IC7 (only at the boundary of their map) to IC8 (included). From the SCUBA colors they found dust temperatures ranging up to 20 K at the outskirts and between column density peaks and down to 10 K in "cores" (coincident with peaks in A_V), embedded condensations that effectively shield the interstellar radiation from which the dust derives its power in the absence of a YSO. Note that along the central filament studied there are no embedded YSOs (Fig. 2.10), except at the two ends.

We have estimated a global dust temperature for the portion of the streamer within the box shown in Figure 2.10, by fitting a relative SED to the pixel-pixel correlation slopes of the image data with respect to 250 μm. We have used the 850 μm SCUBA map to constrain the spectrum at long wavelengths. The filament is not prominent in *IRAS* bands because the dust is cold. Figure 2.12 shows the SED. With a dust emissivity index β of 2.0 the best-fit temperature is 11.7 $\pm$ 0.4 K, which agrees well with Kramer et al. (2003).

2.5.3 Cold Starless Clumps

Because the BLAST bands are sensitive to colder dust emission we can detect cold clumps early in their pre-stellar evolution, when their primary energy source is the external radiation field ("stage E" in Roy et al., 2011b). Good examples confirmed by BLAST are the four "cores" identified by Kramer et al. (2003) and marked by large crosses in Figure 2.10. The core numbered 2 by Kramer et al. (2003) is the warmest (18.2 K).

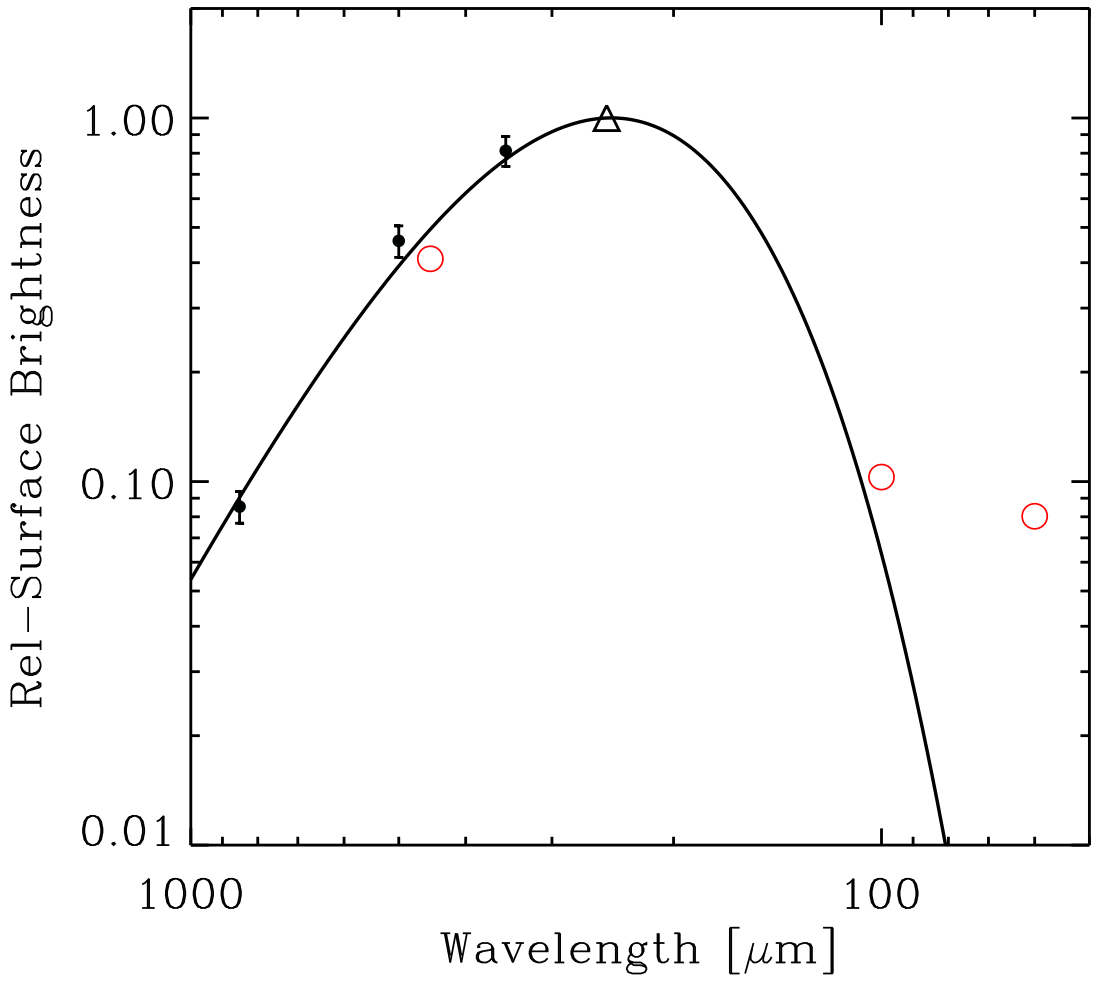

Figure 2.12 Relative SED obtained from pixel-pixel image correlation with respect to 250 μm emission for the area within the dot-dashed box marked in Fig. 2.10. With the dust emissivity index β fixed at 2.0, the best-fit temperature is 11.7 ± 0.4 K. Data points represented by circles are not actually used in the fit, while the triangle shows the value of unity at the normalizing 250 μm point.

This is a complex region near IC8 with large temperature gradients influenced by a YSO visible even to *IRAS* at short wavelengths. However the other three cores are cold and apparently starless.

With the larger spatial coverage of the BLAST survey we have identified other cold clumps that have no signs of star formation yet. Some prominent examples are marked by large diamonds in Figure 2.10, at the positions of the peaks in the 500 μm map. Comparing with the visual extinction map of Lada et al. (1994), we find that these BLAST clumps G93.43−4.28, G93.48−4.30, and G93.54−4.33 have A_V about 10, 20, and 6 mag, respectively.

The morphology in this field is complex and variable with wavelength, because of the different stages of evolution occurring in close proximity. For example, the protostar IC4 occurs at the end of an elongated condensation that has a cold extension in the direction of G93.54−4.33. Studies of this region will benefit from the improved resolution of *Herschel*. With map zero points available from Planck, it will be interesting to map the temperature structure in detail, as has been accomplished in other fields (Bernard et al., 2010; Juvela et al., 2010a).

2.6 Conclusion

The Lucy-Richardson deconvolution algorithm has been applied successfully to improve BLAST05 images obtained with a corrupted (but known) PSF. This deconvolution has enhanced the raw BLAST map of $\sim 3\farcm3$ resolution to $\sim 1'$, near the anticipated diffraction limit. This improves the detectability of faint sources; diffuse structures are revealed in finer detail as well. We have checked via simulations the robustness of applying the L-R scheme, especially the aspects of conserving flux, reliability of restoring intrinsic sizes, and performance in resolving sources in a crowded field. For the actual deconvolved maps of BLAST05 survey fields we have provided further ground truth for the improved detail in crowded fields and for diffuse structures, by comparing with available multi-wavelength high resolution images of dust and other tracers.

We have presented science results enabled by the deconvolved maps of two star-forming regions covered by BLAST05, namely K3-50 and IC 5146. We were able to resolve three crowded sources in K3-50, namely K3-50A, K3-50C, and IRASB, and have also characterized another two sources which had previously remained undetected.

The deconvolved maps of IC 5146 have further shown the richness of the field, consist-

ing of both large scale diffuse structures and compact sources, with a considerable range of dust temperature because of the different stages of evolution. The compact BLAST sources characterized here all have associated YSOs. However, these are not so powerful as to heat up the entire dust clump measured by BLAST, so that $L/M < 1\ L_{\odot}/M_{\odot}$ and the effective dust temperature is rather low; star formation is just getting under way. In fact elsewhere there are high column density structures that are starless, like within the central filament in the Northern Streamer, for which we have obtained an average dust temperature of 11.7 K. We have found further examples in the wider BLAST field surveyed.

Chapter 3

BLAST05: A 10 deg^2 survey of star formation in Cygnus X

3.1 Introduction

We report on an unbiased survey of the Cygnus X (Cyg X) high-mass star formation region, conducted in 2005 by BLAST (see § 2.1). A primary ambition for BLAST was to study the earliest stages of massive protostellar evolution. Massive stars play an important role in Galactic ecology, initially through protostellar outflows and later through radiation pressure, ionization, stellar winds, and supernova explosions, and yet, in spite of their pivotal role, very little is known about their formation (Zinnecker & Yorke, 2007).

Massive molecular clouds are favorable sites for massive star formation. If they are sufficiently dense to be self-gravitating, then they also have high extinction. Even in the near to mid infrared they have significant optical depth, affecting observations of any embedded protostars, and leading to the "infrared dark cloud" (IRDC) phenomenon seen by ISO (Perault et al., 1996), *MSX* (Egan et al., 1998; Simon et al., 2006), and *Spitzer* IRAC and MIPS (Carey et al., 2005; Kraemer et al., 2010a). Some IRDCs are nurseries of young protostellar objects and protoclusters (Simon et al., 2006). However, IRDCs, by definition found in silhouette, require a luminous diffuse background. Massive clouds can be discovered directly, without this detection bias, by their far-infrared to mm-wave optically-thin thermal dust emission. BLAST exploits this fact.

We introduce the BLAST imaging of Cyg X in § 3.2. BLAST detects thermal emission from dust in largely neutral regions and so provides a complementary view of the ISM compared to, for example, radio emission from ionized gas (§ 3.2.1; though both are ulti-

mately dependent on the local stellar radiation field and so are related spatially in some predictable ways). An important feature of BLAST imaging is its capability of observing and characterizing extended structures in the star-forming environment at different spatial scales (§§ 3.2.3 and 3.2.4). In §§ 3.2.5 and 3.2.6 we describe the identification and quantification of BLAST compact sources. Appendix 3.8 discusses measurement of their flux densities at different wavelengths for use in the multi-wavelength SED.

Blind submillimeter surveys with BLAST (Chapin et al., 2008; Netterfield et al., 2009), precursors to those with *Herschel* (e.g., Molinari et al., 2010b), are ideally suited for finding and characterizing cold sources, because of the designed coverage near the peak of the cold dust SED. This allows us to determine where the dust temperature T is low, a key requirement before determining the cold dust column densities and masses. BLAST of course also sees the later evolutionary stages when the dust is warmed up by the forming protostars, and again the multi-wavelength coverage tightly constrains both dust temperature and bolometric luminosity ($L_{\rm bol}$).

In order to interpret the BLAST emission more fully, and place the compact sources in context, we make use of many different surveys of Cyg X in other tracers, including both continuum emission and molecular lines. These rich multi-wavelength, multi-species surveys of Cyg X are the basis of a brief overview of the physical environment in § 3.3.

The SEDs and deduced properties T, L, and mass M of the compact sources are presented in § 3.4. As we discuss in § 3.4.6, the mass of the compact source, along with its luminosity (which maps into T), determine its position on an evolutionary track in the L-M diagram (Molinari et al., 2008). Investigating the stages of high mass protostellar and protocluster evolution is a prime aspect of this chapter.

In the earliest stages, before there is any (significant) internal source of energy from accretion or nuclear burning, the dust is heated only by the external radiation field. Because of the high extinction the dust is cold, with T typically $\sim$ 15 K or lower, but in any case colder than the "ambient" temperature of diffuse dust in the same external radiative environment (which near these star forming molecular clouds might be much more intense than the local interstellar radiation field). Such cold clouds, and the initial gravitationally-bound condensations within them are therefore rather invisible to *IRAS*, but are in principle detectable by BLAST and ground-based surveys targeting regions of high extinction (e.g., Motte et al., 2007 using MAMBO at 1.2 mm). According to the time sequence and nomenclature used for low mass star formation, sources detected in this earlier evolutionary stage could be called "class -1." However, as a reminder of

the energetics, we prefer the physically-motivated shorthand "stage E" (from Externally heated, but also usefully Earliest – see § 3.5.6). Likewise, we call sources in the subsequent evolutionary stage, when there is sufficiently vigorous accretion power internally to raise the dust to the ambient or higher temperature, "stage A" (see § 3.5.5; the low mass analog would be "class 0").

An illustrated view of the evolutionary stages of massive star formation, illuminated from the BLAST submillimeter perspective, is presented in § 3.5. A key factor that is important to the interpretation of our particular observations is that massive stars form in stellar groups and star clusters (Lada & Lada, 2003). The approximately $1'$ angular resolution (FWHM) of the BLAST images corresponds to 0.5 pc at 1.7 kpc. This is the size scale (sometimes called a "clump" – Bergin & Tafalla, 2007) of the observed embedded and newly-emerging clusters in Cyg X (Le Duigou & Knödlseder, 2002; § 3.3.1). Thus it is relatively straightforward to search for the precursors to these protoclusters, within which massive protostars will be the dominant source of luminosity and ionizing radiation. However, resolving protoclusters into unconfused condensations (a smaller linear scale sometimes called "cores") that are destined to form single (proto)stars requires more angular resolution than has been available in surveys (even with the $11''$ beam of MAMBO2 which is smaller than achieved here with BLAST). Submillimeter observations with the larger telescope of *Herschel* will be better ($18''$ at 250 μm with the SPIRE camera), but not immune to these considerations.

Empirically, Bontemps et al. (2009) have made an extensive study of fragmentation and sub-fragmentation inside targeted molecular dense cores in the Cyg X region with interferometric observations at Plateau de Bure. Theoretically, it is still unclear how clusters containing massive stars form (McKee & Tan, 2003; Krumholz & McKee, 2008; Bonnell et al., 1997, 2001, 2007; Smith et al., 2009; Wang et al., 2010). Some insight provided by the BLAST observations and ancillary data, coupled with current theory is the focus of the discussion in § 3.6.

3.2 BLAST Imaging of Cyg X

Cyg X, positioned in the Galactic Plane at about $l = 80^\circ$ and about 1.7 kpc away from the Sun (Schneider et al., 2006a), has long been known for its massive star formation. With BLAST (Pascale et al., 2008; Truch et al., 2008) we surveyed 10 deg^2 in Cyg X for 10.6 hr during the June 2005 flight (BLAST05), mapping the area on three visits

to provide cross-linked scanning. In addition, a significant amount of calibration-related time was spent observing a circular cap of radius 1° centred on W75N, resulting in even higher signal to noise and dynamic range there.

Final maps on 15″ pixels were produced using the map-maker SANEPIC (Patanchon et al., 2008a). The combination of high scan speed and low $1/f$ knee, together with the cross-linking and common-mode removal in SANEPIC, produces a map retaining diffuse low spatial frequency emission, in contrast to current ground-based mm-wave mapping which contends with the atmosphere and therefore is spatially filtered and emphasizes the compact structures. However, preprocessing of the time-ordered data to remove very low frequency drifts makes the SANEPIC map average near zero, the DC level having been effectively removed.

BLAST05 was designed to produce diffraction-limited beams with FWHM 30″, 42″, and 60″ at 250, 350, and 500 μm, respectively. However, BLAST05 suffered from an uncharacterized failure relating to the primary mirror figure and focus. Nevertheless, even with the corrupted beam the resolution is about 3′ full width half power (Truch et al., 2008; Roy et al., 2010), comparable to *IRAS*, though disappointing compared to the diffraction-limited images obtained in the 2006 flight (Truch et al., 2009; Netterfield et al., 2009).

The characteristic beam shape can be seen clearly at many locations throughout the field, indicating the presence of point sources with angular size comparable to the diffraction limit. Obviously we want to work with images with as good resolution as possible. We removed the worst effects of the corrupted beam (Roy et al., 2011a) by a Lucy-Richardson deconvolution algorithm (Richardson, 1972; Lucy, 1974). The significant improvement is illustrated in Figure 3.1. Even so the effective resolution is about 1′, less dependent on wavelength than for diffraction (which has the silver-lining benefit that beam matching is not an issue). Moreover, there are artifacts introduced near very strong sources. Mathematically, Lucy-Richardson deconvolution should conserve flux, and we have verified this through simulations and measurements on isolated compact sources (§ 3.2.6). The astrometric accuracy is good, about 5″ when the deconvolved maps (§ 3.2.6) are aligned with compact sources in common with MAMBO2 (Motte et al., 2007) and/or SCUBA (Di Francesco et al., 2008).

The full 250-μm map is shown in the upper panel of Figure 3.2. BLAST measures the dust continuum emission along the line of sight and probes the major star-forming sites in the region by detecting reprocessed stellar or protostellar radiation. The positions

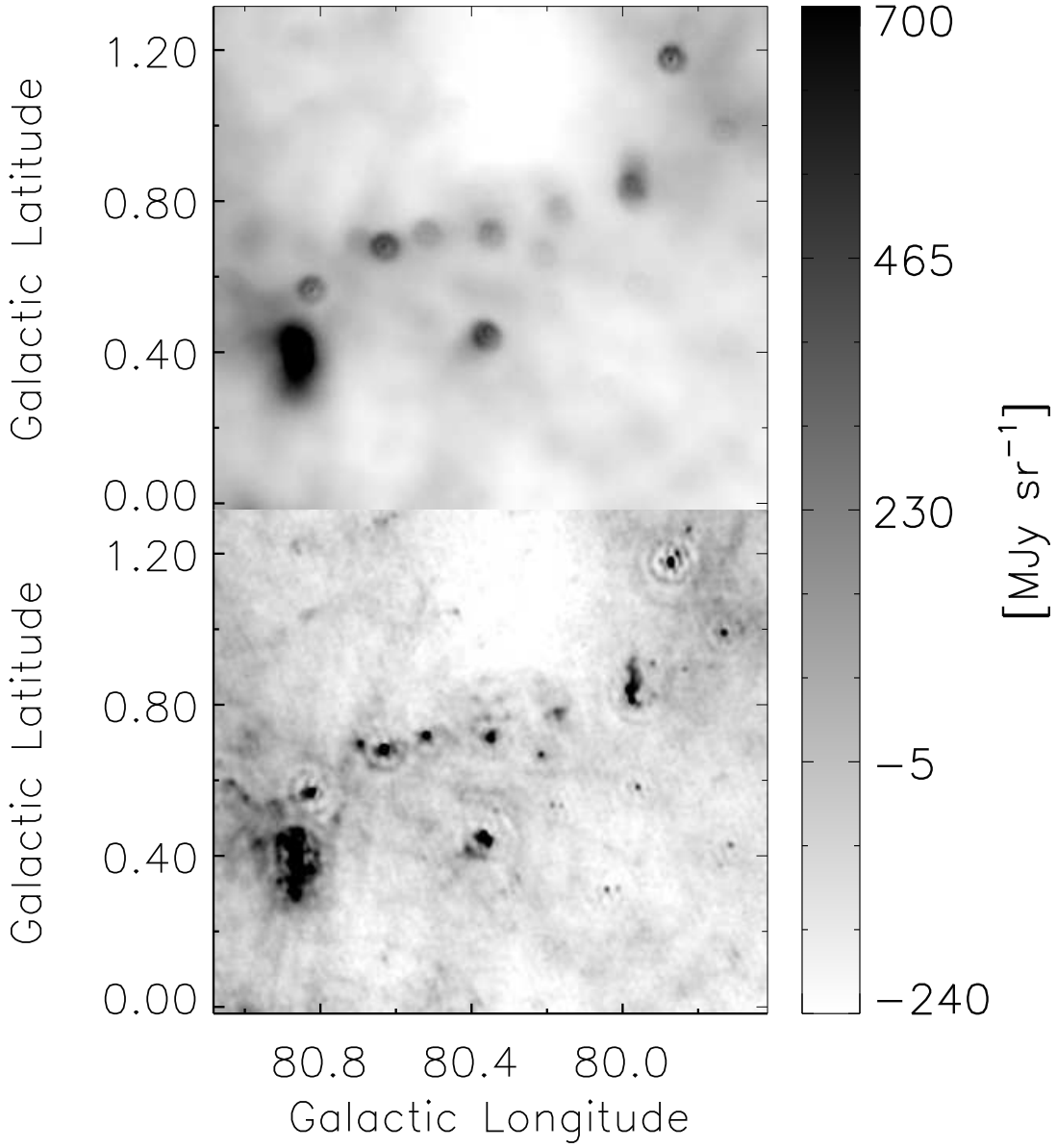

Figure 3.1 Upper: enlarged section of 250 μm BLAST05 image in Fig. 3.2. Lower: deconvolved image using a Lucy-Richardson algorithm. Full width half maxima of the deconvolved sources are about 1′.

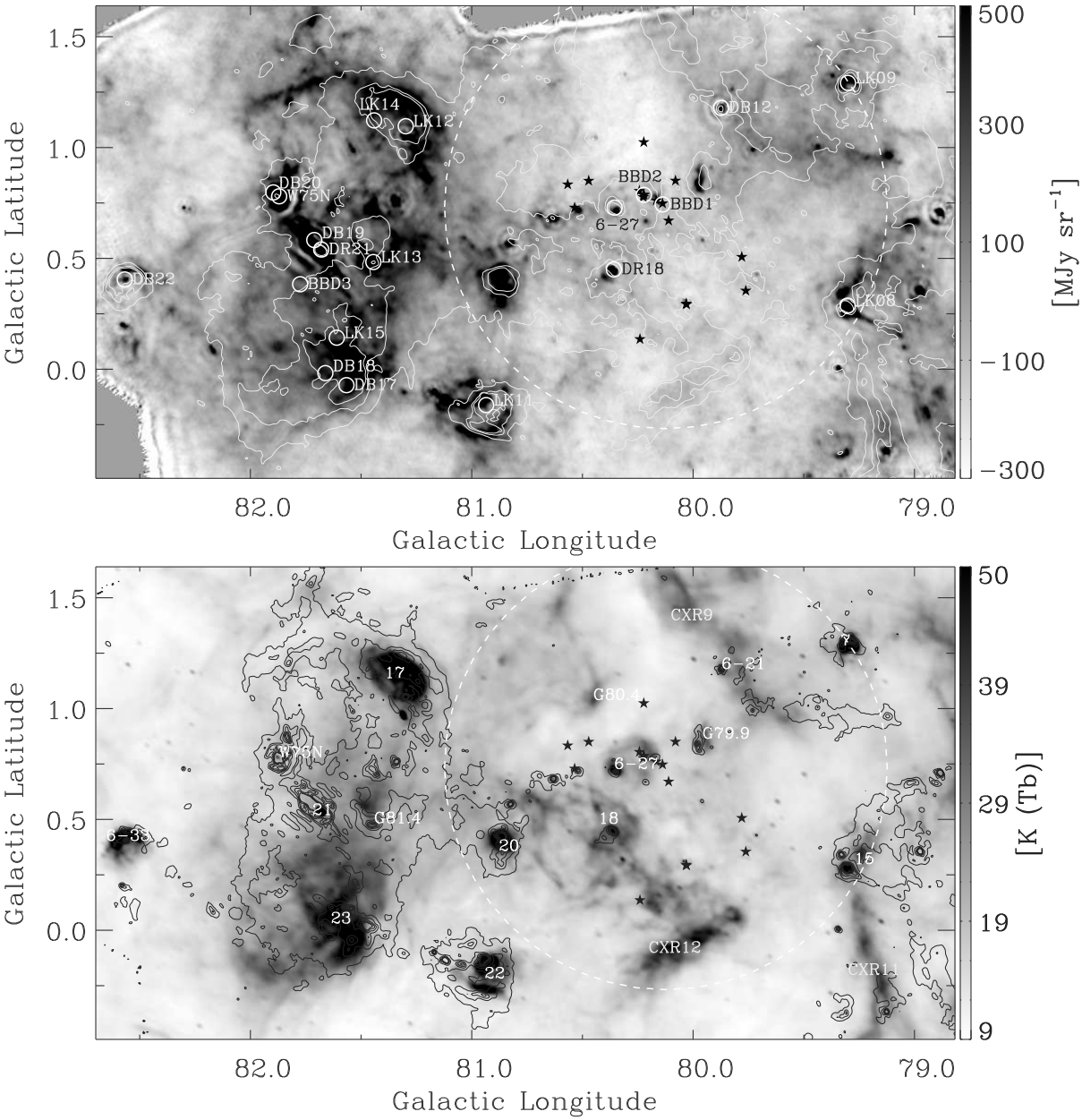

Figure 3.2 Upper panel: BLAST05 deconvolved 250 μm dust emission map of Cyg X. Contours are of 21-cm radio continuum emission from the CGPS in the lower panel. The large dashed circle of radius 60′ shows the extent of the Cyg OB2 association (Knödlseder, 2000) and the stars are the most luminous O stars in the list of Negueruela et al. (2008) (see text). Circles denote the positions (not extent) of star clusters (see § 3.3.1 for nomenclature). Lower panel: The radio image in turn has contours from the BLAST05 image. Prominent H II regions and diffuse ridges are marked (see § 3.2.1 for nomenclature).

of luminous stars in the Cyg OB association (Negueruela et al., 2008) and a number of stellar clusters (§ 3.3.1) are indicated for reference. Expanding H II regions, bubbles, and stellar outflows, and the interplay with structures in the ISM make the morphology of extended emission in the Cyg X region quite complex. A comprehensive review covering important physical aspects of Cyg X is presented by Reipurth & Schneider (2008).

3.2.1 A Complementary View using Radio Continuum Emission

A complementary way to see the effects of the high-energy radiation from hot massive stars is via radio emission from the ionized gas. The lower panel of Figure 3.2 shows the 21-cm continuum map from the CGPS (Taylor et al., 2003), which has $1'$ resolution, about the same resolution as the BLAST maps. A number of H II regions are labelled for reference: numerals n are DRn regions from Downes & Rinehart (1966), ECX6-* from Wendker et al. (1991), and otherwise Gl (accurate coordinates for these three regions being G79.957+0.866, G80.451+1.041 and G81.445+0.480). Note that the recombination line velocity for G79.9 is -14.8 km s^{-1}and for ECX6-27 is -64.4 km s^{-1}(Lockman, 1989), putting these beyond the Cyg OB2 association.

In diffuse regions the free-free emission is optically thin, but for the most dense compact H II regions, it can be self-absorbed. There is rough correspondence with the dust emission, as might be expected given the impact of OB star radiation on both. Note, however, that unlike the dust emission, which depends on the column density, the H II emission depends on the emission measure, involving the square of the local density. Furthermore, ionizing radiation is obviously essential to produce the plasma. This radiation, the rest of the non-ionizing starlight, trapped Lyman-α, and cooling lines all heat any dust surviving in the plasma. Most of the sub-ionizing radiation escapes the plasma to heat any dust outside the H II region. In an edge-on geometry, as occurs in extended regions like DR22, the warm dust immediately outside the arc-shaped ionization front (I-front) can be seen (Fig. 3.2 and magnified views in figures below). In a related way, in DR23 the ionization is clearly stopped on the right by a dense cloud which forms a "bay" in the radio emission, and a corresponding bright feature in the dust map.

There are also large scale ionized structures denoted CXRn (Cyg X Ridges) by Wendker et al. (1991). Those in the BLAST region are labelled in Figure 3.2. These are seen dimly in the BLAST image because they have relatively low column density (they also

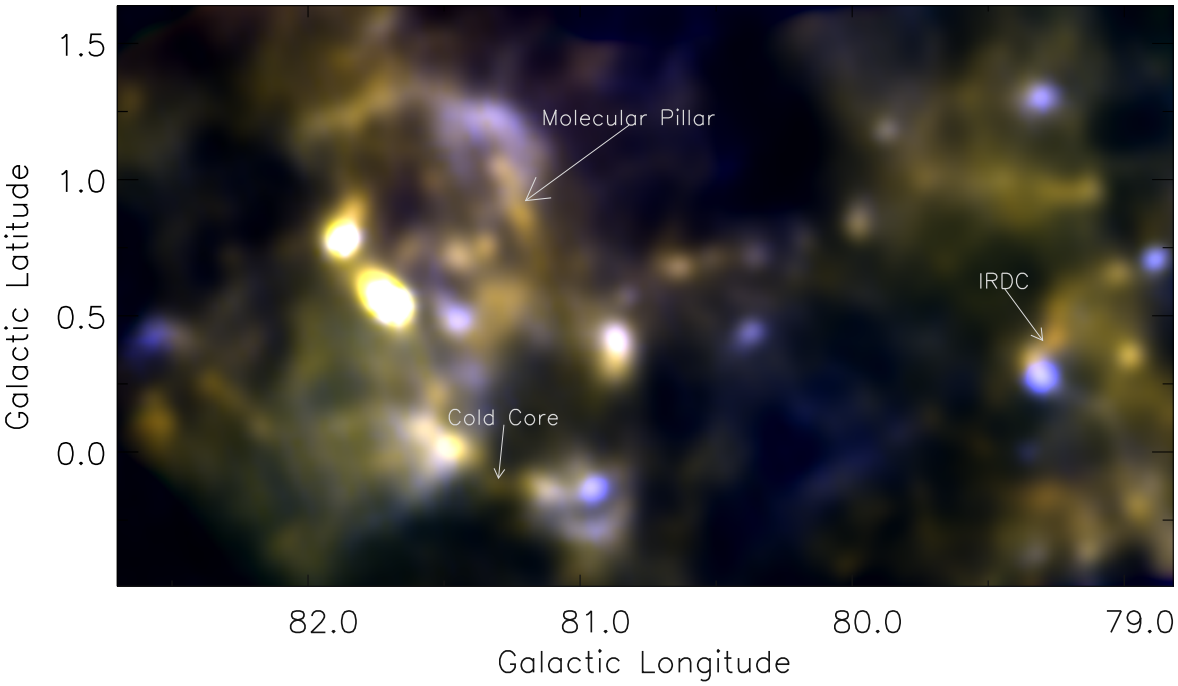

Figure 3.3 Three color BLAST plus *IRAS* image of Cyg X (500, 350, and 100 μm are represented by red, green, and blue, respectively). Images are first convolved to the Planck high frequency $4'$ resolution.

do not show very strongly in the extinction map; § 3.3.4). A much better dust emission tracer (§ 3.2.3) of these ionized ridges, indeed of all of the diffuse ionized gas, is the 24 μm MIPS image, from the *Spitzer* Cyg X Legacy Survey (Hora et al., 2009), which looks remarkably like the radio continuum image.

3.2.2 Planck Cold Core Survey

In the midst of this turmoil, we search for relatively cold structures which could be the precursors of the next generation of stars. This is also the goal of the lower-resolution Planck Cold Core survey (Juvela et al., 2010b), an unbiased search using the Planck all-sky maps of submillimeter dust emission. Cold cores are characterized by a lack of corresponding *IRAS* 100 μm emission. Because the Planck high-frequency angular resolution is $4'$, clumps – even if more extended than the BLAST clumps – will appear as point sources, and smaller structures will be beam-diluted. Even for relatively nearby regions like Cyg X, the Planck beam would correspond to a spatial extent of about 2 pc.

The highest-frequency Planck channels correspond approximately to 350 and 500 μm.

Prior to the availability of Planck imaging data, we explored the possibilities by convolving the two longer-wavelength BLAST images to the Planck resolution and combining them with *IRAS* 100 μm in a three-color image (Fig. 3.3). At this resolution, BLAST stage E sources like C116 (§ 3.4 and § 3.5.6) still stand out as being cool. More extended, elongated structures like the cool IRDC ridge near DR15 (§ 3.5.6) and the DR17 molecular pillar (§ 3.3.6 and § 3.5.1) are also preserved. Of course the regions of warmer dust are highlighted in this image as well.

3.2.3 Diffuse Emission

BLAST maps measure surface brightness (MJy sr^{-1}), hence column density of the dust $M_{\rm d}$:

$$I_\nu = M_{\rm d}\kappa_\nu B_\nu(T) = r\mu m_{\rm H} N_{\rm H}\kappa_\nu B_\nu(T), \tag{3.1}$$

where r is the dust to gas ratio, $N_{\rm H}$ is the H column density, and κ_ν is the mass absorption coefficient of the dust. For later characterization of the SED we note that the spectral dependence of κ_ν is usually scaled with respect to a fiducial frequency as $\kappa_\nu/\kappa_0 = (\nu/\nu_0)^\beta$. Note also that for absolute measures of column density we would have to restore the zero point (DC level) of the maps, as we did for the Cas A region (Sibthorpe et al., 2010) but not here.

In the Galactic Plane, cirrus-like structures in the form of bright diffuse emission, termed "interstellar froth" (Waller & Boulanger, 1994), are distributed everywhere. With the compact structures removed, either explicitly or by clipping (Miville-Deschênes et al., 2007a), the diffuse emission has a cirrus-like power spectrum, with lower fluctuations at high spatial frequencies. In fact, we have found that for this region the power spectrum is quite like that for *IRAS* 100 μm, with amplitude simply scaled by the SED^2 for the appropriate cirrus temperature (Roy et al., 2010).

Somehow, through turbulent motions, thermal instabilities, and phase transitions, massive localized regions become self-gravitating and so at high spatial frequencies they stand out from the dwindling cirrus structure as compact sources. A distribution of masses is expected, but the cirrus confusion limits our ability to distinguish lower mass sources (§ 3.2.5). This situation improves with angular resolution, but even for *Herschel* it is a dominant limitation (Martin et al., 2010).

Actually, the diffuse emission in the submillimeter and mid-infrared wavelengths comes from three different dust components, distinguished principally by their size distri-

bution (Desert et al., 1990; Li & Draine, 2001; Compiègne et al., 2011): Big Grains (BGs), Very Small Grains (VSGs), and polycyclic aromatic hydrocarbons (PAHs). The BGs, which account for the most of the dust mass and therefore most of the longer wavelength emission, are in thermal equilibrium. The VSGs have a relatively lower share of the total dust mass, even smaller in dense regions. They are small enough to experience non-equilibrium heating and so broaden the spectrum toward shorter wavelengths, beyond the spectral peak of the BG emission. Compared to what is expected from equilibrium BGs alone, this excess non-equilibrium emission appears typically at 60 μm and shorter wavelengths. PAHs are also non-equilibrium emitters, in strong spectral bands pumped by far-ultraviolet radiation. The relative amounts of emission in these three components can vary from region to region. Schneider et al. (2006a) used the *MSX* band A images (8.3 μm; Carey et al., 2005) effectively as a tracer of PAHs and the environment. We use *Spitzer* IRAC band 4 images (8.6 μm; Werner et al., 2004) from the Cyg X Legacy Survey (Hora et al., 2009) for the same purpose (§ 3.3.3), since they have better sensitivity and resolution. *Spitzer* MIPS 24 μm images trace VSG emission generally, and the hotter grains associated with ionized gas, and so, as commented above, look remarkably like the radio continuum images.

3.2.4 Dust Temperature from the Diffuse Emission

From the above equation it is clear that the BG emission that BLAST sees is modulated by the dust temperature T which is in equilibrium with the local radiation field, whether in the diffuse medium or within a compact source. We concentrate here on the former. For our exploratory work here on the BGs, we adopt a single-temperature SED and therefore fit only data at 100 μm and larger to avoid contamination by VSG emission.

For a sufficiently large and homogeneous region an estimate of the characteristic temperature can be obtained by fitting an SED to the square root of the amplitudes of power spectra. By this method using data at 100, 250, 350, and 500 μm, Roy et al. (2010) obtained a cirrus dust temperature of 19.9$\pm$1.3 K for a relatively uncrowded region (basically the right half of the BLAST map). However, this more global power spectrum method is not practical when the region considered is relatively small, inhomogeneous, and/or focusing primarily on particular substructures.

An alternative approach for smaller regions begins with pixel-by-pixel correlations of images with respect to some reference image (here 250 μm). Small scale structures are

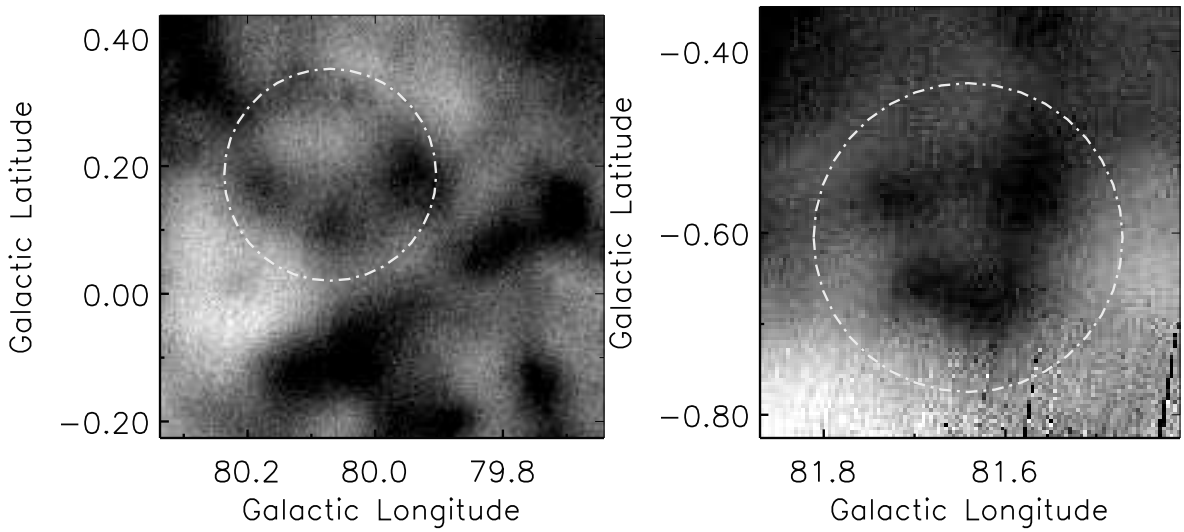

Figure 3.4 Two small regions in Cyg X selected on the basis of a three-color 500, 250, and 100 μm image to have warm (left) and relatively cold dust (images here at 500 μm). Note that as in other figures, white represents lower intensity.

remarkably well correlated across the three BLAST bands. The slopes of these correlations describe the relative SED of the spatially-varying dust emission that is changing in common across these images. Note that this approach cannot give the dust temperature pixel by pixel (that would require the DC offsets too). On the other hand, the emission in each pixel is from dust of different temperatures along the line of sight, whereas our approach isolates and characterizes certain more localized spatial components.

For quantification of the size of the changes in temperature, we selected regions that appeared to have different colors in a map like Figure 3.3.

The first region, shown in 500 μm emission in the left panel of Figure 3.4, is within the relative void created by the Cyg OB2 stars, near CXR12 (Fig. 3.2). Here there is relatively strong 100 and 60 μm emission. When the SED (left panel of Fig. 3.5) is fit using $\beta = 1.5$, which is consistent with the value adopted for the analyses of compact sources, the derived dust equilibrium temperature $T = 29.7 \pm 2.3$ K. For $\beta = 2$, appropriate for local diffuse dust in the atomic gas at high latitudes (Boulanger et al., 1996; Li & Draine, 2001), T is 25.4±2.3 K. This can be compared to the local high-latitude equilibrium temperature, 17.5 K. The higher T in Cyg X results from the much higher effective interstellar radiation field from the OB association. The ridge of warm

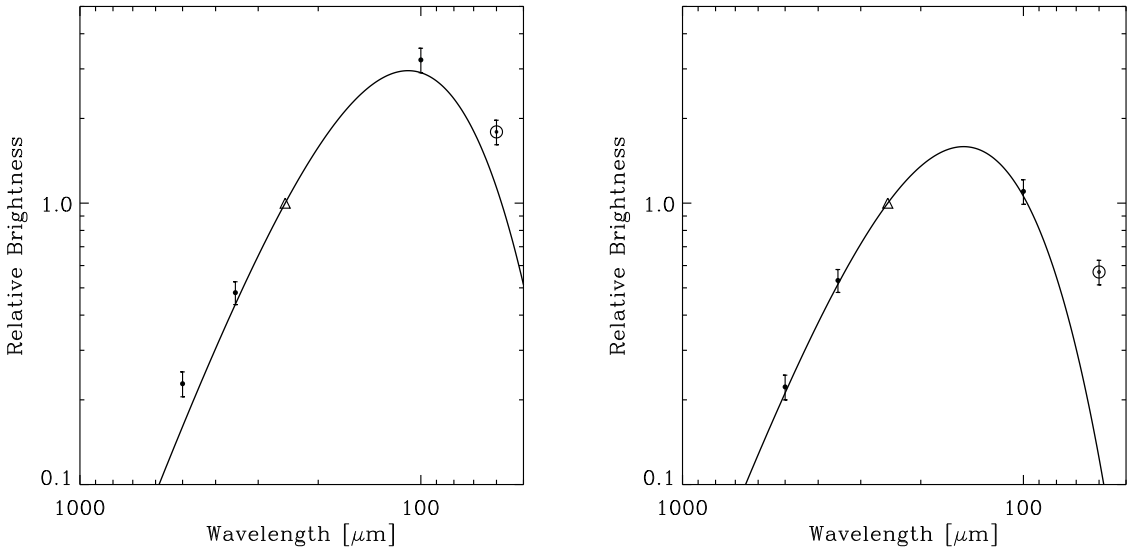

Figure 3.5 Left: Relative SED normalized at 250 μm corresponding to the circular region shown in the left-hand image of Fig. 3.4. Triangle shows the relative value unity at 250 μm. The SED fitted using $\beta = 1.5$ has a temperature of 29.7 $\pm$ 2.3 K. The 60 μm relative brightness (represented by a circle) is not used in the fit. Right: Relative SED corresponding to circular region shown in right-hand image of Fig. 3.4. The fit temperature is 21.6 ± 0.5 K.

dust emission and this particular selected warm region above and to the left are also prominent in diffuse H II emission (Fig. 3.2) and 24 μm emission, which supports the view that the local radiation field is high here. This region is particularly devoid of CO emission (§ 3.3.5). However, the material emitting in the submillimeter must be neutral, because the associated extinction ΔA_V is up to 3 mag above the local background (and is spatially well correlated with the BLAST emission; § 3.3.4). To the lower right of the CXR12 ridge, the dust is cooler, and there is some CO emission. CXR12 is oriented roughly tangentially to the direction to the center of the OB association, and might involve material swept up. However, the geometry is unclear, not immediately recalling a classical edge-on photodissociation region (PDR) in a molecular cloud.

The selected cooler region, judged from relatively low 100 and 60 μm emission, is shown by a circle in the right panel of Figure 3.4. Its SED (right panel of Fig. 3.5) yields an equilibrium temperature of 21.6 $\pm$ 0.5 K. The lower T would imply a lower effective interstellar radiation field, due to the high extinction, with A_V for this molecular structure

(§ 3.3.5) up to 6 mag above the local background.

3.2.5 Compact Sources

When I_ν in equation (3.1) is integrated over a suitable solid angle, accounting for the background, the flux density S_ν (typically in Jy) of a "source" is obtained. Likewise, the source mass M (gas plus dust) is related to the integrated column density when the distance D is known, so that

$$S_\nu = L_\nu/(4\pi D^2) = MD^{-2}r\kappa_\nu B_\nu(T). \tag{3.2}$$

Note that "source" refers to the dust emission that is being observed, not what heats the dust, and so in particular does not imply that there is an embedded source of energy (a star or protostar) within the volume of dust being measured.

The definition and characterization of what is a compact source is a difficult challenge, and different extraction schemes, like Clumpfind (Williams et al., 1994), Gaussclump (Stutzki & Guesten, 1990; Kramer et al., 1998), or the multi-scale method of Motte et al. (2007), can produce different catalogs and source characteristics. Operationally what is called a "compact source" is often basically a structure comparable in size to the beam. This immediately cautions that what is a compact source to one instrument could become resolved into multiple components at higher resolution, as has been illustrated by submm/mm interferometric observations of *IRAS* protoclusters and hot cores (e.g., with the SMA and IRAM Plateau de Bure, Beuther et al., 2007c,d; Bontemps et al., 2009).

As mentioned above, massive stars form in clusters. What BLAST can hope to detect in this survey at $1'$ resolution is unlikely to be a single protostar or its progenitor, but rather a protocluster or stellar nursery possibly containing many unresolved objects. Of course, depending on the mass function, a single object among these might dominate the luminosity and ionizing flux.

We have taken a pragmatic view that since whatever underlying structure that is smeared out as a compact structure does appear quite like a Gaussian, this is an adequate model for extracting flux densities. Furthermore, the deconvolved beam for this BLAST05 survey is of similar size at all three bands, so that the same volume of dust is being examined. A corollary is that when we use other initially higher-resolution data to expand the spectral coverage of multi-wavelength photometry (Appendix 3.8), we

measured the flux density consistently by first convolving these maps to the BLAST05 resolution.

3.2.6 Compact Source Identification and Photometry

For compact source identification we used the IDL-implemented DAOPHOT "FIND" routine, keeping as candidates detected peaks that were above the local background in both the 250 and 350 μm images by 3σ (empirical local rms fluctuation). Both source identification and photometry on individual sources are affected by the presence of cirrus noise; for example, at 250 μm the $1-\sigma$ cirrus noise level was evaluated to be ~ 4 Jy in the fainter right portion of the map (Roy et al., 2010), although it is expected to vary over the map according to the median brightness of the region (making catalog completeness a function of position in the map). The 500 μm map was not productive for further independent identifications due to at least as great apparent relative confusion noise. In fact, for 14 faint sources among the above it was not possible to measure a reliable 500 μm flux density. Given this noise and also the deconvolution artifacts near the brightest sources, we visually checked our candidates from the automated list. Since we were not depending on a complete survey – for example, to find a mass function or relative lifetimes of different stages – we were conservative in rejecting sources and a few were even added to the list. We were most concerned with having sources with accurately determined SEDs, so that reliable physical parameters could be determined (§ 3.4).

Photometry was carried out using a Gaussian non-linear fit, with amplitude, FWHM, position, and linear background as free parameters. Model-independent aperture photometry for isolated sources gave the same fluxes within 7%, confirming that this is an acceptable approach. Cyg X has a sufficiently flat background locally that fitting a linear background is an adequate approximation. However, in a complex crowded star-forming region like much of Cyg X, it is often not possible to extract fluxes by aperture photometry or by fitting a single Gaussian. In such cases, we adopted a multiple Gaussian technique, fitting simultaneously to all candidates within a $2.5'$ radius about the parent source. If a parent source in a crowded region had a low signal to noise ratio compared to its neighbors then we fixed their positions and/or FWHMs as required.

Positions and flux densities for 184 sources are given in Table 3.1. These Cyg X sources are referred to below as 'Cn' where 'n' is an up-to-three digit number, ranging from 0 to 183.

Table 3.1. Measured flux density

BLAST ID	Source Name	l (Degree)	b (Degree)	S_{1200} (Jy)	S_{850} (Jy)	S_{500} (Jy)	S_{450} (Jy)	S_{350} (Jy)	S_{250} (Jy)	S_{100} (Jy)	S_{60} (Jy)
C0	J203057+394248	78.6760	0.1902	···	···	22.0 ± 3.9	···	85.8 ± 3.4	110.7 ± 5.6	15.6[a]	···
C1	J202925+401118	78.8861	0.7091	8.1	28.3	151.5 ± 2.9	226.9	375.3 ± 8.0	1029.3 ± 35.2	5819.4	5699.0
C2	J202904+401506	78.8980	0.8006	···	···	90.7 ± 32.4	···	79.1 ± 17.8	59.9 ± 6.7	40.3	1.3
C3	J203329+394127	78.9454	−0.2135	···	···	23.7 ± 1.3	···	50.9 ± 2.9	85.4 ± 5.0	41.1[a]	7.7[a]
C4	J203323+394253	78.9546	−0.1860	···	···	33.0 ± 1.3	···	68.8 ± 2.9	130.7 ± 5.6	118.2[a]	6.9[a]
C5	J202653+403717	78.9566	1.3528	···	···	5.1 ± 0.4	···	7.7 ± 0.5	11.3 ± 0.9	11.2[a]	6.1[a]
C6	J203023+400926	78.9702	0.5401	···	···	15.2 ± 0.9	···	50.3 ± 2.4	74.4 ± 4.4	···	1.0[a]
C7	J203112+400310	78.9778	0.3528	6.6	17.6	133.8 ± 3.0	187.6	287.8 ± 5.1	512.5 ± 10.1	935.1	688.1
C8	J202957+401533	79.0029	0.6686	4.0	···	42.0 ± 2.5	···	80.6 ± 4.8	150.8 ± 10.2	876.7[a]	253.0[a]
C9	J203242+395409	79.0262	0.0331	···	···	9.7 ± 1.3	···	20.9 ± 2.1	43.3 ± 4.2	40.2[a]	39.8[a]
C10	J203002+401637	79.0279	0.6645	4.0	···	91.3 ± 5.6	···	145.5 ± 7.5	198.4 ± 13.0	195.5[a]	51.8[a]
C11	J203230+395738	79.0499	0.0986	···	···	16.3 ± 1.4	···	37.0 ± 3.0	70.2 ± 5.3	89.3	52.0
C12	J203220+400021	79.0687	0.1497	···	···	11.9 ± 1.6	···	26.3 ± 4.4	71.9 ± 7.4	201.8[a]	42.0[a]
C13	J202903+402817	79.0746	0.9314	···	···	10.9 ± 2.3	···	28.0 ± 5.7	46.2 ± 10.1	10.8[a]	18.8[a]
C14	J202720+404234	79.0776	1.3350	···	···	8.9 ± 1.0	···	19.8 ± 2.6	32.8 ± 2.9	116.3	53.2
C15	J202904+403148	79.1237	0.9637	···	···	107.1 ± 6.9	···	175.6 ± 7.6	259.2 ± 9.4	292.2	122.7[a]
C16	J203442+394448	79.1312	−0.3696	···	···	95.9 ± 5.0	···	167.0 ± 4.0	286.2 ± 6.0	540.8	85.4
C17	J203326+395612	79.1370	−0.0594	···	1.3	5.9 ± 1.1	9.4	10.6 ± 1.6	29.2 ± 3.4	112.1[a]	20.3[a]
C18	J203042+401921	79.1388	0.5894	···	···	11.2 ± 1.4	···	22.3 ± 3.0	32.4 ± 3.5	18.2[a]	···
C19	J203108+401718	79.1606	0.5016	···	···	13.0 ± 1.1	···	29.7 ± 3.1	76.0 ± 4.1	452.1	178.2
C20	J203229+400848	79.1987	0.2105	···	···	19.3 ± 3.5	···	38.7 ± 6.0	91.9 ± 11.3	428.5[a]	137.3[a]
C21	J202655+405517	79.2044	1.5223	···	···	22.7 ± 2.5	···	53.7 ± 3.4	94.8 ± 8.5	12.6[a]	2.3[a]
C22	J202923+403603	79.2173	0.9549	···	···	32.7 ± 2.7	···	82.1 ± 9.5	92.9 ± 11.3	27.8[a]	8.7[a]
C23	J203116+402231	79.2462	0.5321	···	···	31.3 ± 3.2	···	99.8 ± 22.9	92.7 ± 12.6	···	0.1[a]
C24	J203138+401939	79.2477	0.4492	···	···	15.5 ± 3.4	···	10.1 ± 6.4	9.0 ± 4.6	···	69.8[a]
C25	J203146+401843	79.2499	0.4198	···	6.8	67.4 ± 2.1	···	133.5 ± 7.7	121.1 ± 7.2	···	···
C26	J203158+401833	79.2702	0.3877	3.2	10.1	44.2 ± 2.2	135.1	70.1 ± 4.1	87.3 ± 4.5	319.5[a]	45.7[a]

Continued on Next Page...

Table 3.1 – Continued

BLAST ID	Source Name	l (Degree)	b (Degree)	S_{1200} (Jy)	S_{850} (Jy)	S_{500} (Jy)	S_{450} (Jy)	S_{350} (Jy)	S_{250} (Jy)	S_{100} (Jy)	S_{60} (Jy)
C27	J202806+405127	79.2822	1.3037	···	···	32.3 ± 1.8	···	124.4 ± 8.3	292.5 ± 18.7	1312.2	1217.3
C28	J203227+401554	79.2903	0.2855	5.4	···	44.3 ± 4.9	···	92.2 ± 8.4	307.5 ± 31.2	2885.4	2740.1
C29	J202738+405706	79.3081	1.4293	···	···	8.0 ± 1.1	···	12.8 ± 2.2	26.2 ± 2.4	129.3[a]	21.4[a]
C30	J202809+405301	79.3099	1.3099	···	···	91.9 ± 3.1	···	199.9 ± 7.8	453.2 ± 16.4	2654.2	2324.4
C31	J203518+395310	79.3107	−0.3767	···	···	36.9 ± 2.1	···	100.8 ± 5.2	141.7 ± 7.1	651.7[a]	289.6[a]
C32	J203233+401651	79.3145	0.2796	5.1	···	107.2 ± 5.5	···	275.0 ± 9.8	666.5 ± 31.4	8224.0	6221.7
C33	J202818+405309	79.3275	1.2893	···	···	21.7 ± 3.3	···	22.4 ± 4.8	84.9 ± 10.8	3271.4[a]	1948.1[a]
C34	J203525+395328	79.3278	−0.3913	···	···	14.1 ± 1.9	···	33.8 ± 3.2	93.7 ± 7.1	272.3[a]	161.9[a]
C35	J202823+405234	79.3292	1.2704	···	···	6.9 ± 11.2	···	19.2 ± 12.7	73.1 ± 34.6	2234.4[a]	913.7[a]
C36	J203222+401955	79.3337	0.3394	6.6	20.4	123.8 ± 3.3	172.8	238.5 ± 5.5	386.5 ± 13.3	1139.2	277.0
C37	J202802+405636	79.3459	1.3622	···	···	11.6 ± 1.1	···	19.0 ± 2.1	42.8 ± 3.7	382.5[a]	65.3[a]
C38	J203349+400832	79.3471	0.0025	···	···	29.8 ± 0.9	···	68.3 ± 1.9	172.1 ± 3.9	978.1	988.4
C39	J203530+395438	79.3531	−0.3928	···	···	17.6 ± 1.7	···	57.9 ± 5.0	74.2 ± 8.7	444.6[a]	270.6[a]
C40	J203508+395725	79.3492	−0.3102	···	···	32.0 ± 3.2	···	44.3 ± 2.6	103.2 ± 9.2	23.8[a]	1.3[a]
C41	J202818+405638	79.3746	1.3231	···	···	4.2 ± 0.4	···	12.4 ± 2.6	51.0 ± 5.1	479.9[a]	121.4[a]
C42	J203530+400053	79.4371	−0.3311	···	···	21.4 ± 3.0	···	32.8 ± 2.0	44.8 ± 3.2	101.6[a]	11.6[a]
C43	J202952+404842	79.4415	1.0049	···	···	21.2 ± 1.0	···	50.9 ± 1.9	81.5 ± 2.9	245.8	137.6
C44	J202754+410505	79.4460	1.4651	···	···	13.5 ± 1.1	···	39.4 ± 3.4	82.3 ± 6.7	100.4	15.7
C45	J203616+395728	79.4807	−0.4836	···	···	19.7 ± 3.3	···	63.7 ± 3.5	137.7 ± 5.7	87.1	7.1
C46	J203412+401634	79.4985	0.0231	···	···	17.7 ± 1.4	···	32.8 ± 2.0	71.3 ± 8.5	7.6[a]	2.7[a]
C47	J203417+401840	79.5360	0.0314	···	···	16.1 ± 0.8	···	32.0 ± 1.6	26.2 ± 2.2	19.4[a]	12.4[a]
C48	J203423+403039	79.7073	0.1358	···	···	28.6 ± 3.3	···	77.8 ± 10.7	55.7 ± 4.7	46.4[a]	5.2[a]
C49	J203311+404138	79.7185	0.4278	···	···	6.4 ± 0.4	···	11.8 ± 0.6	29.2 ± 1.1	102.4	49.2
C50	J203610+401716	79.7318	−0.2685	···	···	14.7 ± 1.1	···	36.6 ± 2.4	45.3 ± 3.4	···	···
C51	J203050+410224	79.7340	0.9909	···	···	24.3 ± 0.8	···	50.9 ± 1.7	79.5 ± 2.3	95.2	55.4[a]
C52	J203119+410049	79.7670	0.9011	···	···	6.0 ± 0.6	···	13.4 ± 0.9	22.2 ± 1.7	33.4[a]	19.7[a]
C53	J202958+411639	79.8299	1.2628	···	···	10.1 ± 0.6	···	34.6 ± 1.4	53.6 ± 2.2	133.0	84.4
C54	J203134+410357	79.8364	0.8949	···	···	8.4 ± 0.8	···	16.3 ± 1.6	14.8 ± 1.5	53.6[a]	1.6[a]
C55	J203029+411556	79.8764	1.1790	···	···	90.0 ± 2.8	···	200.4 ± 3.5	442.4 ± 7.0	1470.4	820.4

Continued on Next Page...

Table 3.1 – Continued

BLAST ID	Source Name	l (Degree)	b (Degree)	S_{1200} (Jy)	S_{850} (Jy)	S_{500} (Jy)	S_{450} (Jy)	S_{350} (Jy)	S_{250} (Jy)	S_{100} (Jy)	S_{60} (Jy)
C56	J203208+410524	79.9188	0.8234	···	···	90.0 ± 2.8	···	200.4 ± 3.5	442.4 ± 7.0	···	···
C57	J203148+410836	79.9241	0.9065	···	···	-21.5 ± 26.8	···	3.9 ± 1.4	15.6 ± 3.0	166.0[a]	79.9[a]
C58	J203319+405858	79.9643	0.5814	···	···	4.3 ± 0.9	···	16.5 ± 2.9	25.6 ± 4.1	112.4	51.6
C59	J203223+410748	79.9787	0.8099	···	···	7.3 ± 0.7	···	24.5 ± 0.9	40.6 ± 1.4	258.5[a]	242.7[a]
C60	J203201+411053	79.9789	0.8963	···	···	32.1 ± 2.1	···	72.6 ± 5.3	115.4 ± 8.3	579.5[a]	51.7[a]
C61	J203216+410860	79.9813	0.8397	···	···	63.5 ± 11.3	···	133.0 ± 19.8	206.6 ± 35.5	889.9	184.1
C62	J203437+405147	80.0149	0.3127	···	···	87.2 ± 4.1	···	171.6 ± 7.4	311.9 ± 13.1	63.0[a]	70.2[a]
C63	J203745+402529	80.0234	−0.4268	···	···	3.9 ± 0.6	···	9.4 ± 1.5	15.7 ± 1.6	41.7[a]	···
C64	J203443+405308	80.0457	0.3090	···	···	20.9 ± 1.1	···	61.7 ± 5.0	96.7 ± 10.9	126.0	59.7
C65	J203309+411603	80.1752	0.7749	···	···	10.5 ± 0.7	···	17.1 ± 0.9	36.0 ± 1.5	265.8	70.0
C66	J203414+410808	80.1903	0.5331	···	···	57.6 ± 3.5	···	94.2 ± 3.4	168.6 ± 7.3	70.8	76.6
C67	J203345+411415	80.2188	0.6657	···	···	7.9 ± 1.1	···	12.7 ± 0.9	22.8 ± 1.6	208.1	73.9
C68	J203520+410551	80.2851	0.3429	···	···	16.0 ± 0.7	···	43.0 ± 1.3	79.9 ± 2.1	23.6[a]	···
C69	J203112+414229	80.3133	1.3307	···	···	11.4 ± 0.7	···	39.2 ± 3.1	45.2 ± 3.4	31.4	4.0
C70	J203537+410615	80.3220	0.3050	···	···	5.1 ± 0.4	···	13.0 ± 1.1	18.0 ± 1.1	32.3	60.7[a]
C71	J203358+412230	80.3536	0.7148	···	···	3.8 ± 1.1	···	9.9 ± 1.1	14.7 ± 1.6	814.3	443.2
C72	J203347+412449	80.3638	0.7658	···	···	53.3 ± 1.6	···	126.0 ± 2.1	264.7 ± 5.1	337.5[a]	38.6[a]
C73	J203509+411331	80.3665	0.4474	···	···	201.3 ± 102.4	···	12.1 ± 1.9	24.2 ± 3.9	2737.9	1256.9
C74	J203525+411428	80.4095	0.4162	···	···	110.5 ± 3.4	···	221.4 ± 7.0	575.7 ± 17.4	1158.3	184.8
C75	J203252+413846	80.4475	1.0436	···	···	11.8 ± 5.9	···	21.7 ± 7.8	58.1 ± 15.0	167.3	100.5
C76	J203430+413044	80.5233	0.7168	···	···	6.2 ± 0.5	···	24.5 ± 0.9	37.9 ± 1.7	549.0	255.2
C77	J203554+411919	80.5275	0.3939	···	···	41.4 ± 1.8	···	102.0 ± 3.8	212.2 ± 6.0	55.1[a]	9.3[a]
C78	J203215+415540	80.6069	1.3023	···	···	2.6 ± 0.8	···	157.2 ± 641.0	11.1 ± 1.7	70.2[a]	21.6[a]
C79	J203224+415616	80.6316	1.2855	···	···	16.9 ± 5.4	···	10.5 ± 0.9	22.8 ± 1.7	113.7[a]	37.1[a]
C80	J203500+413451	80.6344	0.6827	···	14.6	6.4 ± 1.3	91.9	17.4 ± 1.2	48.9 ± 3.6	1287.8	969.8
C81	J203722+411452	80.6348	0.1286	···	···	96.4 ± 2.8	···	221.8 ± 5.6	413.7 ± 7.0	5.5[a]	···
C82	J203229+415729	80.6566	1.2855	···	···	9.7 ± 1.2	···	32.5 ± 2.2	26.8 ± 2.0	74.3[a]	5.8[a]
C83	J203509+413827	80.6992	0.6963	···	···	13.3 ± 3.4	···	16.4 ± 2.0	19.3 ± 1.9	370.4	157.7
C84	J203614+413412	80.7631	0.4933	···	···	55.5 ± 16.7	···	54.1 ± 4.2	141.8 ± 6.1	117.1[a]	20.8[a]

Continued on Next Page...

Table 3.1 – Continued

BLAST ID	Source Name	l (Degree)	b (Degree)	S_{1200} (Jy)	S_{850} (Jy)	S_{500} (Jy)	S_{450} (Jy)	S_{350} (Jy)	S_{250} (Jy)	S_{100} (Jy)	S_{60} (Jy)
C85	J203608+413959	80.8287	0.5666	5.7	15.8	21.5 ± 3.7	66.5	40.6 ± 5.1	73.9 ± 5.4	1130.5	666.6
C86	J203900+411722	80.8550	−0.0910	···	···	71.6 ± 1.6	···	171.7 ± 4.1	328.5 ± 6.9	85.3[a]	78.5[a]
C87	J203702+413457	80.8634	0.3814	4.0	18.3	37.7 ± 2.1	135.0	74.5 ± 3.5	117.4 ± 6.4	1286.0	190.1
C88	J203652+413620	80.8634	0.4198	6.3	21.2	64.3 ± 3.2	225.5	197.9 ± 12.0	368.9 ± 18.0	3598.8	1299.8
C89	J203944+411155	80.8659	−0.2543	···	···	97.8 ± 3.3	···	259.1 ± 8.3	554.8 ± 14.5	471.9[a]	37.1[a]
C90	J203724+413257	80.8785	0.3064	···	···	3.7 ± 1.8	···	12.7 ± 4.0	67.2 ± 10.6	609.8[a]	28.2[a]
C91	J203634+414338	80.9270	0.5373	···	···	61.1 ± 15.8	···	114.8 ± 20.0	199.9 ± 46.2	58.4[a]	10.1[a]
C92	J203927+412023	80.9460	−0.1272	7.1	···	78.1 ± 32.1	···	53.6 ± 7.7	122.4 ± 21.5	6232.1	5024.8
C93	J204011+411432	80.9519	−0.2949	···	···	210.7 ± 10.2	···	446.2 ± 14.1	826.5 ± 25.2	1331.5[a]	208.0[a]
C94	J203936+411959	80.9566	−0.1519	1.8	···	54.5 ± 6.7	···	129.1 ± 19.0	262.7 ± 25.2	5171.0	2497.3
C95	J203709+414130	80.9641	0.4293	···	···	4.4 ± 2.0	···	3.3 ± 2.9	134.9 ± 15.8	395.1[a]	98.9[a]
C96	J203941+412111	80.9816	−0.1519	···	···	9.8 ± 0.6	···	20.6 ± 1.2	52.5 ± 3.6	3351.5[a]	616.0[a]
C97	J203923+412538	81.0071	−0.0632	···	···	450.6 ± 117.3	···	3592.9 ± 1145.6	286.1 ± 58.8	657.1[a]	44.1[a]
C98	J203646+414744	81.0046	0.5480	···	···	72.6 ± 5.2	···	156.4 ± 10.9	340.5 ± 20.2	103.3	23.6
C99	J204023+411801	81.0211	−0.2892	···	···	49.6 ± 5.4	···	118.7 ± 10.9	198.7 ± 15.9	763.4	81.4
C100	J203644+415112	81.0454	0.5895	···	···	47.5 ± 6.1	···	107.0 ± 12.2	218.7 ± 24.4	188.9[a]	26.1[a]
C101	J203954+412407	81.0470	−0.1563	···	···	8.1 ± 1.0	···	22.3 ± 2.0	57.3 ± 5.6	812.8	218.2
C102	J204025+412009	81.0536	−0.2733	···	···	60.5 ± 3.5	···	179.9 ± 8.0	395.2 ± 20.0	426.7[a]	48.0[a]
C103	J203936+412741	81.0583	−0.0735	···	···	15.9 ± 3.2	···	42.4 ± 5.8	112.0 ± 13.2	308.6[a]	49.1[a]
C104	J204004+412828	81.1230	−0.1364	4.5	···	70.5 ± 79.9	···	47.2 ± 17.7	62.5 ± 11.9	1790.2	611.5
C105	J203713+415407	81.1394	0.5463	···	···	85.2 ± 2.9	···	250.0 ± 6.4	502.0 ± 15.9	160.0[a]	18.1[a]
C106	J203636+415947	81.1457	0.6944	···	···	18.1 ± 1.3	···	36.8 ± 2.5	76.7 ± 5.1	35.6[a]	6.2[a]
C107	J204005+413212	81.1736	−0.1002	3.0	···	30.2 ± 1.3	···	64.7 ± 2.4	97.0 ± 4.5	526.0[a]	65.8[a]
C108	J203605+420851	81.2080	0.8627	···	···	41.1 ± 2.5	···	94.0 ± 5.5	169.3 ± 7.8	164.7[a]	···
C109	J203620+420702	81.2115	0.8075	···	···	93.0 ± 7.8	···	193.0 ± 24.0	353.2 ± 46.7	51.4[a]	7.2[a]
C110	J203527+421435	81.2137	1.0143	···	···	12.7 ± 1.5	···	26.1 ± 3.4	87.9 ± 42.1	575.6	173.7
C111	J203506+421957	81.2465	1.1197	···	···	67.5 ± 7.9	···	74.1 ± 4.2	224.8 ± 12.4	481.4[a]	67.2[a]
C112	J203546+421513	81.2580	0.9729	···	···	21.3 ± 2.1	···	56.9 ± 4.7	121.8 ± 7.8	199.2[a]	7.2[a]
C113	J203601+421336	81.2640	0.9199	···	···	34.5 ± 4.1	···	73.7 ± 6.1	141.8 ± 11.0	247.9[a]	19.4[a]

Continued on Next Page...

Table 3.1 – Continued

BLAST ID	Source Name	l (Degree)	b (Degree)	S_{1200} (Jy)	S_{850} (Jy)	S_{500} (Jy)	S_{450} (Jy)	S_{350} (Jy)	S_{250} (Jy)	S_{100} (Jy)	S_{60} (Jy)
C114	J203541+421649	81.2692	1.0022	···	···	20.4 ± 2.7	···	51.7 ± 5.7	126.7 ± 17.5	···	12.6[a]
C115	J203534+422009	81.3014	1.0517	7.1	···	23.0 ± 2.0	···	54.9 ± 3.6	107.6 ± 6.5	1031.4	239.3
C116	J204034+413836	81.3126	−0.1053	2.0	···	97.0 ± 2.6	···	199.9 ± 5.8	384.0 ± 8.8	···	···
C117	J203448+422732	81.3152	1.2389	···	···	35.4 ± 1.6	···	73.7 ± 3.0	117.8 ± 4.4	1567.2	444.0
C118	J203708+420841	81.3240	0.7043	···	···	43.7 ± 3.9	···	121.0 ± 12.7	329.0 ± 32.1	···	1.8
C119	J203658+421128	81.3407	0.7592	7.8	···	5.5 ± 2.2	···	8.0 ± 3.1	25.0 ± 7.6	450.9	75.8
C120	J203740+420707	81.3616	0.6119	···	···	107.5 ± 2.7	···	247.4 ± 6.2	316.4 ± 9.7	54.2[a]	11.5[a]
C121	J203720+421112	81.3784	0.7021	···	···	27.4 ± 10.0	···	45.3 ± 8.5	140.3 ± 23.8	101.4[a]	···
C122	J204029+414530	81.3955	−0.0248	···	···	15.8 ± 2.3	···	24.5 ± 4.4	37.9 ± 5.7	336.3[a]	25.9[a]
C123	J203505+423125	81.3984	1.2355	···	···	51.2 ± 3.1	···	98.2 ± 6.6	113.5 ± 10.9	695.4[a]	203.3[a]
C124	J203559+422518	81.4155	1.0428	0.6	···	37.9 ± 4.5	···	97.5 ± 13.6	207.8 ± 27.8	28.3[a]	···
C125	J203611+422417	81.4249	1.0021	···	···	8.4 ± 0.8	···	60.2 ± 6.2	145.2 ± 17.0	148.5	64.8
C126	J203730+421353	81.4339	0.7030	4.0	···	9.7 ± 0.9	···	29.1 ± 3.4	57.0 ± 5.7	591.4	45.3
C127	J203831+420549	81.4400	0.4731	4.5	···	105.6 ± 7.5	···	225.9 ± 17.8	440.2 ± 30.1	4000.4	1385.3
C128	J203718+421630	81.4454	0.7598	1.4	···	137.3 ± 25.8	···	362.1 ± 89.3	955.5 ± 172.6	111.6[a]	70.3
C129	J203836+420700	81.4650	0.4731	4.5	···	14.9 ± 3.5	···	34.1 ± 10.3	64.1 ± 13.1	3421.1[a]	980.6[a]
C130	J204046+414844	81.4703	−0.0331	···	···	73.4 ± 8.2	···	189.5 ± 21.6	282.2 ± 40.1	230.5[a]	14.6[a]
C131	J204052+414756	81.4707	−0.0555	···	···	15.4 ± 4.7	···	33.5 ± 9.8	111.5 ± 16.3	785.9[a]	133.2[a]
C132	J204035+415057	81.4779	0.0172	5.0	···	8.1 ± 2.5	···	7.6 ± 4.7	28.8 ± 12.7	1449.3[a]	···
C133	J203831+420938	81.4919	0.5099	···	···	268.0 ± 12.9	···	596.3 ± 29.0	1082.0 ± 51.9	1723.5[a]	159.4[a]
C134	J203822+421144	81.5024	0.5537	1.6	···	19.9 ± 5.3	···	45.6 ± 13.2	171.1 ± 39.3	1036.8[a]	107.5[a]
C135	J203957+415918	81.5163	0.1952	1.6	4.8	41.3 ± 5.6	···	115.0 ± 11.6	240.6 ± 27.4	122.4	75.5
C136	J203954+420055	81.5319	0.2191	···	···	18.8 ± 1.1	···	34.2 ± 2.2	73.9 ± 3.7	263.4[a]	19.0[a]
C137	J203514+423936	81.5230	1.2966	···	···	64.8 ± 2.8	···	165.6 ± 9.1	190.5 ± 10.3	413.8	54.8
C138	J203725+422217	81.5360	0.8000	···	···	54.9 ± 22.5	···	44.4 ± 3.9	575.7 ± 203.2	157.0	16.2
C139	J203638+422921	81.5424	0.9868	0.5	···	9.4 ± 3.2	···	9.4 ± 3.3	23.9 ± 6.6	34.1[a]	12.3[a]
C140	J204104+415147	81.5438	−0.0453	···	···	34.4 ± 1.2	···	53.6 ± 2.8	88.2 ± 3.6	973.0[a]	168.0[a]
C141	J204029+415717	81.5502	0.0965	3.3	9.8	50.9 ± 2.5	65.4	150.7 ± 6.6	396.5 ± 22.9	230.3	36.9
C142	J203944+420413	81.5566	0.2772	···	···	66.1 ± 1.6	···	143.3 ± 5.3	234.9 ± 9.4	254.6[a]	14.6[a]

Continued on Next Page...

Table 3.1 – Continued

BLAST ID	Source Name	l (Degree)	b (Degree)	S_{1200} (Jy)	S_{850} (Jy)	S_{500} (Jy)	S_{450} (Jy)	S_{350} (Jy)	S_{250} (Jy)	S_{100} (Jy)	S_{60} (Jy)
C143	J203635+423047	81.5552	1.0095	···	···	13.1 ± 1.5	···	33.1 ± 3.9	67.3 ± 5.8	14.9[a]	···
C144	J203931+420634	81.5630	0.3331	···	···	22.7 ± 1.6	···	35.8 ± 2.8	61.3 ± 4.3	···	···
C145	J204033+415857	81.5804	0.1026	1.8	6.2	11.6 ± 1.5	38.9	36.4 ± 3.1	68.4 ± 6.2	733.3[a]	81.7[a]
C146	J203430+424933	81.5759	1.5032	···	···	56.4 ± 1.6	···	109.0 ± 4.7	188.7 ± 8.7	186.8[a]	16.8[a]
C147	J203931+420821	81.5869	0.3510	···	···	66.6 ± 13.2	···	125.5 ± 23.7	166.0 ± 20.3	···	···
C148	J203520+424413	81.5967	1.3267	···	···	24.2 ± 6.9	···	27.0 ± 5.8	44.3 ± 9.1	257.7[a]	25.7[a]
C149	J204048+415757	81.5948	0.0568	2.2	···	10.3 ± 1.2	···	27.5 ± 2.6	72.7 ± 4.5	128.0[a]	2.3[a]
C150	J203449+424829	81.5973	1.4446	···	···	21.2 ± 4.4	···	63.1 ± 9.3	132.5 ± 19.7	109.1	10.0
C151	J203914+421221	81.6081	0.4326	···	···	26.2 ± 21.9	···	14.4 ± 3.0	34.4 ± 4.6	162.3	4.8
C152	J203620+423723	81.6164	1.1110	···	···	21.4 ± 4.7	···	38.5 ± 8.7	114.2 ± 16.6	59.0[a]	10.8[a]
C153	J204044+420129	81.6349	0.1012	···	···	14.4 ± 1.1	···	34.0 ± 2.6	74.0 ± 5.3	93.2[a]	101.8[a]
C154	J203807+422443	81.6468	0.7213	···	···	16.0 ± 4.5	···	95.7 ± 24.7	80.1 ± 16.2	184.7[a]	10.8[a]
C155	J203902+421939	81.6811	0.5372	48.7	127.1	33.2 ± 3.9	738.0	78.9 ± 8.2	164.6 ± 23.2	19911.5	13058.7
C156	J204046+420536	81.6920	0.1397	···	···	578.6 ± 27.7	···	1391.9 ± 68.2	3391.8 ± 113.3	207.3	55.2
C157	J203901+422249	81.7217	0.5713	46.8	146.7	15.8 ± 1.1	1160.0	56.0 ± 3.6	135.9 ± 10.1	16765.7	2429.5
C158	J204103+420547	81.7269	0.0994	···	···	838.8 ± 22.4	···	1917.1 ± 61.7	4111.7 ± 98.7	312.1[a]	26.3[a]
C159	J203444+425911	81.7312	1.5634	···	···	4.0 ± 0.9	···	18.2 ± 1.4	42.7 ± 2.8	848.0	257.5
C160	J203901+422506	81.7524	0.5938	27.1	91.6	35.4 ± 3.3	621.3	91.5 ± 6.9	195.7 ± 13.2	7777.6	1145.1
C161	J204236+415454	81.7603	−0.2385	···	···	597.2 ± 75.6	···	1501.2 ± 272.6	1700.2 ± 301.4	297.3	24.4
C162	J203548+425243	81.7607	1.3445	···	···	9.9 ± 1.8	···	24.8 ± 3.6	46.5 ± 4.7	···	···
C163	J203749+423846	81.7992	0.9075	0.6	···	22.6 ± 2.3	···	31.1 ± 3.7	47.3 ± 7.4	283.9[a]	56.6[a]
C164	J203755+423840	81.8093	0.8919	0.6	···	31.1 ± 1.6	···	46.8 ± 8.0	98.2 ± 8.6	451.8[a]	87.6[a]
C165	J203810+423817	81.8316	0.8521	1.6	···	29.7 ± 3.6	···	67.2 ± 8.7	73.2 ± 11.7	432.5	142.7
C166	J203639+425112	81.8337	1.2052	2.4	···	62.1 ± 5.6	···	96.3 ± 16.5	233.3 ± 16.0	307.5	82.3
C167	J203804+423945	81.8399	0.8813	5.4	···	45.7 ± 2.7	···	139.2 ± 6.5	215.2 ± 11.3	812.8[a]	99.0[a]
C168	J203757+424050	81.8410	0.9098	···	···	88.1 ± 3.3	···	204.0 ± 10.2	347.9 ± 14.1	404.6	26.5
C169	J203837+423738	81.8733	0.7795	36.5	87.3	22.5 ± 3.0	1008.0	33.6 ± 6.3	49.5 ± 12.1	15488.2	11970.0
C170	J203644+425507	81.8961	1.2309	···	···	515.9 ± 9.8	···	1140.6 ± 28.2	3202.4 ± 46.1	125.5[a]	13.6[a]
C171	J204237+422613	82.1734	0.0809	···	···	10.6 ± 1.5	···	38.8 ± 3.7	80.4 ± 3.9	219.5	154.5

Continued on Next Page...

Table 3.1 – Continued

BLAST ID	Source Name	l (Degree)	b (Degree)	S_{1200} (Jy)	S_{850} (Jy)	S_{500} (Jy)	S_{450} (Jy)	S_{350} (Jy)	S_{250} (Jy)	S_{100} (Jy)	S_{60} (Jy)
C172	J204234+422726	82.1836	0.1005	···	···	24.8 ± 1.6	···	55.7 ± 3.3	107.7 ± 4.4	98.9[a]	37.1[a]
C173	J204013+425459	82.2814	0.7228	···	···	23.0 ± 1.4	···	40.4 ± 2.8	55.0 ± 3.4	81.9[a]	4.7[a]
C174	J204017+425624	82.3073	0.7280	···	···	17.5 ± 0.7	···	25.5 ± 1.5	21.8 ± 5.2	126.1[a]	40.6[a]
C175	J204227+424151	82.3591	0.2663	···	···	14.8 ± 0.7	···	31.7 ± 1.6	56.6 ± 2.1	22.3[a]	3.7[a]
C176	J204159+424812	82.3909	0.3972	···	···	65.6 ± 5.6	···	91.2 ± 5.3	147.6 ± 8.1	185.1[a]	41.4[a]
C177	J204211+425258	82.4752	0.4182	···	···	13.9 ± 1.1	···	31.4 ± 2.3	80.8 ± 6.1	526.3	80.5
C178	J204209+425519	82.5020	0.4479	···	···	68.2 ± 4.7	···	97.4 ± 6.6	222.5 ± 12.8	618.1[a]	77.6[a]
C179	J204341+424355	82.5271	0.1077	···	···	17.3 ± 1.7	···	10.0 ± 5.3	78.2 ± 9.9	54.9[a]	4.1[a]
C180	J204234+425649	82.5689	0.4029	···	···	80.7 ± 15.1	···	88.9 ± 5.6	141.9 ± 10.1	573.4	769.8
C181	J204346+424707	82.5787	0.1285	···	···	14.3 ± 1.4	···	53.0 ± 4.1	125.3 ± 6.6	9.4[a]	···
C182	J204222+425831	82.5695	0.4482	···	···	31.4 ± 3.3	···	27.3 ± 2.2	32.1 ± 3.9	500.2	179.1
C183	J204329+424954	82.5826	0.1985	···	···	20.5 ± 4.7	···	103.8 ± 6.3	222.2 ± 14.0	168.4	95.5

[a] Upper limit.

3.3 Context: Global Environment and Structural Detail

3.3.1 Cyg OB2 Association and Star Clusters

Cyg OB2 is among the more impressive assemblies of OB stars in the Galaxy. It is more compact than a normal association and rich enough to have been called a "young globular cluster" (Knödlseder, 2000). The latest census indicates that it contains some 60-70 O-type stars (Negueruela et al., 2008). From their semi-observational HR diagram, Negueruela et al. (2008) favor a distance 1.5 kpc, with 1.8 kpc being noticeably too large. Our adopted distance of 1.7 kpc, consistent with Schneider et al. (2006a) and Motte et al. (2007), is close to this and a 10% uncertainty in distance is of no consequence in the analysis that follows.

The most luminous hot stars (selected as $M_{\rm bol} \leq -9.2$, $\log T_{\rm eff} \geq 4.56$ and $M_{\rm bol} \leq -9.9$, $4.46 \leq \log T_{\rm eff} \leq 4.53$) are plotted in Figure 3.2 with positions from Massey & Thompson (1991) and Comerón et al. (2002). Note that star A37 (at G80.240+0.135) has what appears to be a bow-shock to its right in the *Spitzer* images and so might be a runaway star from LK8 in DR15. Kobulnicky et al. (2010) studied the bow-shock morphology of A37 (and others), placing this star slightly behind Cyg OB2 at a distance of 2.1 kpc.

According to Knödlseder (2000), Cyg OB2 extends to a radius of 1° (30 pc), with half-light radius 13′ (6.4 pc). Examination of the substructure reveals two open clusters in the core (BBD1 and BBD2; Bica et al., 2003), each of radius $\sim 2'$ yet separated by only 6′ and appearing to form a physical pair.

A number of highly reddened OB clusters and stellar groups have been found in the surrounding molecular clouds using 2MASS. Dutra & Bica (2001) performed a targeted search toward large angular size H II regions in Cyg X; eight clusters and four stellar groups are in this BLAST survey region. Five of these have been recovered and characterized by Le Duigou & Knödlseder (2002), including the half-population radius R_{50} and central density. They also describe two new clusters. Comerón & Torra (1999) studied DR18, finding a stellar group, and Comerón et al. (2002) targeted other ECX (Wendker et al., 1991) compact H II regions finding four clusters within the BLAST area. The new one, ECX6-27, has a recombination line velocity of -62.4 km s^{-1} (Lockman, 1989) and so is much more distant than Cyg OB2, more like 10 kpc. It has a "double concentration" of

Table 3.2: Clusters and stellar groups

Cluster[a] ID	l Degree	b Degree	Other Names
LK08	79.302	0.286	DB10, ECX6-25
LK09	79.301	1.291	DB11, ECX6-18
DB12[b]	79.879	1.178	ECX6-21
ECX6-27	80.354	0.728	···
DR18[b]	80.357	0.450	···
LK11	80.935	-0.167	DB13, DB14[b]
LK12	81.298	1.096	DB15
LK13	81.445	0.483	DB16
LK14	81.441	1.122	···
DB17	81.566	-0.719	···
LK15	81.610	0.142	···
DB18[b]	81.661	-0.017	···
DR21	81.680	0.540	···
DB19[b]	81.711	0.582	···
W75N	81.870	0.779	···
DB20	81.896	0.797	···
DB22	82.567	0.404	···

[a]LK, DB, and ECX6 are the cluster IDs by Le Duigou & Knödlseder (2002), Dutra & Bica (2001), and Comerón et al. (2002), respectively.

[b] Stellar group.

stars (Comerón et al., 2002) and also a complex double structure in the *Spitzer* images. The catalog of Bica et al. (2003) also includes the W75N and DR21 (W75S) infrared clusters. In total there are thirteen clusters and five stellar groups (see Table 3.2). Their positions (not extents) are shown in Figure 3.2, with names in precedence LK, DB, and ECX6-* where the lists overlap. In subsequent figures, to indicate the cluster angular size we use R_{50} for the OB star population where available (Le Duigou & Knödlseder, 2002), otherwise a radius of $1'$.

3.3.2 The Radiative Environment: Ionization

The signature of radio emission in this region of the Galactic Plane, as distinct from the radio galaxy Cygnus A, led to the name Cyg X (Piddington & Minnett, 1952). A more contemporary large scale view is given in Figure 5 of Uyanıker et al. (2001). Radio

surveys conducted at different frequencies have catalogued the main H II region complexes (1390 MHz, Westerhout, 1958; 5 GHz, Downes & Rinehart, 1966; multifrequency, Wendker et al., 1991). What we have observed with BLAST is only the central portion, all projected within the Cygnus superbubble. The corresponding 1420 MHz image from the CGPS, including the diffuse emission, is shown in Figure 3.2.

The free-free emission traces the compact sources and extended structures like I-fronts, elephant trunks and pillars, and material that is being sculpted by winds. Figure 3.2 shows a striking ridge of emission CXR11 extending downward from DR15. Sculpting seen in the *Spitzer* images indicates illumination from the upper left (Cyg OB2), but like CXR12, this does not appear to be a classical I-front, because the expected neutral tracers in the PDR (§ 3.3.3) are not present immediately to the right.

In a closed geometry, the bolometric luminosity of the dust emission is a calorimeter for radiation from any embedded (proto)stars. Likewise, the spatially-integrated radio flux from the same region is a measure of the number of ionizing photons. Thus one can check for consistency, which is particularly useful in assessing the distribution of masses within an unresolved cluster. For example, dividing the luminosity among several lower mass stars will produce a lower ionizing flux. There are complications of course, in addition to the relative covering factors. For example, one must know the distance. If the distance is overestimated, then the luminosity will imply more massive stars and so a relatively higher ionizing flux (Comerón & Torra, 2001). Furthermore, the radio emission is also affected by self-absorption. Thus the ionized zone around young OB stars deeply embedded in dense gas (ultracompact and hypercompact H II regions) can appear to be underluminous. Multifrequency observations (not pursued here) can of course reveal self-absorption by its spectral signature in the radio SED (see the discussion of DR21 in Wendker et al., 1991), or by the high brightness temperature if the source is resolved.

3.3.3 The Radiative Environment: Far Ultraviolet

The non-ionizing radiation heats dust beyond any ionization front (I-front). This is the main source of the extended submillimeter emission surrounding the H II regions. As described above, in cases with "edge-on" geometries, like in DR22, there is a clear displacement of the BLAST emission to the side of the I-front away from the ionizing stars.

The non-ionizing radiation induces non-equilibrium emission when the relevant species,

VSGs and PAHs, are present. Diffuse PAH emission is well traced by *MSX* band A; the *MSX* map of Cyg X is discussed by Schneider et al. (2006a). PAH emission can now be seen in more exquisite detail in the IRAC band 4 images. Where the geometry is favorable, this reveals impressive PAH-fronts (defined by where the exciting radiation is attenuated) outside the I-fronts. There is also a sweeping arc to the lower right of DR15. This is not immediately adjacent to the ionized ridge CXR11 mentioned above (thus not the standard I-front-PDR geometry). The arc (and ridge) can be seen as well in MIPS 24 μm emission (Hora et al., 2009), which we interpret there as VSG emission.

MIPS 24 μm dust emission also turns out to be a good tracer of the plasma, although because of the different physics there is not a complete morphological or brightness correspondence. In the figures for the selected regions below (§ 3.3.6), we show the 24 μm emission overplotted with 21-cm radio emission contours to illustrate their correlation, and also the relationship to clusters and the BLAST compact sources.

3.3.4 Extinction

Another tracer of column density is near-infrared extinction (often expressed as its equivalent in A_V), which can be estimated from the colors of 2MASS sources. Such a map by S. Bontemps (private communication) is presented in Figure 1 in Motte et al. (2007). A_V and BLAST emission are well correlated. This correlation can be used to calibrate the dust opacity (Martin et al. in preparation). In their Figure 1, Schneider et al. (2006a) show an Hα image which strikingly shows the foreground optical extinction called the Great Cygnus Rift.

3.3.5 The Molecular Reservoir

Numerous surveys of the Cyg X giant molecular cloud (GMC) have been carried out in the molecular line transition ^{12}CO J = 1 $\rightarrow$ 0 (Cong, 1977; Dame et al., 1987; Leung & Thaddeus, 1992). Schneider et al. (2006a) report on an extensive multi-transition survey with KOSMA (^{13}CO J = 2 $\rightarrow$ 1, 3 $\rightarrow$ 2, and ^{12}CO J = 3 $\rightarrow$ 2) to study in detail the spatial structural variations and physical conditions. The relative intensity of ^{13}CO J = 3 $\rightarrow$ 2 to ^{13}CO J = 2 $\rightarrow$ 1 depends on the local density and kinetic temperature. Their ^{13}CO J = 2 $\rightarrow$ 1 channel maps show elongated filamentary structure at scales of 10$'$ to 20$'$, and smaller substructures (CO clumps) embedded in the larger cloud fragments. The peaks of the CO emission profiles occur over a wide range of radial velocities surveyed

from +20 to −20 km s^{-1} (there is not much gas beyond −10 km s^{-1} and gas at more negative "Perseus arm velocities" is not included).

Schneider et al. (2006a) provide a comprehensive treatment of the region from this molecular line perspective. They estimate 4×10^6 $M_\odot$ of molecular gas, at the large end of GMC masses in the Milky Way. Thus, despite the prior star formation, there remains a tremendous reservoir of gas pregnant with star formation, offering the opportunity to study many evolutionary stages. To this end, Motte et al. (2007) have carried out a continuum survey at 1.2 mm with MAMBO further revealing through dust emission the complex and hierarchical morphology in the region. They find that Cyg X hosts about 40 massive protostars destined to be OB stars. As discussed in § 3.5.4, the more massive protostars are already forming (ultra)compact H II regions, famous examples being DR21 (Downes & Rinehart, 1966), W75N (Westerhout, 1958), and AFGL2591, the strongest submillimeter compact sources within the BLAST coverage. Table 3.3 lists the correspondences between the cores and clumps of Motte et al. (2007) and our BLAST sources.

CO emission integrated over the line profile (W) is often taken as a surrogate of the column density of molecular hydrogen and so should be correlated with BLAST emission. We note the good correspondence and explore this in the examples below. Radiation from massive stars can of course in time destroy CO and the detailed correspondence with dust emission.

Table 3.3. Structures observed at 1.2 mm associated with BLAST clumps

BLAST ID	Core ID	Clump ID	$\Sigma_{\rm core}$[a] g cm^{-2}	$\Sigma_{\rm clump}$[a] g cm^{-2}
C1	S26	Cl-S5	0.58	0.33
C7	S30, S31	Cl-S7	0.21	0.18
C8	S29	Cl-S6	0.08	0.08
C26	S34	Cl-S9	0.08	0.08
C28	S39	···	0.12	···
C32	S40, S41	Cl-S11	0.13	0.11
C36	S36, S37, S38	Cl-S10	0.16	0.12
C85	N5, N6	Cl-N3	0.15	0.15
C87	N14	Cl-N6	0.48	0.14
C88	N10	Cl-N4	0.43	0.18
C90	N17	···	0.15	···
C92	N58, N59	Cl-N17	0.22	0.18

Continued on Next Page...

Table 3.3 – Continued

BLAST ID	Core ID	Clump ID	Σ_{core}[a] g cm^{-2}	Σ_{clump}[a] g cm^{-2}
C104	N62	Cl-N20	0.08	0.09
C107	N63	Cl-N21	0.96	0.28
C115	N1, N2	Cl-N1	0.56	0.29
C116	N70	···	0.07	···
C119	N12, N13	Cl-N5	0.58	0.21
C126	N18	Cl-N9	0.07	0.07
C127	N29	Cl-N11	0.06	0.08
C128	N16	···	0.13	···
C132	N67, N69	Cl-N23	0.05	0.09
C134	N26	···	0.06	···
C135	N61	···	0.07	···
C139	N8	···	0.12	···
C141	N65, N64	Cl-N22	0.14	0.10
C145	N68	···	0.29	···
C149	N72	···	0.05	···
C155	N42, N46, N47	Cl-15	2.30	1.67
C157	N36, N38, N41, N44, N48	Cl-N14	1.92	1.24
C160	N37, N43, N51, N53, N54	Cl-N16	0.45	0.45
C163	N20	···	0.18	···
C166	N9	···	0.05	···
C167	N21, N22, N24	Cl-N10	0.08	0.10
C169	N30, N31, N32	Cl-N13	2.49	1.27

[a] Upper limit.

Neither dust continuum emission nor W is sufficient for describing the complete physical environment and geometry of the star formation region. Additional insight can be gained by examination of the CO velocity cubes (Schneider et al., 2006a). Where there is CO coverage in our BLAST map, most of the identified BLAST compact sources are correlated with CO emission features (within the CO clumps mentioned above), thus associating the dust emission with gas at a certain velocity. In § 3.3.6, we provide a few examples using their ^{13}CO J = 2 → 1 cube to emphasize that objects seen closely together in projection in a dust emission image can have quite different velocities. In principle the velocity associations could be used to sort the sources with respect to distance. In Cyg X Schneider et al. (2006a) have argued that the main velocity systems are all at roughly the same distance, 1.7 kpc. Nevertheless, the association with different CO clumps having differing velocities does indicate that the BLAST compact sources are in distinguishable environments, and there certainly are some sources behind the main

Cyg OB2 complex (§ 3.4.2).

3.3.6 Selected Regions

In this section we show the BLAST compact sources in the context of the diffuse submillimeter emission and other tracers discussed above. They are marked in the figures with a 1.3′ square, characteristic of their apparent size in the deconvolved image. In each example, starting with Figure 3.6, the left panel shows the BLAST 250 μm image. On this are contours of the ^{13}CO J = 2 → 1 emission integrated over velocity ranges which highlight the CO clumps discussed in Appendix C of Schneider et al. (2006a). Good correlations between BLAST emission and CO are revealed. The coordinate system chosen for these enlarged views is Equatorial to facilitate comparison with the cutout regions in the annotated figures in Schneider et al. (2006a). Star clusters, local sources of power, ionization, and pressure, are also noted (§ 3.3.1). In the right panel is the MIPS 24 μm image with contours of the 21-cm radio emission from the CGPS map shown in Figure 3.2. Motte et al. (2007) show pairs consisting of their 1.2 mm MAMBO image and the corresponding *MSX* 8.3 μm image, but with no contours of CO or radio emission. The MIPS image here is more sensitive to point-like sources, many coinciding with BLAST sources.

The regions are presented in order of the number of the DR H II region in the field, whose nominal position is marked with an arrow or filled triangle in the right hand panel. To locate the regions in the large overview image in Galactic coordinates (Fig. 3.2), see the DR numbers marked there. Details of the nature of the BLAST compact sources and their evolution are deferred to §§ 3.4 and 3.5.

DR7. The first region highlighted is a field including DR7, as shown in Figure 3.6. Immediately outside the DR7 H II region itself is a rim of BLAST emission containing several compact sources. The typical rim shaped geometry of the DR7 region has been formed by the star cluster (LK09) now residing in the cavity. Interestingly, the DR7 H II region along with its cluster are not associated with the contours of CO shown. This H II region has a recombination line velocity of −40 km s^{-1} (Lockman, 1989) and CO velocity −50 km s^{-1} beyond the velocity coverage in Schneider et al. (2006a), placing it well behind the Cyg OB2 complex, at 3.6 to 7.5 kpc, possibly in the Perseus arm. Another indicator of the larger distance is the lack of signature in the extinction map, which is based on colors of detectable 2MASS stars.

There are, however, several CO clumps that do coincide with BLAST emission and

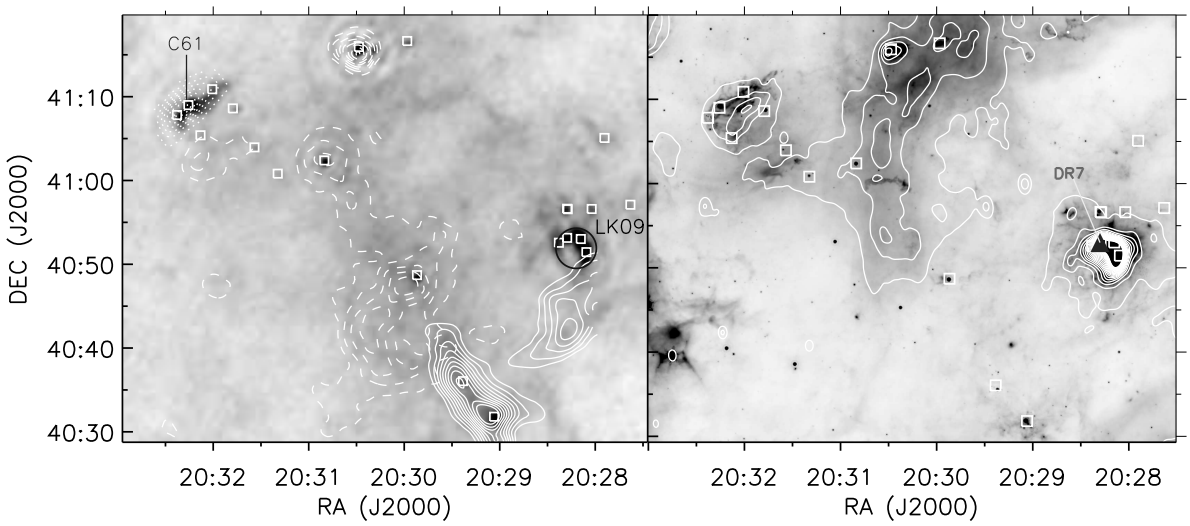

Figure 3.6 Left: BLAST 250 μm image including DR7 overlaid with contours of ^{13}CO J = 2 $\rightarrow$ 1 emission integrated over velocity ranges chosen to highlight the clumps discussed by Schneider et al. (2006a), Fig. B.4. Solid, dash, and dot contour lines correspond to the ranges 3 to 9, -7 to -1, and -13.5 to -8 km s^{-1}, respectively. Circle represents position and extent R_{50} of star cluster (Le Duigou & Knödlseder, 2002). Right: 24 μm MIPS map of the same region, with contours of the 21-cm radio continuum emission from the CGPS (see Fig. 3.2). BLAST compact sources are marked in each image by square boxes of 1.3′ width. Note the MIPS counterparts to many BLAST sources.

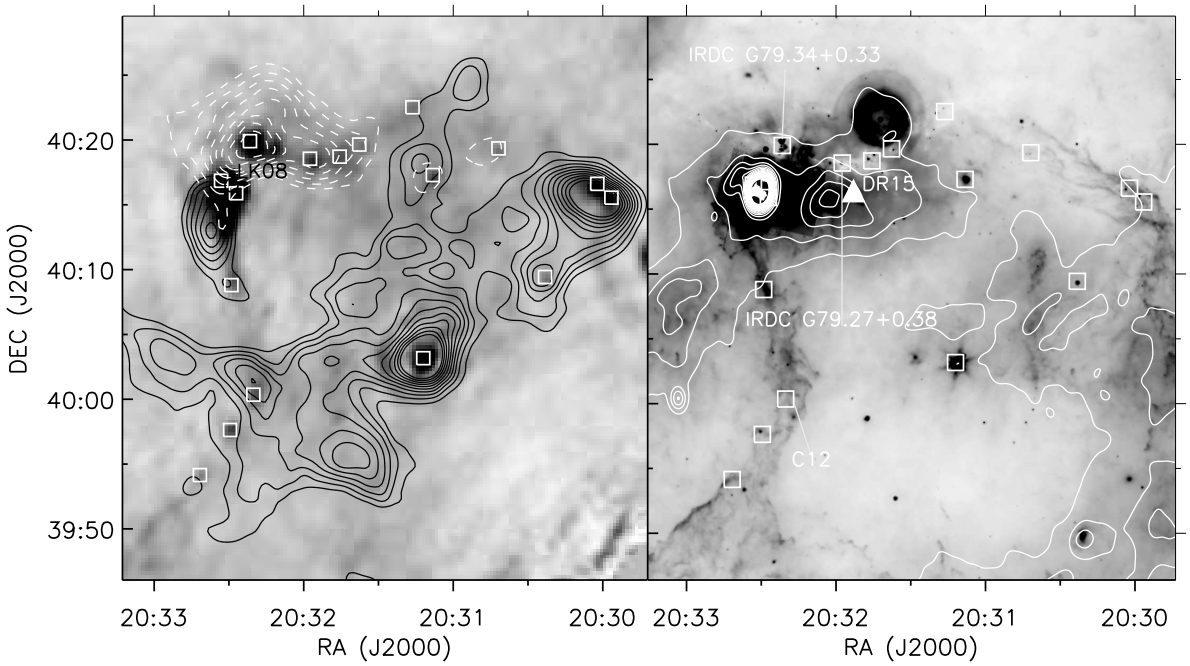

Figure 3.7 Same as Fig. 3.6 but for the DR15 region. Dashed and solid CO contours for ranges −3 to 3 and 3 to 20 km s^{-1}, as used in Fig. B.6 of Schneider et al. (2006a).

compact sources. The strong BLAST emission (with compact sources with MIPS counterparts) to the south coincides with clump 5. Not all clumps (which have different W) are easily seen in the BLAST emission (e.g., clumps 7, 8, and 9). The bright BLAST source at the top, in clump 1, has a compact H II region and a cometary tail linking it to Cyg OB2 (§ 3.5.1).

The emission at the upper left, associated with clump 2, is perhaps the most interesting, having a chaotic morphology in both MIPS and BLAST images (see also Fig. 3.1). In the ridge we find three BLAST sources. Although in projection the center of Cyg OB2 is close by, about 15′ to the east (left), there is no sign of interaction; furthermore, there is a parallel ridge of H II emission on the right, suggesting illumination from that side. It coincides with G79.957+0.866 for which the recombination line velocity is −14.8 km s^{-1}(Lockman, 1989), close to the CO velocity of −11 km s^{-1}. In the entire map, this CO cloud is unique in this velocity range < −10 km s^{-1} and not obviously connected to the other Cyg X molecular complexes. This then seems to be an object somewhat more distant, beyond the influence of Cyg OB2 (§ 3.5.1).

DR15. Figure 3.7 shows the fascinating region containing DR15 and the above-

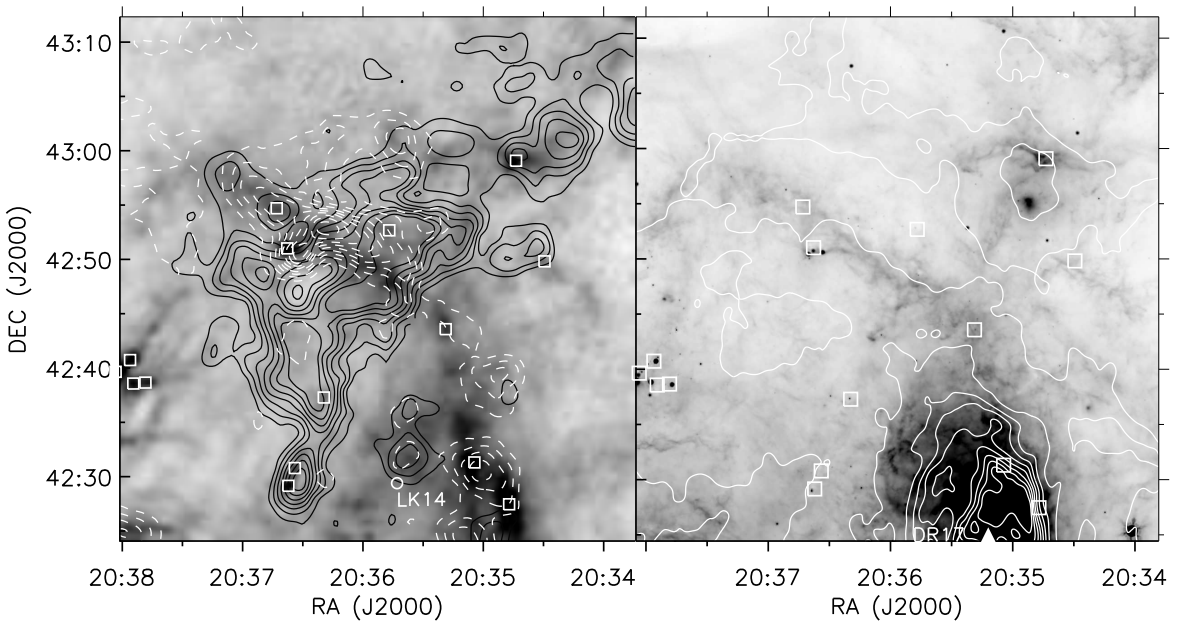

Figure 3.8 Same as Fig. 3.6 but for DR17N. Solid and dashed CO contours are for ranges 1 to 6 and 6 to 14 km s^{-1}, as used in Fig. B.1 of Schneider et al. (2006a).

mentioned PAH arc. Schneider et al. (2006a) argue that the DR15 molecular cloud complex near 0 km s^{-1} is being influenced by Cyg OB2 off to the upper left (see also § 3.5.1). This range also traces the IRDC ridge containing G79.34+0.33 and G79.27+0.38. As shown in Figure 3.3 and in more detail in § 3.5.6, BLAST sees this cold ridge in emission and resolves several compact sources; in the MIPS image, some embedded protostars shine faintly through. Toward the center of this field is the protostar IRAS 20293+3952, part of a different CO system at positive velocity. The pair of BLAST sources to the upper right are associated with streamers in the MIPS image which appear to be "blown" from the right.

DR17N. The lower portion of Figure 3.8 shows the northern part of the extended DR17 region (see also Fig. 3.2 and § 3.5.4). A major arc-shaped extended structure crosses BLAST and MIPS images, and is seen in 8 μm PAH emission as well, confining the H II emission influenced by the OB clusters inside DR17. CO in the higher velocity range 6 to 14 km s^{-1} best traces the arc. The lower velocity system projects across this, and has its own BLAST emission and compact sources.

DR17-Pillars. Schneider et al. (2006a) identified "molecular pillars" (their Fig. B.1)

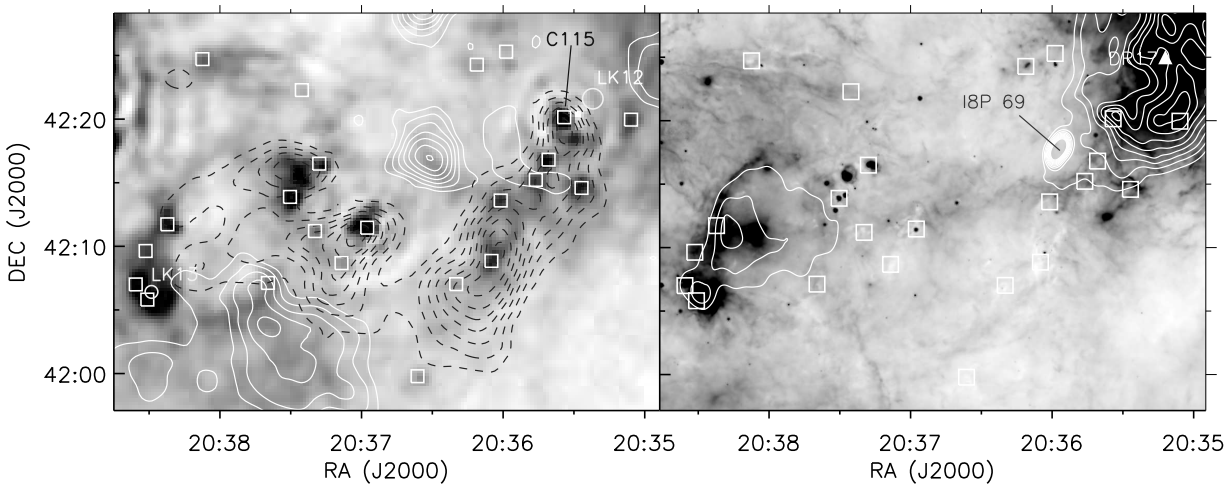

Figure 3.9 Same as Fig. 3.8 but for the DR17-Pillars region to its south (Schneider et al., 2006a). Solid and dashed CO contours are for ranges 1 to 6 and 14 to 20 km s^{-1}, as used in Fig. B.1 of Schneider et al. (2006a). The long molecular pillar on the right is that labelled in Fig. 3.3. A non-thermal extragalactic radio source 18P 69 (Wendker et al., 1991) also prominent in Fig. 3.2 is marked.

in the higher velocity range whose orientation points to the influence of the OB stars in DR17. BLAST finds compact sources associated with these pillars as shown in Figure 3.9. Compared to other dust in DR17, the above-mentioned arc and these molecular pillars are cool (Fig. 3.3). There is another H II region to the left in the image, with BLAST emission and compact sources along its interface as in DR7. This is the "Diamond Ring" (Marston et al., 2004) at an intermediate velocity (8 km s^{-1}), as described further in the DR21 discussion below.

DR20. Figure 3.10 shows DR20, which is at the end of a prominent ridge seen in the low-velocity CO (clump 1) and BLAST emission (see Fig. 3.13 in § 3.4.1 below). There are several BLAST compact sources here and in the complex to the west (clump 2, DR20W). The source in the middle of this image is associated with higher velocity gas (clump 3, DR20NW), as is more diffuse emission and other compact sources along the pillar toward the upper left (§ 3.5.1), possibly connected to the velocity system of the DR17 molecular pillars and arc.

DR21 and W75N. The DR21 and W75N regions shown in Figure 3.11 is obviously very active. The ridge of BLAST emission including DR21 and DR21(OH) points deceptively to W75N. However, the peak CO emission on the ridge (clumps 3 and 4) and clump

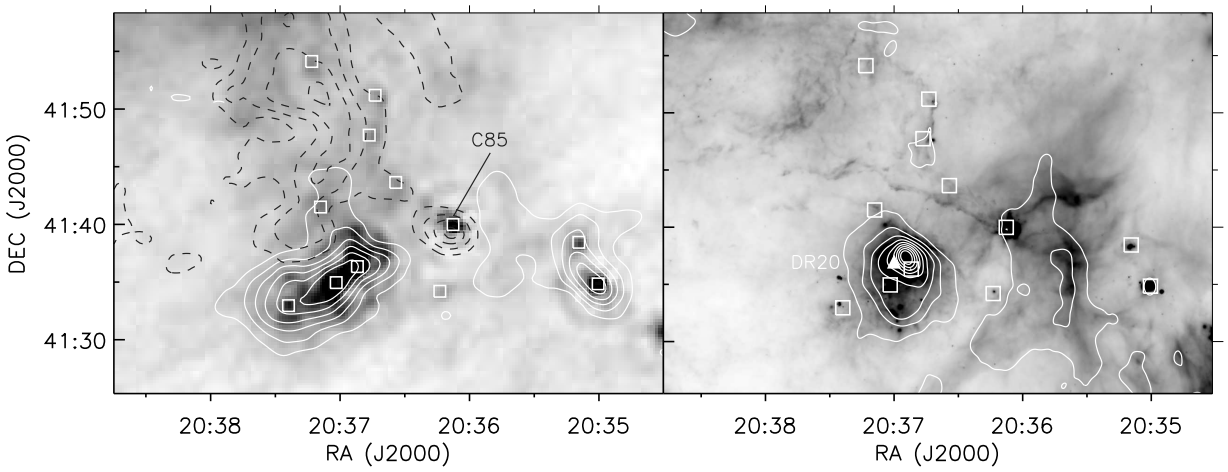

Figure 3.10 Same as Fig. 3.6 but for DR20. Solid and dashed CO contours for ranges −10 to 1 and 6 to 14 km s^{-1}, as used in Fig. B.2 of Schneider et al. (2006a). They called the molecular clump to the right DR20W, in the same velocity system as DR20, and that containing C85, in a different velocity system of a prominent elephant trunk (§ 3.5.1) DR20NW.

8 containing the BLAST sources to the north west of W75N are at −3 km s^{-1} (the low velocity system), whereas clump 10 of W75N is in a quite different higher velocity component at +10 km s^{-1}. The low velocity system is fairly widespread, including a complex to the south west (overlapping the lower edge of the eastern-most DR17 molecular pillar) and extending down to DR23 and DR22 (Fig. 3.12). The mass column density traced by BLAST correlates well with the CO emission. A fascinating feature is the extension of the DR21 ridge to the south, which shows up as a very narrow dark lane in the 24 μm image. This linear feature is at −4.5 km s^{-1}(see also Fig. 3.28 in § 3.5.6 below).

The higher velocity gas also contains prominent sources other than W75N, including the "Diamond" (clump 5) of the "Diamond Ring" (Marston et al., 2004). The more extended H II region along the "Ring" appears to be defined by both velocity systems.

DR22 and DR23. The CO cloud structures in the DR22 and DR23 regions shown in Figure 3.12 correlate well with the BLAST dust emission. Immediately to the south west of DR23 is a dim bay in the MIPS image, where the main CO cloud (clump 1) of the low-velocity system confines the H II region. Along this interface are three BLAST compact sources, including C132, perhaps triggered by the earlier generation of stars in

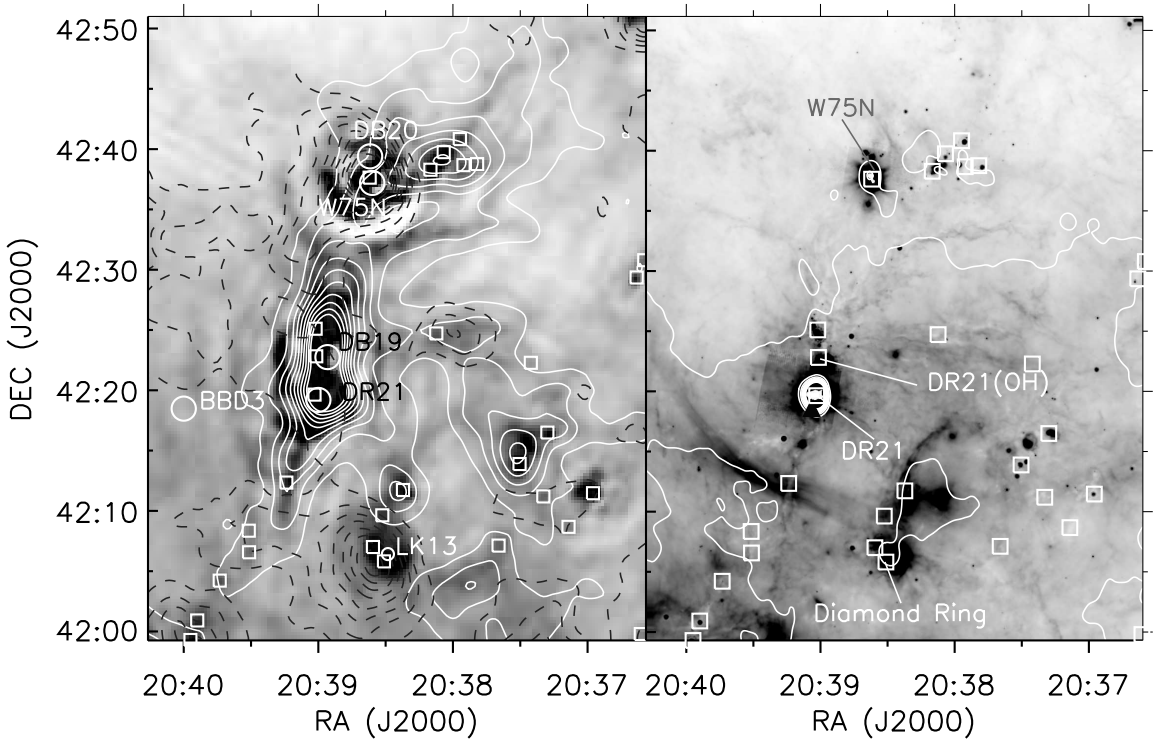

Figure 3.11 Same as Fig. 3.6 but for DR21 and W75N regions. Solid and dashed CO contours are for ranges −10 to 1 and 6 to 14 km s^{-1} as used in Fig. B.3 of Schneider et al. (2006a).

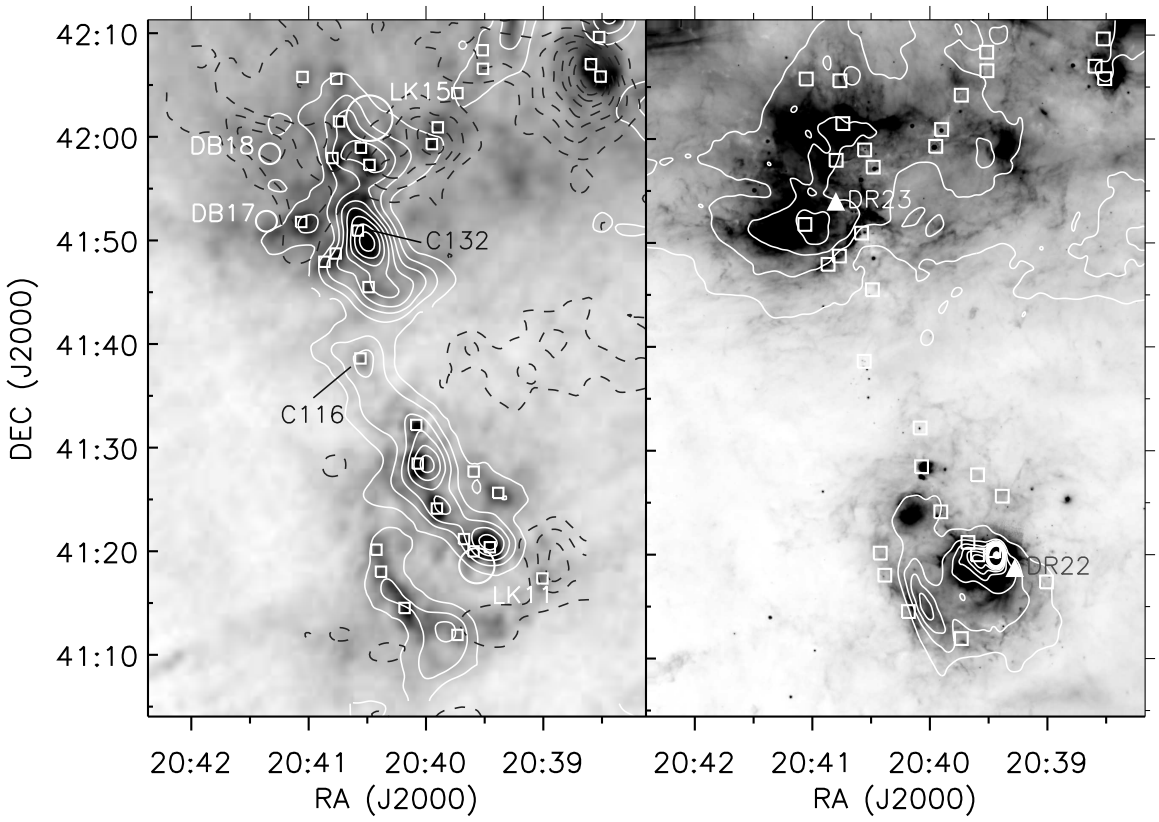

Figure 3.12 Same as Fig. 3.11 but for DR22 and DR23 regions to its south.

the DR23 cluster DB17. The two DR regions are interconnected by a CO filament (several clumps) in the lower velocity range. Along this filament there are BLAST compact sources and dark clouds, one (clump 3) with a protostellar nursery visible with MIPS and IRAC (§ 3.5.6). For DR22, the complementary detail provided by IRAC emission (see Fig. 3.23 in § 3.5.2) confirms a classical PDR geometry, with the lower left being most edge on. The location of the BLAST sources, not just the compact H II region but all around the periphery, is suggestive of triggering.

3.4 Properties of Compact Sources

3.4.1 Submillimeter-MIR SEDs

The SED for cold dust emission at temperature $\sim$ 13 K and emissivity index $\beta = 1.5$ peaks at 250 μm, and so the combination of the three BLAST filters alone is well suited for determining the dust temperature. Nevertheless, there is a range of temperature among sources (§ 3.4.3) and it is always preferable to have a broad wavelength coverage spanning both sides of the peak. Fortunately, Cyg X is well covered by both blind and more-targeted surveys. An example of the multi-wavelength coverage is given in Figure 3.13. Clearly, resolution changes from map to map. Also, for the central source here, the centroid changes at shorter wavelengths (and in the radio). As described in § 3.2.5, we have extracted flux densities consistently within the same size beam, to characterize the same physical structure.

We fit an idealized single-temperature SED expressed by equation (3.2) to data at all available wavelengths to determine temperature, mass, and total luminosity of each source (see Chapin et al., 2008 and Truch et al., 2008 for details). We adopt the same parameter values, namely $\kappa_0 = 10\,\mathrm{cm}^2\ \mathrm{g}^{-1}$, $r = 0.01$, and $\beta = 1.5$, and $D = 1.7$ kpc except for a few distant sources (§ 3.4.2). Single-temperature SEDs based on this value of β fit the data of typical sources well. One of the main systematic uncertainties is the value of $\kappa_0 r$ which is probably not known within a factor of two.

We treated ancillary photometric data for wavelengths less than 100 μm (see Appendix 3.8) in the specific context of each individual SED, including them as upper

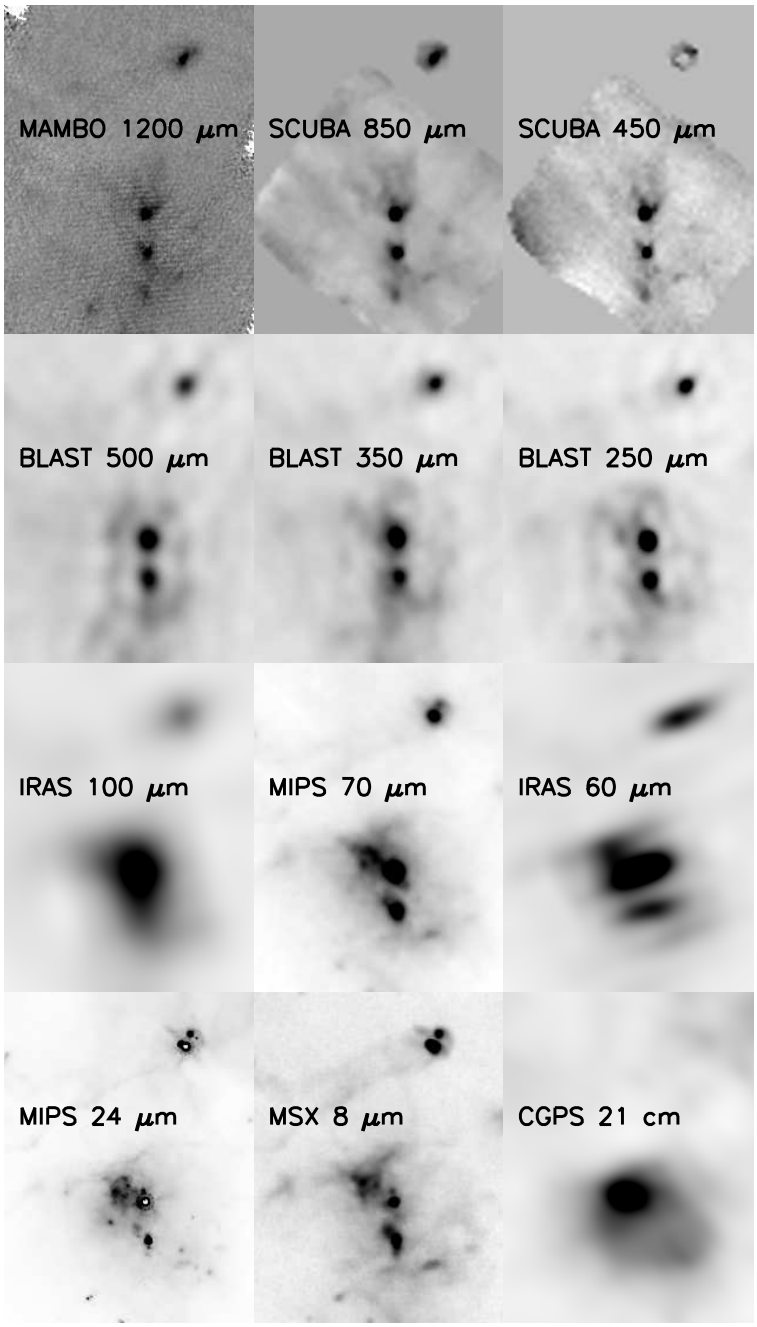

Figure 3.13 Thumbnails zooming in on a 14′ by 18′ section of the BLAST survey area containing DR20 (Galactic coordinates; cf. Fig. 3.10) at multiple wavelengths available for photometry. Relative appearance of structures changes because of different dust temperatures. The lowest in the vertical chain of three sources, seen only at wavelengths 500 μm and longer and so not catalogued as a BLAST source, must be quite cold. At *IRAS* 60 μm (IGA, after HIRES processing), sources appear elliptical across the scan direction. At *IRAS* 100 μm, the emission of crowded sources is often blended.

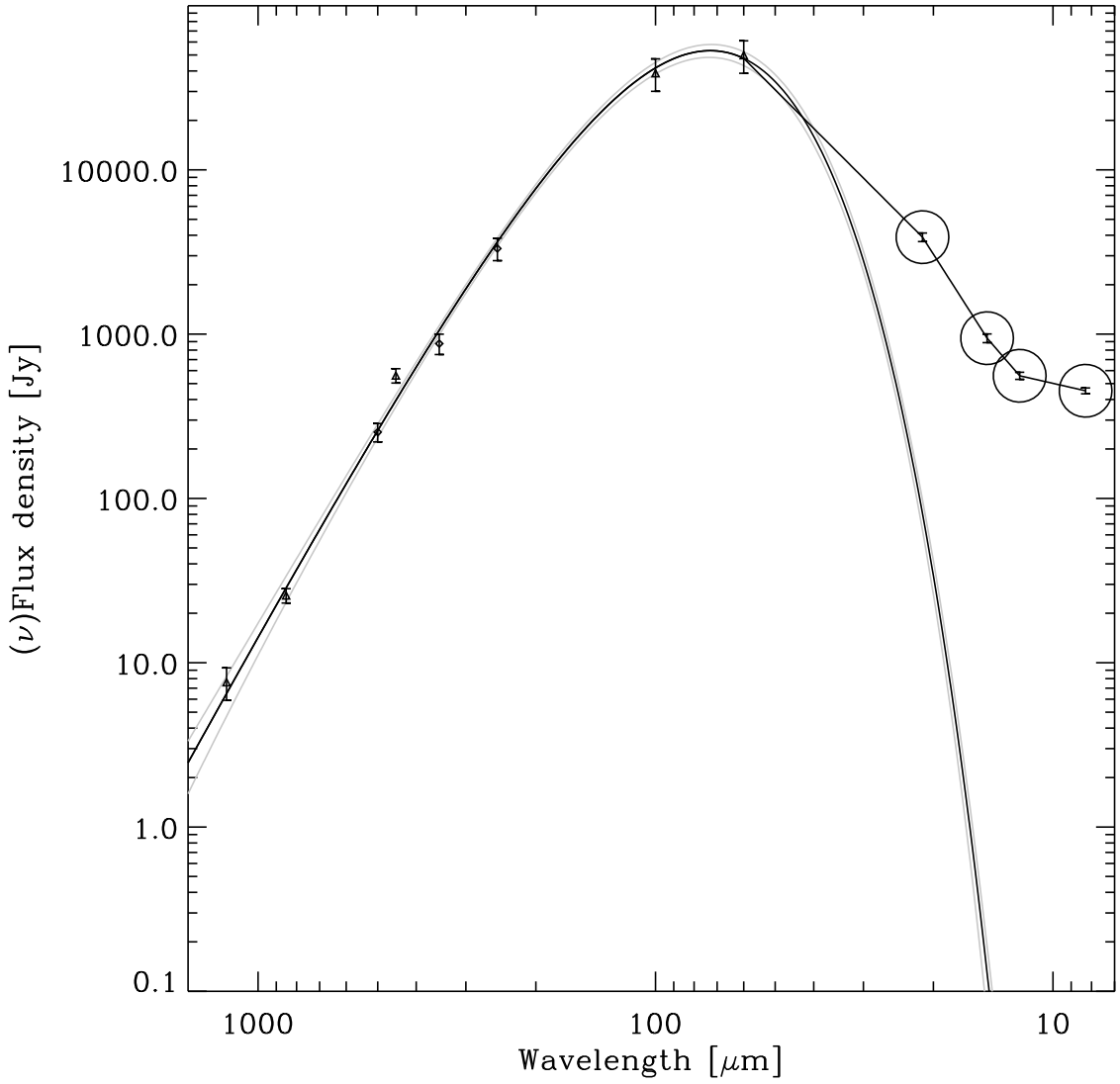

Figure 3.14 SED of C169 (W75N). To show intuitively where the most important contributions to the bolometric luminosity arise, this particular log-log plot uses νF_ν, obtained by multiplying flux densities by ν/ν_{250} with ν_{250} corresponding to 250 μm. The central solid curve shows the best-fit modified blackbody using data at $\lambda \geq$ 60 μm with $\beta = 1.5$. The *MSX* data shown by the circles are not used in the fit but are important in constraining $L_{\rm bol}$ (§ 3.4.5). The bracketing curves represent the 68% confidence envelope of modified blackbody models obtained from Monte Carlo simulations. Best fit parameters are $T = 36.2 \pm 3.6$ K, $M = (7.6 \pm 1.2) \times 10^2\ M_\odot$, and $L = (6.2 \pm 2.2) \times 10^4\ L_\odot$.

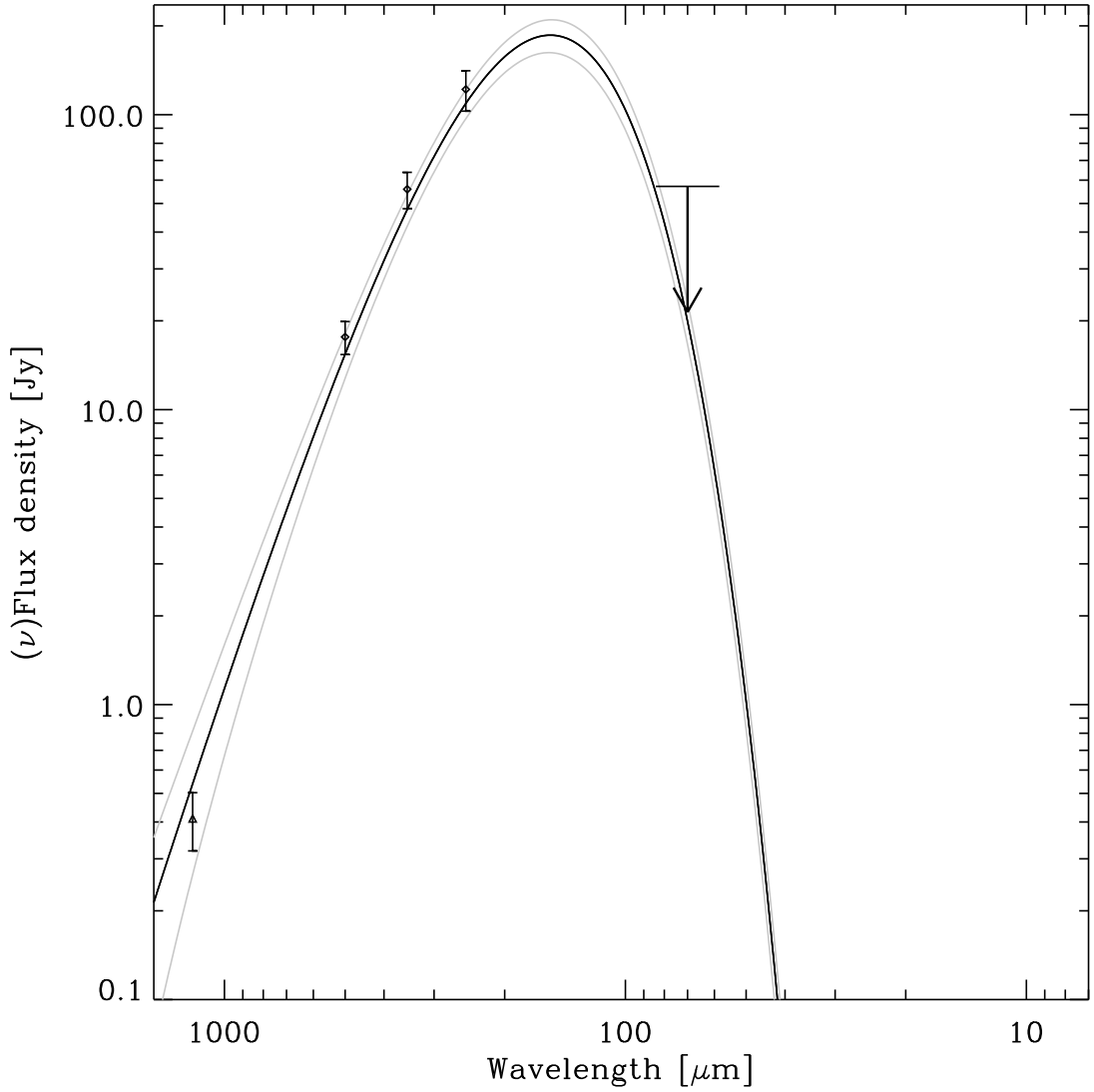

Figure 3.15 Like Fig. 3.14 but for one of the colder sources in Cyg X, C116. At 70 μm we plot the 1-σ (arrow) and 3-σ upper limits (Appendix 3.8); upper limits constrain the SED through a penalty function (Chapin et al., 2008). Best fit parameters are $T = 17.1 \pm 0.9$ K, $M = (1.7 \pm 0.2) \times 10^2\ M_\odot$, and $L = (2.2 \pm 0.4) \times 10^2\ L_\odot$. The 24 μm MIPS image in the upper panel of Fig. 3.26 reveals a deeply embedded stellar nursery but it is not yet very luminous.

limits where available/necessary. Upper limits come with an additional penalty function in the χ^2 minimization through a survival equation (Chapin et al., 2008; Truch et al., 2008). BLAST filters have large spectral widths about the central wavelength. Color correction to monochromatic flux density is carried out as part of the SED fitting described by Truch et al. (2008). The factors are close to unity and fairly consistent from source to source for the range of temperatures encountered here: 1.04, 1.07, and 0.99 for 250, 350, and 500 μm, respectively.

An example of a multi-wavelength SED fit is shown for C169 in Figure 3.14; this is one of the most luminous sources, W75N, and one of the hottest, with a best fit temperature for mm-FIR data of 36 K. In contrast to this, the SED of one of the colder sources is shown in Figure 3.15; this is C116 with a temperature of 17 K. In Table 3.4 we record T, M, Σ, and L and their uncertainties for 170 individual sources, there being no entries for the 14 faint sources either near the map edge or with unreliable 500 μm flux densities. The uncertainties in T, M, and L, and the corresponding 68% confidence envelope of possible modified blackbodies, were obtained by the Monte Carlo technique described by Chapin et al. (2008).

Table 3.4. Results from SED fits

BLAST ID	T (K)	M (100 $M_\odot$)	Σ (g cm^{-2})	L (100 $L_\odot$)	$L_{\rm bol}$ (100 $L_\odot$)
C0	15.5 ± 0.7	1.8 ± 0.4	0.033	1.4 ± 0.2	···
C1	40.1 ± 4.0	1.9 ± 0.4	0.121	277.2 ± 100.7	489.4
C3	16.6 ± 1.1	1.4 ± 0.3	0.021	1.6 ± 0.4	···
C4	17.5 ± 0.7	1.7 ± 0.3	0.022	2.6 ± 0.4	···
C5	13.2 ± 1.3	0.5 ± 0.2	0.022	0.1 ± 0.0	···
C6	19.6 ± 0.6	0.7 ± 0.1	0.009	1.8 ± 0.2	2.0
C7	25.8 ± 0.8	2.6 ± 0.3	0.084	33.4 ± 3.3	50.2
C8	17.3 ± 1.6	2.2 ± 0.6	0.038	3.1 ± 1.0	···
C9	20.4 ± 2.0	0.4 ± 0.1	0.006	1.3 ± 0.4	···
C10	15.7 ± 1.3	4.1 ± 1.0	0.051	3.4 ± 1.0	···
C11	25.7 ± 0.8	0.4 ± 0.1	0.008	4.4 ± 0.4	···
C12	20.9 ± 0.6	0.4 ± 0.1	0.007	1.8 ± 0.2	···
C13	15.7 ± 0.8	0.8 ± 0.2	0.014	0.7 ± 0.1	···
C14	29.9 ± 1.7	0.1 ± 0.0	0.003	3.8 ± 0.6	4.5
C15	20.8 ± 0.9	2.7 ± 0.5	0.024	10.5 ± 1.1	15.3
C16	23.7 ± 0.6	2.1 ± 0.3	0.096	16.5 ± 1.4	···
C17	21.5 ± 1.8	0.2 ± 0.0	0.005	1.0 ± 0.3	···
C18	15.1 ± 2.0	0.8 ± 0.3	0.015	0.5 ± 0.2	···

Continued on Next Page...

Table 3.4 – Continued

BLAST ID	T (K)	M (100 $M_\odot$)	Σ (g cm^{-2})	L (100 $L_\odot$)	$L_{\rm bol}$ (100 $L_\odot$)
C19	32.5 ± 1.1	0.2 ± 0.0	0.003	9.8 ± 1.2	10.1
C20	23.6 ± 3.8	0.5 ± 0.2	0.006	4.1 ± 1.8	···
C21	15.2 ± 0.6	1.6 ± 0.3	0.009	1.1 ± 0.1	···
C22	14.7 ± 1.2	2.5 ± 0.7	0.021	1.5 ± 0.3	2.3
C23	15.0 ± 1.6	2.2 ± 0.8	0.015	1.5 ± 0.5	···
C25	15.1 ± 1.2	2.4 ± 0.5	0.018	1.6 ± 0.5	···
C26	13.4 ± 0.9	3.7 ± 0.6	0.059	1.3 ± 0.3	···
C27[a]	40.1 ± 4.2	0.4 ± 0.1	0.007	62.3 ± 24.9	55.4
C28	47.0 ± 9.7	0.4 ± 0.1	0.009	144.3 ± 211.5	113.5
C29	17.3 ± 2.7	0.4 ± 0.2	0.007	0.5 ± 0.2	···
C30[a]	37.7 ± 4.6	1.1 ± 0.5	0.020	110.6 ± 37.2	102.5
C31	18.0 ± 2.3	1.8 ± 0.6	0.033	3.3 ± 1.2	···
C32	46.2 ± 2.8	1.1 ± 0.2	0.024	330.7 ± 72.1	···
C34	25.4 ± 1.3	0.4 ± 0.1	0.006	4.3 ± 0.7	···
C36	25.5 ± 1.1	2.6 ± 0.4	0.039	30.6 ± 4.3	···
C37	18.8 ± 2.5	0.4 ± 0.2	0.011	1.0 ± 0.4	···
C38	37.6 ± 1.9	0.4 ± 0.1	0.014	38.3 ± 6.0	48.7
C39	19.4 ± 2.8	0.8 ± 0.3	0.010	2.0 ± 1.3	···
C40	15.5 ± 1.2	1.7 ± 0.5	0.009	1.3 ± 0.3	···
C41	35.1 ± 1.9	0.1 ± 0.0	0.002	4.4 ± 0.9	5.4
C42	13.0 ± 1.6	2.0 ± 0.8	0.027	0.6 ± 0.2	···
C43	28.9 ± 1.1	0.4 ± 0.1	0.010	8.4 ± 0.9	···
C44	23.0 ± 0.5	0.4 ± 0.1	0.003	3.0 ± 0.2	···
C45	18.4 ± 0.3	1.1 ± 0.1	0.012	2.2 ± 0.2	···
C46	14.9 ± 0.7	1.2 ± 0.3	0.004	0.8 ± 0.1	···
C47	11.0 ± 0.9	2.6 ± 0.7	0.032	0.3 ± 0.1	0.9
C48	11.8 ± 1.2	3.8 ± 1.3	0.025	0.7 ± 0.2	···
C49	27.0 ± 0.9	0.1 ± 0.0	0.005	2.1 ± 0.2	2.8
C50	15.3 ± 1.7	1.0 ± 0.3	0.010	0.8 ± 0.2	···
C51	22.2 ± 1.0	0.7 ± 0.1	0.026	3.7 ± 0.5	5.0
C52	17.8 ± 3.0	0.3 ± 0.1	0.005	0.5 ± 0.1	1.2
C53	27.8 ± 1.1	0.2 ± 0.0	0.005	4.2 ± 0.5	4.9
C54	11.5 ± 1.1	1.2 ± 0.4	0.055	0.2 ± 0.0	···
C55	30.2 ± 1.3	1.6 ± 0.2	0.117	48.2 ± 6.2	52.9
C57	28.8 ± 1.4	0.1 ± 0.0	0.004	2.3 ± 0.4	3.6
C58	28.3 ± 1.0	0.2 ± 0.0	0.007	3.3 ± 0.4	4.1
C59[a]	17.6 ± 1.9	1.7 ± 0.5	0.053	2.6 ± 0.9	6.8
C60[a]	16.4 ± 1.3	3.8 ± 1.6	0.021	4.0 ± 2.4	···
C61[a]	25.7 ± 0.9	1.8 ± 0.2	0.029	22.8 ± 2.9	24.8
C63	17.5 ± 0.7	1.1 ± 0.3	0.006	1.7 ± 0.2	···
C64	30.6 ± 1.7	0.1 ± 0.0	0.006	4.3 ± 0.6	6.0
C65	24.4 ± 0.9	1.1 ± 0.2	0.008	10.0 ± 0.9	···
C66	30.5 ± 1.7	0.1 ± 0.0	0.003	2.6 ± 0.4	8.0
C67	25.5 ± 0.8	0.4 ± 0.0	0.009	4.9 ± 0.5	5.6

Continued on Next Page...

Table 3.4 – Continued

BLAST ID	T (K)	M (100 $M_\odot$)	Σ (g cm^{-2})	L (100 $L_\odot$)	$L_{\rm bol}$ (100 $L_\odot$)
C68	17.2 ± 1.5	0.6 ± 0.1	0.006	0.8 ± 0.3	···
C69	22.4 ± 0.6	0.1 ± 0.0	0.008	0.9 ± 0.1	···
C70	34.3 ± 2.3	0.0 ± 0.0	0.001	2.6 ± 0.4	···
C71[a]	30.7 ± 1.3	0.9 ± 0.1	0.016	30.6 ± 4.5	31.3
C73	33.4 ± 1.5	1.6 ± 0.2	0.030	84.3 ± 17.1	87.6
C74	23.2 ± 2.6	0.3 ± 0.3	0.006	2.3 ± 0.7	3.1
C75	34.8 ± 2.6	0.1 ± 0.0	0.002	6.2 ± 1.3	6.3
C76	28.4 ± 1.0	0.8 ± 0.1	0.016	18.3 ± 2.1	21.8
C78	21.9 ± 2.9	0.2 ± 0.1	0.003	0.8 ± 0.3	···
C79	27.4 ± 1.4	0.2 ± 0.0	0.002	2.8 ± 0.4	···
C80	30.0 ± 1.0	1.5 ± 0.2	0.056	43.4 ± 5.1	48.9
C81	13.5 ± 1.2	0.9 ± 0.3	0.017	0.3 ± 0.1	···
C82	11.5 ± 1.3	1.5 ± 0.8	0.037	0.2 ± 0.1	···
C83	28.8 ± 1.1	0.5 ± 0.1	0.007	10.8 ± 1.3	11.6
C84	23.4 ± 0.8	0.5 ± 0.1	0.006	3.7 ± 0.4	···
C85	29.9 ± 1.0	1.2 ± 0.1	0.053	35.4 ± 5.0	51.8
C86	16.0 ± 1.9	2.3 ± 0.8	0.025	2.1 ± 0.6	···
C87	26.8 ± 1.0	1.8 ± 0.2	0.058	28.0 ± 4.9	33.6
C88	32.5 ± 1.1	1.9 ± 0.2	0.091	85.7 ± 11.3	106.0
C89	25.7 ± 1.2	0.1 ± 0.0	0.002	1.8 ± 0.3	···
C90	16.8 ± 2.3	3.3 ± 1.7	0.019	4.0 ± 1.3	···
C91	17.2 ± 1.2	1.5 ± 2.3	0.008	2.0 ± 0.4	···
C92	39.3 ± 5.5	1.9 ± 0.7	0.024	240.6 ± 91.8	323.2
C93	22.0 ± 2.1	1.8 ± 0.5	0.015	9.7 ± 2.1	···
C95	24.4 ± 1.7	0.3 ± 0.1	0.001	2.4 ± 0.6	···
C97	21.0 ± 1.2	2.6 ± 0.5	0.013	10.6 ± 2.0	···
C98	19.1 ± 0.5	2.1 ± 0.3	0.009	5.1 ± 0.4	···
C99	25.3 ± 0.9	1.2 ± 0.2	0.007	13.7 ± 2.0	···
C100	23.5 ± 0.6	0.3 ± 0.0	0.002	1.9 ± 0.2	···
C101	26.3 ± 0.8	1.6 ± 0.2	0.013	21.9 ± 2.4	23.0
C102	22.4 ± 0.7	0.6 ± 0.1	0.007	3.4 ± 0.3	···
C104	28.2 ± 0.9	1.8 ± 0.2	0.027	37.7 ± 3.8	44.7
C105	19.9 ± 1.7	0.7 ± 0.2	0.007	2.1 ± 0.6	···
C106	15.6 ± 1.3	2.0 ± 0.5	0.018	1.6 ± 0.4	···
C107	22.2 ± 0.6	1.3 ± 0.2	0.071	7.3 ± 0.7	···
C108	15.4 ± 0.6	6.4 ± 1.1	0.029	4.8 ± 0.7	···
C109	16.6 ± 2.8	0.7 ± 0.2	0.003	0.8 ± 0.4	···
C110	28.7 ± 0.9	0.7 ± 0.1	0.006	15.5 ± 1.5	···
C111	23.6 ± 1.4	0.6 ± 0.1	0.008	5.0 ± 0.9	···
C112	19.5 ± 0.5	1.4 ± 0.2	0.015	3.9 ± 0.4	···
C113	17.7 ± 0.5	1.1 ± 0.2	0.012	1.7 ± 0.2	···
C114	19.6 ± 0.8	1.0 ± 0.2	0.021	2.7 ± 0.4	···
C115	25.6 ± 0.8	2.2 ± 0.3	0.115	27.5 ± 3.1	31.4
C116	17.1 ± 0.9	1.7 ± 0.2	0.022	2.2 ± 0.4	···

Continued on Next Page...

Table 3.4 – Continued

BLAST ID	T (K)	M (100 $M_\odot$)	Σ (g cm^{-2})	L (100 $L_\odot$)	$L_{\rm bol}$ (100 $L_\odot$)
C117	32.1 ± 0.9	0.8 ± 0.1	0.005	34.6 ± 3.6	···
C118	18.3 ± 2.4	0.2 ± 0.5	0.006	0.4 ± 0.2	···
C119	21.8 ± 0.5	3.0 ± 0.5	0.115	15.2 ± 1.5	···
C120	17.1 ± 0.7	1.3 ± 0.3	0.009	1.8 ± 0.3	···
C121	13.8 ± 2.2	1.3 ± 0.6	0.033	0.5 ± 0.3	···
C122	12.9 ± 1.2	5.4 ± 1.5	0.079	1.5 ± 0.4	···
C123	21.0 ± 0.9	1.4 ± 0.2	0.008	5.9 ± 0.8	···
C124	22.4 ± 1.2	0.2 ± 0.0	0.001	1.4 ± 0.3	···
C125	28.1 ± 0.8	0.2 ± 0.0	0.002	4.4 ± 0.6	5.0
C126	21.9 ± 1.1	2.7 ± 0.4	0.019	14.0 ± 3.4	15.1
C127	33.9 ± 3.7	1.7 ± 0.3	0.006	95.1 ± 71.1	91.3
C128	27.1 ± 1.6	0.3 ± 0.1	0.012	5.4 ± 0.9	6.9
C129	20.3 ± 2.3	2.7 ± 0.7	0.026	9.1 ± 3.8	25.7
C130	23.2 ± 1.2	0.5 ± 0.1	0.008	3.7 ± 0.7	···
C132	27.2 ± 1.5	2.7 ± 0.5	0.015	46.0 ± 9.3	···
C133	23.1 ± 1.3	0.6 ± 0.2	0.004	4.5 ± 0.9	···
C134	22.7 ± 0.6	1.0 ± 0.1	0.009	6.4 ± 0.6	···
C135	25.5 ± 1.3	0.4 ± 0.1	0.011	5.3 ± 0.8	7.5
C136	14.6 ± 1.1	5.1 ± 1.2	0.040	2.9 ± 0.6	···
C139	20.7 ± 0.7	0.4 ± 0.1	0.011	1.4 ± 0.2	···
C140	22.0 ± 0.6	1.7 ± 0.2	0.009	9.1 ± 1.0	···
C141	21.5 ± 0.6	1.7 ± 0.2	0.041	8.3 ± 0.7	8.9
C142	21.6 ± 1.1	0.5 ± 0.1	0.007	2.3 ± 0.4	···
C143	14.6 ± 1.5	1.6 ± 0.5	0.034	0.9 ± 0.3	···
C144	19.4 ± 0.7	0.5 ± 0.1	0.006	1.4 ± 0.2	···
C145	21.9 ± 1.2	1.1 ± 0.1	0.026	5.6 ± 1.2	···
C146	13.8 ± 1.9	5.8 ± 2.7	0.027	2.4 ± 0.8	···
C147	13.3 ± 2.5	1.7 ± 1.9	0.022	0.6 ± 0.3	···
C148	21.9 ± 0.6	0.4 ± 0.0	0.002	1.8 ± 0.2	···
C149	19.5 ± 0.8	1.1 ± 0.2	0.022	3.0 ± 0.6	···
C150	19.3 ± 0.9	0.3 ± 0.1	0.004	0.8 ± 0.1	···
C151	20.2 ± 0.9	0.8 ± 0.2	0.014	2.7 ± 0.4	···
C152	18.9 ± 0.8	0.6 ± 0.1	0.006	1.5 ± 0.2	···
C153	19.7 ± 2.5	0.7 ± 0.3	0.019	2.2 ± 0.7	···
C154	17.4 ± 0.8	1.8 ± 0.3	0.013	2.7 ± 0.4	···
C155	36.0 ± 4.4	8.8 ± 2.4	0.432	697.6 ± 250.4	776.6
C156	26.1 ± 0.7	0.4 ± 0.1	0.004	5.5 ± 0.6	···
C157	26.7 ± 2.0	18.8 ± 2.4	1.019	291.6 ± 108.6	319.3
C158	24.6 ± 0.8	0.2 ± 0.0	0.001	1.5 ± 0.2	···
C159	28.6 ± 0.8	0.8 ± 0.1	0.007	17.0 ± 1.7	···
C160	25.9 ± 2.3	11.2 ± 2.2	0.903	145.3 ± 47.4	152.0
C161	21.4 ± 2.9	0.4 ± 0.1	0.004	1.7 ± 0.7	···
C162	12.4 ± 1.9	2.4 ± 1.2	0.035	0.5 ± 0.2	···
C163	26.4 ± 2.7	0.3 ± 0.1	0.010	4.9 ± 2.3	5.8

Continued on Next Page...

Table 3.4 – Continued

BLAST ID	T (K)	M (100 $M_\odot$)	Σ (g cm^{-2})	L (100 $L_\odot$)	$L_{\rm bol}$ (100 $L_\odot$)
C164	25.6 ± 3.2	0.3 ± 0.1	0.007	4.1 ± 1.8	···
C165	27.3 ± 1.5	0.8 ± 0.1	0.012	14.0 ± 2.5	17.3
C166	24.0 ± 0.6	1.2 ± 0.2	0.013	10.0 ± 1.0	···
C167	20.2 ± 2.1	3.2 ± 0.8	0.045	10.6 ± 2.8	···
C168	24.4 ± 1.3	0.4 ± 0.2	0.014	3.7 ± 0.5	4.9
C169	36.2 ± 3.6	7.6 ± 1.2	0.689	624.4 ± 229.4	664.9
C170	22.9 ± 0.7	0.4 ± 0.0	0.002	2.5 ± 0.3	···
C171	27.1 ± 0.9	0.5 ± 0.1	0.011	8.3 ± 1.0	11.5
C172	13.7 ± 1.6	2.0 ± 0.6	0.069	0.8 ± 0.3	···
C173	10.2 ± 1.1	3.5 ± 1.2	0.007	0.3 ± 0.1	···
C174	18.6 ± 2.0	0.7 ± 0.2	0.039	1.4 ± 0.7	···
C175	13.3 ± 1.1	5.5 ± 1.4	0.034	1.8 ± 0.5	···
C176	25.2 ± 1.7	0.4 ± 0.1	0.004	4.0 ± 0.9	···
C177	24.6 ± 0.8	1.3 ± 0.2	0.013	12.4 ± 1.5	···
C179	14.1 ± 2.1	4.3 ± 2.3	0.035	2.0 ± 0.7	···
C180	42.6 ± 2.4	0.2 ± 0.0	0.006	34.4 ± 6.5	49.4
C181	9.3 ± 1.3	6.2 ± 3.5	0.084	0.3 ± 0.1	···
C182	29.4 ± 1.0	0.6 ± 0.1	0.007	15.3 ± 1.8	···
C183	25.0 ± 2.2	0.7 ± 0.7	0.023	7.1 ± 1.0	10.2

[a] M and L not corrected for different distance than Cyg OB2 (see § 3.4.2).

3.4.2 Sources Behind Cyg OB2

There are eight sources at distances larger than the main Cyg OB2 complex, C27, C30, C33, and C35 in DR7 (§ 3.3.6), C59, C60, and C61 in G79.957 + 0.866 (§§ 3.3.6 and 3.5.1), and C71 in ECX6-27 (§§ 3.2.1 and 3.3.1). For calculating L and M we assigned these rough distances of 6.8, 3.4, and 8.5 kpc, respectively, making L and M 16, 4, and 25 times larger than if the Cyg OB2 distance of 1.7 kpc were adopted. This makes C30 the most luminous source and C71 the most massive. Both are of course integrated over much larger spatial scales than for the sources at 1.7 kpc. Note that L/M and T are preserved.

3.4.3 Temperature

Temperature is obtained directly as a free parameter of the SED fit. Figure 3.16 shows the temperature histogram of BLAST sources detected in the Cyg X field. The super-

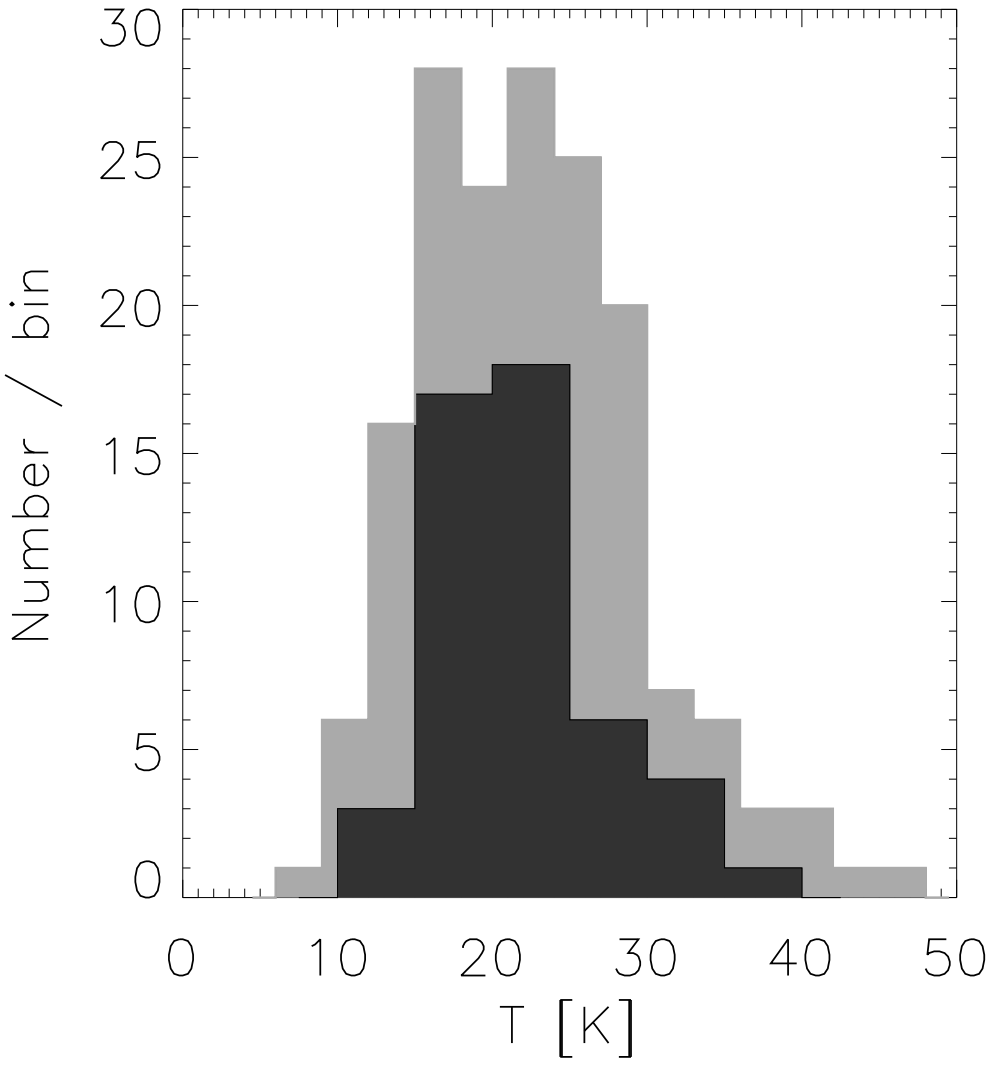

Figure 3.16 Light grey histogram shows the distribution of source temperatures for the Cyg X field. Dark over-plotted histogram is for the BLAST05 Vulpecula field (Chapin et al., 2008).

imposed histogram is for the Vulpecula region (Chapin et al., 2008). The median of the distribution in Cyg X is about 22 K which is comparable to the median for Vulpecula at 21 K. Recall that these are for $\beta = 1.5$. A somewhat higher β combined with a temperature distribution might be a more realistic model (Netterfield et al., 2009), though in the simple model here there is a single T. For $\beta = 2$, the temperatures would be about 10% lower.

3.4.4 Mass

Source mass M is obtained from the best fit amplitude and temperature of the SED and equation (3.2), which shows how any uncertainties in κ, r, and D are propagated as systematic errors. Recall that our sources typically have an apparent FWHM of $1'$, which corresponds to about 0.5 pc. This is more characteristic of a "clump" mass, as distinguished from the high resolution measurements of "cores" by Motte et al. (2007). (Note that the values adopted for κ_0 and β do provide consistency with the 1.2 mm opacity of 1 cm^2 g^{-1} adopted by Motte et al. (2007), following Ossenkopf & Henning (1994). However, without the multi-wavelength coverage, they were forced to adopt a temperature.) From these derived masses, ranging from 10 to 2000 $M_\odot$, the BLAST sources have the potential to form (many) massive stars under favorable physical conditions. For example, in the context of the turbulent core model Krumholz & McKee (2008) predicted a critical surface density for the formation of massive stars, as opposed to fragmentation into much lower masses (see § 3.6.3 for further discussion).

The surface column density for fragments of radius R is given by

$$\Sigma = 2.7 \times 10^{-2} \left(\frac{M}{100 \text{ M}_\odot} \right) \left(\frac{R}{0.5 \text{ pc}} \right)^{-2} \text{ g cm}^{-2}. \quad (3.3)$$

We adopt the deconvolved FWHM of the brightness profile as the radius. Surface densities of the cores (and clumps) of Motte et al. (2007) are listed in Table 3.3. (Note that the assumption of a temperature of 20 K for the cores means that the surface density reported might be an upper limit.) As discussed below, the surface density of BLAST clumps is somewhat lower, in part because of the low angular resolution which limits the ability to discern substructure at small R.

Following equation (2) of Motte et al. (2007), the volume-averaged molecular hydrogen density is

$$\langle n_{\text{H}_2} \rangle = 3.3 \times 10^3 M/(100 \ M_\odot) \text{ cm}^{-3}. \quad (3.4)$$

Because of the BLAST beam size, these clump densities are more than an order of magnitude lower than for the embedded cores found by Motte et al. (2007). The corresponding free-fall time scale (Stahler & Palla, 2005) is also longer,

$$t_{\rm ff} = 5.6 \times 10^5 [M/(100\ {\rm M}_\odot)]^{-1/2}\ {\rm yr}. \tag{3.5}$$

3.4.5 Luminosity

The best fit single-temperature SED is a good and integrable interpolating function from which the far-infrared luminosity L is derived analytically. The frequencies at which the most important contributions arise can be visualized most readily when the SED is plotted in νF_ν form like Figure 3.14.

Often the short-wavelength mid-infrared data lie in excess of this simple SED and to allow for that we simply integrate the piecewise curve connecting that short-wavelength data where available. This is normally a small contribution to the total bolometric luminosity $L_{\rm bol}$ (Table 3.4). For example, for W75N (C169, Fig. 3.14) L rises from 6.2 to $6.6 \times 10^4\ L_\odot$. In the context of position in the logarithmic L-M plot below, this is not a big correction.

The luminosity range in Cyg X is large, extending over three orders of magnitude from $7 \times 10^4\ L_\odot$ down to 40 $L_\odot$, beyond which we lose many sources in the (cirrus) noise (note that the approximate 250 μm completeness line is about 30 Jy; see Chapin et al., 2008).

3.4.6 The $L - M$ Diagram

The $L-M$ diagram can be exploited to assess evolutionary stages (Molinari et al., 2008). Figure 3.17 shows our results in the $L - M$ plane for those sources at the distance of Cyg OB2; the results for the few distant sources (§ 3.4.2) are in Figure 3.18 (note the scales to larger masses and luminosities).

Lines of constant T are diagonal lines (constant L/M) in this L-M diagram: a mass M radiates a predictable L, depending on $\kappa_0 r$ and β. To be consistent with the analytical loci, we plot L from the SED fit rather than the only slightly larger $L_{\rm bol}$. "Orthogonal" to these diagonal lines are loci of constant 250 μm flux density. Note that there are relatively fewer sources between the 30 and 10 Jy loci because of the growing effect of cirrus noise.

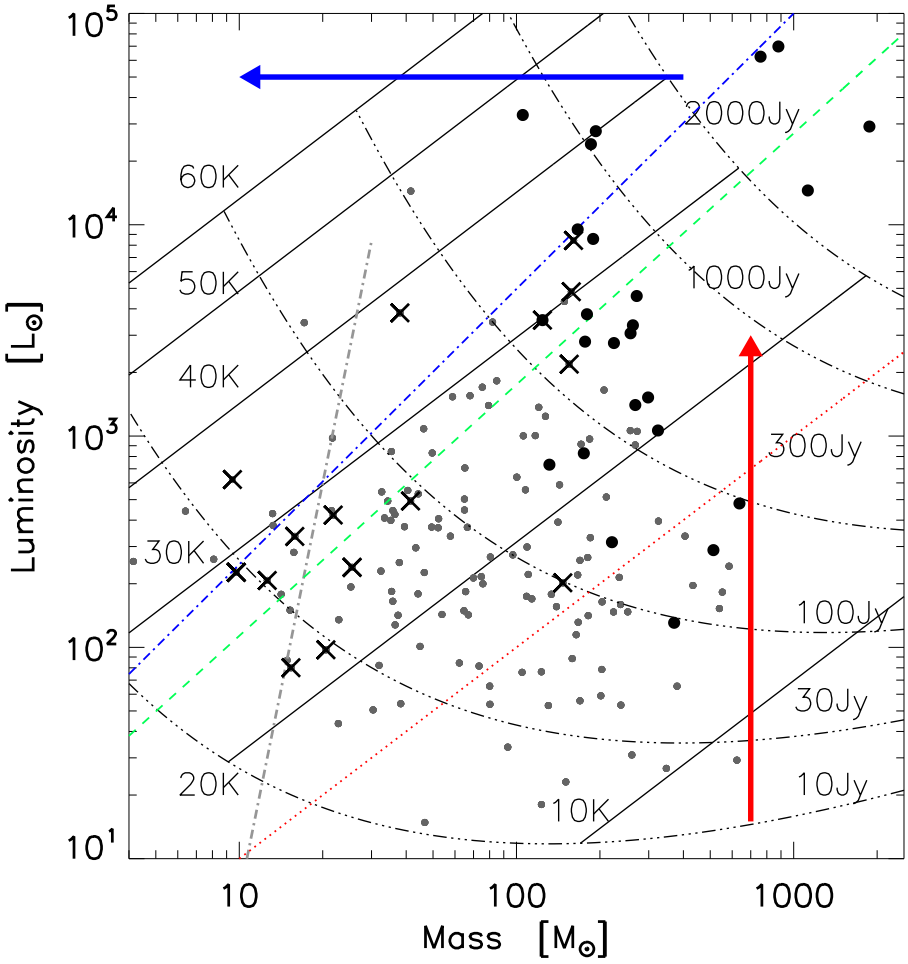

Figure 3.17 Distribution of BLAST sources in the Cyg OB2 complex in the L-M plane. Those to the right of the steep dash-dot (gray) curve are above the Bonner-Ebert mass. Solid diagonal lines are loci of constant T or L/M. The dotted line (red) is $L = M$. Dot-dash curves "orthogonal" to these are for constant 250 μm flux density. Dash (green) and dot-dash (blue) lines denote the location of sources powered by accretion and nuclear burning, respectively, as derived empirically in Fig. 9 of Molinari et al. (2008). Cool sources discovered by BLAST with low L/M still are externally heated (stage E). These appear to be gravitationally bound, but have no significant internal power from star formation yet. The vertical arrow indicates the direction of evolution in this diagram as protostar formation takes hold within a clump. The horizontal arrow indicates the direction of evolution as the embedding material is dispersed by the formed stars/cluster, assuming the surrounding dust still reprocesses most of the internally-generated L. Otherwise (as appears to be the case), the re-radiated L, measured here, is less. Black filled circles are BLAST sources corresponding to clumps of Motte et al. (2007) (Table 3.3). Crosses are sources with morphological evidence of mass-stripping from radiative interaction with Cyg OB2; some at lower luminosity exhibit the effects of external ionization.

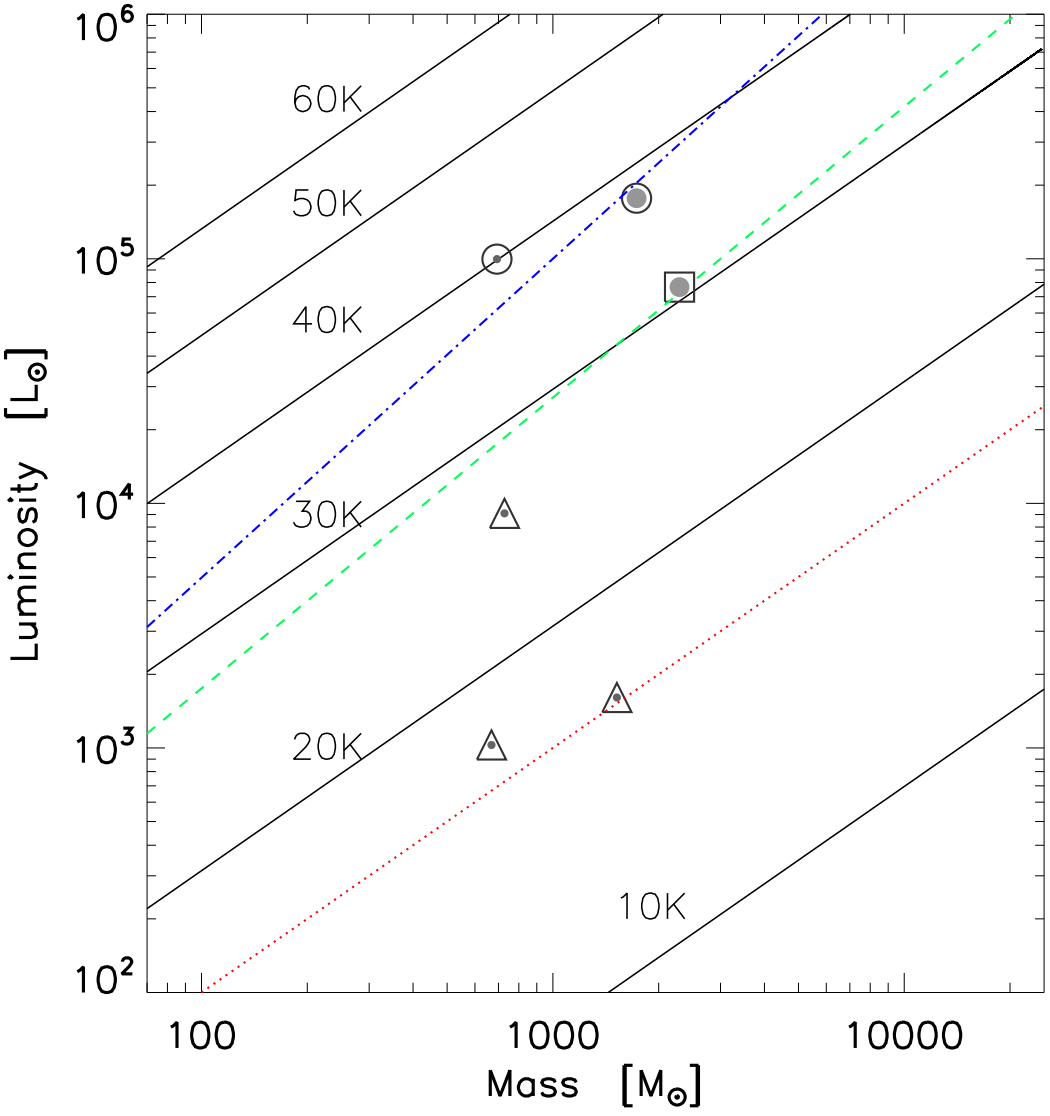

Figure 3.18 Like Fig. 3.17, but for sources more distant than Cyg OB2 (§ 3.4.2). Triangles, circles, and square represent sources about 3.4, 6.8, and 8.5 kpc away, respectively. These include the most luminous and most massive sources in the survey.

In this diagram the "error ellipse" determined by the Monte Carlo technique is elongated along the locus for the source flux density and the extent is well described by $\Delta T/T$. We examined the histogram of $\Delta T/T$ and rejected outliers > 0.19; these were 18 sources with poorly constrained SEDs, usually lacking in definitive data near 100 μm combined with their poor image quality at 500 μm.

The dashed and dot-dash thick lines, roughly lines of constant T, are the loci obtained empirically by Molinari et al. (2008) for sources thought to be in the accretion stage and the later nuclear burning stage (when envelope dispersal begins), respectively. For single low mass stars, these would correspond to the spectroscopically defined "class 0" and "class 1," respectively. With BLAST, we detect sources of the size of "clumps" and furthermore even smaller angular-size high-mass "cores" are capable of forming multiple stars. This warns against a simple interpretation of this diagram based on single-star evolutionary tracks, although it is possible that once high mass stars form, the most massive will dominate the luminosity and ionization (this will depend on the IMF, star formation efficiency, and also small-number statistics).

We think that the most illuminating way to think of pre-stellar evolution in this diagram is in terms of the energy source for the clump, which determines the appropriate equilibrium temperature T for the approximate SED. In the very earliest stages being sought in submillimeter surveys, the energy source for the clumps is predominantly external, namely the impinging interstellar radiation field. In Cyg X the radiation field is in principle higher than in the local ISM because of all the massive stars that have already formed, but this radiation is attenuated by the dusty molecular material in which the pre-stellar clumps are embedded. A useful point of reference is the equilibrium temperature corresponding to $L = M$, which for the adopted $\kappa_0 r$ and β (§ 3.4.1) is 16.2 K.

Massive sources located below this $L = M$ locus (see § 3.5.6) still can have substantial L by virtue of a lot of mass, but cannot have any predominant internal source of energy (either accretion or nuclear), and so could be called "starless." This term is probably best avoided for these clumps, within which there might actually be a few low mass stars already forming and detectable by sensitive telescopes like *Spitzer* (§ 3.6.2). The key consideration is what is the dominant source of energy determining T. As mentioned in the introduction, these clumps could be said to be in stage E ("E" for "external" or "earliest"), which seems to us a better terminology than "starless," or "class -1" for single-star pre-stellar cores. Figure 3.17 shows that there are many clumps in this stage. We can calculate the Bonner-Ebert mass, above which (within the assumptions) a clump

is gravitationally unstable (e.g., Stahler & Palla, 2005):

$$M_{\rm BE} = 1\ [T_{\rm g}/(10\ {\rm K})]^{3/2}[n_{\rm H_2}/(10^4\ {\rm cm}^{-3})]^{-1/2}\ M_\odot. \tag{3.6}$$

Thus, assuming that $T_{\rm g} \leq T$, the low-luminosity, low-temperature BLAST clumps are unstable. As discussed below, in the simplest theory they would evolve into the higher-luminosity, higher-temperature clumps seen higher in the diagram at the same M.

As gravitational collapse progresses, more and more mass accretes into protostellar cores. The actual luminosity in this accretion-powered stage depends on the accretion rate and the potential well. In recognition of the underlying energetics, these clumps could be said to be in stage A ("A" for accretion-powered). Consistent with this interpretation, sources observed to be in this part of the L-M diagram have a characteristic signature of active accretion (§ 3.5.5).

Ultimately, nuclear fusion becomes the dominant source of power. Unlike for low mass stars, massive pre-main sequence stars probably continue accreting after first beginning nuclear burning, increasing their mass further (Zinnecker & Yorke, 2007). When this accretion ends, an individual star is at its final position on the ZAMS. It will still be embedded, and so optically obscured, but its vast power reprocessed will produce a relatively warm far-infrared source. For sufficiently massive stars, significant ionization of the surroundings will ensue, producing a hypercompact H II region. There could be many within a single clump, for example (Rivera-Ingraham et al., 2010). These clumps would appear in the $L-M$ diagram near the empirical nuclear burning locus (see § 3.5.4).

As the massive stars clear their local environment through the expansion of the H II region and via radiation pressure on dust (successively ultracompact then compact H II regions), the individual objects will become more extended far-infrared sources. The strong short-wavelength stellar radiation field will enhance both thermal emission and non-equilibrium emission from PAHs in nearby photodissociation region material, making the SED of the integrated re-emission of the clump broader and more complex. Evolution in the L-M diagram will initially be at constant L with decreasing M; ultimately, the optical depth and/or covering factor would decrease so that the reprocessed L will fall.

A stellar cluster with an extended H II region would emerge. Even though such clusters are found in Cyg X, they are not detected as compact BLAST sources and so do not appear in the L-M diagram; only objects like their precursors would.

3.4.7 Census

It is interesting to ask how many objects are in each evolutionary stage. To address this we have concentrated on the mass range between 50 and 500 $M_\odot$ where there is an abundance of sources (100 omitting the sources more distant than Cyg OB2) and the lower luminosity end is minimally affected by completeness, at least down to $L = M$. Figure 3.19 presents a histogram showing the relative populations in terms of L/M, which we have argued is at least qualitatively related to the successive stages. Note that this figure looks quite similar to Figure 3.16, there being a non-linear mapping of L/M into T.

Figure 3.19 shows that there are many sources in stage E ($L/M < 1$ $L_\odot/M_\odot$), even though it is clear that there are selection effects (basically the combination of low flux density and cirrus noise) beginning to limit their detectability. Most of the sources are in the accretion-dominated stage A (L/M up to about 30 or $T = 30$ K). The relatively fewer hotter sources, where nuclear burning is taking over, presumably reflects the shorter lifetime of this stage, which could be characterized by more rapid final collapse and then envelope dispersal.

3.5 Evolutionary Stages

Although our BLAST survey is "blind and unbiased", in surveying the entire region rather than selecting sub-regions with, say, high extinction (Schneider et al., 2006a; Motte et al., 2007), it is not unbiased in another sense. This region is obviously well known for its GMC and having formed the Cyg OB2 association, which has dramatically influenced the surrounding molecular material (§ 3.5.1). In such a region one expects there to be both triggered and/or sequential star formation, supplementing spontaneous star formation. The conditions could be quite different now than what preceded the formation of Cyg OB2. We find no evidence for the precursor of another such massive compact association. Nevertheless, within this reservoir several smaller, but still notable, embedded clusters have been identified (§ 3.3.1). The OB stars in the more evolved ones have produced extended H II regions like DR17 and DR22 (Downes & Rinehart, 1966).

As discussed in § 3.3.5, in their ^{13}CO J = 2 → 1 data cubes, Schneider et al. (2006a) have identified many clumps (detailed in their Appendix C). Where the coverage overlaps, each of the BLAST compact sources can be linked through the morphology to one of these

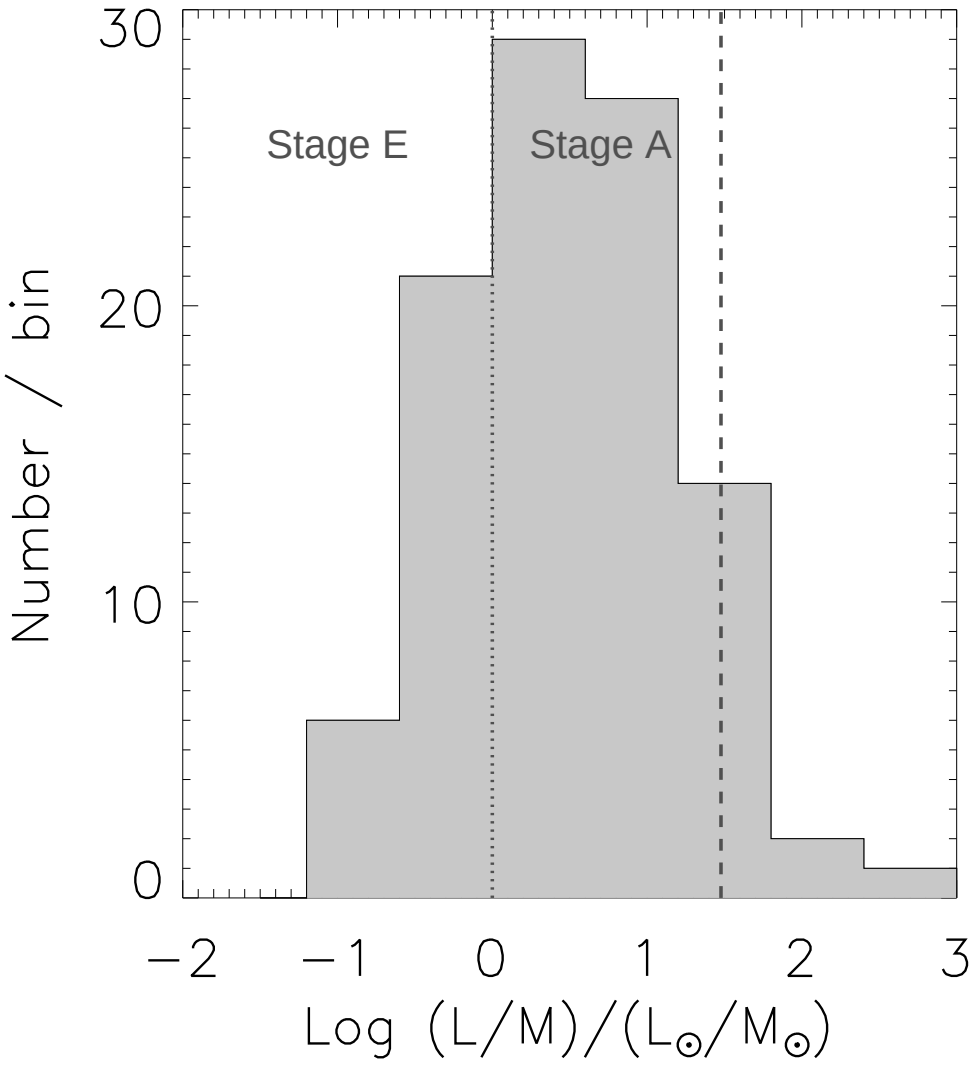

Figure 3.19 Histogram of L/M ratio of the Cyg X compact sources in the mass range 50 – 500 $M_{\odot}$. The dotted vertical line separates stage E sources below the locus $L = M$ in Fig. 3.17. Most sources are in the accretion-powered stage A, up to the dashed line ($L/M \approx 30\ \ L_{\odot}/M_{\odot}$), beyond which nuclear burning becomes predominant.

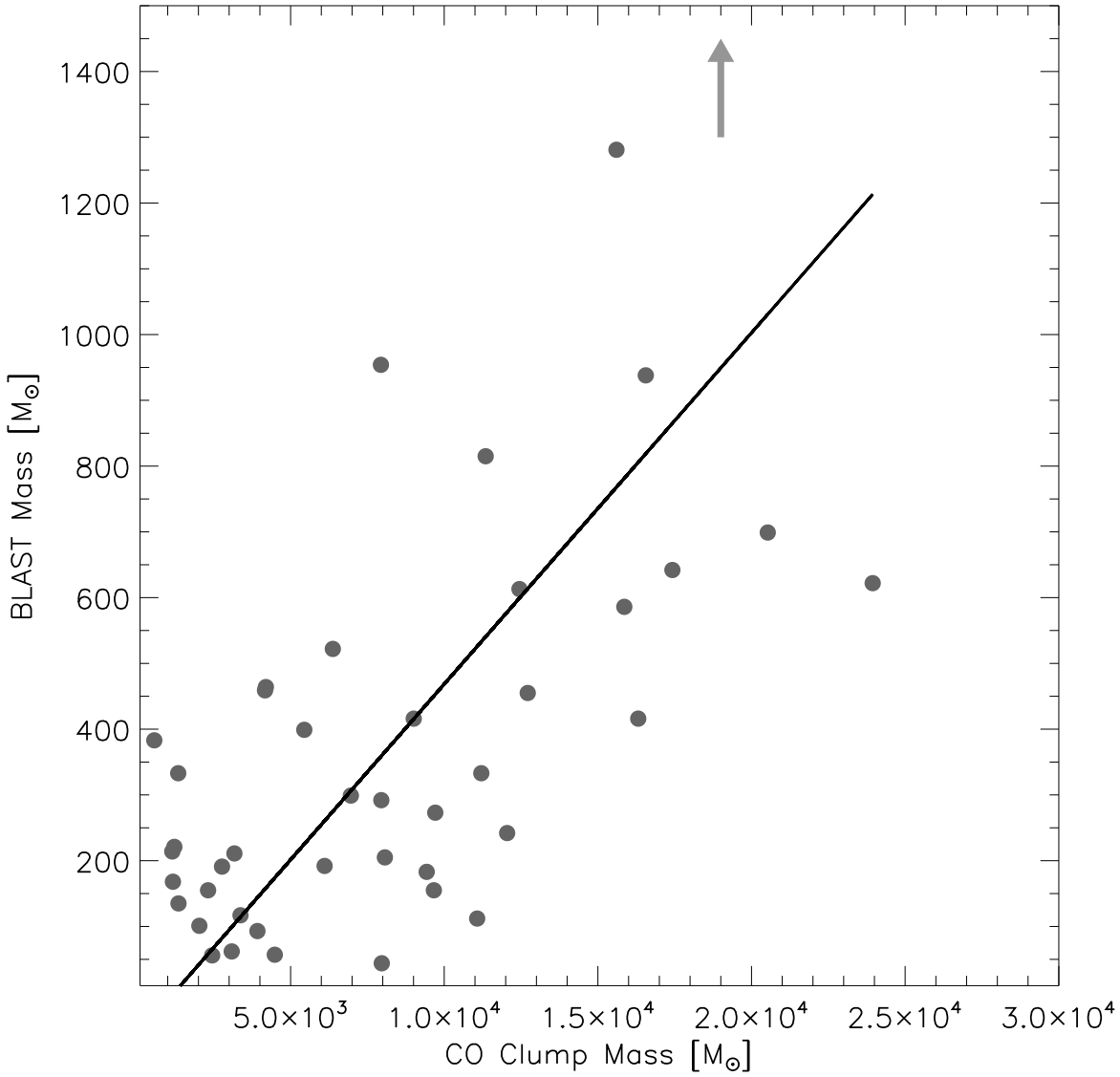

Figure 3.20 Sum of the masses of the BLAST sources within CO clumps of Schneider et al. (2006a) versus the CO-estimated clump mass. Linear correlation has a slope of 0.05. An outlier at 3000 $M_{\odot}$ along the y direction, pointed to by the arrow, is not included in the fit.

clumps (see examples in § 3.3.6). In Figure 3.20 we compare the sum of the masses of the BLAST sources (§ 3.4.4) within each clump to the tabulated CO-estimated clump mass. These are fairly well correlated, and we find typically that only a few percent of the material over these extended regions is in the form of compact sources, in some way related to the (potential) star formation efficiency. This plus the timescales for clump evolution indicate that there is still an interesting future for star formation in this GMC.

From this perspective on the complex range of star formation going on in Cyg X, our goal is to work toward submillimeter evidence for the earliest stages of massive star formation. The somewhat later stages have been detected by a variety of earlier observations, and BLAST sees these too. The many clusters in Cyg X are agents producing complex morphologies in the medium, through expanding H II regions and strong UV radiation fields, and they might play a pivotal role in inducing further star formation in the molecular clouds. We work in reverse chronological order, finding what the outcome of a particular stage looks like in multi-wavelength data, and then asking what this tells us to look for in the stages that came before.

3.5.1 The Influence of the Massive Cluster Cyg OB2

Comparing the estimated mass of Cyg OB2 (§ 3.3.1), 4 to 10×10^4 $M_\odot$ (Knödlseder, 2000) to the remaining molecular reserve in Cyg X, 4×10^6 $M_\odot$ (§ 3.3.5; Schneider et al., 2006a), indicates that formation of this OB2 association was the major event for this GMC, perhaps not to be repeated. Both of the central clusters, BBD1 and BBD2, are more massive than the Trapezium. Again, will there be more elsewhere in Cyg X? There is no BLAST clump that could be a precursor to such a prominent cluster and even adding the mass of an embedding CO clump (the most massive of which is 2×10^4 $M_\odot$) would fall short. Nevertheless, in unevolved GMCs, massive and compact precursors to such clusters might be detectable in the Planck Cold Core survey (§ 3.2.2; Juvela et al., 2010b). It will of course depend on how long-lived the precursor stage is.

Massive young stars, through ionization and radiation pressure, dramatically influence their environment. Cyg OB2 has an age of about 2.5×10^6 yr (Negueruela et al., 2008), and in that time has created in the ISM a lower density region of radius 1° (30 pc), ionized in the interior (see Fig. 3.2) and surrounded by distinctive molecular cloud complexes. The connectivity of these clouds in the CO data cube and the signs of interaction through UV radiation (*MSX* Band A data) led Schneider et al. (2006a) to conclude that they

were all located at the same distance. While obviously not yet disrupted, the clouds have been reorganized and so Cyg OB2 might have induced some of the further star formation that is on-going.

Above Cyg OB2 in Figure 3.2 is a relative void (nevertheless, it is projected on an emission and extinction plateau), with no high-contrast structures of significant column density in any tracer (molecules, dust, ionized gas). The right hand edge is defined by CXR9 whereas the left, though well-defined and containing some BLAST emission too, is unnamed. This void could be a "chimney" blown out by Cyg OB2, channeling high pressure gas out of the Galactic disk.

Pillars

Radiative forces sculpt pillars, where there are pre-existing dense molecular structures. The range of radiative influence of Cyg OB2 extends to a radius of at least 2° (60 pc), as illustrated by the prominent pillars near G79.4-1.1 and G81.4+2.2 in the *Spitzer* IRAC and 24 μm MIPS images. Figure 3.21 shows an example of a long pillar or elephant trunk pointing toward the Cyg OB2 core. At the end of the trunk is a luminous BLAST clump C85. In CO emission, it is called DR20NW by Schneider et al. (2006a), with CO velocity +12 km s^{-1} (see also Fig. 3.10). The clump is the obstruction defining the trunk structure. Star formation is occurring in this clump, suggestive of triggering by Cyg OB2. This geometry is seen elsewhere; for example, C75 on the left edge of the chimney is also at the head of a pillar facing Cyg OB2 (see also the cometary tails below).

Such a peninsular structure is continually eroded, which would produce eventually an isolated clump with a cometary tail, but this particular trunk appears to be attached to the molecular cloud, curving round and broadening out to include C91, C98, and C100 along the interface. These structures also evolve due to instabilities at the interface of the H II region and the neutral molecular cloud, and evidently on-going star formation is commonly induced.

Note that DR20 (C88, C87, C90) is at a projected distance of 6′ from this trunk, and yet does not display the same hallmark interactions. However, this complex is at a very different velocity −3 km s^{-1}, more closely associated with DR21. Schneider et al. (2006a) note that clump DR20W, at the same velocity, does have an elongated shape pointing to Cyg OB2 (see Fig. 3.10). BLAST C80 is at the brighter head of its CO emission and C83 in the dimmer tail. Inspection of the *Spitzer* images shows signs of interaction with

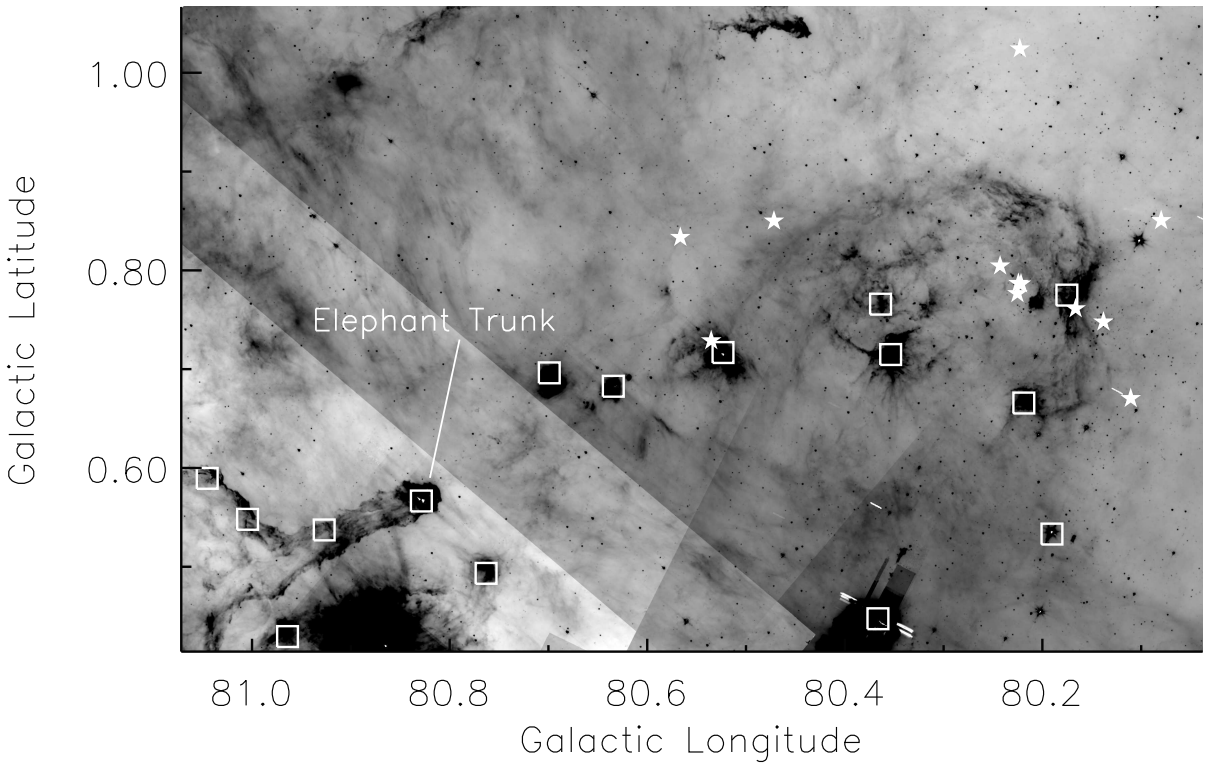

Figure 3.21 IRAC band 4 image showing a prominent pillar or "elephant trunk" structure pointing to Cyg OB2. Squares are BLAST sources and stars show the position of the OB stars.

nearby stars in Cyg OB2, but at a different position angle than the CO clump which is oriented more toward the core.

Schneider et al. (2006a) also identify other molecular pillars in the CO channel maps, the most prominent of which is the long "DR17 pillar" at a velocity about -13 km s^{-1} (Fig. 3.9). From its direction of elongation, it appears to be influenced by the cluster LK12 in DR17, but there is not perfect alignment (possibly there is some influence of LK14 to the north). This cluster does produce a bright mid-infrared interface at BLAST C115, near the end of the pillar. The molecular pillar stretches from C115 through C114, C112, C113, and C108 to C109 and possibly C106 (Fig. 3.9). The CO channel maps hint at a connection between this DR17 pillar and the above-mentioned elephant trunk, but this pillar does not appear to be influenced by Cyg OB2.

Cometary Tails

Further striking evidence for interaction is provided by cometary tails in more detached structures, pointing away from the core of Cyg OB2. These too are seen most clearly in *Spitzer* IRAC and 24 μm MIPS images.

DR18 is a large scale prototype, with a ionized edge facing the Cyg OB2 core, the BLAST clump C73 in the neutral region next to this, and an extended tail seen in both CO and dust emission (mid-infrared to submm). It is actually more complicated than this in detail, because a loose aggregate of early B stars has formed (triggered?) near the leading edge adding additional ionizing power and sculpting of the immediate PDR environment (Comerón & Torra, 1999).

Another interesting example in the opposite direction is the cluster ECX6-21 (DB12) containing BLAST C55 in the head. C55 corresponds to OB2 globule 2 of Schneider et al. (2006a) with CO velocity -4.5 km s^{-1}. About $5'$ "downstream" is a miniature version containing C53. These are located on the inner edge of the ionized ridge CXR9.

Further afield from Cyg OB2 is DR15, with a cluster and two BLAST clumps, C32 and C28. Here the putative tail (see Fig. 3.7) appears to be part of an extended structure prominent in presumed PAH emission, which bends significantly toward lower latitude at a distance of $17'$, near C12. There are several other BLAST clumps along this structure, C21 before the bend, and C11, C9, C4, and C3 beyond.

Figure 3.22 shows a field quite close by, spanning the ionized ridge CXR11. There are two BLAST clumps C38 (on the left) and C17 with material ablated from the clump

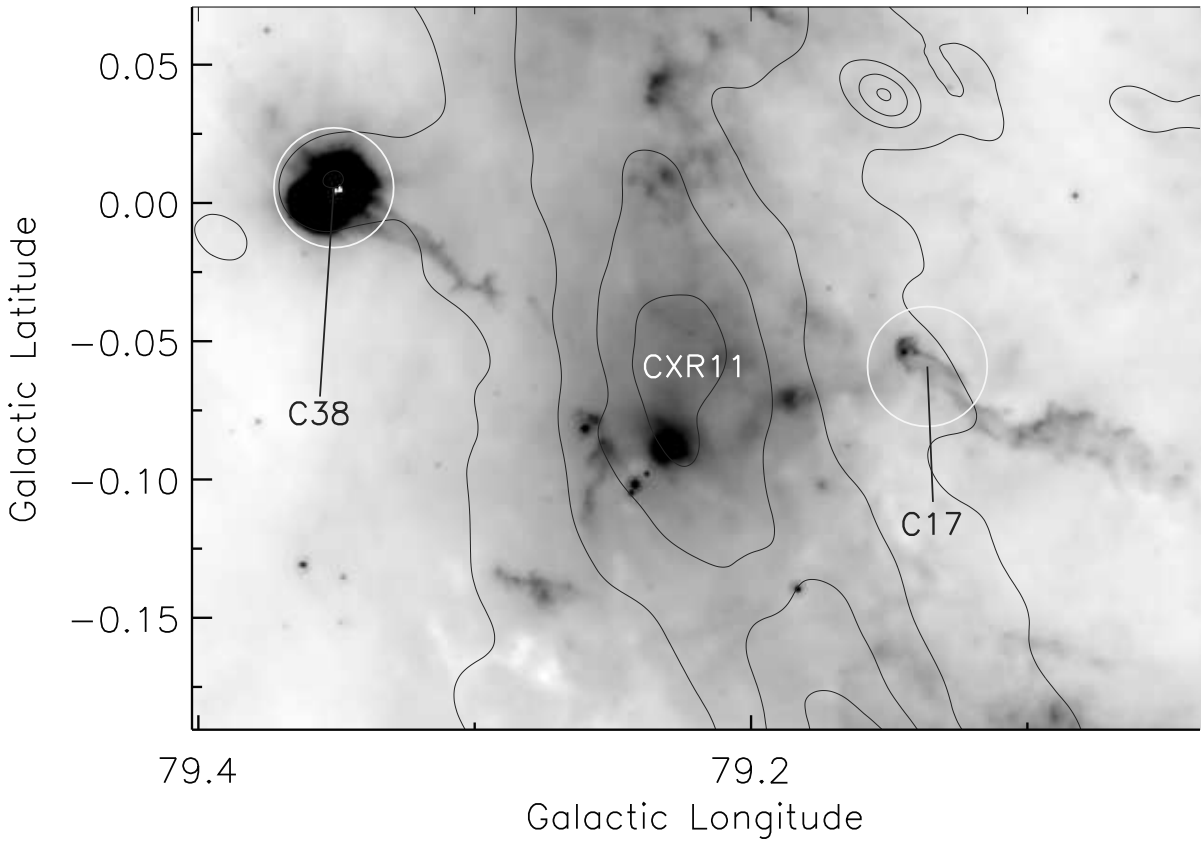

Figure 3.22 MIPS 24 μm image showing two BLAST sources, C38 and C17, with cometary tails. The spatial extents of the tails are roughly 1.5 and 3 pc, respectively. Contours of 21-cm radio emission from CGPS show ridge CXR11.

clearly being blown away. However, in the BLAST image these cometary tails are not detected because of low column density. C38 is massive enough to have a detectable ionized edge. The C17 tail extends to an angular distance of 6′ or about 3 pc in spatial scale. If, for illustration, the clump lifetime were 10^5 yr the required material speed would be 30 kms^{-1} to reach such an extent.

There are many other sources like this with obvious interactions. Their positions in the L-M diagram are highlighted in Figure 3.17. For these exposed sources, it is clear that a sizable amount of mass is lost due to this erosion, and so the more evolved sources occupy a region towards the lower end of the mass axis in the L-M plot.

The ridge of submillimeter emission containing sources C59, C61, and C60 provides an interesting counter-example. The superimposed CO ridge is called "OB2 globule 1" by Schneider et al. (2006a) who suggest an interaction due to its compactness and proximity to the core of Cyg OB2, in projection about 15′ away. However, inspection of the detailed *Spitzer* images now available reveals no signs of interaction. Furthermore, the displaced ionized ridge parallel to the dust emission is on the side away from Cyg OB2 (see Fig. 3.6). Together with the peculiar velocity, the evidence is that this object is more distant, beyond the influence of Cyg OB2.

3.5.2 Clusters and Extended H II Regions

Interactions of clusters with the ISM produces large scale complex structures and directly affect the next generation star formation efficiency in the region. The Cyg X region hosts numerous young open clusters (§ 3.3.1). In the BLAST region, there are five which have well-resolved H II regions with a fairly classical geometry. Expansion of the ionized gas, stellar winds, and radiation pressure have evacuated the core of the parent molecular cloud and produced a dense shell which appears in an arc-shaped geometry surrounding the cavity and cluster. Partial shells are suggestive of a blow-out or blister geometry. The 21-cm radio emission traces the ionization front, and slightly outside of this is the FIR and submillimeter continuum, where dust in the shell absorbs the FUV radiation emitted by the star cluster.

To illustrate this, Figure 3.23 shows an IRAC band 4 image highlighting the most massive of these clusters, LK11, with about 80 OB stars powering the DR22 region. Note that the PAH emission in this image is from the PDR, outside the ionization front, whereas the 24 μm emission in Figure 3.12 shows greater correlation with the ionized

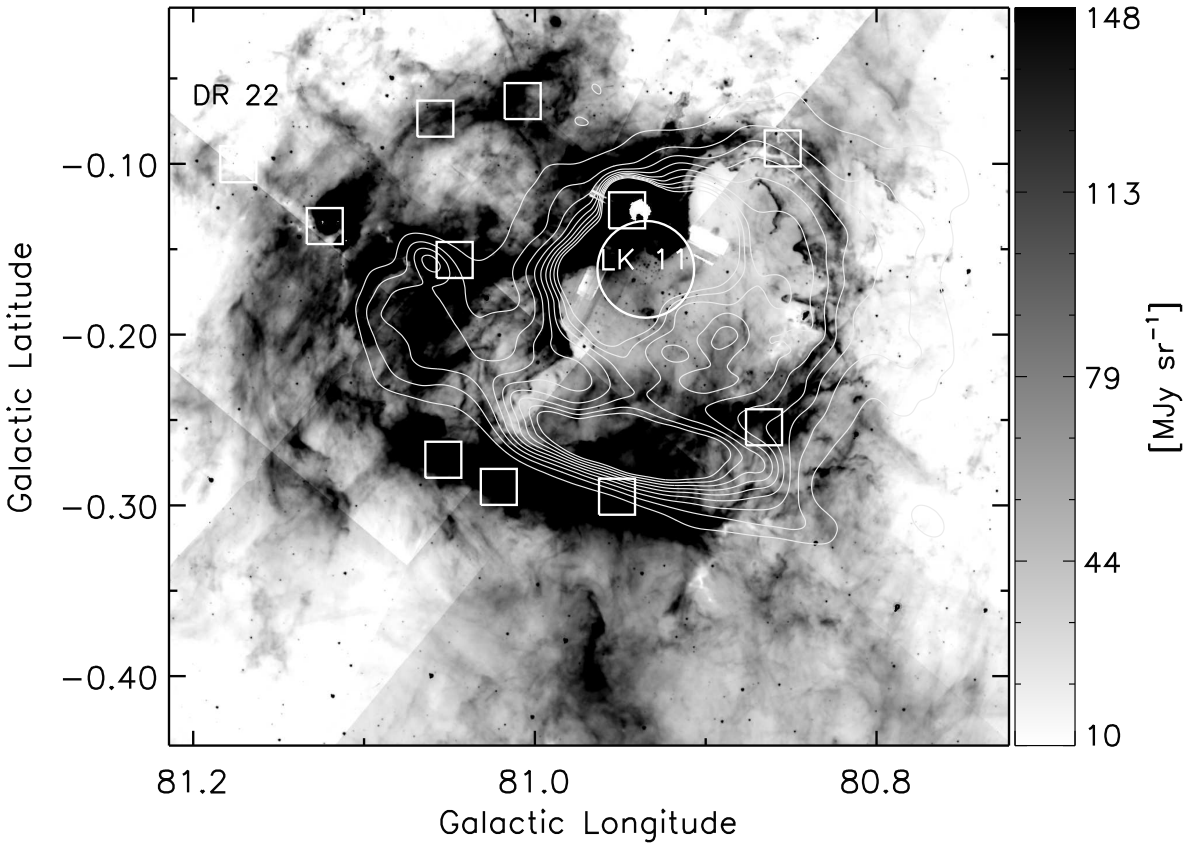

Figure 3.23 IRAC band 4 (8.6 μm) image of DR22. Circle marks the position and size (R_{50}) of the LK11 OB star cluster (Le Duigou & Knödlseder, 2002). Overlaid contours are 21-cm radio continuum emission from the CGPS. Squares indicate the BLAST sources, embedded in arcs of submillimeter emission outside the ionization front (Fig. 3.12).

gas. The BLAST sources occur along CO ridges to the north and south-east, the latter clearly arc-shaped (making this the "smiley nebula"). The most luminous source C92, coincident with a compact H II region, must be internally powered (see below). LK11 is shaping this clump and both the geometry and proximity suggest that star formation has been triggered there.

Similar geometrical statements can be made about LK09 and C30 (and C27, C33) in DR7 (Fig. 3.6), LK12 and C115 in DR17 (Fig. 3.9), LK13 and C127 in G81.445+0.485 (the Diamond; Fig. 3.11), and DB22 and C182 (and C177, C178) in ECX6-33.

Although these H II regions have evolved, the exciting clusters are still quite young; their stellar density is typically five times higher than for evolved open clusters (Le Duigou & Knödlseder, 2002). Thus their radii R_{50} (half population radius), about 1′

(0.5 pc), are perhaps indicative of the size of the precursor molecular clump. The stellar masses are estimated by Le Duigou & Knödlseder (2002) to be 300 to 2000 $M_{\odot}$ (a few times more for DR22) and so the precursor clump would be more massive still. BLAST clumps are of this angular size, but not nearly as massive, not even up to these stellar masses let alone allowing for inefficiency of star formation. We conclude that there are presently no BLAST clumps capable of forming such massive clusters. The embedding CO clumps are perhaps massive enough, but would have to condense considerably to form a concentrated cluster. The lifetime of these condensations could be quite short, lowering the likelihood of detecting this stage in a single GMC.

3.5.3 Triggered Star Formation

Spatially, a massive star cluster can promote further star formation in nearby molecular material by driving winds and shocks, which both sweep up material and overrun and compress pre-existing condensations. Subsequent gravitational instability and/or radiatively-driven implosion of the overrun condensations collectively lead to what is known as "triggered" star formation (Elmegreen, 1998; Zinnecker & Yorke, 2007; Koenig et al., 2008). Thus a sequence of generations of star formation can occur with spatial ordering (recognized as "sequential" star formation). For example, Koenig et al. (2008) studied these phenomena in W5 with *Spitzer*.

As discussed, in the vicinity of the OB star clusters in Cyg X there is evidence of further star formation. The most persuasive, if circumstantial, evidence for triggering is in the DR22, DR8, DR17, and DR15 molecular clouds.

3.5.4 Compact H II Regions

Earlier in their development, when massive protostars first become hot enough to emit ionizing UV photons, they initially ionize only a dense core, producing a hypercompact H II region, potentially optically thick at lower radio frequencies. Subsequent expansion of the ionized gas leads successively to ultracompact, compact, and then evolved H II regions (Churchwell, 2002). The initial stage, which occurs when accretion is still strong, is accompanied by energetic bipolar outflows.

Circumstellar dust reprocesses the absorbed radiation from the protostar, re-radiating the energy at infrared wavelengths. Thus in the Galactic Plane, embedded H II regions

are the most luminous objects observed in the mid and far-infrared, first by *IRAS* and then *MSX*.

Hot cores, dense molecular clouds with temperature ≥ 100 K as classified by Kurtz et al. (2000), are often thought to be precursors of UC H II regions. In our survey, we do not detect any source warmer than ~ 40 K. Nevertheless, some of the brightest sources detected by BLAST in Cyg X are found among well-known H II regions, with previous studies revealing them to be compact or ultracompact; they are all detectable in 21-cm radio continuum emission in the CGPS. Five of these studied by Motte et al. (2007) are tablulated in Table 3.5 and discussed in the next subsection. Motte et al. (2007) obtained masses of these sources assuming a dust temperature of 40 K. We are actually able to measure the temperature, finding 30 to 40 K. Still, it should be remembered that BLAST measures dust emission including the outer envelope of these sources, which is cooler than dust near the core; with higher angular resolution MAMBO should sample slightly warmer dust on average.

These five sources are marked in Figure 3.24 with special symbols. They are clearly internally powered, beyond the transition to predominant nuclear burning. For reference, a 20 $M_\odot$ zero-age main sequence star of spectral type O9V has $L_{\rm bol} = 10^5\ L_\odot$ (Schaerer & de Koter, 1997). Even the most luminous of these embedded stars at the distance of Cyg OB2 is not that luminous. Given the mass of these clumps, $> 100\ M_\odot$, they also seem likely to host more than a single star.

The precursors to these sources should be cooler, at similar mass. In the range of a few 100 $M_\odot$, there are many such BLAST sources in Figure 3.24, the earlier stages to be discussed below. However, there do not seem to be the cooler equivalents of most massive sources (W75N, DR21, DR21 OH), suggesting that the precursor stage to the most massive (dense) clumps is relatively short-lived or that when cooler the clump is too extended to have been classified as a BLAST source (§ 3.6.4).

Also recorded in Table 3.5 are another 11 instances (including two distant ones) of BLAST sources with apparently associated compact 21-cm radio emission, not targeted by Motte et al. (2007). These are slightly cooler, with median temperature 27 K. These are marked in Figures 3.18 and 3.24 with grey filled circles.

A histogram of the bolometric luminosities of all of these sources, including the luminosity corrections for the two distant ones, is given in Figure 3.25. The luminosities of the five marked sources are at the high end, whereas most of the others have much lower luminosities. The luminosities can be used to calculate the corresponding photoionizing

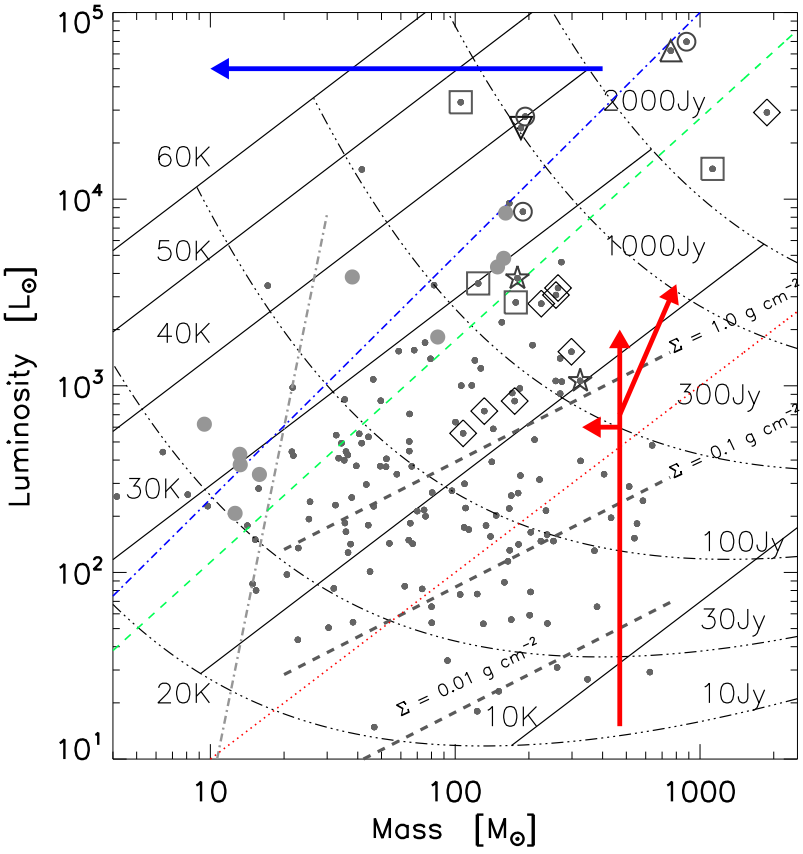

Figure 3.24 Same as Fig. 3.17, but highlighting physical properties deduced from ancillary data. Many of the most luminous sources are ionizing and have associated radio continuum emission. Close to the nuclear burning locus, these contain deeply embedded massive stars (Motte et al., 2007): △ HCH II; ◯ UCH II; ▽ CH II. Grey filled circles are other BLAST sources with compact 21-cm continuum emission, outside the survey area of MAMBO. Protostars in stage A are at somewhat smaller L/M than the compact H II regions, near the accretion locus. These are classified by Motte et al. (2007) as □ HLIRPC; ◇ MIRQP; and ★ IRQP. At the lowest L/M, clumps are externally heated (stage E), while at intermediate values the clumps are probably powered by low mass protostars; the thick dashed lines are the model predictions of Krumholz & McKee (2008) (eq. [3.7] in § 3.6.3) for surface densities Σ = 1.0, 0.1, and 0.01 g cm^{-2}. The vertical arrow signifies the result of evolution in L as star formation progresses in a clump. This might be interpreted as the result of the evolution of a single massive protostar (Molinari et al., 2008). However, the initial rise seems more likely to be the result of power from low-mass YSOs (§ 3.6.2). According to the model of Krumholz & McKee (2008), unless Σ exceeds a critical value near 1.0 g cm^{-2}, a massive star will not form and so the rise in L will be arrested (§ 3.6.4); this possibility is indicated schematically by the short horizontal arrow. Finally, the arrow segment pointing to the upper right represents qualitatively the evolution in the simulations by Smith et al. (2009) and Wang et al. (2010), where mass is fed into gravitational potential minima from larger scale structure.

Table 3.5: Compact H II regions and protostars

BLAST ID	T (K)	M (100 $M_\odot$)	L (100 $L_\odot$)	Source Name	MAMBO 1.2 mm	Figure[a] No
C1	40	1.9	489.0	S26, AFGL2591	UCH II	3.7
C7	26	2.6	50.2	S30, IRAS 20293+3952	MIRQP	3.7
C14	30	3.8	4.5	IRAS 20255+4032	···	3.6
C30[b]	38	17.6	1640.0	IRAS 20264+4042	···	···
C32	46	1.1	330.7	S41, IRAS 20306+4005	HLIRPC	3.7
C36	26	2.6	30.6	S37, IRAS 20305+4010	MIRQP	3.7
C38	38	0.4	48.7	IRAS 20319+3958	···	···
C49	27	0.1	2.8	···	···	···
C55	30	1.6	52.9	IRAS 20286+4105	···	···
C58	28	0.2	4.1	IRAS 20315+4046	···	···
C64	31	0.1	6.0	IRAS 20328+4042	···	···
C71[b]	31	22.5	782.5	IRAS 20320+4115	···	···
C73	33	1.6	87.6	IRAS 20333+4102	···	···
C76	28	0.8	21.8	IRAS 20327+4120	···	···
C80	30	1.5	48.9	IRAS 20332+4124	···	···
C85	30	1.2	51.8	N6, IRAS 20343+4129	HLIRPC	3.10
C87	27	1.8	33.6	N14, IRAS 20352+4124	HLIRPC	3.10
C88	33	1.9	106.3	N10, IRAS 20350+4126	UCH II	3.10
C92	39	1.9	323.2	N58, IRAS 20375+4109	CH II	3.12
C104	28	1.8	44.7	N62	IRQP	3.12
C107	22	1.3	7.3	N63	MIRP	3.12
C115	26	2.2	31.4	N3	MIRQP	3.9
C119	22	3.0	15.2	N12	MIRQP	3.9
C141	22	1.7	8.9	N65	MIRQP	3.12
C145	22	1.1	10.7	N68	MIRQP	3.12
C155	36	8.8	776.6	N46, DR21	UCH II	3.11
C157	27	18.8	319.3	N44, DR21(OH)	MIRQP	3.11
C167	20	3.2	10.6	N24	IRQP	3.11
C169	36	7.6	664.1	N30, W75N	HCH II	3.11

[a]Figure number of the images containing individual sources.

[b]M and L corrected for distance (see § 3.4.2).

flux Q_0 and check for consistent radio emission (assuming no optical depth; see § 3.3.2). The lowest luminosity sources in Figure 3.25 would not account for the associated H II emission. Inspection of the IRAC image reveals all but C76 to have cometary structure (those of higher mass and luminosity were already mentioned above: C55, C73, C80; all but C14 appear to be influenced by Cyg OB2) and our interpretation is that the radio emission comes from external ionization. C76 lies in close projection to the O7 V star MT771.

Specific Embedded H II Regions in Cyg X

Here we make brief comments on the five marked sources from Motte et al. (2007) in Table 3.5, plus three others that appear to be in the same advanced stage of evolution.

C1, AFGL 2591: C1 coincides with AFGL 2591, an UCH II region that is among the most luminous sources in Cyg X. Motte et al. (2007) identify a core S26 within a clump S5. We find dust temperature 40 K, bolometric luminosity 2.7×10^4 $L_\odot$, and mass 190 $M_\odot$. Campbell (1984) discovered that AFGL 2591 is comprised of a young stellar group and deduced that the H II region is being generated by B0 stars. This region also has powerful outflows (Bally & Lada, 1983; Poetzel et al., 1992). Schneider et al. (2006a) argue that the cometary shape is due to the influence of Cyg OB2.

C88, DR20: Compared to C1, C88 is slightly cooler (32 K), less luminous (8.6×10^3 $L_\odot$), but equally massive (190 $M_\odot$). It corresponds to clump N4 (core N10) of Motte et al. (2007). The embedding region (see Fig. 3.10) is bright in 21-cm radio continuum, mid-infrared, and PAH emission. C88 and C87 are two bright sources along a ridge containing C90. C88 is closest to the CGPS radio peak, but offset to lower longitude, whereas the UCH II region G80.86+0.4 observed by Kurtz et al. (1994) is centered on C88. C88 also coincides with IRAS 20350+4126. Odenwald et al. (1990) suggest excitation by an O5-6 ZAMS star, but this seems too early.

The source C87 (clump N6, core N14) is relatively cold, 27 K, with no free-free emission. Its position on the L-M plot suggests most of the luminosity is generated from accretion (see below).

C92, DR22: C92, also known as IRAS 20375+4109, is a compact H II region in DR22 with a massive dense core, N58 (Motte et al., 2007). We find dust temperature 39 K, bolometric luminosity 2.4×10^4 $L_\odot$, and mass 220 $M_\odot$. Odenwald et al. (1986) studied this region at both radio and far-infrared wavelengths and assuming it to be 45

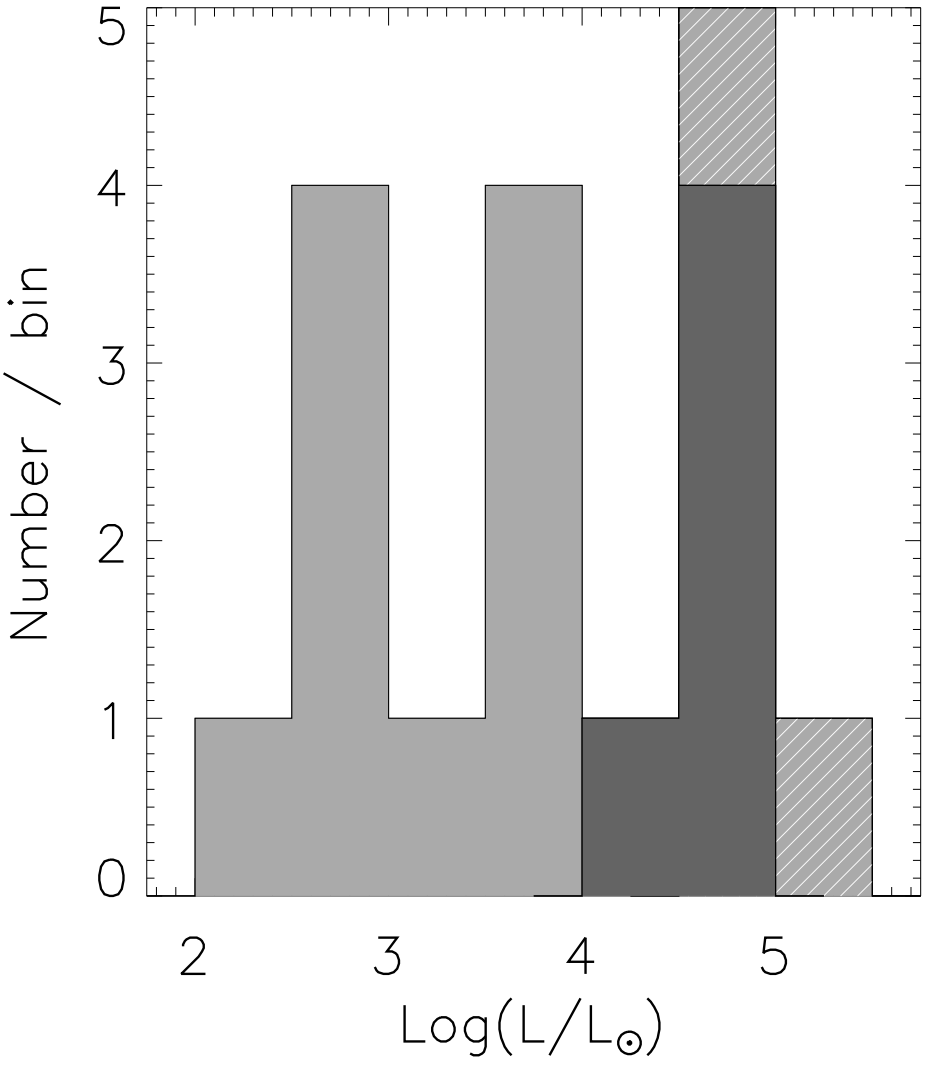

Figure 3.25 Histogram of $L_{\rm bol}$ for BLAST sources with compact H II emission. Two of the most luminous (stripes) are at a larger distance than Cyg OB2. The five noted by Motte et al. (2007) are shaded black. Other lower luminosity sources appear to have external ionization (§ 3.5.4).

K and 3 kpc distant, they deduced that a single O6 ZAMS star was accounting for a luminosity of 3×10^5 $L_\odot$. This would be relaxed for the closer distance adopted here, and as mentioned above there is likely more than a single star in a BLAST clump (§ 3.5.4).

C155, DR21: C155 is the most luminous source in the BLAST survey region with dust temperature 36 K, luminosity 7.0×10^4 $L_\odot$, and mass 880 $M_\odot$. DR21 has a dense core N46 with signatures of outflows (Motte et al., 2007), suggestive of an early stage OB cluster. Supportive of multiplicity, Motte et al. (2007) detected another two cores within a $1'$ radius in their clump N15; our mass agrees with the total mass of the three cores. This clump in the DR21 cloud complex (see Fig. 3.11) harbors one of the most studied UC H II regions: microwave (Downes & Rinehart, 1966); radio (Kurtz et al., 1994); near-infrared (Davis et al., 2007); and ^{13}CO Schneider et al. (2006a). Studying hydrogen recombination and the ammonium line, Cyganowski et al. (2003) found cometary morphology associated with the H II region. It is also identified as MSX6C G81.6802+0.5405, an *MSX* source, specifically bright at 8 μm, and has saturated *Spitzer* sources. There is an embedded near-infrared cluster, W75S (Bica et al., 2003). The position of C155 in the *L*-*M* diagram confirms that star formation is well established.

C169, W75N: The W75N cloud complex shown in Figure 3.11 is a well-known massive star forming region. After first being detected at low resolution in the radio by Westerhout (1958); Downes & Rinehart (1966), this complex was studied to decipher numerous "protostellar physical conditions." A wide variety of sources was found embedded in this cloud, e.g., a group of infrared sources (Moore et al., 1991; Persi et al., 2006; Davis et al., 2007), UCH II regions, and H_2O and OH masers (Hunter et al., 1994). Haschick et al. (1981) identified three ionized regions within W75N, namely W75N (A); W75N (B); and W75N (C). Subsequent higher resolution Hunter et al. (1994) resolved W75N (B) into another three subregions. Motte et al. (2007) found three sources associated with the W75N cloud (clump N13), of which W75N (B) is the most massive object, with a dense core N30. They classified this source as a HCH II region. BLAST with $1'$ resolution observes only one source. The derived properties are dust temperature 36 K, luminosity 6.2×10^4 $L_\odot$, and mass 760 $M_\odot$, very close to C155. The radio emission at 21-cm is however much less, probably because of self absorption (there is appreciable self-absorption in the spectrum of DR21 too, Wendker et al., 1991) but possibly because of a different IMF in the embedded clusters.

There is another embedded cluster DB20 a few arc minutes to the north, coincident with clump N14 of Motte et al. (2007) and its core N28.

C32, DR15 cloud: The DR15 complex was previously observed at radio wavelengths by Colley (1980), and Odenwald et al. (1990), who predicted that it hosts OB stars. Both free-free emission and PAH emission observed by *MSX* suggest on-going star formation. The morphology of this cloud is complex, with extended emission on a range of scales. We could resolve two sources, C32 and C28. The cluster LK08 and radio peak are located between these (Fig. 3.7). Motte et al. (2007) detected three embedded sources, of which two, MSX 79.2963+0.2835 and MSX 79.3070+0.2768 are within C32. The *Spitzer* sources are saturated. We find dust temperature 46 K, luminosity 3.3×10^4 $L_\odot$, and mass 110 $M_\odot$. Motte et al. (2007) designated core S41 in clump S11 (corresponding to C32) as a HLIRPC. Our analysis based on the location of C32 in the L-M plot suggests a slightly later stage like the other embedded H II regions being discussed. However, it is a complex region that will benefit from better resolution as provided by *Herschel*. It is possible that the temperature of the dust is influenced by the nearby cluster LK08, and fitting a single temperature SED for this source would probably underestimate the clump mass.

C73, DR18: DR18 was studied extensively in the near infrared by Comerón & Torra (1999) who found a stellar group. Most of the illumination is due to a single B0.5 V star which can be observed in the visible as well as the infrared. The CGPS radio peak is at the head of the larger cometary structure (see above) and probably is affected by external ionization. Consistent with the cometary structure, C73 lies between the ionized gas and the CO clump. C73 has properties very similar to C88 in DR20. This interesting region is outside the coverage of Motte et al. (2007).

C30, DR7: Figure 3.6 shows LK09 located in the centre of the DR7 H II region arc. The CGPS H II emission peak and ECX6-18 lie between BLAST sources C30 and C27, the former much more massive. This region is not covered by Motte et al. (2007). The derived parameters for C30 are very close to those for C32, assuming the same distance. However, as remarked in § 3.3.6, its velocity places it well behind the Cyg OB2 complex, at 3.6 to 7.5 kpc (we adopted 6.8 kpc in § 3.4.2). Thus this source should be about 16 times more massive and luminous, as listed in Table 3.5, ranking it with the most powerful sources in this survey.

3.5.5 Stage A: Accretion Power, Protostars, and MYSOs

As mentioned, BLAST cannot hope to see single stars, though the clump might be dominated by the most massive member of the group. During the next earlier stage, precursor to the embedded H II regions, matter collapses under gravity at multiple sites inside the clump, which are newly born stellar cores (Mac Low & Klessen, 2004). The luminosity of the clump originates from the cumulative energy of accretion onto cores. During this accretion stage, protostars build up luminosity with little loss of envelope mass. In our *L*-*M* diagram (Fig. 3.24), the evolution should be vertical, crossing the region between the dotted red line ($L/M = 1\ \ L_\odot/M_\odot$) and the dashed green line. The former is coincidentally close to diffuse cirrus emission in equilibrium with interstellar radiation field at 17.5 K (Boulanger et al., 1996). The latter, taken from Figure 9 of Molinari et al. (2008), is a best fit to class 0 sources. Sources plotting in this region would have cooler dust temperatures, in the range $18\ -\ 25$ K and $L/M \geq 1\ \ L_\odot/M_\odot$ would clearly indicate internally powered sources.

Motte et al. (2007) have identified several massive infrared quiet protostellar cores (MIRQP), sources with mass greater than 40 $M_\odot$ with at least some evidence of stellar activity and yet weak emission in the mid infrared. All of the massive infrared-quiet cores are associated with high velocity SiO emission, providing convincing evidence of powerful outflows and on-going accretion. The SiO emission of MIRQPs is typically stronger than from high luminosity infrared protostellar cores (HLIRPCs), indicating that the former are in a more vigorous accretion phase.

Of the 17 MIRQP, 8 are within our BLAST survey area and are readily detected and characterized (Table 3.5). In the *L*-*M* evolutionary diagram, they occupy the predicted region (see diamonds in Fig. 3.24). Judging from Figure 3.24, there are many other BLAST sources with similar properties. The sensitive *Spitzer* images reveal the substructure, with many accreting cores over a range of fluxes (see also § 3.6.2).

C157, DR 21(OH): The most luminous MIRQP is in DR21(OH), which is lacking in 21-cm radio free-free emission. However, high-sensitivity subarcsecond observations with the VLA at centimeter wavelengths by Araya et al. (2009) reveal a cluster of radio sources; the strongest emission is toward the molecular core MM1, but is perhaps from shock-ionized gas in a jet rather than from a nascent compact H II region. C157 is also cooler than the strongly ionizing sources discussed above, as one might expect. It has a dense core N14 along with five neighboring fragments (Motte et al., 2007) in clump

N14. Harvey-Smith et al. (2008) have observed 6.7 GHz methanol emission in all five spots, but only two of them (DR21(OH) and DR21(OH)N) exhibited strong peaks. Our limited resolution integrates the dust emission from all nearby fragments. Though Motte et al. (2007) has classified the core as MIRQP, we note that the significant bolometric luminosity of C157, 2.9×10^4 $L_\odot$, is probably indicative of the entire cluster, detected in the near-infrared as DB19.

The next most luminous MIRQPs are in C7 and C115. C7 is an isolated source whereas C115 is at the tip of the DR17 molecular pillar. C119 is similarly at the tip of an adjacent pillar (Fig. 3.9). C36, among the coolest, is just north of DR15, at the most evolved end of the IRDC G79.34+0.33 discussed below(§ 3.5.6). There is a variety of indications of star formation (Redman et al., 2003), and *Spitzer* images indicate a rich stellar group.

There are two sources classified as infrared quiet protostar (IRQP, not so massive as MIRQP) by Motte et al. (2007) which appear to BLAST to be as luminous as the MIRQP-containing sources. The more luminous is C104 (N62 in clump N20 to the north-east of DR22) in the molecular filament (velocity -5 km s^{-1}) extending from DR22 through MIRQP C107 to MIRQPs C141, C145 and cluster LK15 in DR23 (see Fig. 3.12). The most prominent molecular clump along this filament contains C138 (N69, in clump N23); it defines the boundary of brightest ionized part of DR23, powered by cluster DB17 to the east (Fig. 3.12). The other is C167 (N24 in clump N10 to the north-west of W75N). At CO velocity -3 km s^{-1}, this is in the DR21 cloud complex (Fig. 3.11). The *Spitzer* images indicate widespread embedded star formation in the C167 cloud and adjacent BLAST sources.

The two HLIRPC (other than C32 discussed above) plot toward the high luminosity (high temperature) side of this region in the L-M plane. These correspond to the BLAST sources C85 and C87. C85 contains source N6 in clump N3 of Motte et al. (2007). It coincides with DR20NW (Schneider et al., 2006a) at the head of the above-mentioned elephant trunk. There is an ionized rim on the face toward Cyg OB2, but apparently little internal ionization. Its position on the L-M plot suggests most of the luminosity is generated from accretion. Compared to C88 also in the DR20 molecular cloud, C87 (clump N6, core N14) is relatively cold, 27 K, with no free-free emission.

3.5.6 Stage E: Externally-heated Cold Early Stage

Prior to the stage of active accretion, there must pre-exist a cold molecular clump with only external heating. A low temperature and corresponding low luminosity to mass ratio ($L/M \leq 1\ \ L_{\odot}/M_{\odot}$) would be diagnostic of this stage. As a forerunner of SPIRE on *Herschel*, BLAST was designed to search for the submillimeter emission from such objects in the earliest stages of pre-stellar evolution, and according to Figure 3.17 has been quite successful, with 28 sources down to the approximate 250 μm completeness line of about 30 Jy. These compact sources are sufficiently cold and massive to be above the nominal Bonnor-Ebert critical mass. The higher mass objects can be considered as potential precursors of the MIRQP accretion-powered stage.

Cold Clouds with Nascent Star Formation

It is a general consensus that massive stars should begin to form within stellar nurseries deeply embedded in a dense envelope of dust and molecular gas. Because *Spitzer* is so sensitive and probes at wavelengths where the dust can be penetrated, evidence for such nascent star formation (not a lot of total power) is readily found. Figure 3.26 shows two examples. One is a cold BLAST source C116 (along the DR22 to DR23 filament) corresponding to the Motte et al. (2007) core N70. We find dust temperature 17.1±0.8 K, bolometric luminosity $(2.2 \pm 0.4) \times 10^2\ L_{\odot}$, and mass $(1.6 \pm 0.4) \times 10^2\ M_{\odot}$. The other is C36, already containing a low temperature MIRQP (§ 3.5.5), embedded in an IRDC (§ 3.5.6).

IRDCs

Given the appropriate geometry, highly dense, massive molecular clouds with significantly large extinction can be seen in silhouette as infrared dark clouds (IRDC). With the spatial resolution and sensitivity of *MSX*, many IRDCs have been found at Band A (8.6 μm) (Simon et al., 2006). The signature of an IRDC without a developed protostar is lack of dust emission at mid-infrared *IRAS* wavelengths (Egan et al., 1998). However, that does not mean there is no low-power nascent star formation, as illustrated below.

Because of the high column density, BLAST sees prominent IRDCs in emission. An example is the ridge (filament) shown in Figure 3.27 which contains the IRDCs G79.34+0.33 and G79.27+0.38 (Egan et al., 1998) with corresponding BLAST clumps C36 and C26, respectively. Although it was initially suspected that G79.34+0.33 was

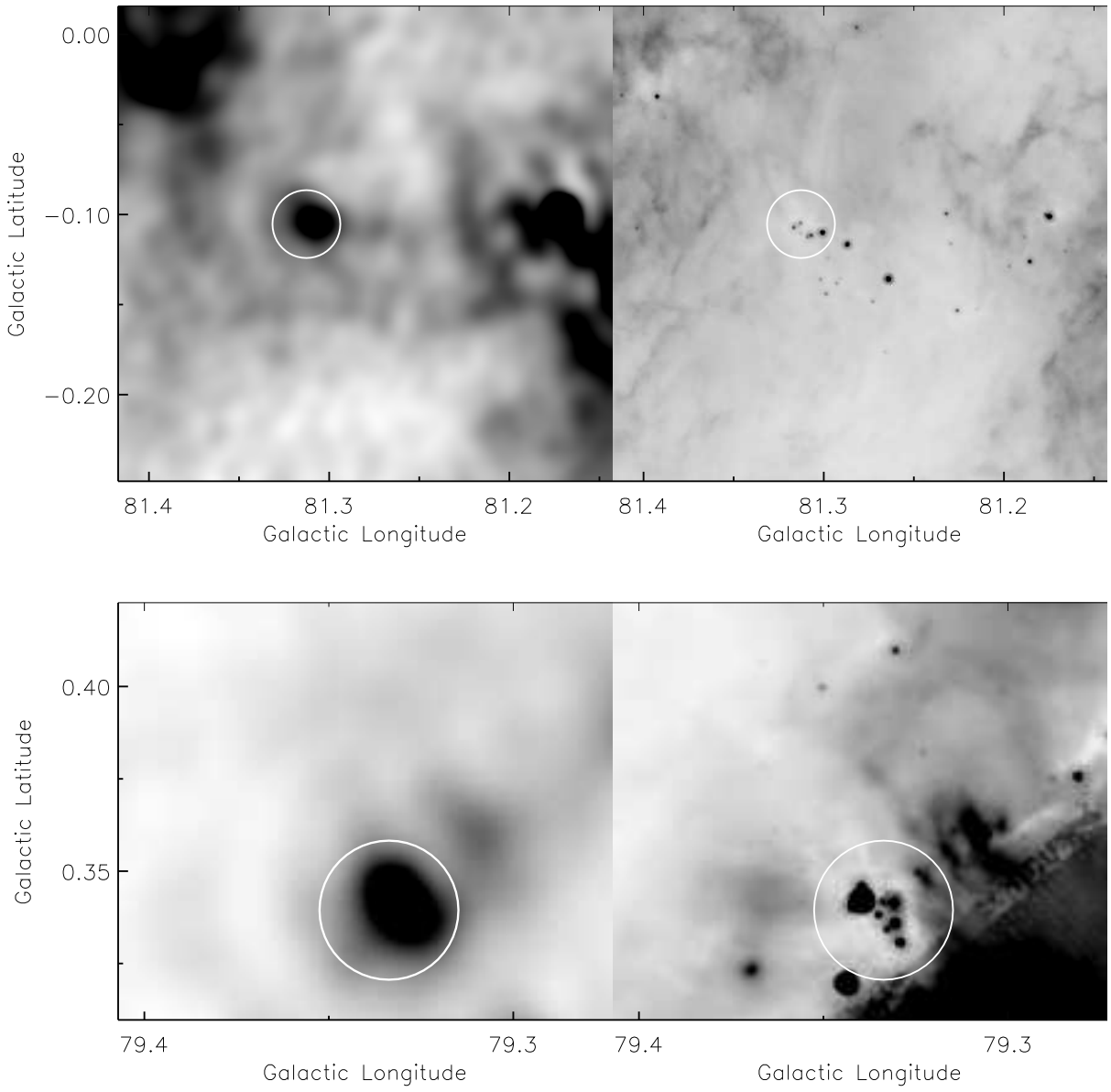

Figure 3.26 Left: cool BLAST sources at 250 μm. Right: corresponding 24 μm MIPS images, showing evidence for nascent star formation. Top: C116. Bottom: C36 at the transition to MIRQP, in IRDC G79.34+0.33. Radius of circles 1.3′.

associated with the DR15 cloud, later Redman et al. (2003) found no such evidence. This filamentary ridge is associated with distinct ^{13}CO emission at velocities near 1 km s^{-1} (Fig. 3.7). G79.27+0.38 in the central part of the ridge was studied by Wu & Yang (2005).

Finer details can be found with the *Spitzer* images, both in extinction and in the presence of point sources. Both of these BLAST sources show evidence of nascent star formation (Figs. 3.26 and 3.27). In fact there are embedded mid-infrared objects right along the filament, even the upper part of the ridge where the less massive condensations are C25, C24, and C23.

Note that this ridge is seen in extinction against the shell of the LBV star G79.29+0.46 (Wendker et al., 1991), providing relative distance information which locates the star behind the Cyg X region. The shell, even the faint outer halo seen at 24 μm, shows no signs of interaction with Cyg OB2, indicating considerable separation. Kraemer et al. (2010b) have quantified this using the stellar parameters, obtaining a distance of 3 kpc.

Figure 3.28 shows an interesting long filament that shows up well in the 24 μm image, in emission but changing to absorption in front of a bright band of cirrus. At IRAC 8 μm it is only in emission, the bright cirrus band being absent. This structure is detected in BLAST emission as well as CO, extending the DR21 ridge to the south (Fig. 3.11). The characteristic CO velocity, -3 km s^{-1}, confirms that this is related to the DR21 molecular cloud. The extended mid-infrared source in the upper part is apparently warm and has no BLAST counterpart.

Starless Cold Clouds

Focusing on the earliest stage, are there any sources that are so far starless? The best candidates to search should be those in the region with $L/M < 1\ \ L_\odot/M_\odot$. In terms of internally generated power, they all can be considered "starless." But when examined in the MIPS 24 μm image, most of these candidates do in fact have point sources, indicating nascent star formation though probably only low mass YSOs (§ 3.6.2).

However, we found one instance that is apparently starless at 24 μm, C81, an isolated feeble source with a weak CO signature at +6 km s^{-1}. While there are some point sources at IRAC 8 μm, these do not have spectra rising to 24 μm as might be expected of YSOs; also there is no special concentration to the BLAST source and so they are probably field star contamination. The IRAC image also shows several small IRDCs.

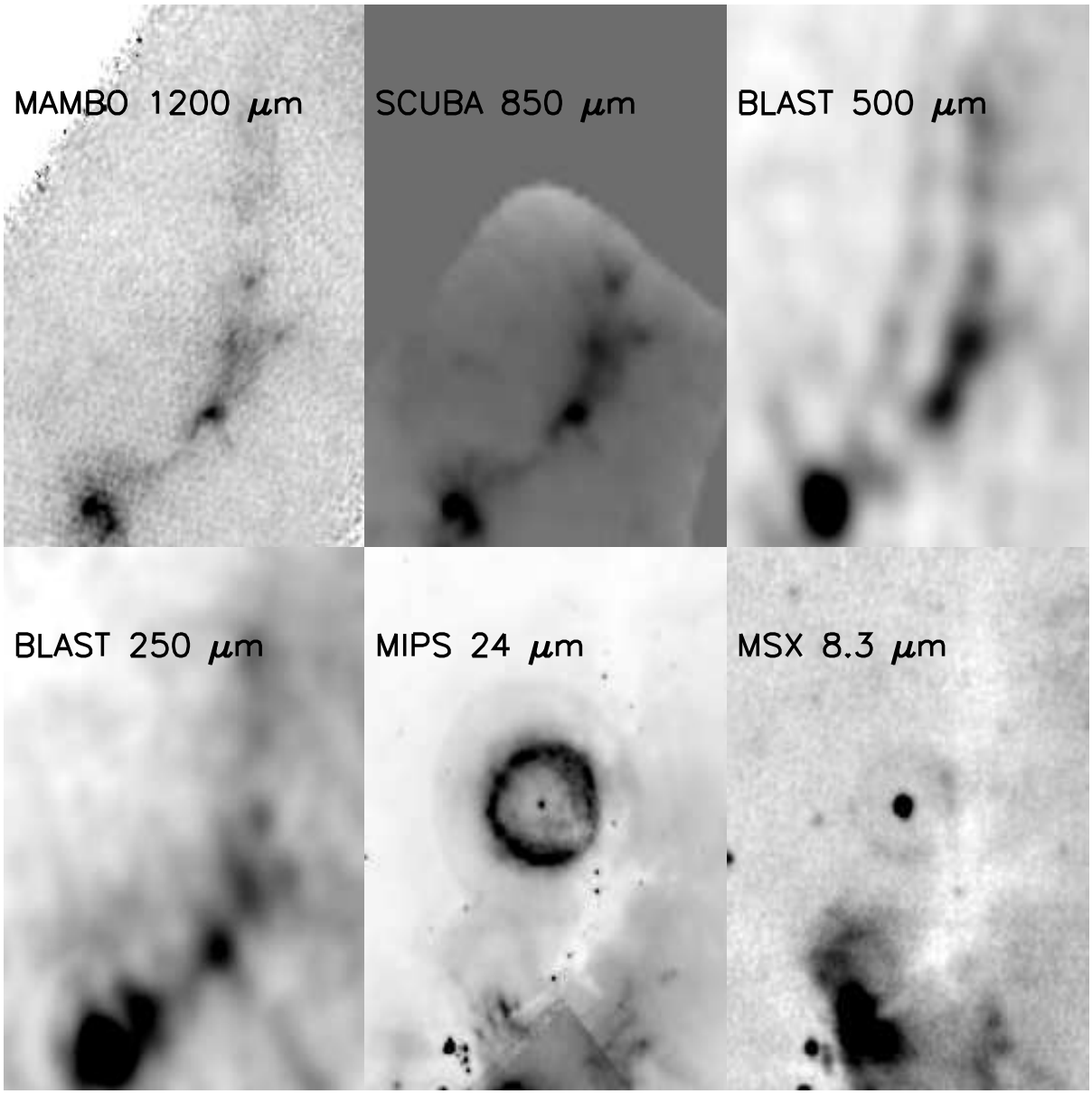

Figure 3.27 Multi-wavelength views of the IRDC ridge in Cyg X near $l = 79°.23$ and $b = 0°.45$. Each thumbnail has dimension $12' \times 16'$.

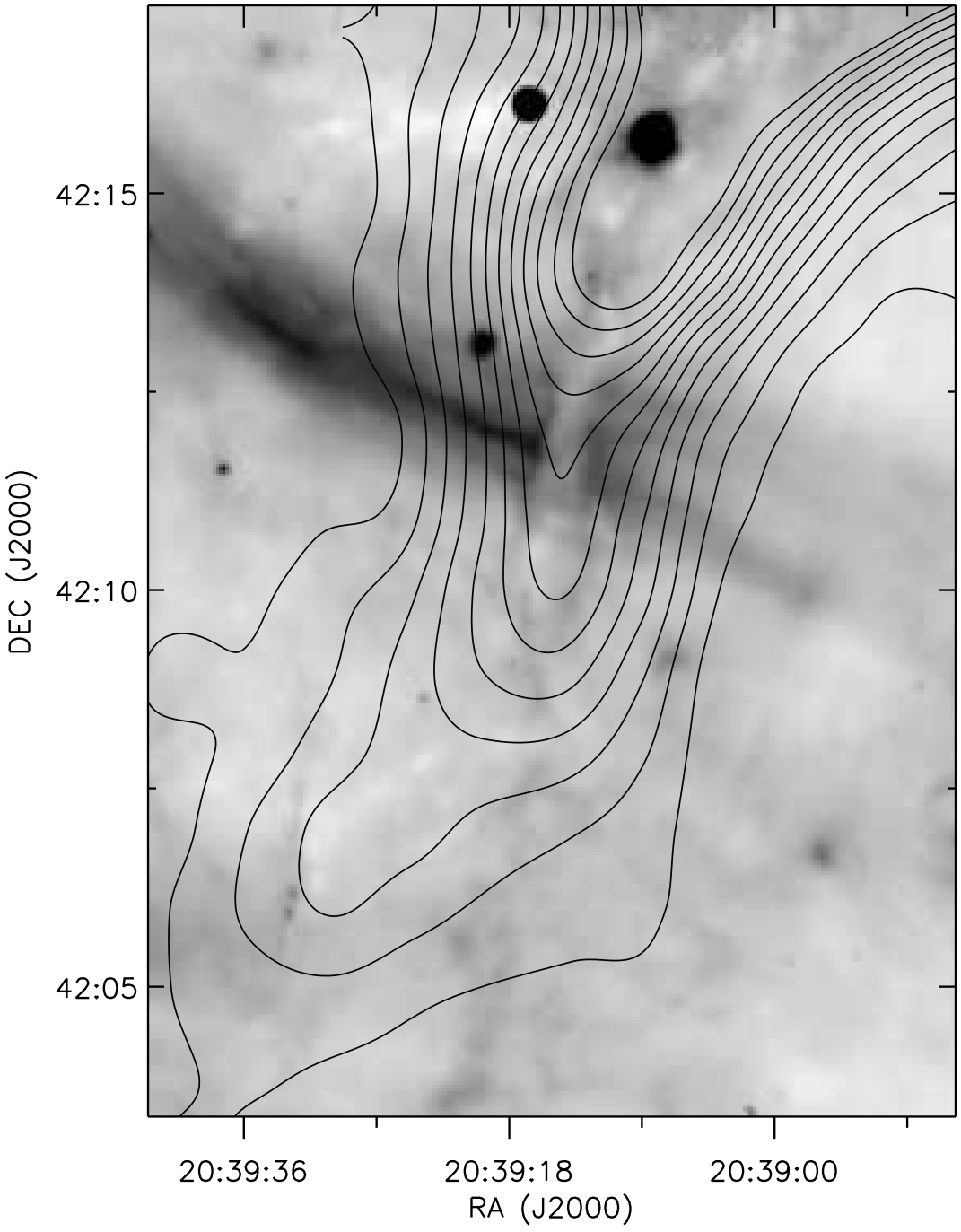

Figure 3.28 MIPS 24 μm image showing dark lane extending from DR21 ridge. BLAST sees this lane in emission (Fig. 3.11). The contours are ^{13}CO emission (Schneider et al., 2006a) integrated over -7 to 1 km s^{-1}.

Two other possibilities are C103 and C121. (Curiously, C103 exhibits diffuse emission at 24 μm including being crossed by a partial thin shell of radius 2.8′ centered at G81.0425-0.1155.) C108, clump N2 of Motte et al. (2007) with no core, is crossed by IRDCs at 24 and 8 μm, and might be another good example of a starless clump.

3.6 Discussion

The L-M diagram (Figs. 3.17 and 3.24) can be adopted as a diagnostic tool for describing the early evolutionary stages of massive star formation (Molinari et al., 2008). With our sample of compact sources now covering a broad range of luminosity and mass, particularly extending to low L/M, we are in a position to further assess its utility. We first review how independent empirical evidence for evolutionary stages relates to the characteristic position in the L-M diagram and then, to the extent possible, use theoretical models to provide insight into the evolution.

3.6.1 High L/M

In the Cyg X region, 16 BLAST sources have detectable compact 21-cm continuum emission. All have strong 100 μm emission and so are not background radio galaxies. Our detections of these sources are represented by filled light-grey circles in Figure 3.24. Five of these were also noted and classified for H II region compactness by Motte et al. (2007) and are marked as triangles, circles, and inverted triangles. All of these clumps appear in the higher T (> 30 K) and L/M region, near the nuclear burning locus, above the stage A sources and the empirically-obtained accretion line. An extensive discussion of individual embedded H II regions in Cyg X has been presented in § 3.5.4. High mass protostars inside these massive clumps account for the high ionization rate and luminosity. We do not have the angular resolution to distinguish multiplicity, but the clumps contain multiple sources when examined in the near and mid infrared (§ 3.6.2).

SiO ($2 \rightarrow 1$) emission is often used as a tracer of shocked gas, associated with outflows which are an intrinsic consequence of accretion process. After the onset of nuclear burning stage, massive stars build up an intense radiation pressure which halts further accretion. In accordance with this expectation, the luminous sources DR21 and W75N have only low intensity SiO ($2 \rightarrow 1$) emission (Motte et al., 2007). In fact, all of their high luminosity IR Protostellar cores (HLIRPC) correspond to BLAST sources with high L/M and also

do not have a striking molecular emission accretion signature.

Slightly earlier in the evolution, clumps are already quite luminous, near the empirical accretion locus for massive stars; single-star cores within them would be classified as class 0, at least for lower mass stars. On the basis of their position in this region in the *L*-*M* plot, we would expect these BLAST sources to show independent and direct evidence of (bipolar) outflow and indeed this is the case (§ 3.5.5). Motte et al. (2007) identified a class of massive IR-quiet protostellar cores (MIRQP) with strong SiO(2→1) emission, indicative of on-going active accretion. The eight BLAST sources corresponding to their MIRQP are marked by diamonds in Figure 3.24 and all of them lie in the stage A accretion-dominated region of the diagram.

3.6.2 Low L/M

In the Cyg X region we have discovered a significant fraction of the clumps with low L/M devoid of massive protostellar cores. This low L/M regime is for us the most intriguing part of the *L*-*M* diagram, potentially containing the story of the earliest stages of massive star formation. Molinari et al. (2008) show vertical tracks corresponding to the evolution of a *single and massive* protostar, and this is suggested by the vertical arrow in our *L*-*M* diagram. However, this is probably a misleading interpretation for low L/M. Even though these clumps appear above the '$L = M$' line, and are arguably self-luminous, there is no obvious signature of a high mass star being formed. Given that massive protostars probably evolve rapidly through this region, it is statistically improbable to observe this stage.

The more likely alternative energy source is the collective power of many lower mass YSOs. In § 3.5.6 we have already previewed some evidence for multiple YSOs in cold massive clumps. Since the BLAST observations were carried out, a census of YSOs has been obtained by Beerer et al. (2010) based on SEDs from *Spitzer* imaging of the northern part of the Cyg X region. Using their map of *Spitzer* YSO positions (their Fig. 8) we find YSOs, often multiple YSOs, associated with most of our clumps. For the brighter sources, we probably underestimate the number of (crowded) YSOs when using their Figure 8 rather than a catalog. Figure 3.29 demonstrates that the observed L/M is correlated with the total number of YSOs per unit clump mass, as expected energetically. This also suggests considerable fragmentation into low-mass stars, an inevitable result of the initially low Jeans' masses in the cold gas (Krumholz, 2006).

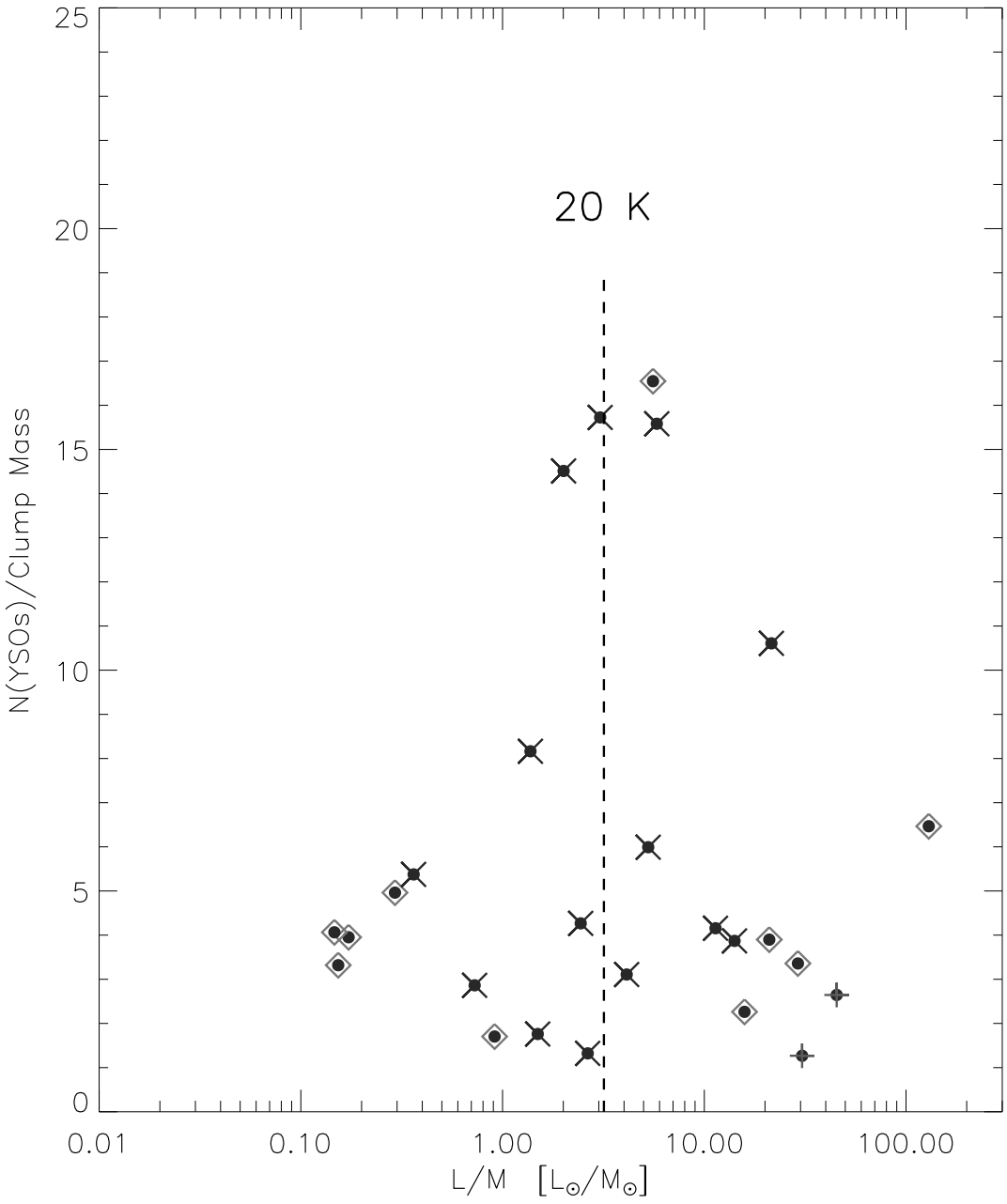

Figure 3.29 Number of YSOs (classes 0, I, and II) per 100 $M_\odot$ vs. L/M. The cross, diamond, and plus symbols represent surface densities Σ in the ranges 0.005 to 0.02, 0.02 to 0.08, and 0.08 to 0.4 g cm^{-2}, respectively. The vertical (dashed) line corresponds to 20 K, a typical value where Σ in the model of Krumholz & McKee (2008) is about 1 g cm^{-2} for the masses of BLAST sources (see § 3.6.3 and Fig. 3.24).

There are (at least) two hypotheses for massive star formation, namely the competitive accretion model (Bonnell et al., 1998) where massive stars are formed due to dynamical coalescence of low-mass stars in a dense clustered medium, and the turbulent core model (McKee & Tan, 2003) in which massive cores with non-thermal support provided by the turbulence evolve in a quasi-static way. Both of these theories predict that high mass star formation is preceded by an epoch of the low-mass star formation, converting a larger proportion of the total mass in the competitive accretion model. Owing to low resolution, BLAST observations cannot differentiate between these two hypotheses on this basis. Nor do we have masses for the *Spitzer* YSOs. However, the intermediate resolution MAMBO data resolves substructures (cores) of size ~ 0.1 pc within our clumps. In Figure 3.30 we compare the total mass of the cores within each clump to the clump mass (assuming the cores are at the same temperature as BLAST observes for the clump). We find that (only) 20% of the clump mass is in cores, however, four bright sources (W75N, DR21, DR21(OH) and C160) were excluded in the fit.

3.6.3 Relationship to Surface Density

According to the model of Krumholz & McKee (2008), for the low L/M regime the steady-state accretion luminosity generated by the low-mass YSOs is:

$$L = 390 \left(\frac{\Sigma}{1 \text{ g cm}^{-2}} \frac{M}{100 \text{ M}_\odot} \right)^{0.67} L_\odot. \tag{3.7}$$

In order to show the relative position of BLAST sources with respect to this model prediction, we plot loci in the L-M diagram of Figure 3.24 for $\Sigma = 1.0$, 0.1, and 0.01 g cm^{-2}.

If this theory is adopted then we can directly determine surface density from equation (3.7) for any source in the L-M diagram. This is the surface density that would be required for a clump of mass M to produce a luminosity of L. However, we can also measure the surface density directly. In Figure 3.31, we plot surface densities of BLAST sources versus the model surface density, for sources below $L/M < 6\ L_\odot/M_\odot$ where most of the luminosity arguably comes from low-mass stars. The measured surface density of the most of the sources is below the one-to-one line. This might be because we have underestimated Σ owing to poor angular resolution; qualitative support for this is the evidence of substructure (§ 3.6.2). However, there are about 8 sources with surface density above the one-to-one line. These are very interesting, possibly a very early stage

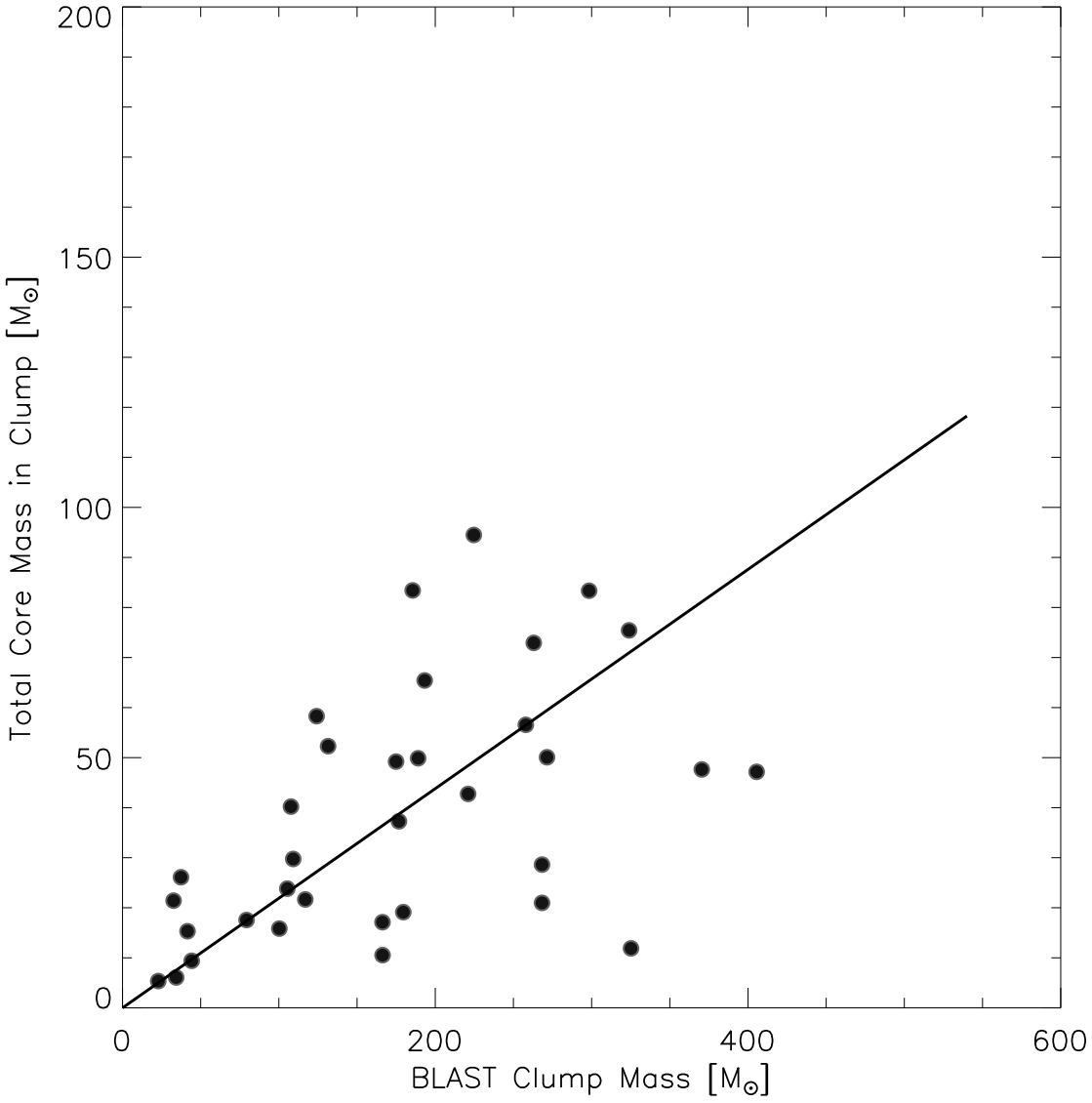

Figure 3.30 Sum of the masses of cores within the BLAST clumps versus the clump mass. The linear correlation shown has a slope 0.20.

where the presumed steady state of low mass YSO formation has not been achieved. We have confirmed that there is a lower number of YSOs associated with these sources, except for the source shown by a cross in Figure 3.31 which was difficult to measure near the edge of the image at 500 μm.

Krumholz & McKee (2008) note that because cores with higher Σ are warmer due to the power of the low-mass YSOs, there is a critical Σ such that by the time the steady-state heating is achieved fragmentation into further low-mass YSOs halts. The threshold surface density is about 1 g cm^{-2} and this is plotted in Figure 3.24. This characteristic surface density should be a marker of (potential) massive star forming regions, and there is some evidence consistent with this, at least for evolved objects. In the BLAST survey we find that the few most luminous sources containing compact H II regions have such a high surface density. The MAMBO cores containing compact H II regions and MIRQPs with strong SiO emission also have a high measured surface density (Table 3.3). Similarly, Garay et al. (2006) found an average surface density of 0.8 g cm^{-2} for dense cores of ultracompact H II regions. We find that the typical surface density of massive embedded star clusters observed by Le Duigou & Knödlseder (2002) in the Cyg X region is about 1 g cm^{-2} (allowing for the presence of some additional gas – now dispersed – in the precursor).

An observed high Σ associated with MYSOs might not be a signature unique to the turbulent core model, or even a prerequisite. In the simulations by Smith et al. (2009) of a competitive accretion model, "massive stars were not formed from a single massive thermally supported fragment, but instead from a smaller core which accreted additional material channelled towards it by the potential of the forming stellar cluster." Likewise, in the simulations by Wang et al. (2010) of a model of "clump-fed massive star formation" regulated by outflow feedback (ORCF), "the most massive object is not formed out of a pre-existing dense core" but rather "is controlled by the global clump dynamics." Recently Csengeri et al. (2010) observed a few of the massive young dense cores (C107, C115, C119, DR21(OH), DR21) in Cyg X to study the kinematic properties of the underlying environment. They found that non-thermal support due to turbulence at the scale of the dense core is not enough for a quasi-static evolution of the massive protostars as predicted by the turbulent core model of McKee & Tan (2003), and they favor competitive accretion.

Therefore, a key question in investigating the mode of evolution is whether there is evidence for cold high-Σ clumps or cores before high mass protostar(s), and even the

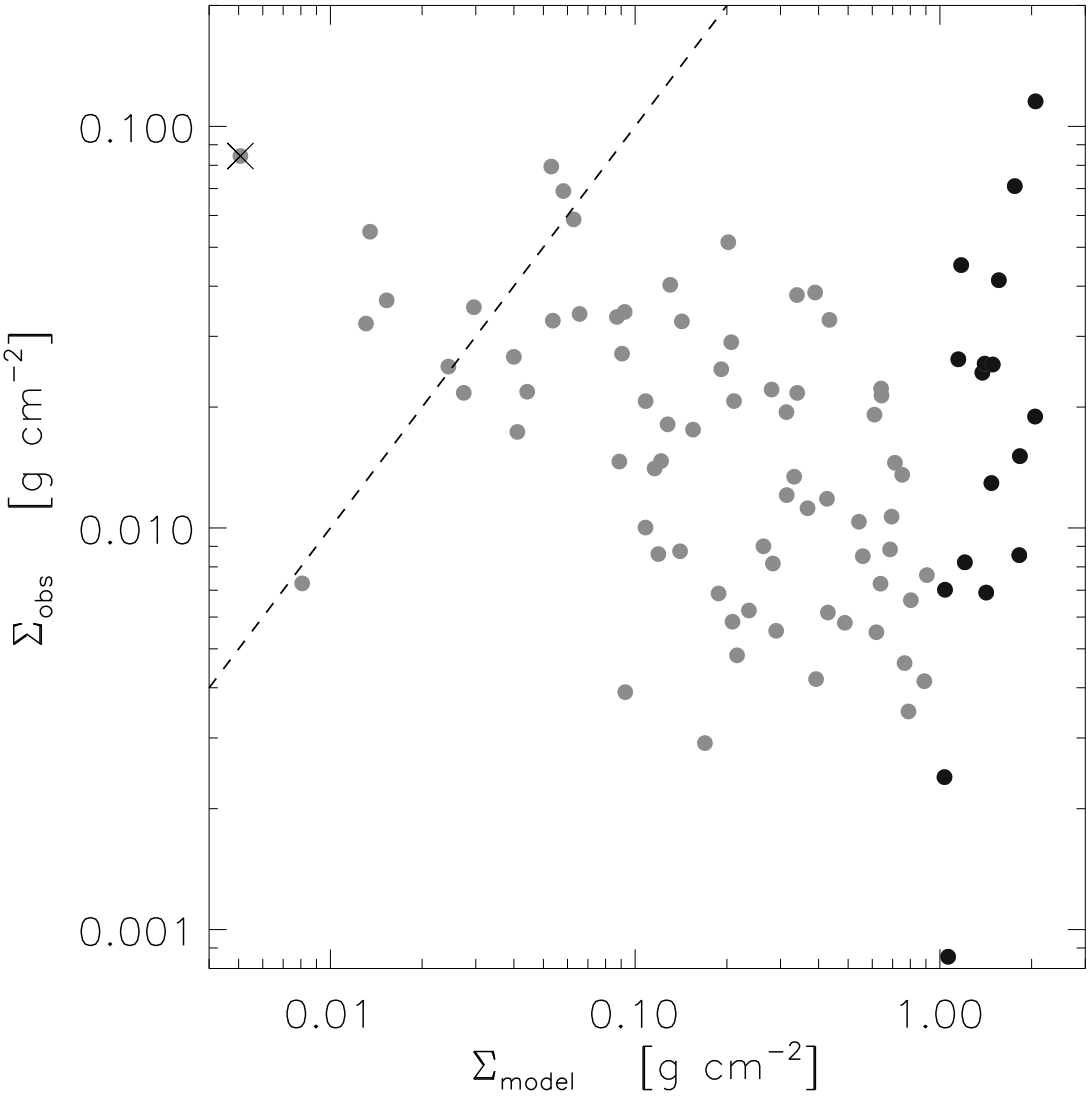

Figure 3.31 Observed surface density of BLAST clumps with $L/M < 6\ L_{\odot}/M_{\odot}$ vs. the surface density required in the low-mass YSOs model of Krumholz & McKee (2008) to produce the observed L given the observed M. Sources above the one-to-one line (dashed) are under-luminous compared to the prediction from the model, and so possibly very young. The source shown by a cross is near the map edge at 500 μm. Sources with model surface density more than 1 g cm^{-2} are highlighted.

preceding low-mass YSOs, are established. Even if the evolution timescale were favorably long, this is difficult with BLAST, as can be seen directly from equation (3.3): at the spatial resolution of 0.5 pc about 4000 $M_\odot$ is needed to produce a surface density of 1 g cm^{-2}. We have noted that we do not see such massive cold objects; if such dense cold objects do exist at lower mass, we cannot identify them by directly measuring their true Σ. Higher resolution is required for such detections; for example, MAMBO observations at the resolution of 0.1 pc in Cyg X need a mass of only 150 $M_\odot$ to produce equivalent contrast. The predominantly low surface densities obtained by Elia et al. (2010) suggest that even the *Herschel* resolution is not sufficient for finding such dense substructures in most cold sources.

3.6.4 Vertical Evolution in the L-M Diagram?

Given the different theories, it is still unclear to us which of the low L/M BLAST clumps will give rise to massive star formation. If there is a universal IMF, then statistically a massive clump will be required to give birth to massive protostars. Therefore, the massive clumps identified by BLAST are certainly of interest in this regard. Naively, the evolution in the L-M diagram would be vertical (constant M) as the luminosity increases from accretion onto the massive protostar and then nuclear burning. Even this is complicated because the power produced by low mass YSOs in most theories can mask the earliest low L stage of the massive protostar.

However, it does not follow that massive clumps/cores always form massive stars. In fact, the model by Krumholz & McKee (2008) explicitly predicts that this will not happen unless Σ is above a critical value of about 1 g cm^{-2}. Otherwise, their prediction is that the clump is destined to continue to produce only low mass stars, at some presumed steady-state rate. Thus the vertical rise in L is arrested at a ceiling for a given Σ. We have marked such a possibility in Figure 3.24 with a horizontal red arrow at a level which would correspond to the sub-critical Σ of the clump. The end result is a cluster or association of only low mass stars, i.e., one with a truncated IMF. Because the precursor is of low Σ the resulting assemblage of stars must be as well, making them more difficult to detect, and there is no high mass star to draw attention to the region by its high luminosity and ionization.

The empirical context, a snapshot of the stages of evolution, is that there is a hierarchy of structures. BLAST identifies compact sources of size about 0.5 pc within the CO

clumps of spatial extent about 10 pc (Schneider et al., 2006a). Within most of the BLAST clumps, MAMBO is able to find smaller and denser substructures of scale 0.1 pc. Presumably these structures have been created and evolve by accumulating mass in the dynamical environment of the larger reservoir and possibly also simultaneously transfer mass to the immediately lower scale substructures. At any given time these structures will each have a characteristic Σ. At some point does this become frozen in time so that we can discuss the fate of objects of fixed Σ? Or tracking a clump, could Σ and M evolve, allowing evolution toward the upper right in the L-M diagram? We have indicated this latter possibility as well in Figure 3.24 – of course only schematically. Recent numerical simulations of the competitive accretion model (Smith et al., 2009), and the ORCF model (Wang et al., 2010) which has features of both competitive accretion and the turbulent core model, show a channeling of mass to bound potential energy minima of the parsec-scale dense clumps studied, emphasizing the importance of clump-level dynamics. In these models, when the material is cold it is more distributed and so would not be identified as a high mass, high Σ, cold clump. By the time that mass builds up in massive cores, accreting on massive protostars, the compact source would have low mass YSOs as well and have been warmed up. Thus the cold precursors of dense clusters might be more extended objects than clumps, a massive reservoir yet to be channeled by gravity into a higher surface density state. Some cold IRDCs (§ 3.5.6, Fig. 3.3), within which BLAST identifies substructure as sources, might fit into this scenario, but dynamical diagnostics would be needed to pursue the relevance of this possibility.

3.7 Conclusion and Future Work

An unbiased survey conducted by BLAST has enabled us to detect both compact sources and the embedding diffuse emission as a basis for studying the earliest stages of star formation. We have quantified contrasting dust temperatures of diffuse extended structures by correlating the fluctuating emission in *IRAS* and BLAST bands. To reveal the global morphology, we have studied the relationship between dust continuum emission and radio, mid-infrared, and ^{13}CO line emission. Comparing the total mass present in the BLAST compact sources with the parent ^{13}CO clump mass (Schneider et al., 2006a), we have obtained a linear correlation with slope of 0.05, which might be indicative of the star formation efficiency but also relates to the relative lifetime of the compact clump phase. With multi-wavelength photometry we have tightly constrained the dust emission SEDs

of the compact sources to measure temperature, luminosity and mass. We have diagnosed the earliest stages of star formation in Cyg X, and the evolution, in the context of the luminosity – mass diagram of the compact sources. We have studied eight DR regions which are known as massive star formation sites in Cyg X. We have identified 16 sources which have compact H II emission and found an average dust temperature of 33 K. Not all of these identified sources have sufficient luminosity to be ionizing sources, pointing to the influence of Cyg OB2 creating external ionization. The complex morphology along with the direction of cometary shapes of some compact sources provide direct evidence of interaction with the massive Cyg OB2 association. Along the periphery of the evacuated H II region created by some of the more evolved stellar clusters, there is a signature of triggered star formation. We have observed a complex of infrared quiet dark clouds where star formation has already started to take place. To BLAST, and also SCUBA and MAMBO, this appears as an impressive ridge of cold dust emission. However, in sensitive high resolution 24 μm MIPS and 8 μm IRAC images, there is evidence of a stellar nursery, indicating a potential site of massive star formation. In our search for the precursors of clusters, however, we have not found any cold compact clump which is massive enough to become a star cluster like the Cyg OB2 association or even the other lesser embedded clusters. In the future, the unbiased Planck Cold Core survey might find such objects in unevolved GMCs, possibly in a more extended lower surface density state than in the final cluster. Resolving multi-scale structures is a new challenge underlying investigations of the earliest stages of star formation. BLAST with its limited resolution could only resolve spatial structures of 0.5 pc at 1.7 kpc away. On the other hand, MAMBO with its 11$''$ resolution was successful in separating substructures on a scale of 0.1 pc; further progress should be possible with *Herschel*. To determine the role of surface density and more generally which cold high mass clumps will evolve to produce high mass protostars even higher resolution observations will be required, and so there appears to be a rich future in uncovering the unseen story using SCUBA2 (8$''$ resolution at 450 μm, Holland et al., 2006), CCAT (3.5$''$ at 350 μm, Sebring, 2010), and ALMA[1] (down to sub-arcsecond resolution at submillimeter wavelengths)

[1]http://www.almaobservatory.org/en/about-alma/essentials/numbers

3.8 Appendix: Multi-wavelength Photometry

Flux densities at many supplementary wavelengths are presented in Table 3.1 and Table 3.6. They were obtained as follows.

MAMBO 1200 μm. The MAMBO camera mounted on the IRAM 30-m telescope imaged all regions having column density greater than ($A_V \geq 15$) at wavelength of 1.2 mm (Motte et al., 2007). With its 11″ beam, MAMBO has the ability to resolve multiple cores (if present) within BLAST clumps. Combining our data with MAMBO helps in multi-wavelength photometry, especially when any cold source is undetected in the mid to far-infrared spectrum. To obtain consistent photometry, we first convolved the MAMBO map to 1′, about the resolution of the BLAST maps. This has two effects: blending together any MAMBO cores; and bringing in flux from the more extended emission (halo or plateau) usually associated with these multi-scale structures. Gaussian photometry was performed on the convolved map.

SCUBA 850 and 450 μm. The archival data from the Submillimeter Common User Bolometer (SCUBA) on the 15-m James Clerk Maxwell Telescope (JCMT), Di Francesco et al. (2008) sample many high extinction regions of the Galactic Plane, including Cyg X, with diffraction-limited beams of 14.5″ and 7.5″, at 850 and 450 μm, respectively. Due to the higher spatial resolution, SCUBA can also identify numerous small-scale cores. The archival images consist of discontinuous smaller maps and so could not be convolved to BLAST resolution prior to photometry. Instead, we used flux densities using the SCUBA legacy catalogs of Di Francesco et al. (2008). We obtained flux densities from the Extended Map Object Catalog (EMOC) and added up all flux densities for sources within 1′ of the BLAST source. Because of the small SCUBA maps, some BLAST sources are not completely scanned near the map edges and the resulting flux density is low.

IRAS 100 and 60 μm. Bright dust emission is observed at 100 and 60 μm throughout Cyg X, and for most of the more luminous, hotter BLAST sources these *IRAS* bands cover the peak of the SED. The *IRAS* point source catalog does not have any entries for about half of our Cyg X region. This arose because of the very bright source DR21 (C. Beichman, private communication). Nevertheless, the *IRAS* images that have been made subsequently are not seriously affected. We extract flux densities at 100 and 60 μm from the Infrared Galaxy Atlas images (IGA; Cao et al., 1997), made using HIRES (Aumann et al., 1990), a resolution enhancing algorithm. There is some elongation of sources across the dominant scan direction. The resolution at 100 and 60 μm is about

$2'$ and $1'$, respectively, substantially better resolution than in the original ISSA product. Most of the isolated BLAST sources are warm enough to have a counterpart in the IGA map. BLAST counterparts at 100 μm were measured with a circular aperture of $2.4'$. Similarly, at 60 μm elliptical apertures of dimension $1.8' \times 1.2'$ were placed with the major axis aligned across the scan direction. In the crowded regions, multiple Gaussian photometry (elliptical in the case of 60 μm) was carried out by fixing centroids of nearby sources.

The counterparts to BLAST sources in the 60 μm images are often affected by extended cirrus-like structure and sometimes by deconvolution artifacts. Such sources show inconsistent structure between the 100 and 60 μm images. We preferred not to use such photometric data as detections to constrain the Wien part of the SED, rather using them as upper limits through a penalty function (Chapin et al., 2008). In crowded regions, the flux density measurements of fainter sources are highly uncertain and for such cases we also used the photometric data as an upper limit. These upper limits are indicated by a superscript 'u' in Table 3.1.

MIPS 70 μm. *Spitzer* MIPS observations at 70 μm have better resolution and sensitivity than *IRAS* IGA 60 μm data and so are particularly useful for detecting or placing upper limits on colder and fainter BLAST sources. The MIPS images were destriped, which is advantageous for probing faint sources, and corrected at the pixel level for nonlinearity (Dale et al., 2007). Measurements using a Gaussian model of fixed FWHM $40''$ (typical extent of actual MIPS sources) at the positions of 39 faint BLAST sources where we have found no apparent counterparts in the MIPS image give an rms flux density of 5.7 Jy. This provides a very useful upper limit for these sources, constraining the SED on the Wien side of the peak. For flux densities of somewhat brighter sources, we first convolved the 70 μm map to $1'$, to be comparable to BLAST, and then made measurements using multi-Gaussian photometry with a linear background model. This provided useful detections for 56 sources and upper limits for the others. For six BLAST sources, pixels at the peaks of the bright MIPS counterparts are blanked; however, the *IRAS* data for these are sufficient to constrain the SED. The resolution of our convolved maps is also closer to the IGA 60 μm resolution, facilitating a comparison with isolated sources with a good *IRAS* detection. We find that the MIPS flux densities are slightly higher than at 60 μm ($F_{60}/F_{70} = 0.78$), as expected for these SEDs. At the native resolution, without beam matching, the MIPS flux densities are systematically lower, as is discussed by Mottram et al. (2010).

MSX *8, 12, 14, and 21 μm. MSX* (Price et al., 2001) observed in A, C, D, and E bands at 8.3, 12.1, 14.7 and 21.3 μm, respectively. Among the four bands, A is the most sensitive and is dominated by diffuse emission from PAH molecules. It has angular resolution 18.3″.

MSX sources have relatively small positional uncertainties (within 4″ - 5″). *MSX* sources were identified within a search radius of 30″ about the BLAST coordinate. After visual inspection, we rejected some *MSX* "matches" that were either in a PDR and/or excited by some nearby OB stars, and so had nothing to do with the star formation history of the subject BLAST source.

We extracted flux densities from the map in its native resolution directly by fitting multiple Gaussians, assuming a constant (not tilted) background. We find that our flux densities in all the bands are systematically higher than reported in the *MSX* point source catalog, and the deviation is more noticeable for less bright sources. This trend was also observed by Molinari et al. (2008).

Results of *MSX* photometry are given in Table 3.6. In our present analysis, *MSX* flux densities in no way constrain temperature and total mass. We use *MSX* flux densities in the SEDs only to calculate a small correction to the bolometric luminosity by connecting data points piecewise continuously (Chapin et al., 2008). See for example, the SED for W75N in Figure 3.14; note the "rising spectrum" from 4 to 21 μm, characteristic of a MYSO. We find that this correction does not change the results significantly as the Cyg X sources detected by BLAST are quite cool.

Table 3.6. *MSX* counterparts

BLAST ID	$\Delta\alpha^a$ (″)	$\Delta\delta^a$ (″)	S_8 (Jy)	S_{12} (Jy)	S_{14} (Jy)	S_{25} (Jy)
C1	5.9	3.0	313.8	568.0	798.5	1023.4
C6	−1.5	6.0	0.2	0.8	0.6	1.6
C7	−7.8	13.7	17.1	23.5	23.4	100.0
C14	11.6	−5.1	0.4	1.0	1.2	2.4
C15	17.2	−6.2	4.6	5.8	3.7	13.6
C19	4.4	2.3	1.8	1.7	0.9	1.3
C22	−27.6	15.4	0.7	1.3	2.0	2.5
C27	15.4	−6.3	2.1	4.7	3.0	8.7
C28	34.4	−12.6	4.8	9.1	6.6	37.7
C30	−35.0	−12.5	0.5	4.0	7.6	13.8

Continued on Next Page...

Table 3.6 – Continued

BLAST ID	$\Delta\alpha$ ($''$)	$\Delta\delta$ ($''$)	S_8 (Jy)	S_{12} (Jy)	S_{14} (Jy)	S_{25} (Jy)
C38	8.7	3.6	12.5	13.4	11.1	64.3
C41	8.0	−5.8	1.0	1.0	0.7	2.0
C47	−4.4	−10.7	0.2	0.6	1.3	1.5
C49	3.9	−0.7	0.7	1.4	1.3	2.7
C51	6.9	−1.5	0.2	0.6	0.7	2.3
C52	11.6	4.7	0.4	1.0	0.4	1.5
C53	4.1	−4.8	0.8	1.6	1.0	1.4
C55	−18.3	−6.0	6.3	8.1	4.0	13.2
C57	10.2	6.4	0.5	0.8	0.4	1.8
C58	−3.7	−6.3	0.7	1.2	1.1	2.5
C59	−5.3	18.7	0.7	1.2	2.3	2.7
C61	17.2	0.7	2.7	3.5	1.8	3.7
C64	2.1	0.6	2.6	4.7	4.2	5.7
C66	2.1	5.9	9.1	15.9	20.2	26.8
C67	−2.0	−1.4	1.0	1.6	0.4	1.3
C71	0.3	10.5	1.0	1.9	1.4	2.8
C73	−17.3	−2.2	3.2	5.8	7.0	19.5
C74	28.1	−12.9	0.4	0.8	0.5	1.3
C75	1.0	3.1	0.5	0.6	0.5	1.2
C76	0.1	−7.6	7.9	9.1	8.2	7.4
C80	6.9	−5.2	4.7	5.7	3.9	18.5
C83	−1.2	−6.4	1.3	1.6	0.7	1.5
C85	2.7	0.8	10.2	17.1	23.7	90.9
C87	0.8	9.6	3.4	6.3	9.6	19.7
C88	9.2	−0.0	5.4	14.6	26.2	99.3
C92	−21.6	0.2	27.1	66.1	98.5	634.1
C101	1.6	−13.0	1.5	1.7	1.6	1.4
C104	−6.0	12.4	4.9	5.7	4.4	26.6
C115	4.9	8.8	1.5	2.7	3.0	3.7
C125	−1.2	15.0	0.6	0.9	0.7	1.2
C126	−1.0	32.9	1.4	1.7	1.5	2.0
C127	−13.5	22.0	1.9	3.4	2.3	5.8
C128	−6.5	16.7	3.1	4.0	1.8	3.9
C129	11.6	18.3	0.8	1.0	0.7	1.3
C135	8.0	−7.8	0.8	2.7	5.2	11.6
C141	2.1	−13.7	0.3	0.6	0.7	1.4
C155	3.3	15.6	8.8	29.6	68.4	543.9
C157	−31.6	26.6	9.2	16.3	21.6	72.7
C160	62.8	13.0	2.8	3.3	3.4	10.8
C163	−14.0	16.5	0.3	0.8	1.2	2.1
C165	2.6	31.5	6.2	6.1	4.3	10.4
C168	−10.4	11.2	0.5	1.3	2.4	3.7
C169	19.9	8.7	15.0	27.1	55.4	331.8
C171	−0.4	−6.4	3.2	4.1	3.3	17.0
C180	0.9	2.5	11.5	17.0	23.8	124.5

Continued on Next Page...

Table 3.6 – Continued

BLAST ID	$\Delta\alpha$ ($''$)	$\Delta\delta$ ($''$)	S_8 (Jy)	S_{12} (Jy)	S_{14} (Jy)	S_{25} (Jy)
C183	3.2	11.8	2.9	6.5	10.0	13.3

[a] Offsets of *MSX* sources with respect to BLAST counterparts.

Chapter 4

BLAST05: Power Spectra of Bright Galactic Cirrus at Submillimeter Wavelengths

4.1 Introduction

Energy is being injected continually into the ISM through spiral shocks, violent outflows from massive protostars, stellar winds, expanding H 2 regions and supernova explosions. The result is a turbulent medium where the dust is well mixed in the structures produced. The emission from the relatively nearby ISM at high Galactic latitude is known as Galactic Cirrus. Cirrus-like structure in the brighter emission near the Galactic Plane has been called 'interstellar froth' (Waller & Boulanger, 1994); this might be an interesting distinction with a physical basis, but here we will simply use the term 'cirrus'. The dynamics of the ISM appear to have made the distribution of density structures self-similar, with fluctuations in column density and surface brightness present on all observable scales, though decreasing towards smaller scales. Statistical description of random fluctuations through structure functions is an important method of extracting physical properties hidden in diffuse emission as well as for providing a quantitative measure to compare with simulations. A common statistical tool used to estimate the level of cirrus noise is the power spectrum. This is valid for Gaussian random fields. However, Gautier et al. (1992) found evidence for non-Gaussianity and recent studies by Miville-Deschênes et al. (2007b) have revealed non-vanishing skewness and excess kurtosis in the

underlying brightness fluctuation fields. Nevertheless, for estimating the variance the power spectrum is still indicative.

Using power spectra, Gautier et al. (1992) quantified how fluctuations associated with Galactic cirrus are a source of confusion noise which limits the detectability of point sources. Even with the improved angular resolution of imagers like SPIRE and PACS on the *Herschel Space Observatory*[1] (hereafter *Herschel*), this 'cirrus noise' remains important, often dominant. Therefore, to assess the noise it is vital to know the statistical properties of the interstellar diffuse emission at the relevant wavelengths.

A number of other statistical analyses of emission have been carried out on the basis of power spectra for high latitude clouds, e.g., by Kiss et al. (2003), Jeong et al. (2005), and Miville-Deschênes et al. (2007b). In this chapter we analyse diffuse dust emission in the Galactic Plane and present for the first time multi-wavelength power spectra in the submillimeter, based on observations in Cygnus X (Cyg X) and Aquila with BLAST (Pascale et al., 2008) at 250, 350, and 500 μm. We also analyse the same regions at 100 and 60 μm using IRIS, *IRAS* data reprocessed by Miville-Deschênes & Lagache (2005). Compared to high latitude studies, analysing diffuse emission in the Galactic Plane in terms of the structure of the ISM resulting from its turbulent properties is more challenging because of the long path lengths, high column density, high star-formation rate, and contamination by compact sources. In addition, in the Galactic Plane, self-gravity can play an important role in shaping diffuse structures at smaller scales. Of particular importance are the potentially strong spatial variations of the radiation field due to star formation activity. As discussed further in § 4.6.1, this could produce variations in the dust emission independently of any changes in structure of the ISM.

This chapter is organized as follows. We begin with a brief description of BLAST observations (§ 4.2) and then introduce important aspects of the power spectrum and accompanying cirrus noise (§ 4.3). We analyse IRIS data in § 4.4, placing this in the context of earlier studies and providing a short-wavelength reference for our submillimeter studies. In § 4.5 we examine the BLAST data: the noise; effect of the point spread function (PSF) or beam; removal of compact sources; and the exponents and amplitudes of the submillimeter power spectra. We estimate the cirrus noise for these maps and compare it with the completeness depth of the BLAST05 point-source catalogs at 250 μm. In § 4.5.6 we also discuss some implications for related approved observations with *Herschel*. We

[1] http://www.esa.int/SPECIALS/Herschel/index.html

show in § 4.6 how the observed wavelength dependence of the amplitude of the power spectrum can be understood as a straightforward consequence of the SED of the dust and we fit a simple modified black body to estimate the dust temperature. Our empirical results provide new insight into what cirrus noise might be expected in submillimeter observations.

4.2 Observations

Submillimeter dust continuum emission maps obtained by BLAST05 (see § 2) are used. Chapin et al. (2008) analysed a 4 deg^2 field in Vulpecula and here we used data from the two largest surveys. Aquila (Rivera-Ingraham et al., 2010) is a 6 deg^2 region observed for 6.1 h, while Cyg X (Roy et al., 2011b) covers 10 deg^2 observed over 10.6 h. Both have good cross-linking from orthogonal scanning. The maps were made with the SANEPIC algorithm (Patanchon et al., 2008b) and were calibrated using the procedure discussed in Truch et al. (2008).

Although a 2-m telescope, BLAST05 produced maps of only $3'$ resolution (see § 4.5.2) due to an anomalous PSF, corrupted by some uncharacterized combination of mirror distortion and de-focus (Truch et al., 2008).[2] Nevertheless, maps from the 2005 flight have high signal-to-noise and are oversampled with $15''$ pixels, so that Lucy-Richardson (L-R) deconvolution can be used to improve the resolution significantly (see § 2). This goal is particularly important for extracting point sources (§ 4.5.3) but otherwise not essential for the study of diffuse emission. We analysed the two largest surveys, selecting in Aquila a square sub-field of size 1.83° centred on $l = 45.85°$, $b = -0.12°$ and a similar-sized field in Cyg X centred on $l = 79.89°$, $b = 0.47°$. The latter does not include the brighter star-forming regions to the east containing W75-N and DR21 (Schneider et al., 2006b).

We also analysed IRIS maps at 100 and 60 μm toward these selected regions. These maps have $\sim 4'$ resolution on $1.5'$ pixels (Miville-Deschênes et al., 2002) and we used the version in which the sources have been removed by the technique described by Miville-Deschênes & Lagache (2005).

[2]This problem was fixed for the 2006 flight from Antartica (Truch et al., 2009).

4.3 Power Spectrum and Cirrus Noise

The power spectrum is the Fourier transform of the auto-correlation function of the intensity map $I(x, y)$. In k-space, $P(k_x, k_y)$ is simply related to an image by

$$P(k_x, k_y) = \langle \tilde{I}(k_x, k_y)\tilde{I}^{\star}(k_x, k_y)\rangle, \tag{4.1}$$

where $\tilde{I}(k_x, k_y)$ is the Fourier transform of the image and $\tilde{I}^{\star}$ its complex conjugate. We used the IDL routine FFT to compute the two-dimensional Fourier transforms. To ensure a smooth periodic boundary condition near the edges (Miville-Deschênes et al., 2002), the maps were apodized by a sine function over a range 10% the width of the map. The power spectrum $P(k)$ is obtained by averaging $P(k_x, k_y)$ over an annulus placed at $k = \sqrt{k_x^2 + k_y^2}$.

In practice, contributions to the total power spectrum come not only from diffuse dust emission, but also point sources, the cosmic infrared background (CIB), and the noise. When these components are statistically uncorrelated, the total power spectrum can be expressed as (Miville-Deschênes et al., 2007b)

$$P(k) = \Gamma(k)\,[P_{\rm cirrus}(k) + P_{\rm source}(k) + P_{\rm CIB}(k)] + N(k), \tag{4.2}$$

where $\Gamma(k)$ is the power spectrum of the PSF (the square of the modulus of the two-dimensional Fourier transform of the PSF), which decays at large k. For the bright Galactic Plane fields targeted here, the contribution from the CIB to the power spectrum is negligible. While the noise is measurable (§ 4.5.5), it too makes an insignificant contribution.

Gautier et al. (1992), followed by many other authors (Kiss et al., 2001, 2003; Miville-Deschênes et al., 2002), have shown that the power spectrum of Galactic cirrus follows a power law

$$P(k) = P(k_0)(k/k_0)^{\alpha}, \tag{4.3}$$

quantified by an amplitude $P_0 \equiv P(k_0)$ at some fiducial k_0 and an exponent α that is typically -3 (Miville-Deschênes et al., 2007b). From their analysis, the associated 'cirrus noise' for a telescope with mirror diameter D working at wavelength λ can be quantified as

$$\sigma_{\rm cirrus} = 100\ (r/1.6)^{2.5} \left(\frac{\lambda/250\ \mu{\rm m}}{D/3.5\ {\rm m}}\right)^{2.5} [P(k = 0.1\ {\rm arcmin}^{-1})/10^{-3}\ {\rm MJy}^2\ {\rm sr}^{-1}]^{0.5}\ {\rm mJy} \tag{4.4}$$

Here our assumptions about the measurement strategy for point sources are the same as made by Helou & Beichman (1990) and adopted by Kiss et al. (2001), which in the notation of Gautier et al. (1992) are a 'resolution ratio' $r = d/(\lambda/D)$ of 1.6, where d is the measuring aperture, and a reference annulus with 'separation ratio' 2. Also $\alpha = -3$, close to what we find below. The beam-related factor quantifies the effect of a smaller beam probing smaller spatial scales where the power in the fluctuations is weaker.

If the sources being measured are extended, as will be the case in many Galactic surveys, then the measuring aperture needs to be larger. The main consequence of this on increasing $\sigma_{\rm cirrus}$ is captured by the factor $r^{2.5}$ for the range of interest (see also Fig. 3 in Gautier et al., 1992).

Working with 100 μm *IRAS* data on fields of different average surface brightness $\langle I_{100}\rangle$, and adopting a fiducial scale $k_0 = 0.01$ arcmin^{-1} at which the amplitude is P_{100}, Gautier et al. (1992) found the trend that $P_{100} = C\langle I_{100}\rangle^3$, where C is a proportionality constant. If this is substituted in the above, we recover the formula given by Helou & Beichman (1990) and evaluated by Kiss et al. (2001) estimating the cirrus noise for different levels of cirrus brightness. Note that the cirrus noise estimate described by Miville-Deschênes et al. (2007b) used a slightly different definition of the noise, as well as incorporating a trend giving a slightly steeper power law with increasing $\langle I_{100}\rangle$, and in effect a lower C, which together conspire to lower the noise estimate by about a factor six for bright cirrus.

For reasons discussed below, both estimating P_{100} from $\langle I_{100}\rangle$ and scaling it to the appropriate wavelength of observation are problematical. Therefore, if possible the exponent and amplitude of $P(k)$ should be measured directly for the field of interest at the relevant wavelength. Measuring and normalizing at a scale as close as possible to the beam also avoids issues of extrapolation. With *Herschel* in mind, we have chosen $k = 0.1$ arcmin^{-1}. The normalization of the amplitude in equation (4.4) anticipates what we find at 250 μm for the two bright fields we examined.

4.4 IRIS Power Spectra

Our primary goals are to analyse statistical fluctuations of diffuse dust emission in the Galactic Plane using the power spectrum, and to measure the wavelength dependence of the amplitude of this power spectrum. To connect with previous work and provide a reference at shorter wavelengths, we begin with IRIS. IRIS (like *IRAS*) data come in

'plates' 12.5° on a side. We computed the power spectrum for the entire plate containing the Aquila field (plate 263) but because of a gap in the *IRAS* sky coverage near Cyg X (plate 361) we had to settle for a smaller region, 6° on a side in Galactic coordinates centred on $l = 80.69°$ and $b = 0.76°$. Binned estimates of $P(k)$ and their uncertainties were evaluated as in § 4.5.4.

The power spectrum $P(k)$ for the Aquila field at 100 μm is shown in Figure 4.1. The behavior of $P(k)$ is very much like that seen at higher latitudes and with BLAST (§ 4.5.5). To find $P_{\rm cirrus}(k)$ from equation (4.2), we need an estimate of the power spectrum of the noise, $N(k)$. This can be achieved using maps of the differences of independent *IRAS* maps (HCONs; Miville-Deschênes et al., 2002) after source removal (Miville-Deschênes & Lagache, 2005) and is shown in the lower curve in Figure 4.1. There is a feature at $k \sim 0.08$ arcmin^{-1} which is not seen in $P(k)$. This arises because of striping in the HCONs which affects the difference maps but is smoothed out in the average of the HCONs. To eliminate this spurious feature in the noise power spectrum to be subtracted, we have simply fit a power law for the range $k < 0.06$ arcmin^{-1} and extrapolated this to higher k (see lower dashed curve). The exponent -1.5 ± 0.2; Miville-Deschênes & Lagache (2005) find a range of -1.5 to 0. The extrapolation meets $P(k)$ at the highest k showing that it is a reasonable estimate of the noise, including that induced by the source removal technique which is greatest in Galactic Plane fields like this where the surface density of sources is large. For the beam $\Gamma(k)$ we used a Gaussian as specified by Miville-Deschênes & Lagache (2005) which is clearly just an approximation to the complicated effective beam of the images formed from the IRAS timestreams. In any case, neither the noise estimate nor the fine details of the beam are critical, because here we use only the part of the power spectrum at lower $k < 0.08$ arcmin^{-1}. We do not compensate for the apodization of the image edges, but instead simply avoid small values of $k < 0.004$ arcmin^{-1} where the power is significantly affected (Miville-Deschênes et al., 2002). Figure 4.1 confirms empirically that this is a good choice for the range of k used for the power law fit. The non-linear weighted fits were carried out with the IDL routine MPFIT (Markwardt, 2009).

Figure 4.2 shows the power spectrum for the square 6° region in Cyg X. Here the IRAS map coverage in the individual HCONs is not complete, so it is not possible to make a direct estimate of $N(k)$. However, comparison of the rms of the difference maps (in the areas covered) indicates that at the highest k, $N(k)$ should have a level comparable to $P(k)$, as found in Aquila. Therefore, an approximation to $N(k)$ is to extrapolate this to

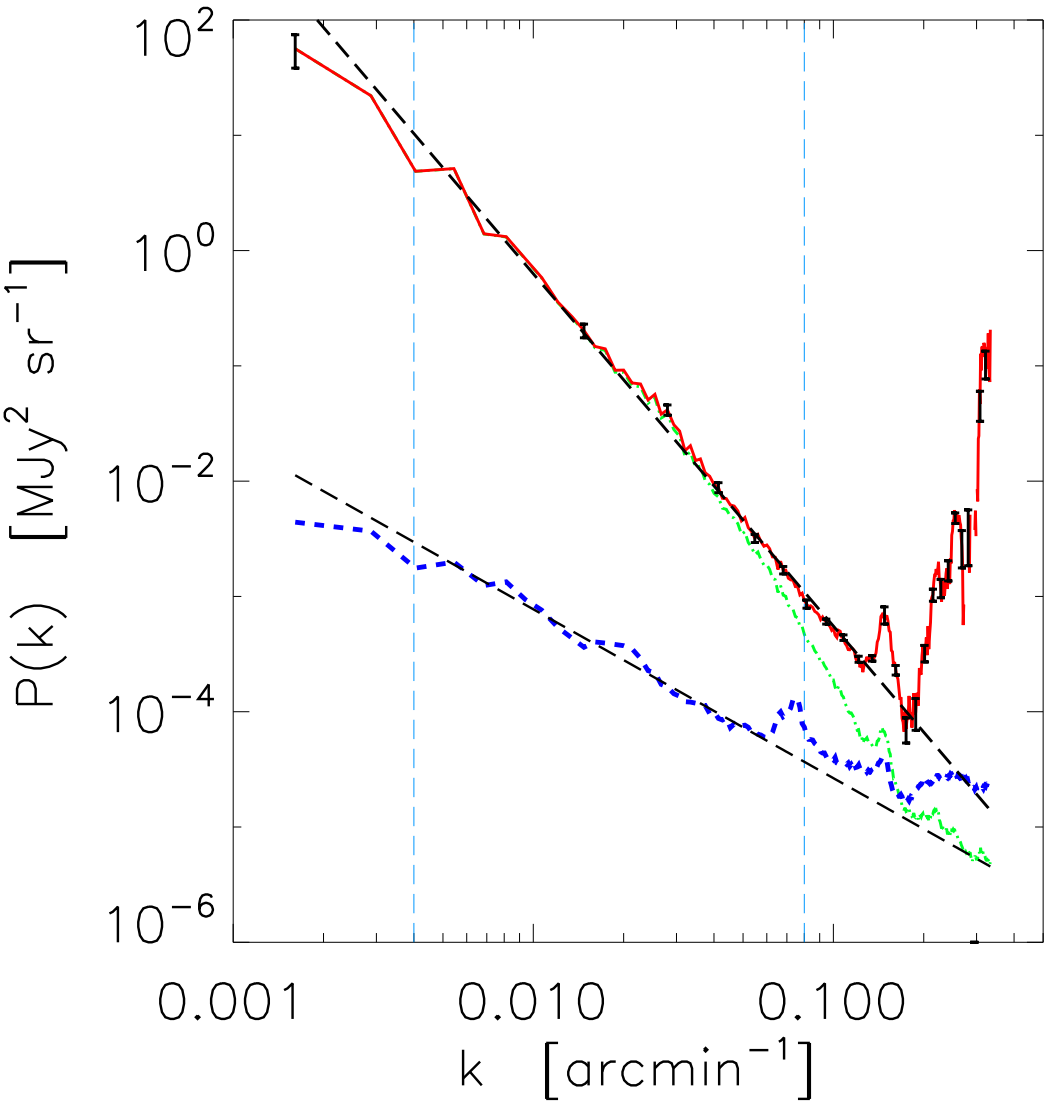

Figure 4.1 IRIS 100 μm power spectrum (dot-dash curve) of a square 12.5° on a side in Aquila spanning the Galactic Plane. $P_{\rm cirrus}$ (solid) is obtained by subtracting $N(k)$ and dividing by $\Gamma(k)$. The estimate of $N(k)$ adopted (lower dashed power law) was obtained using differences of independent IRIS maps (HCONs; see text). The error bars, plotted only every tenth point for clarity, do not account for the imperfect approximation to the beam whose effect is clearly present at large k. We fit the power law (dashed line) over the range 0.004 arcmin^{-1} $< k <$ 0.08 arcmin^{-1} marked by the vertical dashed lines. The exponent is -3.06 ± 0.02 and $P_{100} = 0.62 \pm 0.02$ MJy^2 sr^{-1}.

lower k along a power law, as show in the figure. Again, this is not critical to $P_{\rm cirrus}(k)$ given the conservative range used for the power-law fit.

For 100 μm we find an exponent α of -2.67 ± 0.09 in Cyg X and -3.06 ± 0.02 in Aquila, where the errors are statistical based on the fit to the data. The systematic errors, from the estimate adopted for $N(k)$ and from the (conservative) choice of upper limit in the range of k used for the fit, are comparable. Miville-Deschênes et al. (2007b) find that the steepness of the power spectrum increases as a slow function of $\langle I_{100} \rangle$. For the two fields $\langle I_{100} \rangle$ is 260 and 120 MJy sr^{-1}, respectively, and the expected exponents from this trend are -3.4 and -3.3, slightly steeper than what we find. Note however that they find a scatter of 0.3 about their trend.

We find $P_{100} = 1.5 \pm 0.2$ and 0.62 ± 0.02 MJy^2 sr^{-1} for Cyg X and Aquila, respectively. These can be compared to values of 4.3 and 0.59 MJy^2 sr^{-1} from the trend in Miville-Deschênes et al. (2007b), about which there is a factor of three scatter at high $\langle I_{100} \rangle$. Again the agreement is better for the Aquila field, despite the fact that there are significant asymmetries in the image (the bright swath of the Galactic Plane and residual striping) which make the two-dimensional power spectrum not quite circularly symmetric.

For more direct comparison with the BLAST power spectra, we computed the IRIS $P_{\rm cirrus}(k)$ for the smaller BLAST sub-fields. The exponents of the power spectra are -3.14 ± 0.27 and -2.92 ± 0.17, respectively. These are harder to measure, given the smaller dynamic range, but do not appear to have changed significantly despite the larger $\langle I_{100} \rangle$ values (430 and 330 MJy sr^{-1}). Expressing amplitudes as P_{100} (though $k = 0.01$ arcmin^{-1} is beyond our range in these small sub-fields), we find 3.1 ± 1.3 and 0.75 ± 0.11 MJy^2 sr^{-1}, respectively, compared to trend values of 29 and 13 MJy^2 sr^{-1}. Because of the $P^{1/2}$ dependence in equation (4.4), predictions of cirrus noise depend less strongly on any deviations from the trends. Nevertheless, these results illustrate the important point that when attempting to assess the cirrus noise, one should, if possible, measure the exponent and amplitude near the spatial frequencies of interest.

Because the cirrus noise is wavelength dependent, ideally P_0 would be measured at each relevant wavelength too. The amplitude might in principle be scaled, say from P_{100}. Not all scaling prescriptions in the literature can be valid, however, and we discuss our recommendation in § 4.6.

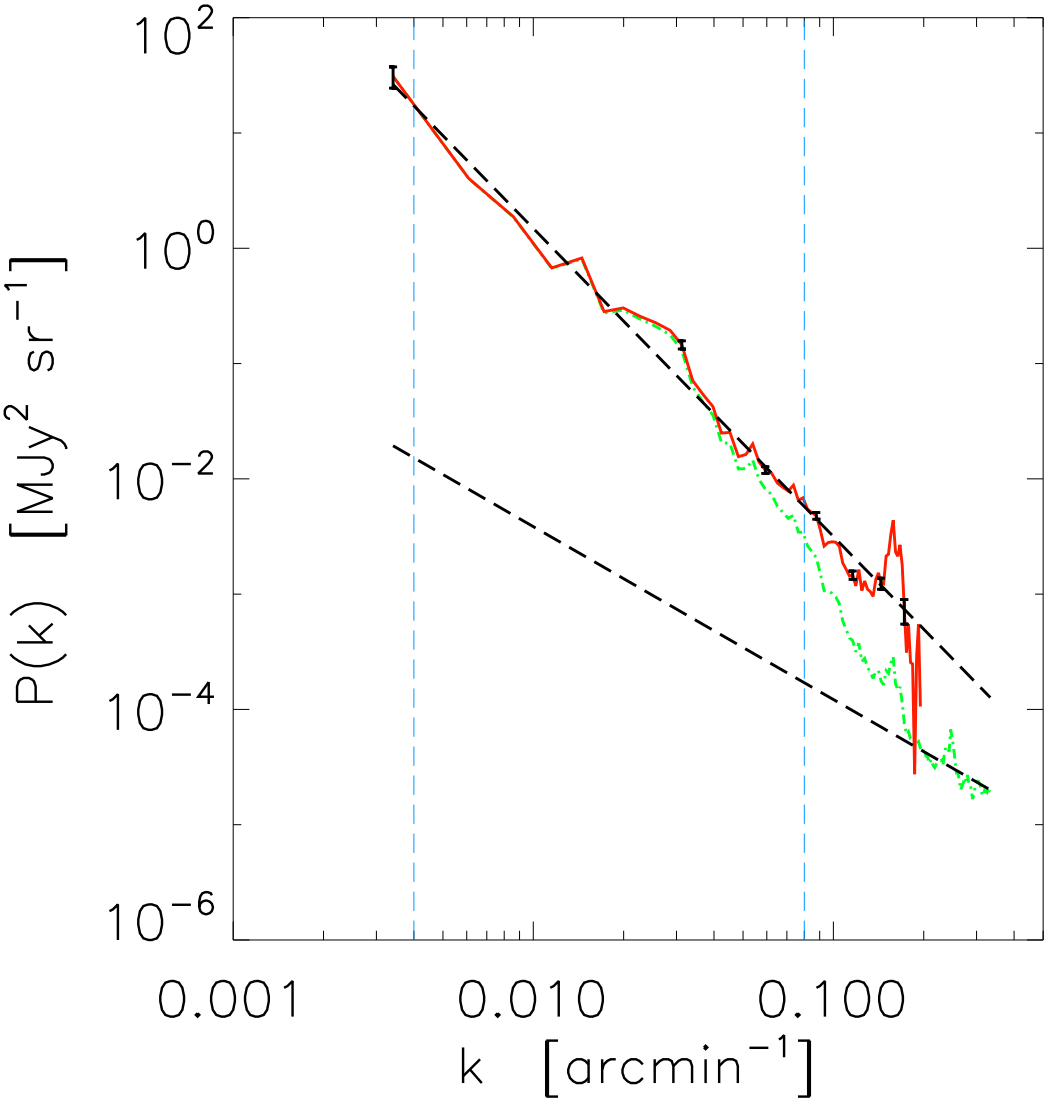

Figure 4.2 Like Fig. 4.1 but for a smaller square 6° region in Cyg X. The exponent is -2.67 ± 0.09 and $P_{100} = 1.5 \pm 0.2$ MJy^2 sr^{-1}.

4.5 BLAST Power Spectra

4.5.1 Noise Power Spectrum

In the BLAST map-making procedure (Patanchon et al., 2008b), a variance map $V(x, y)$ is produced based on the noise in the time-stream data and the map coverage by the bolometers in the arrays. For these BLAST surveys, the resulting maps of V are quite uniform. A realization of the noise map $N(x, y)$ can be constructed for each independent, uncorrelated pixel from $N(x, y) = \sqrt{V(x, y)}v$, where v is a Gaussian random variable with unit standard deviation and zero mean. Given the relative uniformity of the variance map, the resulting simulated noise map is close to white on all scales and thus the power spectrum of this noise is quite flat (see the example for Cyg X at 250 μm in Fig. 4.6). At large k the total power spectrum decays to this noise level, because of the combined effects of the decreasing power in the diffuse cirrus emission and the PSF. There is also a component of low frequency noise in the map arising from the very long time scale $1/f$ noise present in the time streams. However, in cross-linked maps produced using data from multiple scanning directions this is greatly reduced by the SANEPIC algorithm (e.g., Fig. 10 in Patanchon et al., 2008b) and is not important here because the cirrus signal at small k is so large.

4.5.2 Effect of the Beam

The BLAST05 PSF in telescope coordinates is shown in Truch et al. (2008). A synthetic beam can be made for a particular map, taking into account the scan angles and coverage (Chapin et al., 2008). Because this synthetic beam is not known out to the full size of the map, we have not derived its power spectrum $\Gamma(k)$ directly. Instead, we convolved the noise map with the PSF directly, found the power spectrum of that map, and divided by the power spectrum of the noise map. Figure 4.3 shows $\Gamma(k)$ for the BLAST05 PSF at 250 μm for the Cyg X field. This has a number of features characterizing scales seen in the corrupted PSF. Clearly, the observed $P(k)$ will be seriously suppressed at high k and so we will use data only for $k < 0.2$ arcmin^{-1}. At these scales, where the beam correction is not too large and so both more reliable and of less import, $\Gamma(k)$ can be described by a Gaussian with $\sigma_\Gamma = 0.08$ arcmin^{-1}. Using the Fourier relation $2\sqrt{2}\pi\sigma_\Gamma\sigma_\mathrm{b} = 1$, this corresponds to a Gaussian beam of $\sigma_\mathrm{b} = 1.4'$, or FWHM $= 3.3'$, slightly smaller than for IRIS. This is close to the $3.1'$ full width at half-power found by Truch et al. (2008). The

corruption of the BLAST05 PSF is such that the initial falloff in $\Gamma(k)$ is rather similar for the three wavelengths, and for both fields.

4.5.3 Source Removal

In the Galactic Plane, the power spectrum is seriously contaminated by compact sources. To remove them, we first deconvolve the BLAST maps using the L-R method which, importantly, conserves flux. Compact sources are of size $\sim 1.5'$ in these maps and more easily identified. They are fairly well described by Gaussians. We fit Gaussians (multiple if crowded) to obtain flux densities, positions, and FWHM (major axes and position angle) of the compact sources. We then convolve these Gaussians with the synthetic beam and subtract them from the original maps. For the Cyg X sub-field analysed, the upper and lower panels of Figure 4.4 show BLAST maps at 250 μm before and after source removal, respectively. Faint residuals appear near some of the brightest sources, because of multiscale structure in the ISM in which they are embedded.

4.5.4 Two-dimensional Power Spectrum

Figure 4.5 shows the two-dimensional power spectrum for the Cyg X region at 250 μm. Because $\alpha \sim -3$ produces a large intrinsic dynamic range in the power spectrum, we have multiplied it by $(k/k_0)^3$, with $k_0 = 0.1$ arcmin^{-1}. The dark rings are produced by the same features giving the dips in $\Gamma(k)$. Noise is being amplified at large k because of the k^3 multiplier.

The two-dimensional power spectrum is circularly symmetric, justifying the annular averaging to find the mean $P(k)$. Most of the information relevant to the diffuse emission is contained in the plateau in the central region of Figure 4.5, and the average there in this representation is close to $P(k = 0.1 \text{ arcmin}^{-1})$.

The error in $P(k)$ for each annulus is the standard error of the mean. While removing the effect of beam from the power spectrum, we have only scaled this error by the inverse beam, not accounting for the fact that its shape is not perfectly known at high k. However, this is of no consequence because we do not fit the data at large k where the beam correction is significant.

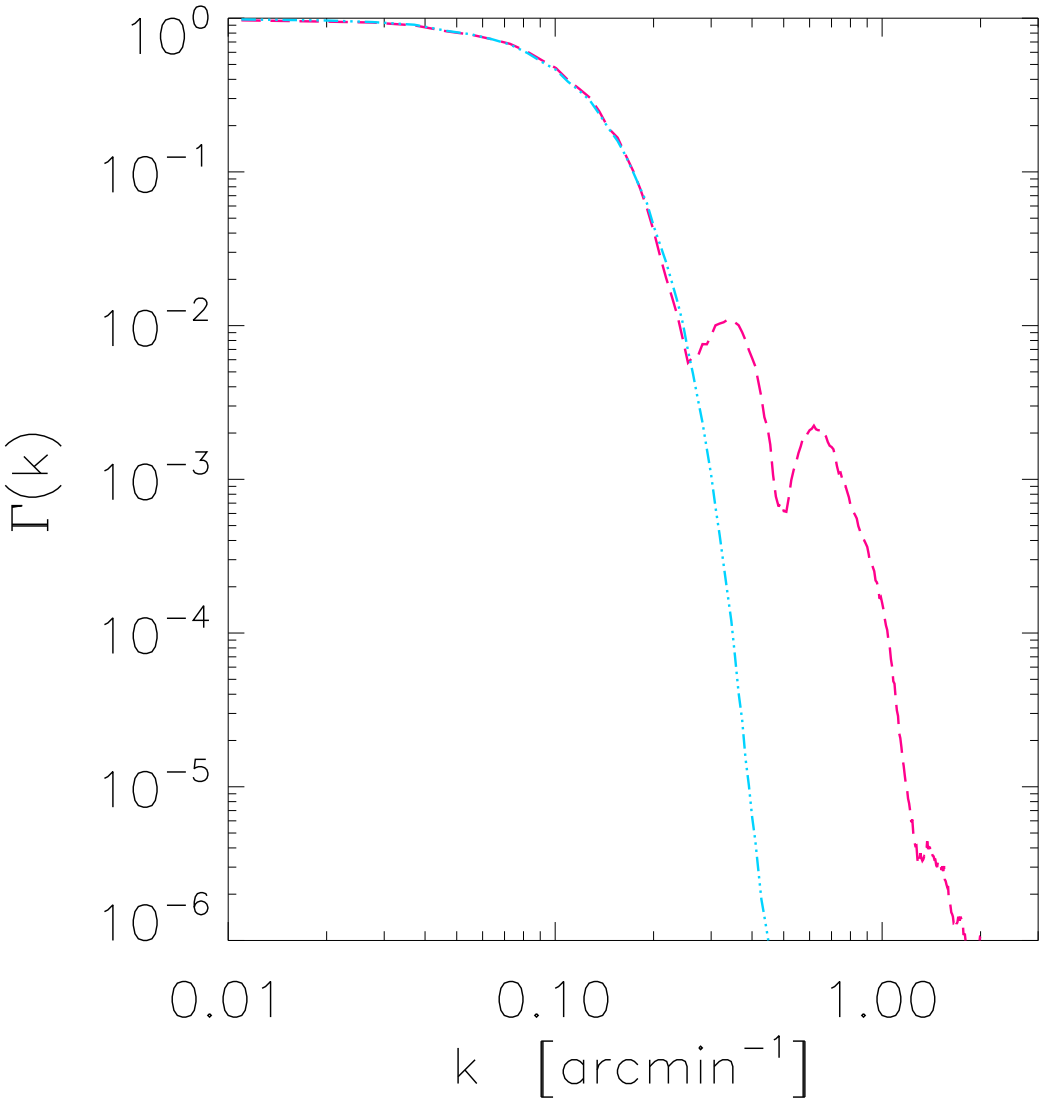

Figure 4.3 $\Gamma(k)$ for BLAST05 in Cyg X at 250 μm (dashed curve). The dot-dash line shows how this can be approximated by the power spectrum of a Gaussian PSF of FWHM 3.3′.

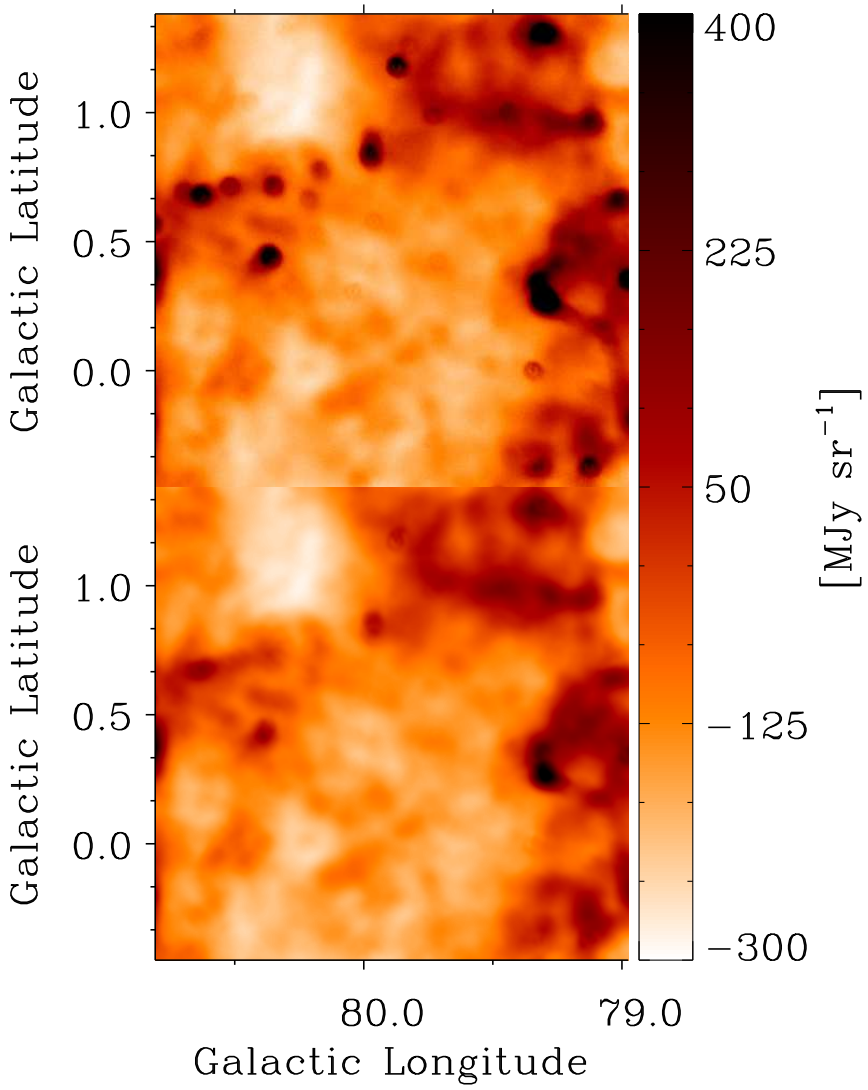

Figure 4.4 BLAST05 map at 250 μm of the selected region of Cyg X used for studying diffuse emission. The map in the upper panel includes point sources which, due to the corrupted BLAST05 beam, are compact structures of size $\sim 3.3'$. In the lower panel the sources have been removed.

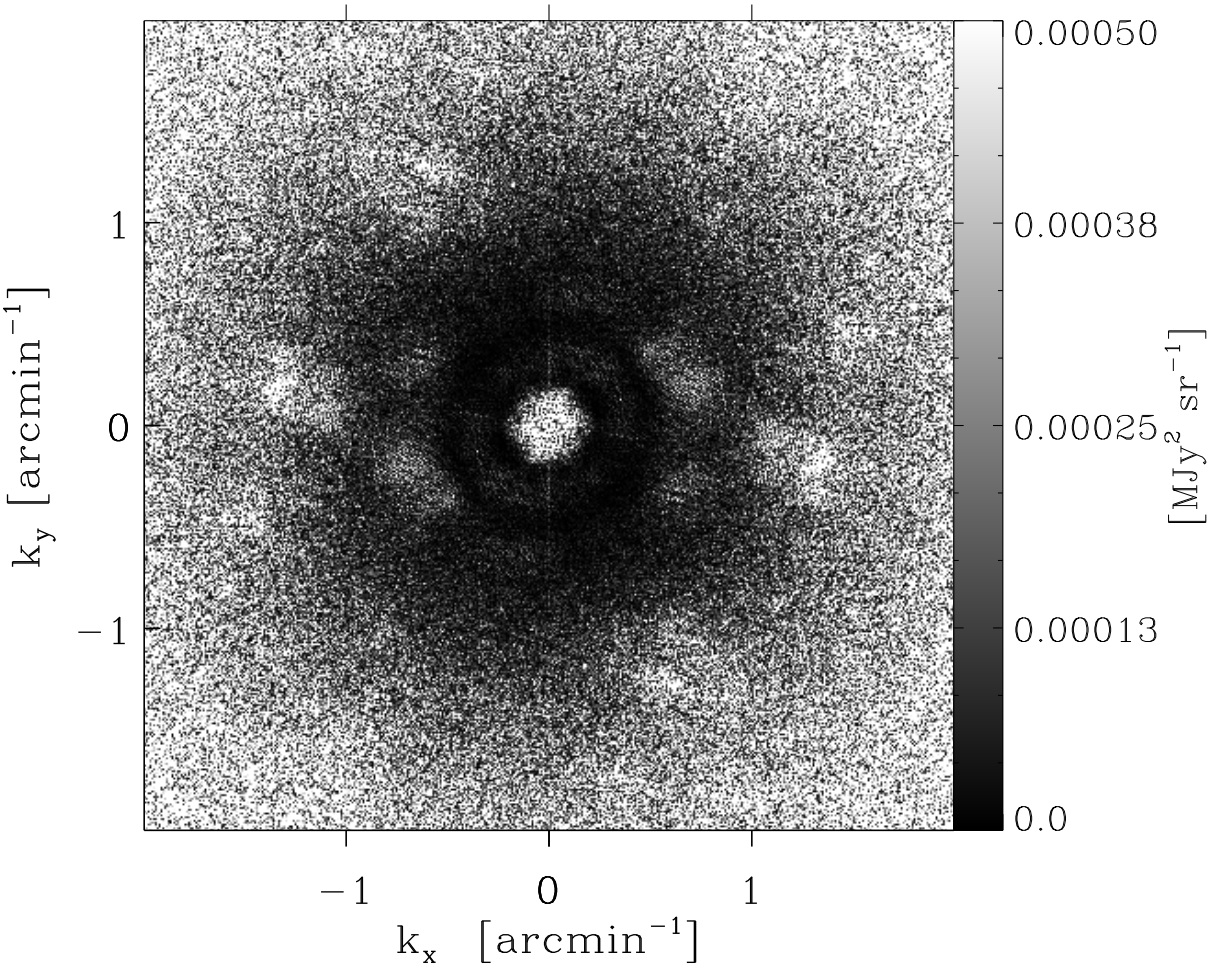

Figure 4.5 Two dimensional power spectrum multiplied by $(k/k_0)^3$ (with $k_0 = 0.1$ arcmin^{-1}), for the Cyg X map with compact sources removed, as shown in the lower panel of Fig. 4.4. Dark rings are an imprint from the BLAST05 PSF (Fig. 4.3). Scaling by k^3 has amplified noise at large k and highlighted the bright central plateau, which contains the information most relevant for this study.

4.5.5 Exponent and Amplitude

Figure 4.6 shows $P(k)$ for 250 μm for the Cyg X region, for the original map and with sources removed. The effect of the beam is dramatic at high k, showing that it is important to have a good estimate of the PSF. There is also clearly excess power due to sources and so it is important to remove them carefully.

At small k, the power spectrum is dominated by the dust structures; it decays toward higher k, as seen previously in IRIS data at shorter wavelengths. The oscillatory effect of $\Gamma(k)$ can be seen clearly at $k > 0.2$ arcmin^{-1} and at higher k the power spectrum meets the independently-predicted noise level shown.

$P_{\rm cirrus}(k)$, obtained by dividing the source-removed, noise-subtracted power spectrum by $\Gamma(k)$, is also shown in Figure 4.6. It appears to have a power-law form over the limited dynamic range in k available. We fit only over the range 0.025 arcmin^{-1} $< k <$ 0.2 arcmin^{-1}, restricted for the reasons discussed in § 4.4. In particular, at large k the effect of correcting for the PSF is very large. The synthetic PSF is an average for the entire observed field and so is imperfectly modeled to the precision that would be required for precise compensation at high k. Convincing evidence for any deviation from a power law for the higher k range will have to await the higher resolution observations anticipated with *Herschel* which will probe to beyond $k = 1$. At smaller k the observed power spectrum is affected both by apodization and by the effective filtering of the map-making procedure, such that the largest scales are not recovered. For the relatively small size of these maps and the characteristics of these BLAST05 observations these effects set in at about the same k (Patanchon et al., 2008b). In earlier work with *IRAS*, the amplitude P_0 is often cited for $k_0 = 0.01$ arcmin^{-1}. This fiducial value is below the range of our observations. Using $k_0 = 0.1$ arcmin^{-1} would seem preferable and probably more relevant to small maps at higher resolution to be made with *Herschel*.

Figure 4.7 shows $(k/k_0)^3 P_{\rm cirrus}(k)$ for all three BLAST bands (250, 350, and 500 μm) for Cyg X. We find $P(0.1 \text{ arcmin}^{-1}) = (1.60 \pm 0.05) \times 10^{-3}$ MJy^2 sr^{-1} at 250 μm. P_0 increases with decreasing wavelength for the BLAST bands and for the IRIS bands (§ 4.4) remains about the same at 100 μm and then decreases at 60 μm. We obtain an exponent α equal to -2.60 ± 0.07 at 250 μm. This can be compared with the value found above at 100 μm, -2.97 ± 0.23. The exponents are quite similar for all bands, except for 60 μm which is discussed further in § 4.6.1. If the power spectrum were less steep moving into the submillimeter, this would provide important evidence for a change in the statistical

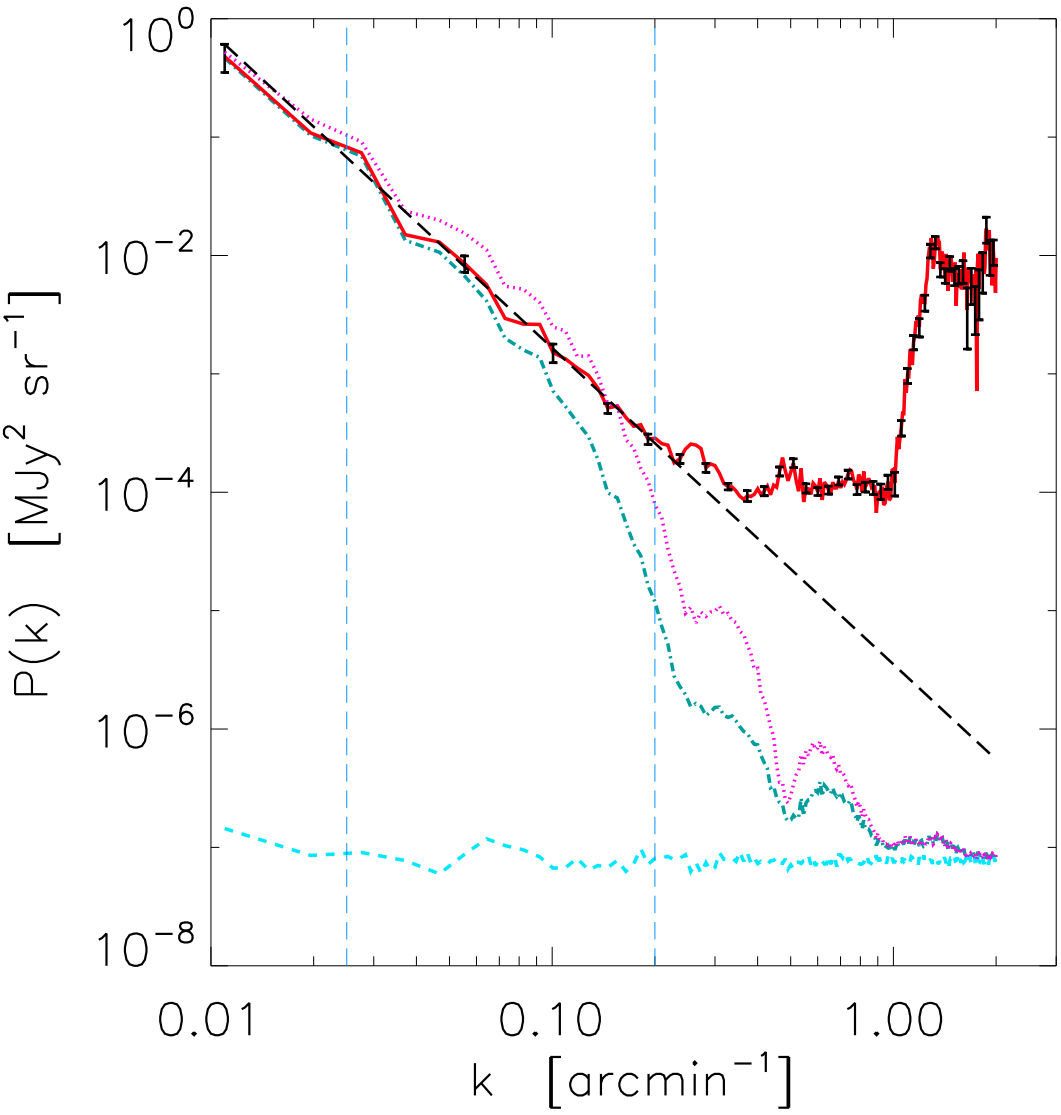

Figure 4.6 BLAST power spectra at 250 μm for the Cyg X region shown in Fig. 4.4. The dotted curve, corresponding to the upper panel of Fig. 4.4, shows that a significant amount of power is present at intermediate scales due to compact sources. The lower dot-dash line is $P(k)$ of the same region after removing sources (corresponding to Fig. 4.5). The oscillatory behavior at large k is due to the corrupted BLAST05 PSF (Fig. 4.3). The almost horizontal dashed line is the power spectrum of the noise map (§ 4.5.1). At very small scales where the astronomical signals become correlated within the beam, the power spectra meet the noise level. The solid line is the power spectrum $P_{\rm cirrus}(k)$, after subtracting the noise and dividing by $\Gamma(k)$ to remove the effect of the beam (as in Fig. 4.1, error bars at high k do not include the imperfect knowledge of the beam and noise). The vertical dashed lines indicate the restricted range 0.025 arcmin^{-1} $< k <$ 0.2 arcmin^{-1} used for fitting the power law. The exponent is -2.60 ± 0.07 and $P(0.1 \text{ arcmin}^{-1}) = (1.60 \pm 0.05) \times 10^{-3}$ MJy^2 sr^{-1}.

properties of the emission and the underlying mass column density and temperature distribution (§ 4.6.1). Definitive searches for such wavelength dependence should benefit from the higher spatial dynamic range anticipated in observations with *Herschel*.

Figure 4.8 presents the results from our analysis of the Aquila field. Overall the same behavior is seen, though the exponent appears to be slightly steeper (-3.14 ± 0.10) at 250 μm, P_0 at 250 μm is larger, $(3.03 \pm 0.15) \times 10^{-3}$ MJy^2 sr^{-1}, and the relative amplitudes at the IRIS bands are much lower.

4.5.6 Catalog Depth

Equation (4.4) can be used to predict the depth reached in a compact source catalog. To apply this to the BLAST05 Cyg X survey, (where the compact sources are of apparent size $\sim 1.5'$ in the L-R maps in which they are detected and measured), the appropriate r is ~ 3.6. With $D = 1.9$ m and $P(0.1 \text{ arcmin}^{-1}) = (1.60 \pm 0.05) \times 10^{-3}$ MJy^2 sr^{-1} for the somewhat dimmer part of the survey field examined here, $\sigma_{\rm cirrus} = 4.2$ Jy at 250 μm. This compares well to the empirically-estimated 3-σ detection threshold of ~ 15 Jy (Roy et al., 2011a). The effective noise near bright sources can be somewhat higher because of contaminating artifacts produced in the L-R deconvolution.

For the large survey of Vela carried out by BLAST in 2006, where the beam of the 1.8 m mirror was diffraction limited (Netterfield et al., 2009), we have not measured P_0 directly, because the region was not covered by orthogonal scanning and so the cirrus structure is not well constrained over all scales in the cross-scan direction (Patanchon et al., 2008b). Nevertheless, following the scaling suggested in § 4.6, we can estimate P_0 from $\langle I_{100} \rangle \sim 100$ MJy sr^{-1} and $T_{\rm d} \sim 18$ K, giving $P(0.1 \text{ arcmin}^{-1}) = 10^{-3}$ MJy^2 sr^{-1} at 250 μm, from which $\sigma_{\rm cirrus} \sim 0.6$ Jy. However, the sources were actually extended, with typical apparent sizes of $1'$, so that $r \sim 2.4$, and then $\sigma_{\rm cirrus} \sim 1.6$ Jy. For comparison, the catalog depth judged from simulations of completeness was 6 Jy (Netterfield et al., 2009). We conclude that the depth is dominated by the influence of the cirrus noise.

With *Herschel* and assuming the source sizes are compatible with $r = 1.6$, $\sigma_{\rm cirrus}$ in the Cyg X region should be closer to 100 mJy at 250 μm. While a distinct improvement, this is nevertheless substantial compared to the instrument noise (r.m.s. ~ 5 mJy) predicted using HSPOT[3] for the planned parallel PACS-SPIRE map scanning strategy

[3]http://www.ipac.caltech.edu/Herschel/hspot.shtml

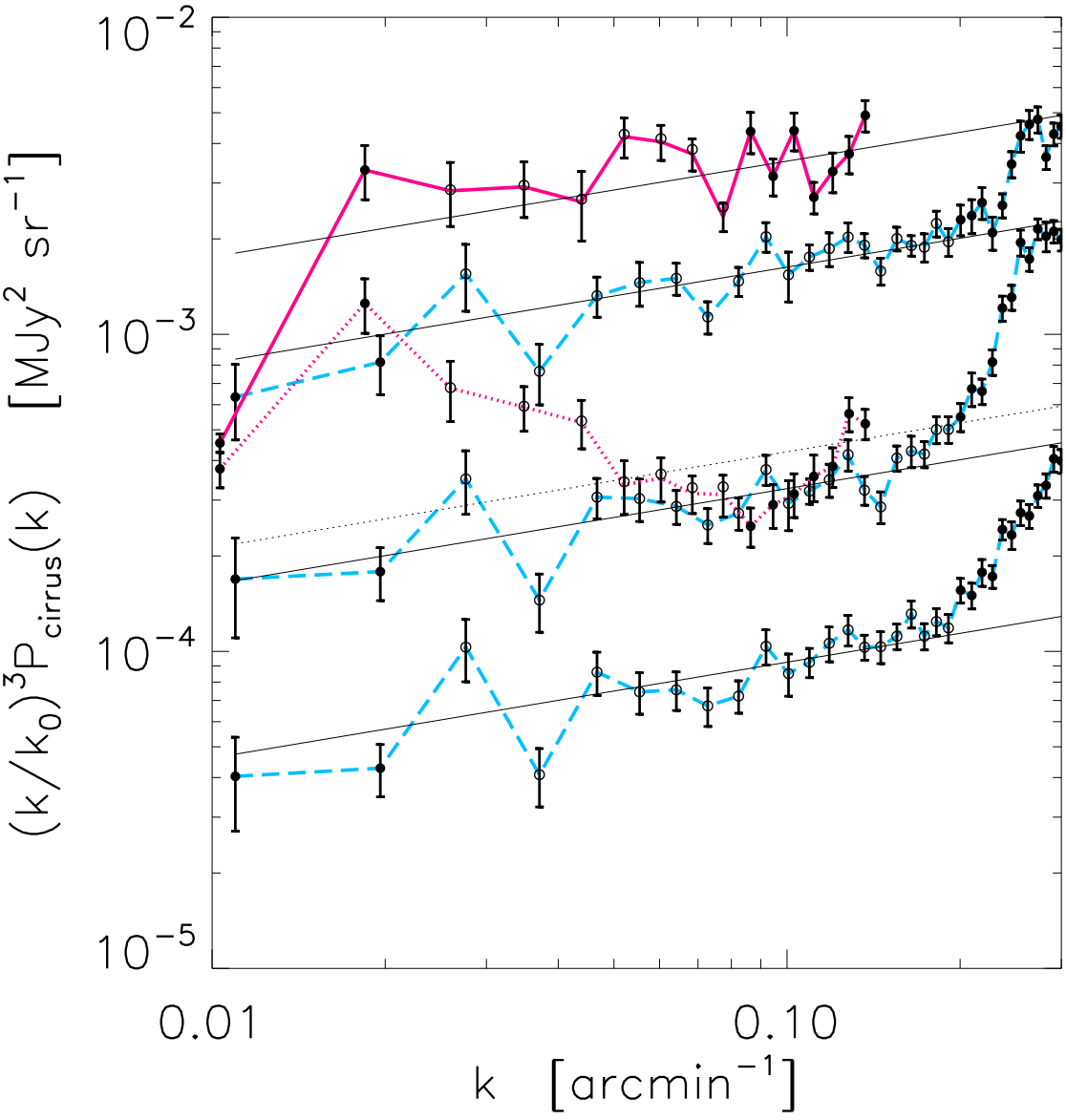

Figure 4.7 $(k/k_0)^3 P_{\rm cirrus}(k)$ for the three BLAST bands and two IRIS bands, for the Cyg X field with $k_0 = 0.1$ arcmin^{-1}. Data at high k (solid circles) are not used (or shown for the IRAS bands) because of the large and uncertain beam correction and eventually the dominance of noise (see Figs. 4.2 and 4.6). The exponents are similar for all bands. The amplitude increases with decreasing wavelength for the BLAST bands and IRIS 100 μm band (solid), and then decreases at 60 μm (dotted). Lines represent a power law with common exponent -2.69 fit to the data plotted with open circles.

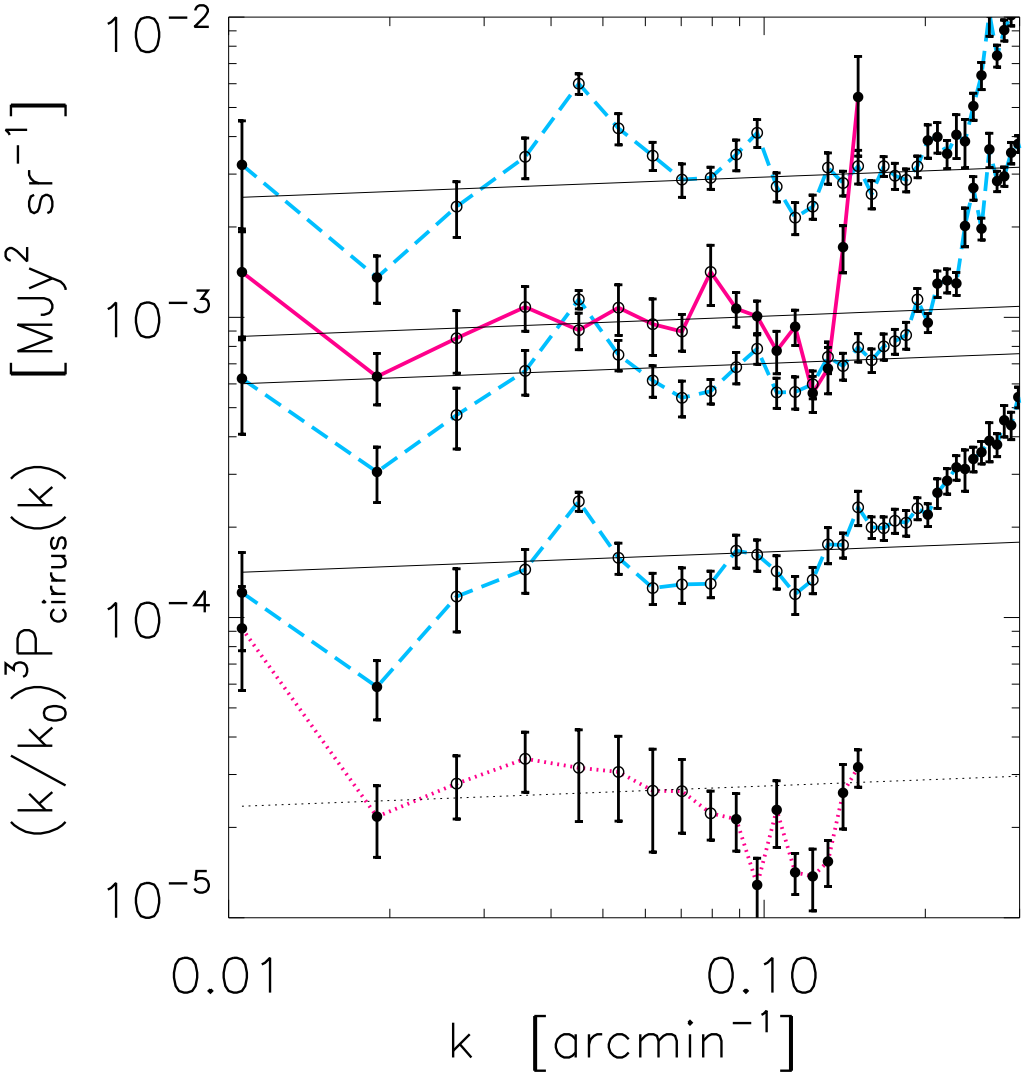

Figure 4.8 Like Fig. 4.7, but for the Aquila region. The amplitudes at 100 and 60 μm are relatively lower, which indicates that the cirrus in this region is cooler. The common exponent used for the fits was -2.91.

in the guaranteed-time key project HOBYS[4] (Herschel imaging survey of OB Young Stellar objects). We expect substantial regional variations. For example, in Aquila, simply from the larger P_0 the depth achieved should be 1.4 times worse. And this is not even the brightest part of the Galactic Plane to be surveyed in the open-time key project Hi-GAL[5] (Herschel infrared Galactic plane survey).

Extraction of sources with wavelength-dependent and multi-scale structure will be especially problematical and it will be necessary both to measure the cirrus properties and to simulate its effects. For SPIRE maps, in particular those made with the parallel PACS-SPIRE mode, a corollary is that the high signal-to-noise ratio resulting from the redundant coverage is well suited to studying the statistical properties of the bright cirrus. Of particular interest is how the power spectrum varies with wavelength, which can be used to determine physical properties of the diffuse dust.

4.6 Wavelength Dependence

4.6.1 Mass Column Density Distribution

BLAST and *IRAS* maps record surface brightness I which, in turn, depends on the dust mass column density $M_{\rm d}$:

$$I_\nu = M_{\rm d}\kappa_\nu B_\nu(T_{\rm d}), \tag{4.5}$$

where κ_ν is the dust emissivity, B_ν is the Planck function for dust temperature $T_{\rm d}$ and it is understood that the right-hand side is summed over various dust components which might have different κ and T_d.

The underlying spatial property being probed is $M_{\rm d}$ which is in turn the projection of the three-dimensional density distribution. $M_{\rm d}$ is modulated as a function of frequency by the emissivity and temperature, and can also have modulations caused by spatial differences in these properties. The ISM in the Galactic Plane is far from homogeneous, containing diffuse atomic and ionized regions and shielded molecular regions with possibly different mixes of dust compositions and sizes, and along any line of sight there will be a range of interstellar radiation field intensities, all of which could affect $T_{\rm d}$. The surface brightness I_ν is particularly sensitive to $T_{\rm d}$ for frequencies near or above the peak in the SED, i.e., for 100 μm and shorter for typical interstellar diffuse dust temperatures.

[4]http://starformation-herschel.iap.fr/hobys/
[5]https://hi-gal.ifsi-roma.inaf.it/higal

Therefore, it is somewhat surprising that the power spectra exponents that we obtained are so similar. The potential for wavelength dependence should be particularly high at 60 μm where non-equilibrium emission from very small grains (VSGs) starts to become important (Desert et al., 1990; Li & Draine, 2001) and is even more directly responsive to the ultraviolet radiation field. The Cyg X field analysed definitely has different spatial structures appearing in the images at the shorter wavelengths and there is some evidence in Figure 4.7 for an effect on the exponent of the power spectrum.

Furthermore, the exponent for a particular region must depend, through the structure of $M_{\rm d}$, on the environments probed along the line of sight and the energy injection at large scales that is responsible for the apparent turbulence in the ISM.

In the simple case of homogeneous correlation in the ISM, I_ν everywhere in the map would scale with frequency according to the simple relative SED S_ν of the emitting dust. From equation (4.5), $S_\nu \propto \kappa_\nu B_\nu(T_{\rm d})$. Therefore, P_0, measuring the same structure in $M_{\rm d}$, would scale simply as S_ν^2 (see eq. [4.1]) while $\sigma_{\rm cirrus}$ would scale as S_ν (see eq. [4.4]). This scaling is what is assumed by the prescriptions of Lagache & Puget (2000) and Miville-Deschênes et al. (2007b), for example, and appreciated by Jeong et al. (2005). However, on making the substitution $P_{100} \propto \langle I_{100}\rangle^3$, Helou & Beichman (1990) end up assuming that P scales as S^3 and thus $\sigma_{\rm cirrus}$ scales as $S^{1.5}$. Kiss et al. (2001) find some empirical support for the latter over the *ISO* ISOPHOT wavelength range.

Note that the wavelength dependence of the signal-to-noise ratio of a point source will vary by the factor $(D/\lambda)^{2.5}$ from equation (4.4), and also the ratio of the SED of the source relative to that of the confusing cirrus. At submillimeter wavelengths, the situation is more favorable for detecting cold sources in warm cirrus than vice versa. Therefore, the completeness depth of a survey as a function of wavelength will depend on these factors. Source size and structure can also change with wavelength (Netterfield et al., 2009) but we will not dwell on this quantitatively here.

4.6.2 Characteristic Temperature

The similarity in the exponents of the power spectra as a function of wavelength is no guarantee of underlying homogeneous conditions. Nevertheless, we can assume that there is some characteristic SED for each region, and use the relative frequency dependence of $P_0^{1/2}$ to recover it. To be consistent with this picture , we evaluated $P(0.1\ \mathrm{arcmin}^{-1})$ using a common exponent, which is simply the average of the exponents found at each

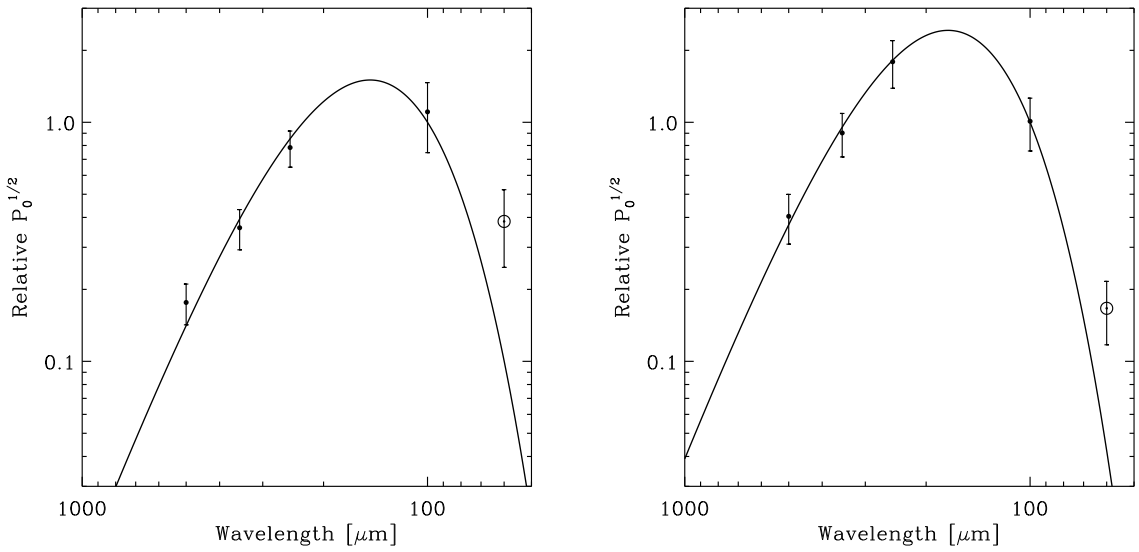

Figure 4.9 Relative SED obtained from the square root of the amplitudes of the power spectra fit in Figs. 4.7 and 4.8. Left Cyg X; right, Aquila. Solid curve is the best-fit modified blackbody with $\beta = 2$. The 60 μm power spectrum values (open circles) were not used for the fits (see text). The best-fit temperatures of Cyg X and Aquila are 19.9 ± 1.3 and 16.9 ± 0.7 K, respectively. For ease of comparing the two fields and results in Figs. 4.10 and 4.11, data and curves have been displayed normalized to the value of the best-fit modified blackbody at 100 μm.

wavelength (excluding 60 μm). This relative SED is shown in Figure 4.9 for each region.

For Cyg X, the best fit temperature is 19.9±1.3 K, which appears to be slightly warmer than the local high latitude diffuse medium dust temperature of 17.5 K (Boulanger et al., 1996). Finding warmer dust in Cyg X is not particularly surprising, because this region, which lies along the local spiral feature ($l = 80°$), is one of active star formation, with an OB association and numerous H II regions. In the 21-cm radio continuum this region includes areas of strong diffuse thermal emission. To account for the higher equilibrium temperature the ambient radiation field absorbed in Cyg X would have to be about $(19.9/17.5)^6 = 2.1$ times higher than locally.

By contrast, for Aquila the characteristic temperature derived is somewhat lower, about 16.9 ± 0.7 K. This line of sight passes through the inner Galaxy ($l = 45°$), with significant molecular clouds but much less star formation (Rivera-Ingraham et al., in preparation).

As we have noted, under uniform conditions, maps at different wavelengths will have to be highly correlated in their spatial structures, and so they will have the same power spectrum scaled by S^2. But the fact that the relative SED derived from $P_0^{1/2}$ appears reasonable is no guarantee that the maps are simply scaled versions of one another (since phases could be different). However, this can be checked directly. Inspection of the BLAST maps shows that they are remarkably similar in all three bands. This is quantified through the correlations with respect to the 250 μm map shown in Figure 4.10 for Cyg X. The linear fits shown are the ordinary least squares bisector solution (Isobe et al., 1990) obtained with the IDL routine SIXLIN. Note that the correlation of BLAST 250 μm with IRIS 100 μm is not as high as it is between BLAST bands. This is expected, because of the above-mentioned greater sensitivity of 100 μm emission to $T_{\rm d}$. Differences with respect to the submillimeter images become more apparent at 60 μm, where in addition the power spectrum is found to be somewhat steeper (Fig. 4.7). Figure 4.11 shows the even better correlations for the Aquila region. A clue to understanding the good correlation is, of course, the very detailed similarity of the power spectra at the different wavelengths.

As a consistency check, the slopes of the correlations can be used to construct another relative SED. As seen in Figures 4.10 and 4.11, these look very similar to the respective SEDs based on the power spectra (Fig. 4.9) and the best-fit temperatures 18.6 ± 0.5 K and 17.3 ± 0.3 K are very similar to those found above.

We therefore have some evidence that the appropriate scaling of $\sigma_{\rm cirrus}$ is as S, not

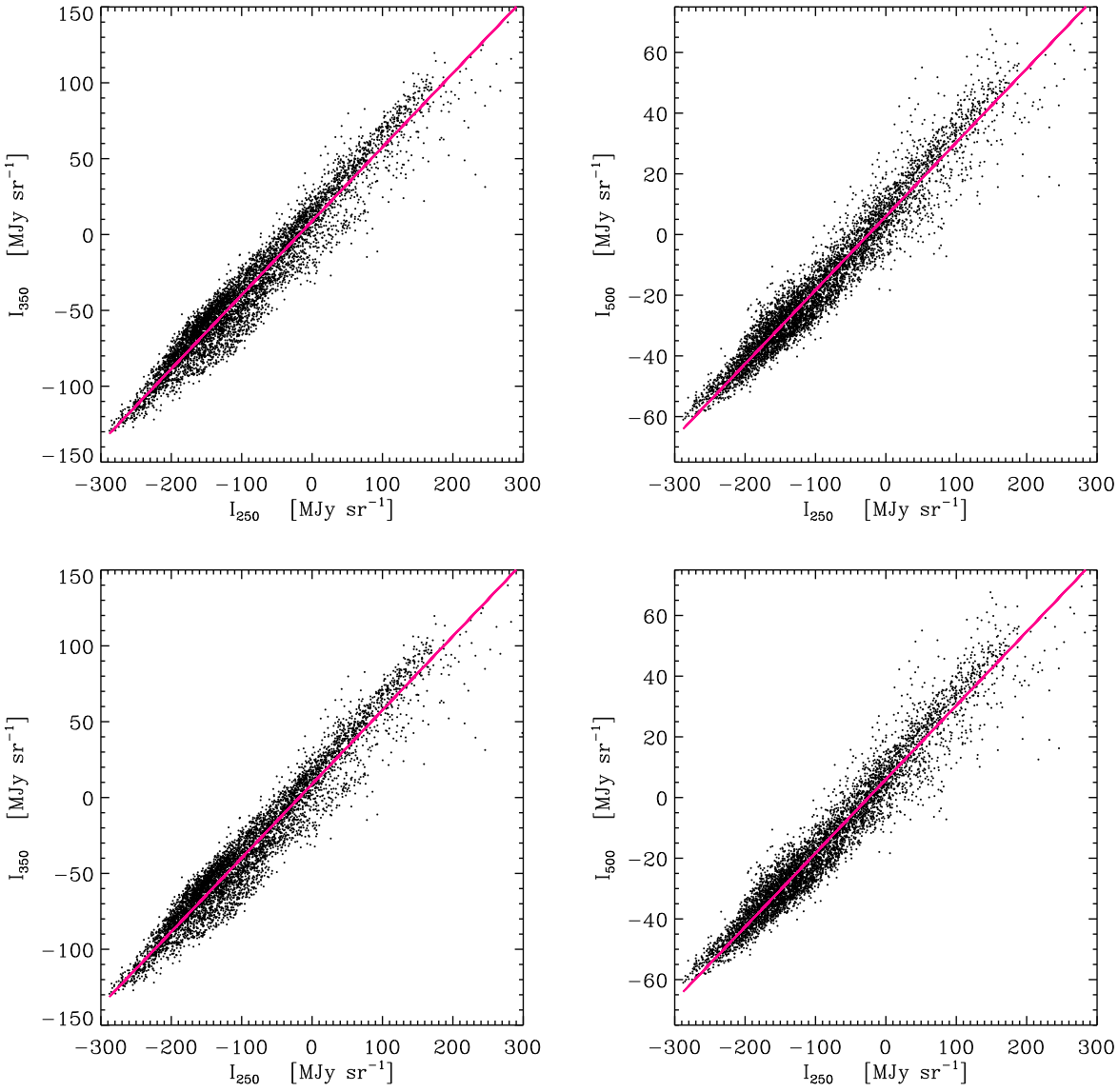

Figure 4.10 Pixel-pixel correlation of 500, 350, and 100 μm maps with respect to the 250 μm map for the Cyg X region, with the best-fit correlation line plotted. The lower right panel shows a relative SED obtained from the slopes of these correlations. With $\beta = 2$, the best-fit temperature is 18.6 ± 0.5 K. The normalization here is the same as in Fig. 4.9. The value at 250 μm, indicated by the triangle in this normalization, is not used explicitly for the fit. The open circle (from the 60 μm slope) was also not used.

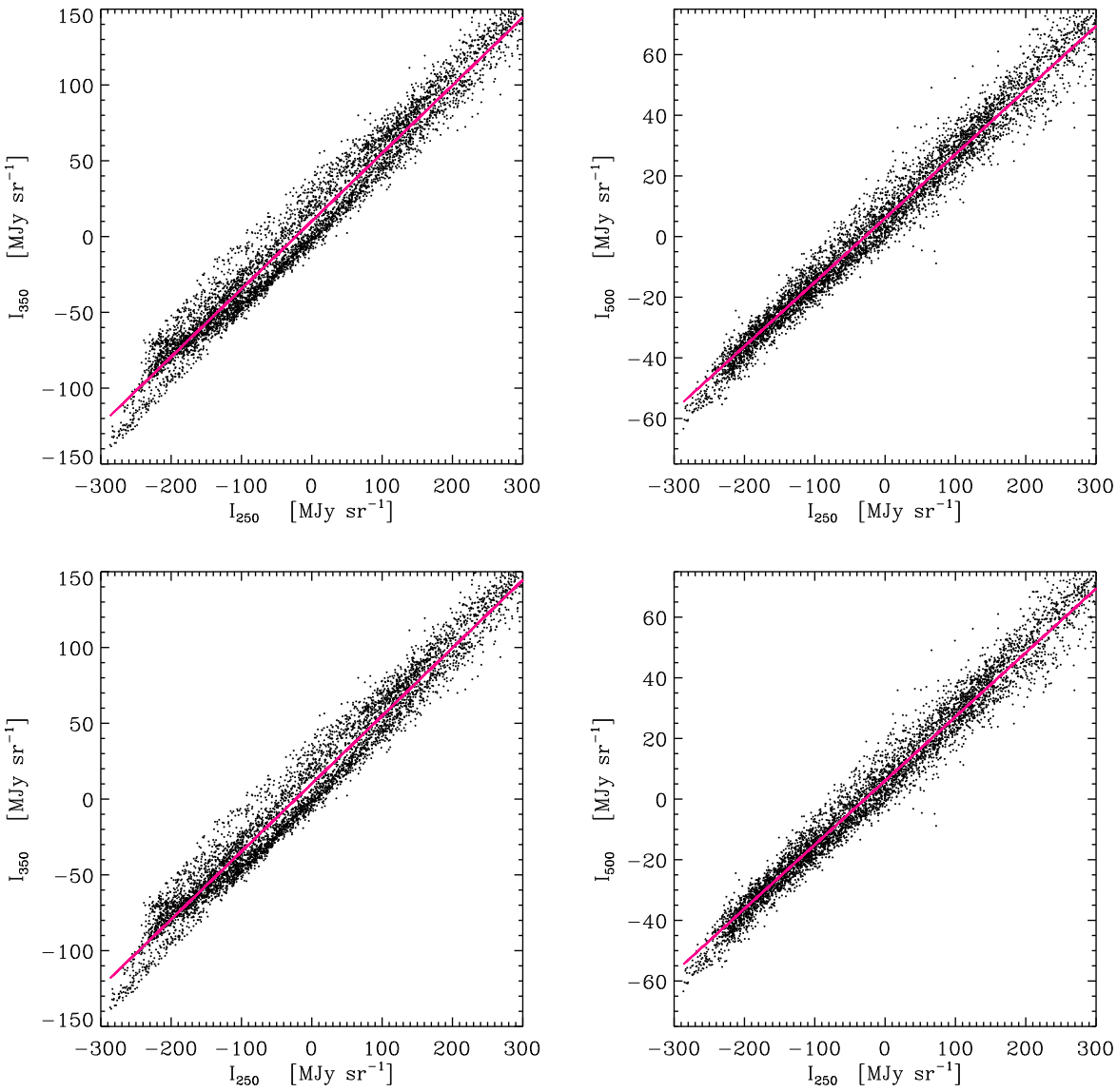

Figure 4.11 Like Fig. 4.10, but for the Aquila region. The slope of the 100 μm correlation is much shallower than in the Cyg X field, and the best-fit temperature is 17.3 ± 0.3 K.

$S^{1.5}$. However, this is not immediately generally useful, unless there is some independent evidence about the frequency dependence of S (or the effective $T_{\rm d}$ and β), since this can clearly vary significantly from region to region. The best approach is to measure P_0 directly at each wavelength.

4.7 Conclusion

In these fields in the Galactic Plane, the exponent of the power spectrum of the 100 μm IRIS map is close to -3, within the dispersion seen by Miville-Deschênes et al. (2007b) despite the average brightness $\langle I_{100} \rangle$ being beyond the range studied by these authors. On the other hand, the amplitudes of the 100 μm power spectra estimated for these bright $\sim 2^\circ \times 2^\circ$ fields are significantly below what would be extrapolated from the trend with $\langle I_{100} \rangle$ found by Miville-Deschênes et al. (2007b). Therefore, particularly in such bright star forming regions, it is recommended that the power spectrum be computed directly. The power spectra derived from the BLAST observations are also well fit by power laws, with similar exponents. The frequency dependence of the amplitude of the power spectrum can be described by the square of an SED which is a simple modified black body function with a reasonable characteristic temperature. This is confirmed by direct correlations between the maps at different wavelengths. However, this characteristic temperature does appear to change in different Galactic environments, and unless its value is known independently the power spectra and/or map correlations need to be evaluated for all wavelengths.

Cirrus noise will be important in many planned multi-wavelength Galactic Plane, high latitude, and extragalactic surveys carried out with *Herschel*. Our results provide important empirical support for a proposed prescription for the wavelength dependence of the cirrus noise, which incorporates a factor which varies directly as the SED. In practice the noise will be best evaluated, most free of assumptions, simply by measuring $P_0^{1/2}$ at each wavelength and using equation (4.4).

Chapter 5

Summary and future work

In this thesis I have studied Galactic dust emission at submillimeter wavelengths to unveil some of the deeper questions of astrophysical interest related to star formation and large scale structures in the ISM. Massive stars are born inside cold and dense molecular clouds of high extinction. Moreover, during their early phases of formation they remain enshrouded by dust, which is why they are undetected in near infrared and optical observations. BLAST observations, precursor to those now being carried out with SPIRE on *Herschel* (Griffin et al., 2010; Molinari et al., 2010a; André et al., 2010; Bontemps et al., 2010a; Motte et al., 2010; Hennemann et al., 2010) were unique due to the strategic spectral coverage where the SED of cold dust emission peaks and provided for unbiased studies of some major star-forming clouds including their surrounding environment. BLAST's unbiased mode of scanning large regions can be contrasted to surveys with SCUBA (Di Francesco et al., 2008) and MAMBO (Motte et al., 2007) at longer wavelengths which were limited to high extinction regions. The BOLOCAM survey (Aguirre et al., 2011) had broad sky coverage, but because of limitations imposed by the atmosphere was not sensitive to diffuse emission.

5.1 Summary

I have demonstrated the applicability of the L-R method of deconvolution to the BLAST05 images which were originally at $\sim 3'$ resolution due to some uncharacterrized optical distortion. This has been one of the important steps in preparing images at near diffraction limited resolution before beginning scientific analysis. I have performed simulations to test the performance of the L-R algorithm in restoring both compact sources and diffuse

structures. To illustrate the benefits, Chapter 2 is supplemented with analyses of two small star-forming fields, the K3-50 and IC 5146 regions.

A major contribution of this thesis is presented in Chapter 3, where I have extensively studied the Cygnus X (Cyg X) region and diverse phenomena associated with this "typical" relatively nearby high mass star-forming region. Utilizing available ancillary multi-wavelength observations as well, I have studied the influence of OB stars and stellar clusters on Cyg X, revisiting the well-known DR H II regions and their surroundings in the light of submillimeter continuum dust emission and CO line emission. An interesting question arising is whether there are any compact cold sources which could be precursors to massive stellar clusters as powerful as the DR regions. There is no BLAST clump that could be a precursor to such a prominent cluster; even adding the mass of the embedding CO clump would fall short. However, in an unevolved GMC such clusters might be detected. I have assessed the evolutionary sequence of the compact sources of spatial extent of about ~ 1 pc in the context of the L-M diagram. Subsequently, I have reviewed how independent empirical evidence for evolutionary stages relates to the characteristic position in the L-M diagram and then I related this to ideas from theoretical models to provide insight into the evolution. I have found evidence in *Spitzer* data for incipient fragmentation into low-mass stars in this early stage of evolution, which can be understood as an initially low Jeans mass. I have examined the star formation efficiency. Comparing the total mass of the BLAST compact sources within a CO clump to the clump mass I have obtained a linear correlation between the two, with a ratio of 0.05. This clearly relates to the star formation efficiency *within* a GMC and might approximate the overall efficiency.

Finally, a power spectrum analysis of the large scale brightness fluctuations in the Galactic plane has been performed in Chapter 4. A characteristic power law exponent of ~ -2.7 has been found for sub-regions of Aquila and Cyg X. I have also shown that the observed relative amplitudes of the power spectra at different wavelengths can be related through an SED. This analysis has produced a consistent quantification of the cirrus confusion noise level for BLAST observations. Moreover, it was predicted that *Herschel* observations, even at their higher resolution, would not be immune to the cirrus noise.

This work has been extended by Martin et al. (2010) through analyses of Galactic cirrus maps obtained with *Herschel*. In Martin et al. (2010), we have estimated noise directly on *Herschel* images from which bright sources were removed and on simulated images of similar cirrus structures. To estimate photometric confusion noise, a more

practical Gaussian photometric template (a strategy important while doing photometry in crowded regions) has been used.

5.2 Future Work

In this thesis I have touched upon various aspects of star formation. However, the observations have been limited to a relatively small part of the sky. For a complete census of the early evolution preceding prestellar cores a uniform characterization of an unbiased sample in a variety of environments is required. Moreover, the limited BLAST resolution was insufficient to relate the large-scale properties to the inner details of the star forming clumps. These issues are being addressed, at least in part, by the Guaranteed Time Key Project on *Herschel* (André et al., 2010; Motte et al., 2010) and by the Hi-GAL survey of the inner Galactic plane (Molinari et al., 2010a) and soon the outer (I am also involved in Hi-GAL).

In the following sections I will discuss progress that is needed on several fronts.

1. **Diagnosis of Accretion Powered Compact Sources**
   BLAST has discovered many sources located in the accretion-dominated region of the *L*-*M* diagram. There is some direct empirical evidence for this: a few of these sources are known to have active stellar outflows based on the intensity of SiO lines. However, a broader and unbiased survey of molecular outflow tracers would be valuable to establish the ubiquity and evolution of outflow activity from low to high L.

2. **Physical Properties of IRDCs**

   These high column density regions harbor various evolutionary stages of star formation and are probably the best targets for studying the initial conditions of massive star formation and for probing early fragmentation of a molecular cloud (Carey et al., 1998; Simon et al., 2006). The BLAST work demonstrates that IRDC-like clouds can be discovered as regions of high surface density in dust continuum maps at submillimeter wavelengths. These too can be investigated for their potential to turn the molecular cloud mass into the massive stars. The extensive dust continuum surveys being conducted by *Herschel* (Molinari et al., 2010a; Peretto et al., 2010; Wilcock et al., 2011) will enable us to study a large sample of IRDC-like

clouds. Moreover, high resolution molecular line emission surveys will be needed to probe the internal dynamical state of the cloud. It is of great astrophysical interest to know their evolutionary state, if virially they are bound and unstable to gravitational collapse.

3. **Clump Mass Function**

   The similarity between the stellar IMF (Salpeter, 1955) and the core mass function at least in low mass regions (André et al., 2009; Kroupa, 2001) encourages the probably overly simplistic view that the origin of IMF can be closely related to the physical processes such as fragmentation and collapse of the parent molecular cloud. For a deeper understanding of the evolution of a molecular cloud the clump mass function should be investigated too. Massive clumps host more than one dense core. In the literature (Reid et al., 2010; Reid & Wilson, 2005; Kramer et al., 1998; André et al., 2009), studies of the clump mass function do not show a one-to-one correspondence with the IMF, but rather a shallower slope. In Chapter 3 of this thesis, however, I have avoided computing the clump mass function due to incompleteness of the BLAST sources below 30 Jy at 250 μm and the compromised resolution which increases the effective cirrus confusion. With the ongoing *Herschel* continuum dust emission observations towards diverse molecular clouds, a rigorous constraint on the slope might be determined, (once it is agreed what is a clump!).

4. **Confronting Theory at Small Scales**

   What physical mechanisms are involved in the formation of (individual) massive stars? Possibly, the answer is hidden in the small scale details of massive dense cores. Both high resolution continuum and line emission data will be essential tools for unraveling the mystery. Fragmentation is certainly revealed in late stages within BLAST clumps by VLA observations of hypercompact H II regions (Rivera-Ingraham et al., 2010). High angular resolution dust continuum observations obtained with the IRAM Plateau de Bure interferometer have opened a new avenue for studying sub-fragments within ~ 0.1 pc cores (Bontemps et al., 2010b). Moreover, precise imaging by the forthcoming ALMA at an angular resolution of $0.1''$ will further show how dense cores are being formed. This will indeed help to answer whether a single dense core turns most of its mass into at least one massive protostar or into protoclusters of low-mass stars. Possibly it will help to quantify fragmentation efficiency as a function of surface density. The next question would

be to ask if the origin of these sub-fragments is regulated by the turbulent field or is purely due to dynamical processes. In order to answer this, the kinematic properties of dense ambient gas at the scale of 0.01 to 0.1 pc are needed. Again ALMA will be useful. An adequate velocity dispersion is required to support the quasi static evolution of cores (as motivated by the turbulent core model). It would also be of great importance to investigate the line-width relations at subsonic scales.

5. **Improved Power Spectrum Analysis for Galactic Cirrus**
   For high latitude Galactic images it is a reasonable model to consider the total power spectrum as a sum of independent powers due to $P_{\rm cirrus}(k)$, $P_{\rm sources}(k)$, $P_{\rm CIB}(k)$, and noise $N(k)$. Indeed, at the high Galactic latitudes, the distributions of compact sources and the dust emission are not correlated as the sources are mostly extragalactic. The integrated dust emission due to unresolved extragalactic sources which appears as the CIB is comparatively unimportant in star-forming regions given the already bright Galactic emission. However, for the star-forming regions, the column density distribution is correlated with compact sources, because not surprisingly stars are found to form inside the high column density filaments and structures (e.g., André et al., 2010). This scenario indicates a non-trivial contribution to the total power spectrum due to cross-correlation of compact sources and the underlying cirrus distribution. Being motivated by this scenario, we can rewrite the power spectrum P(k) of the submillimeter dust emission maps as

$$P(k) = \Gamma(k)[P_{\rm cirrus}(k) + P_{\rm source}(k) + 2P_{\rm source,cirrus}(k)] + N(k), \qquad (5.1)$$

   where $\rm P_{source,cirrus}(k)$ is the cross-power spectrum of compact sources and the cirrus field. To the extent that bright unconfused compact sources can be removed from the images, these terms in $P(k)$ can be removed. However, there will always be contamination from unresolved and confused sources. Furthermore, self gravity can modify the density and velocity fields and the very act of star formation re-organizes the local surrounding material through physical processes such as accretion and outflows. Therefore the interpretation of the power spectrum will have to allow for more than a turbulent origin. Hydrodynamical simulation of a star-forming region would be helpful in determining and understanding effects on the power spectrum in this more complicated situation. One approach would be to compare density structures just before the onset of star-formation and after.

6. **BLAST-pol Observations**

   BLAST-pol will map polarized emission from high extinction regions having A_V ranging from 4 to 100 mag at a high spatial resolution of about 30″. It will trace dust emission from filamentary structures, clumps, and cores. It is still unclear what role the magnetic field plays in the formation of the elongated structures. Empirically, does the orientation of the magnetic field align with the direction of elongation of the filamentary structures? Moreover, the geometry of molecular cloud cores can provide an understanding of the physical processes involved in their evolution (Jones & Basu, 2002). In the absence of gravity, molecular clouds are spherical, but, the competition between a threaded magnetic field and gravity produces a oblate and triaxial shape. Jones & Basu (2002) showed that empirically clumps less than 1 pc in size are oblate. Basu (2000) also showed that if the magnetic fields are aligned with the minor axis, the projection of the field on the sky is not always along the minor axis. High spatial resolution polarization data will be very interesting for such investigations.

Bibliography

Aguirre, J. E., Ginsburg, A. G., Dunham, M. K., Drosback, M. M., Bally, J., Battersby, C., Bradley, E. T., Cyganowski, C., Dowell, D., Evans, II, N. J., Glenn, J., Harvey, P., Rosolowsky, E., Stringfellow, G. S., Walawender, J., & Williams, J. P. 2011, ApJS, 192, 4

André, P., Basu, S., & Inutsuka, S. The formation and evolution of prestellar cores, ed. Chabrier, G. (Cambridge University Press), 254–+

André, P., Men'shchikov, A., Bontemps, S., Könyves, V., Motte, F., Schneider, N., Didelon, P., Minier, V., Saraceno, P., Ward-Thompson, D., di Francesco, J., White, G., Molinari, S., Testi, L., Abergel, A., Griffin, M., Henning, T., Royer, P., Merín, B., Vavrek, R., Attard, M., Arzoumanian, D., Wilson, C. D., Ade, P., Aussel, H., Baluteau, J., Benedettini, M., Bernard, J., Blommaert, J. A. D. L., Cambrésy, L., Cox, P., di Giorgio, A., Hargrave, P., Hennemann, M., Huang, M., Kirk, J., Krause, O., Launhardt, R., Leeks, S., Le Pennec, J., Li, J. Z., Martin, P. G., Maury, A., Olofsson, G., Omont, A., Peretto, N., Pezzuto, S., Prusti, T., Roussel, H., Russeil, D., Sauvage, M., Sibthorpe, B., Sicilia-Aguilar, A., Spinoglio, L., Waelkens, C., Woodcraft, A., & Zavagno, A. 2010, A&A, 518, L102+

Araya, E. D., Kurtz, S., Hofner, P., & Linz, H. 2009, ApJ, 698, 1321

Aumann, H. H., Fowler, J. W., & Melnyk, M. 1990, AJ, 99, 1674

Ballesteros-Paredes, J. & Mac Low, M. 2002, ApJ, 570, 734

Bally, J. & Lada, C. J. 1983, ApJ, 265, 824

Baraffe, I., Chabrier, G., Barman, T. S., Allard, F., & Hauschildt, P. H. 2003, A&A, 402, 701

Barlow, M. J., Krause, O., Swinyard, B. M., Sibthorpe, B., Besel, M., Wesson, R., Ivison, R. J., Dunne, L., Gear, W. K., Gomez, H. L., Hargrave, P. C., Henning, T., Leeks, S. J., Lim, T. L., Olofsson, G., & Polehampton, E. T. 2010, A&A, 518, L138+

Bastien, P., Jenness, T., & Molnar, J. 2005, in Astronomical Society of the Pacific Conference Series, Vol. 343, Astronomical Polarimetry: Current Status and Future Directions, ed. A. Adamson, C. Aspin, C. Davis, & T. Fujiyoshi, 69–+

Basu, S. 2000, ApJ, 540, L103

Basu, S. & Mouschovias, T. C. 1994, ApJ, 432, 720

—. 1995a, ApJ, 452, 386

—. 1995b, ApJ, 453, 271

Beerer, I. M., Koenig, X. P., Hora, J. L., Gutermuth, R. A., Bontemps, S., Megeath, S. T., Schneider, N., Motte, F., Carey, S., Simon, R., Keto, E., Smith, H. A., Allen, L. E., Fazio, G. G., Kraemer, K. E., Price, S., Mizuno, D., Adams, J. D., Hernández, J., & Lucas, P. W. 2010, ApJ, 720, 679

Bergin, E. A., Ciardi, D. R., Lada, C. J., Alves, J., & Lada, E. A. 2001, ApJ, 557, 209

Bergin, E. A. & Tafalla, M. 2007, ARA&A, 45, 339

Bernard, J., Paradis, D., Marshall, D. J., Montier, L., Lagache, G., Paladini, R., Veneziani, M., Brunt, C. M., Mottram, J. C., Martin, P., Ristorcelli, I., Noriega-Crespo, A., Compiègne, M., Flagey, N., Anderson, L. D., Popescu, C. C., Tuffs, R., Reach, W., White, G., Benedetti, M., Calzoletti, L., Digiorgio, A. M., Faustini, F., Juvela, M., Joblin, C., Joncas, G., Mivilles-Deschenes, M., Olmi, L., Traficante, A., Piacentini, F., Zavagno, A., & Molinari, S. 2010, A&A, 518, L88+

Beuther, H., Churchwell, E. B., McKee, C. F., & Tan, J. C. 2007a, Protostars and Planets V, 165

—. 2007b, Protostars and Planets V, 165

Beuther, H., Leurini, S., Schilke, P., Wyrowski, F., Menten, K. M., & Zhang, Q. 2007c, A&A, 466, 1065

Beuther, H., Schilke, P., Menten, K. M., Motte, F., Sridharan, T. K., & Wyrowski, F. 2002a, ApJ, 566, 945

Beuther, H., Schilke, P., Sridharan, T. K., Menten, K. M., Walmsley, C. M., & Wyrowski, F. 2002b, A&A, 383, 892

Beuther, H., Zhang, Q., Bergin, E. A., Sridharan, T. K., Hunter, T. R., & Leurini, S. 2007d, A&A, 468, 1045

Bica, E., Bonatto, C., & Dutra, C. M. 2003, A&A, 405, 991

Bodenheimer, P. & Sweigart, A. 1968, ApJ, 152, 515

Boldyrev, S., Nordlund, Å., & Padoan, P. 2002, ApJ, 573, 678

Bonnell, I. A., Bate, M. R., Clarke, C. J., & Pringle, J. E. 1997, MNRAS, 285, 201

—. 2001, MNRAS, 323, 785

Bonnell, I. A., Bate, M. R., & Zinnecker, H. 1998, MNRAS, 298, 93

Bonnell, I. A., Larson, R. B., & Zinnecker, H. 2007, Protostars and Planets V, 149

Bontemps, S., André, P., Könyves, V., Men'shchikov, A., Schneider, N., Maury, A., Peretto, N., Arzoumanian, D., Attard, M., Motte, F., Minier, V., Didelon, P., Saraceno, P., Abergel, A., Baluteau, J., Bernard, J., Cambrésy, L., Cox, P., di Francesco, J., di Giorgo, A. M., Griffin, M., Hargrave, P., Huang, M., Kirk, J., Li, J., Martin, P., Merín, B., Molinari, S., Olofsson, G., Pezzuto, S., Prusti, T., Roussel, H., Russeil, D., Sauvage, M., Sibthorpe, B., Spinoglio, L., Testi, L., Vavrek, R., Ward-Thompson, D., White, G., Wilson, C., Woodcraft, A., & Zavagno, A. 2010a, A&A, 518, L85+

Bontemps, S., Motte, F., Csengeri, T., & Schneider, N. 2009, ArXiv e-prints

—. 2010b, A&A, 524, A18+

Boulanger, F., Abergel, A., Bernard, J.-P., Burton, W. B., Desert, F.-X., Hartmann, D., Lagache, G., & Puget, J.-L. 1996, A&A, 312, 256

Bryan, R. K. & Skilling, J. 1980, MNRAS, 191, 69

Campbell, B. 1984, ApJ, 287, 334

Cao, Y., Terebey, S., Prince, T. A., & Beichman, C. A. 1997, ApJS, 111, 387

Carey, S. J., Clark, F. O., Egan, M. P., Price, S. D., Shipman, R. F., & Kuchar, T. A. 1998, ApJ, 508, 721

Carey, S. J., Feldman, P. A., Redman, R. O., Egan, M. P., MacLeod, J. M., & Price, S. D. 2000, ApJ, 543, L157

Carey, S. J., Noriega-Crespo, A., Price, S. D., Padgett, D. L., Kraemer, K. E., Indebetouw, R., Mizuno, D. R., Ali, B., Berriman, G. B., Boulanger, F., Cutri, R. M., Ingalls, J. G., Kuchar, T. A., Latter, W. B., Marleau, F. R., Miville-Deschenes, M. A., Molinari, S., Rebull, L. M., & Testi, L. 2005, in Bulletin of the American Astronomical Society, 1252–+

Caselli, P. & Myers, P. C. 1995, ApJ, 446, 665

Chabrier, G. & Baraffe, I. 1997, A&A, 327, 1039

Chabrier, G., Baraffe, I., Allard, F., & Hauschildt, P. H. 2005, ArXiv Astrophysics e-prints

Chapin, E. L., Ade, P. A. R., Bock, J. J., Brunt, C., Devlin, M. J., Dicker, S., Griffin, M., Gundersen, J. O., Halpern, M., Hargrave, P. C., Hughes, D. H., Klein, J., Marsden, G., Martin, P. G., Mauskopf, P., Netterfield, C. B., Olmi, L., Pascale, E., Patanchon, G., Rex, M., Scott, D., Semisch, C., Truch, M. D. P., Tucker, C., Tucker, G. S., Viero, M. P., & Wiebe, D. V. 2008, ApJ, 681, 428

Churchwell, E. 2002, ARA&A, 40, 27

Ciolek, G. E. & Basu, S. 2000, ApJ, 529, 925

Colley, D. 1980, MNRAS, 192, 377

Comerón, F., Pasquali, A., Rodighiero, G., Stanishev, V., De Filippis, E., López Martí, B., Gálvez Ortiz, M. C., Stankov, A., & Gredel, R. 2002, A&A, 389, 874

Comerón, F. & Torra, J. 1999, A&A, 349, 605

—. 2001, A&A, 375, 539

Compiègne, M., Verstraete, L., Jones, A., Bernard, J., Boulanger, F., Flagey, N., Le Bourlot, J., Paradis, D., & Ysard, N. 2011, A&A, 525, A103+

Cong, H. I. L. 1977, PhD thesis, National Aeronautics and Space Administration. Goddard Space Flight Center, Greenbelt, MD.

Crutcher, R. M. 1999, ApJ, 520, 706

Crutcher, R. M., Nutter, D. J., Ward-Thompson, D., & Kirk, J. M. 2004, ApJ, 600, 279

Csengeri, T., Bontemps, S., Schneider, N., Motte, F., & Dib, S. 2010, ArXiv e-prints

Cyganowski, C. J., Reid, M. J., Fish, V. L., & Ho, P. T. P. 2003, ApJ, 596, 344

Dale, D. A., Gil de Paz, A., Gordon, K. D., Hanson, H. M., Armus, L., Bendo, G. J., Bianchi, L., Block, M., Boissier, S., Boselli, A., Buckalew, B. A., Buat, V., Burgarella, D., Calzetti, D., Cannon, J. M., Engelbracht, C. W., Helou, G., Hollenbach, D. J., Jarrett, T. H., Kennicutt, R. C., Leitherer, C., Li, A., Madore, B. F., Martin, D. C., Meyer, M. J., Murphy, E. J., Regan, M. W., Roussel, H., Smith, J. D. T., Sosey, M. L., Thilker, D. A., & Walter, F. 2007, ApJ, 655, 863

Dame, T. M., Hartmann, D., & Thaddeus, P. 2001, ApJ, 547, 792

Dame, T. M., Ungerechts, H., Cohen, R. S., de Geus, E. J., Grenier, I. A., May, J., Murphy, D. C., Nyman, L., & Thaddeus, P. 1987, ApJ, 322, 706

Davis, C. J., Kumar, M. S. N., Sandell, G., Froebrich, D., Smith, M. D., & Currie, M. J. 2007, MNRAS, 374, 29

Desert, F.-X., Boulanger, F., & Puget, J. L. 1990, A&A, 237, 215

di Francesco, J., Evans, II, N. J., Caselli, P., Myers, P. C., Shirley, Y., Aikawa, Y., & Tafalla, M. 2007, Protostars and Planets V, 17

Di Francesco, J., Johnstone, D., Kirk, H., MacKenzie, T., & Ledwosinska, E. 2008, ApJS, 175, 277

Dobashi, K., Onishi, T., Iwata, T., Nagahama, T., Patel, N., Snell, R. L., & Fukui, Y. 1993, AJ, 105, 1487

Dobashi, K., Yonekura, Y., & Hayashi, Y. 2001, PASJ, 53, 811

Dobashi, K., Yonekura, Y., Mizuno, A., & Fukui, Y. 1992, AJ, 104, 1525

Dobbs, C. L., Bonnell, I. A., & Clark, P. C. 2005, MNRAS, 360, 2

Downes, D. & Rinehart, R. 1966, ApJ, 144, 937

Dutra, C. M. & Bica, E. 2001, A&A, 376, 434

Dwek, E., Arendt, R. G., Fixsen, D. J., Sodroski, T. J., Odegard, N., Weiland, J. L., Reach, W. T., Hauser, M. G., Kelsall, T., Moseley, S. H., Silverberg, R. F., Shafer, R. A., Ballester, J., Bazell, D., & Isaacman, R. 1997, ApJ, 475, 565

Egan, M. P., Shipman, R. F., Price, S. D., Carey, S. J., Clark, F. O., & Cohen, M. 1998, ApJ, 494, L199+

Elia, D., Schisano, E., Molinari, S., Robitaille, T., Anglés-Alcázar, D., Bally, J., Battersby, C., Benedettini, M., Billot, N., Calzoletti, L., di Giorgio, A. M., Faustini, F., Li, J. Z., Martin, P., Morgan, L., Motte, F., Mottram, J. C., Natoli, P., Olmi, L., Paladini, R., Piacentini, F., Pestalozzi, M., Pezzuto, S., Polychroni, D., Smith, M. D., Strafella, F., Stringfellow, G. S., Testi, L., Thompson, M. A., Traficante, A., & Veneziani, M. 2010, A&A, 518, L97+

Elias, J. H. 1978, ApJ, 223, 859

Elmegreen, B. G. 1998, in Astronomical Society of the Pacific Conference Series, Vol. 148, Origins, ed. C. E. Woodward, J. M. Shull, & H. A. Thronson Jr., 150–+

Evans, N. J., Dunham, M. M., Jørgensen, J. K., Enoch, M. L., Merín, B., van Dishoeck, E. F., Alcalá, J. M., Myers, P. C., Stapelfeldt, K. R., Huard, T. L., Allen, L. E., Harvey, P. M., van Kempen, T., Blake, G. A., Koerner, D. W., Mundy, L. G., Padgett, D. L., & Sargent, A. I. 2009, ApJS, 181, 321

Falgarone, E., Puget, J., & Perault, M. 1992, A&A, 257, 715

Fish, D. A., Brinicombe, A. M., Pike, E. R., & Walker, J. G. 1995, Journal of the Optical Society of America A, 12, 58

Fissel, L. M., Ade, P. A. R., Angilè, F. E., Benton, S. J., Chapin, E. L., Devlin, M. J., Gandilo, N. N., Gundersen, J. O., Hargrave, P. C., Hughes, D. H., Klein, J., Korotkov, A. L., Marsden, G., Matthews, T. G., Moncelsi, L., Mroczkowski, T. K., Netterfield,

C. B., Novak, G., Olmi, L., Pascale, E., Savini, G., Scott, D., Shariff, J. A., Soler, J. D., Thomas, N. E., Truch, M. D. P., Tucker, C. E., Tucker, G. S., Ward-Thompson, D., & Wiebe, D. V. 2010, in Society of Photo-Optical Instrumentation Engineers (SPIE) Conference Series, Vol. 7741, Society of Photo-Optical Instrumentation Engineers (SPIE) Conference Series

Franceschini, A., Rodighiero, G., & Vaccari, M. 2008, A&A, 487, 837

Fuller, G. A. & Myers, P. C. 1992, ApJ, 384, 523

Garay, G., Brooks, K. J., Mardones, D., & Norris, R. P. 2006, ApJ, 651, 914

Gautier, III, T. N., Boulanger, F., Perault, M., & Puget, J. L. 1992, AJ, 103, 1313

Griffin, M. J., Abergel, A., Abreu, A., Ade, P. A. R., André, P., Augueres, J., Babbedge, T., Bae, Y., Baillie, T., Baluteau, J., Barlow, M. J., Bendo, G., Benielli, D., Bock, J. J., Bonhomme, P., Brisbin, D., Brockley-Blatt, C., Caldwell, M., Cara, C., Castro-Rodriguez, N., Cerulli, R., Chanial, P., Chen, S., Clark, E., Clements, D. L., Clerc, L., Coker, J., Communal, D., Conversi, L., Cox, P., Crumb, D., Cunningham, C., Daly, F., Davis, G. R., de Antoni, P., Delderfield, J., Devin, N., di Giorgio, A., Didschuns, I., Dohlen, K., Donati, M., Dowell, A., Dowell, C. D., Duband, L., Dumaye, L., Emery, R. J., Ferlet, M., Ferrand, D., Fontignie, J., Fox, M., Franceschini, A., Frerking, M., Fulton, T., Garcia, J., Gastaud, R., Gear, W. K., Glenn, J., Goizel, A., Griffin, D. K., Grundy, T., Guest, S., Guillemet, L., Hargrave, P. C., Harwit, M., Hastings, P., Hatziminaoglou, E., Herman, M., Hinde, B., Hristov, V., Huang, M., Imhof, P., Isaak, K. J., Israelsson, U., Ivison, R. J., Jennings, D., Kiernan, B., King, K. J., Lange, A. E., Latter, W., Laurent, G., Laurent, P., Leeks, S. J., Lellouch, E., Levenson, L., Li, B., Li, J., Lilienthal, J., Lim, T., Liu, S. J., Lu, N., Madden, S., Mainetti, G., Marliani, P., McKay, D., Mercier, K., Molinari, S., Morris, H., Moseley, H., Mulder, J., Mur, M., Naylor, D. A., Nguyen, H., O'Halloran, B., Oliver, S., Olofsson, G., Olofsson, H., Orfei, R., Page, M. J., Pain, I., Panuzzo, P., Papageorgiou, A., Parks, G., Parr-Burman, P., Pearce, A., Pearson, C., Pérez-Fournon, I., Pinsard, F., Pisano, G., Podosek, J., Pohlen, M., Polehampton, E. T., Pouliquen, D., Rigopoulou, D., Rizzo, D., Roseboom, I. G., Roussel, H., Rowan-Robinson, M., Rownd, B., Saraceno, P., Sauvage, M., Savage, R., Savini, G., Sawyer, E., Scharmberg, C., Schmitt, D., Schneider, N., Schulz, B., Schwartz, A., Shafer, R., Shupe, D. L., Sibthorpe, B.,

Sidher, S., Smith, A., Smith, A. J., Smith, D., Spencer, L., Stobie, B., Sudiwala, R., Sukhatme, K., Surace, C., Stevens, J. A., Swinyard, B. M., Trichas, M., Tourette, T., Triou, H., Tseng, S., Tucker, C., Turner, A., Vaccari, M., Valtchanov, I., Vigroux, L., Virique, E., Voellmer, G., Walker, H., Ward, R., Waskett, T., Weilert, M., Wesson, R., White, G. J., Whitehouse, N., Wilson, C. D., Winter, B., Woodcraft, A. L., Wright, G. S., Xu, C. K., Zavagno, A., Zemcov, M., Zhang, L., & Zonca, E. 2010, A&A, 518, L3+

Habing, H. J. & Israel, F. P. 1979, ARA&A, 17, 345

Harris, S. 1975, MNRAS, 170, 139

Harvey, P. M., Huard, T. L., Jørgensen, J. K., Gutermuth, R. A., Mamajek, E. E., Bourke, T. L., Merín, B., Cieza, L., Brooke, T., Chapman, N., Alcalá, J. M., Allen, L. E., Evans, II, N. J., Di Francesco, J., & Kirk, J. M. 2008, ApJ, 680, 495

Harvey-Smith, L., Soria-Ruiz, R., Duarte-Cabral, A., & Cohen, R. J. 2008, MNRAS, 384, 719

Haschick, A. D., Reid, M. J., Burke, B. F., Moran, J. M., & Miller, G. 1981, ApJ, 244, 76

Helou, G. & Beichman, C. A. 1990, in Liege International Astrophysical Colloquia, Vol. 29, Liege International Astrophysical Colloquia, ed. B. Kaldeich, 117–123

Hennemann, M., Motte, F., Bontemps, S., Schneider, N., Csengeri, T., Balog, Z., di Francesco, J., Zavagno, A., André, P., Men'shchikov, A., Abergel, A., Ali, B., Baluteau, J., Bernard, J., Cox, P., Didelon, P., di Giorgio, A., Griffin, M., Hargrave, P., Hill, T., Horeau, B., Huang, M., Kirk, J., Leeks, S., Li, J. Z., Marston, A., Martin, P., Molinari, S., Nguyen Luong, Q., Olofsson, G., Persi, P., Pezzuto, S., Russeil, D., Saraceno, P., Sauvage, M., Sibthorpe, B., Spinoglio, L., Testi, L., Ward-Thompson, D., White, G., Wilson, C., & Woodcraft, A. 2010, A&A, 518, L84+

Herbig, G. H. & Dahm, S. E. 2002, AJ, 123, 304

Herbig, G. H. & Reipurth, B. Young Stars and Molecular Clouds in the IC 5146 Region, ed. Reipurth, B., 108–+

Herbstmeier, U., Abraham, P., Lemke, D., Laureijs, R. J., Klaas, U., Mattila, K., Leinert, C., Surace, C., & Kunkel, M. 1998, A&A, 332, 739

Holland, W., MacIntosh, M., Fairley, A., Kelly, D., Montgomery, D., Gostick, D., Atad-Ettedgui, E., Ellis, M., Robson, I., Hollister, M., Woodcraft, A., Ade, P., Walker, I., Irwin, K., Hilton, G., Duncan, W., Reintsema, C., Walton, A., Parkes, W., Dunare, C., Fich, M., Kycia, J., Halpern, M., Scott, D., Gibb, A., Molnar, J., Chapin, E., Bintley, D., Craig, S., Chylek, T., Jenness, T., Economou, F., & Davis, G. 2006, in Society of Photo-Optical Instrumentation Engineers (SPIE) Conference Series, Vol. 6275, Society of Photo-Optical Instrumentation Engineers (SPIE) Conference Series

Hora, J. L., Bontemps, S., Megeath, S. T., Schneider, N., Motte, F., Carey, S., Simon, R., Keto, E., Smith, H. A., Allen, L. E., Gutermuth, R., Fazio, G. G., Adams, J. D., & Cygnus-X 24 Micron Data Processing Team. 2009, in Bulletin of the American Astronomical Society, Vol. 41, Bulletin of the American Astronomical Society, 498–+

Howard, E. M., Pipher, J. L., Forrest, W. J., & de Pree, C. G. 1996, ApJ, 460, 744

Hunter, T. R., Taylor, G. B., Felli, M., & Tofani, G. 1994, A&A, 284, 215

Isobe, T., Feigelson, E. D., Akritas, M. G., & Babu, G. J. 1990, ApJ, 364, 104

Israel, F. P. 1976, A&A, 48, 193

Jeong, W.-S., Mok Lee, H., Pak, S., Nakagawa, T., Minn Kwon, S., Pearson, C. P., & White, G. J. 2005, MNRAS, 357, 535

Jones, C. E. & Basu, S. 2002, ApJ, 569, 280

Juvela, M., Mattila, K., & Lemke, D. 2000, in ESA Special Publication, Vol. 455, ISO Beyond Point Sources: Studies of Extended Infrared Emission, ed. R. J. Laureijs, K. Leech, & M. F. Kessler, 99–+

Juvela, M., Ristorcelli, I., Montier, L. A., Marshall, D. J., Pelkonen, V., Malinen, J., Ysard, N., Tóth, L. V., Harju, J., Bernard, J., Schneider, N., Verebélyi, E., Anderson, L., André, P., Giard, M., Krause, O., Lehtinen, K., Macias-Perez, J., Martin, P., McGehee, P. M., Meny, C., Motte, F., Pagani, L., Paladini, R., Reach, W., Valenziano, L., Ward-Thompson, D., & Zavagno, A. 2010a, A&A, 518, L93+

—. 2010b, A&A, 518, L93+

Kerton, C. R., Martin, P. G., Johnstone, D., & Ballantyne, D. R. 2001, ApJ, 552, 601

Kessler, M. F., Steinz, J. A., Anderegg, M. E., Clavel, J., Drechsel, G., Estaria, P., Faelker, J., Riedinger, J. R., Robson, A., Taylor, B. G., & Ximénez de Ferrán, S. 1996, A&A, 315, L27

Kiss, C., Ábrahám, P., Klaas, U., Juvela, M., & Lemke, D. 2001, A&A, 379, 1161

Kiss, C., Ábrahám, P., Klaas, U., Lemke, D., Héraudeau, P., del Burgo, C., & Herbstmeier, U. 2003, A&A, 399, 177

Knödlseder, J. 2000, A&A, 360, 539

Kobulnicky, H. A., Gilbert, I. J., & Kiminki, D. C. 2010, ApJ, 710, 549

Koenig, X. P., Allen, L. E., Gutermuth, R. A., Hora, J. L., Brunt, C. M., & Muzerolle, J. 2008, ApJ, 688, 1142

Kraemer, K. E., Hora, J. L., Adams, J., Allen, L. E., Bontemps, S., Carey, S. J., Fazio, G. G., Gutermuth, R., Keto, E., Koenig, X., Megeath, S. T., Mizuno, D. R., Motte, F., Price, S. D., Schneider, N., Simon, R., & Smith, H. A. 2010a, in Bulletin of the American Astronomical Society, Vol. 42, Bulletin of the American Astronomical Society, 253–+

Kraemer, K. E., Hora, J. L., Egan, M. P., Adams, J., Allen, L. E., Bontemps, S., Carey, S. J., Fazio, G. G., Gutermuth, R., Keto, E., Koenig, X. P., Megeath, S. T., Mizuno, D. R., Motte, F., Price, S. D., Schneider, N., Simon, R., & Smith, H. A. 2010b, AJ, 139, 2319

Kramer, C., Richer, J., Mookerjea, B., Alves, J., & Lada, C. 2003, A&A, 399, 1073

Kramer, C., Stutzki, J., Rohrig, R., & Corneliussen, U. 1998, A&A, 329, 249

Kroupa, P. 2001, MNRAS, 322, 231

Krumholz, M. R. 2006, ApJ, 641, L45

Krumholz, M. R. & Matzner, C. D. 2009, ApJ, 703, 1352

Krumholz, M. R. & McKee, C. F. 2008, Nature, 451, 1082

Kurtz, S., Cesaroni, R., Churchwell, E., Hofner, P., & Walmsley, C. M. 2000, Protostars and Planets IV, 299

Kurtz, S., Churchwell, E., & Wood, D. O. S. 1994, ApJS, 91, 659

Lada, C. J. & Lada, E. A. 2003, ARA&A, 41, 57

Lada, C. J., Lada, E. A., Clemens, D. P., & Bally, J. 1994, ApJ, 429, 694

Lagache, G. & Puget, J. L. 2000, A&A, 355, 17

Larson, R. B. 1981, MNRAS, 194, 809

—. 2003, Reports on Progress in Physics, 66, 1651

Larson, R. B. & Starrfield, S. 1971, A&A, 13, 190

Le Duigou, J.-M. & Knödlseder, J. 2002, A&A, 392, 869

Leung, H. O. & Thaddeus, P. 1992, ApJS, 81, 267

Levreault, R. M. 1983, ApJ, 265, 855

Li, A. & Draine, B. T. 2001, ApJ, 554, 778

Lockman, F. J. 1989, ApJS, 71, 469

Lucy, L. B. 1974, AJ, 79, 745

—. 1992, A&A, 261, 706

Mac Low, M.-M. & Klessen, R. S. 2004, Reviews of Modern Physics, 76, 125

Markwardt, C. B. 2009, in Astronomical Society of the Pacific Conference Series, Vol. 411, Astronomical Society of the Pacific Conference Series, ed. D. A. Bohlender, D. Durand, & P. Dowler, 251–+

Marsden, G., Ade, P. A. R., Benton, S., Bock, J. J., Chapin, E. L., Chung, J., Devlin, M. J., Dicker, S., Fissel, L., Griffin, M., Gundersen, J. O., Halpern, M., Hargrave, P. C., Hughes, D. H., Klein, J., Korotkov, A., MacTavish, C. J., Martin, P. G., Martin, T. G., Matthews, T. G., Mauskopf, P., Moncelsi, L., Netterfield, C. B., Novak, G., Pascale,

E., Olmi, L., Patanchon, G., Rex, M., Savini, G., Scott, D., Semisch, C., Thomas, N., Truch, M. D. P., Tucker, C., Tucker, G. S., Viero, M. P., Ward-Thompson, D., & Wiebe, D. V. 2008, in Society of Photo-Optical Instrumentation Engineers (SPIE) Conference Series, Vol. 7020, Society of Photo-Optical Instrumentation Engineers (SPIE) Conference Series

Marston, A. P., Reach, W. T., Noriega-Crespo, A., Rho, J., Smith, H. A., Melnick, G., Fazio, G., Rieke, G., Carey, S., Rebull, L., Muzerolle, J., Egami, E., Watson, D. M., Pipher, J. L., Latter, W. B., & Stapelfeldt, K. 2004, ApJS, 154, 333

Martin, P. G., Miville-Deschênes, M., Roy, A., Bernard, J., Molinari, S., Billot, N., Brunt, C., Calzoletti, L., Digiorgio, A. M., Elia, D., Faustini, F., Joncas, G., Mottram, J. C., Natoli, P., Noriega-Crespo, A., Paladini, R., Robitaille, J. F., Strafella, F., Traficante, A., & Veneziani, M. 2010, A&A, 518, L105+

Massey, P. & Thompson, A. B. 1991, AJ, 101, 1408

Matsuhara, H., Kawara, K., Sato, Y., Taniguchi, Y., Okuda, H., Matsumoto, T., Sofue, Y., Wakamatsu, K., Cowie, L. L., Joseph, R. D., & Sanders, D. B. 2000, A&A, 361, 407

Matzner, C. D. 2002, ApJ, 566, 302

McKee, C. F. & Ostriker, E. C. 2007, ARA&A, 45, 565

McKee, C. F. & Tan, J. C. 2003, ApJ, 585, 850

Meinel, E. S. 1986, Journal of the Optical Society of America A, 3, 787

Mestel, L. & Spitzer, Jr., L. 1956, MNRAS, 116, 503

Mezger, P. G., Altenhoff, W., Schraml, J., Burke, B. F., Reifenstein, III, E. C., & Wilson, T. L. 1967, ApJ, 150, L157+

Mezger, P. G. & Henderson, A. P. 1967, ApJ, 147, 471

Mill, J. D., O'Neil, R. R., Price, S., Romick, G. J., Uy, O. M., Gaposchkin, E. M., Light, G. C., Moore, Jr., W. W., Murdock, T. L., & Stair, Jr., A. T. 1994, Journal of Spacecraft and Rockets, 31, 900

Miville-Deschênes, M.-A. & Lagache, G. 2005, ApJS, 157, 302

Miville-Deschênes, M.-A., Lagache, G., Boulanger, F., & Puget, J.-L. 2007a, A&A, 469, 595

—. 2007b, A&A, 469, 595

Miville-Deschênes, M.-A., Lagache, G., & Puget, J.-L. 2002, A&A, 393, 749

Molinari, S., Brand, J., Cesaroni, R., & Palla, F. 2000, A&A, 355, 617

Molinari, S., Brand, J., Cesaroni, R., Palla, F., & Palumbo, G. G. C. 1998, A&A, 336, 339

Molinari, S., Pezzuto, S., Cesaroni, R., Brand, J., Faustini, F., & Testi, L. 2008, A&A, 481, 345

Molinari, S., Swinyard, B., Bally, J., Barlow, M., Bernard, J., Martin, P., Moore, T., Noriega-Crespo, A., Plume, R., Testi, L., Zavagno, A., Abergel, A., Ali, B., Anderson, L., André, P., Baluteau, J., Battersby, C., Beltrán, M. T., Benedettini, M., Billot, N., Blommaert, J., Bontemps, S., Boulanger, F., Brand, J., Brunt, C., Burton, M., Calzoletti, L., Carey, S., Caselli, P., Cesaroni, R., Cernicharo, J., Chakrabarti, S., Chrysostomou, A., Cohen, M., Compiegne, M., de Bernardis, P., de Gasperis, G., di Giorgio, A. M., Elia, D., Faustini, F., Flagey, N., Fukui, Y., Fuller, G. A., Ganga, K., Garcia-Lario, P., Glenn, J., Goldsmith, P. F., Griffin, M., Hoare, M., Huang, M., Ikhenaode, D., Joblin, C., Joncas, G., Juvela, M., Kirk, J. M., Lagache, G., Li, J. Z., Lim, T. L., Lord, S. D., Marengo, M., Marshall, D. J., Masi, S., Massi, F., Matsuura, M., Minier, V., Miville-Deschênes, M., Montier, L. A., Morgan, L., Motte, F., Mottram, J. C., Müller, T. G., Natoli, P., Neves, J., Olmi, L., Paladini, R., Paradis, D., Parsons, H., Peretto, N., Pestalozzi, M., Pezzuto, S., Piacentini, F., Piazzo, L., Polychroni, D., Pomarès, M., Popescu, C. C., Reach, W. T., Ristorcelli, I., Robitaille, J., Robitaille, T., Rodón, J. A., Roy, A., Royer, P., Russeil, D., Saraceno, P., Sauvage, M., Schilke, P., Schisano, E., Schneider, N., Schuller, F., Schulz, B., Sibthorpe, B., Smith, H. A., Smith, M. D., Spinoglio, L., Stamatellos, D., Strafella, F., Stringfellow, G. S., Sturm, E., Taylor, R., Thompson, M. A., Traficante, A., Tuffs, R. J., Umana, G., Valenziano, L., Vavrek, R., Veneziani, M., Viti, S., Waelkens, C., Ward-Thompson, D., White, G., Wilcock, L. A., Wyrowski, F., Yorke, H. W., & Zhang, Q. 2010a, A&A, 518, L100+

Molinari, S., Swinyard, B., Bally, J., Barlow, M., Bernard, J., Martin, P., Moore, T., Noriega-Crespo, A., Plume, R., Testi, L., Zavagno, A., Abergel, A., Ali, B., André, P., Baluteau, J., Benedettini, M., Berné, O., Billot, N. P., Blommaert, J., Bontemps, S., Boulanger, F., Brand, J., Brunt, C., Burton, M., Campeggio, L., Carey, S., Caselli, P., Cesaroni, R., Cernicharo, J., Chakrabarti, S., Chrysostomou, A., Codella, C., Cohen, M., Compiegne, M., Davis, C. J., de Bernardis, P., de Gasperis, G., Di Francesco, J., di Giorgio, A. M., Elia, D., Faustini, F., Fischera, J. F., Fukui, Y., Fuller, G. A., Ganga, K., Garcia-Lario, P., Giard, M., Giardino, G., Glenn, J. ., Goldsmith, P., Griffin, M., Hoare, M., Huang, M., Jiang, B., Joblin, C., Joncas, G., Juvela, M., Kirk, J., Lagache, G., Li, J. Z., Lim, T. L., Lord, S. D., Lucas, P. W., Maiolo, B., Marengo, M., Marshall, D., Masi, S., Massi, F., Matsuura, M., Meny, C., Minier, V., Miville-Deschênes, M., Montier, L., Motte, F., Müller, T. G., Natoli, P., Neves, J., Olmi, L., Paladini, R., Paradis, D., Pestalozzi, M., Pezzuto, S., Piacentini, F., Pomarès, M., Popescu, C. C., Reach, W. T., Richer, J., Ristorcelli, I., Roy, A., Royer, P., Russeil, D., Saraceno, P., Sauvage, M., Schilke, P., Schneider-Bontemps, N., Schuller, F., Schultz, B., Shepherd, D. S., Sibthorpe, B., Smith, H. A., Smith, M. D., Spinoglio, L., Stamatellos, D., Strafella, F., Stringfellow, G., Sturm, E., Taylor, R., Thompson, M. A., Tuffs, R. J., Umana, G., Valenziano, L., Vavrek, R., Viti, S., Waelkens, C., Ward-Thompson, D., White, G., Wyrowski, F., Yorke, H. W., & Zhang, Q. 2010b, PASP, 122, 314

Moore, T. J. T., Mountain, C. M., & Yamashita, T. 1991, MNRAS, 248, 79

Motte, F., Bontemps, S., Schilke, P., Schneider, N., Menten, K. M., & Broguière, D. 2007, A&A, 476, 1243

Motte, F., Zavagno, A., Bontemps, S., Schneider, N., Hennemann, M., di Francesco, J., André, P., Saraceno, P., Griffin, M., Marston, A., Ward-Thompson, D., White, G., Minier, V., Men'shchikov, A., Hill, T., Abergel, A., Anderson, L. D., Aussel, H., Balog, Z., Baluteau, J., Bernard, J., Cox, P., Csengeri, T., Deharveng, L., Didelon, P., di Giorgio, A., Hargrave, P., Huang, M., Kirk, J., Leeks, S., Li, J. Z., Martin, P., Molinari, S., Nguyen-Luong, Q., Olofsson, G., Persi, P., Peretto, N., Pezzuto, S., Roussel, H., Russeil, D., Sadavoy, S., Sauvage, M., Sibthorpe, B., Spinoglio, L., Testi, L., Teyssier, D., Vavrek, R., Wilson, C. D., & Woodcraft, A. 2010, A&A, 518, L77+

Mottram, J. C., Hoare, M. G., Lumsden, S. L., Oudmaijer, R. D., Urquhart, J. S., Meade, M. R., Moore, T. J. T., & Stead, J. J. 2010, A&A, 510, A89+

Myers, P. C. & Goodman, A. A. 1988, ApJ, 329, 392

Nakano, T. 1998, ApJ, 494, 587

Narayan, R. & Nityananda, R. 1986, ARA&A, 24, 127

Negueruela, I., Marco, A., Herrero, A., & Clark, J. S. 2008, A&A, 487, 575

Netterfield, C. B., Ade, P. A. R., Bock, J. J., Chapin, E. L., Devlin, M. J., Griffin, M., Gundersen, J. O., Halpern, M., Hargrave, P. C., Hughes, D. H., Klein, J., Marsden, G., Martin, P. G., Mauskopf, P., Olmi, L., Pascale, E., Patanchon, G., Rex, M., Roy, A., Scott, D., Semisch, C., Thomas, N., Truch, M. D. P., Tucker, C., Tucker, G. S., Viero, M. P., & Wiebe, D. V. 2009, ApJ, 707

Odenwald, S., Shivanandan, K., Campbell, M., Fazio, G., Schwartz, P., & Moseley, H. 1986, ApJ, 306, 122

Odenwald, S. F., Campbell, M. F., Shivanandan, K., Schwartz, P., Fazio, G. G., & Moseley, H. 1990, AJ, 99, 288

Ohashi, N., Lee, S. W., Wilner, D. J., & Hayashi, M. 1999, ApJ, 518, L41

Okamoto, Y. K., Kataza, H., Yamashita, T., Miyata, T., Sako, S., Takubo, S., Honda, M., & Onaka, T. 2003, ApJ, 584, 368

Ossenkopf, V. & Henning, T. 1994, A&A, 291, 943

Padoan, P. 1995, MNRAS, 277, 377

Padoan, P., Cambrésy, L., & Langer, W. 2002, ApJ, 580, L57

Padoan, P. & Nordlund, Å. 2002, ApJ, 576, 870

Panagia, N. 1973, AJ, 78, 929

Pascale, E., Ade, P. A. R., Bock, J. J., Chapin, E. L., Chung, J., Devlin, M. J., Dicker, S., Griffin, M., Gundersen, J. O., Halpern, M., Hargrave, P. C., Hughes, D. H., Klein, J., MacTavish, C. J., Marsden, G., Martin, P. G., Martin, T. G., Mauskopf, P., Netterfield, C. B., Olmi, L., Patanchon, G., Rex, M., Scott, D., Semisch, C., Thomas, N., Truch, M. D. P., Tucker, C., Tucker, G. S., Viero, M. P., & Wiebe, D. V. 2008, ApJ, 681, 400

Patanchon, G., Ade, P. A. R., Bock, J. J., Chapin, E. L., Devlin, M. J., Dicker, S., Griffin, M., Gundersen, J. O., Halpern, M., Hargrave, P. C., Hughes, D. H., Klein, J., Marsden, G., Martin, P. G., Mauskopf, P., Netterfield, C. B., Olmi, L., Pascale, E., Rex, M., Scott, D., Semisch, C., Truch, M. D. P., Tucker, C., Tucker, G. S., Viero, M. P., & Wiebe, D. V. 2008a, ApJ, 681, 708

—. 2008b, ApJ, 681, 708

Perault, M., Omont, A., Simon, G., Seguin, P., Ojha, D., Blommaert, J., Felli, M., Gilmore, G., Guglielmo, F., Habing, H., Price, S., Robin, A., de Batz, B., Cesarsky, C., Elbaz, D., Epchtein, N., Fouque, P., Guest, S., Levine, D., Pollock, A., Prusti, T., Siebenmorgen, R., Testi, L., & Tiphene, D. 1996, A&A, 315, L165

Peretto, N. & Fuller, G. A. 2010, ApJ, 723, 555

Peretto, N., Fuller, G. A., Plume, R., Anderson, L. D., Bally, J., Battersby, C., Beltran, M. T., Bernard, J., Calzoletti, L., Digiorgio, A. M., Faustini, F., Kirk, J. M., Lenfestey, C., Marshall, D., Martin, P., Molinari, S., Montier, L., Motte, F., Ristorcelli, I., Rodón, J. A., Smith, H. A., Traficante, A., Veneziani, M., Ward-Thompson, D., & Wilcock, L. 2010, A&A, 518, L98+

Persi, P., Tapia, M., & Smith, H. A. 2006, A&A, 445, 971

Piddington, J. H. & Minnett, H. C. 1952, Australian Journal of Scientific Research A Physical Sciences, 5, 17

Planck Collaboration. 2011, arXiv, 1101.2028

Plume, R., Jaffe, D. T., & Evans, II, N. J. 1992, ApJS, 78, 505

Plume, R., Jaffe, D. T., Evans, II, N. J., Martin-Pintado, J., & Gomez-Gonzalez, J. 1997, ApJ, 476, 730

Poetzel, R., Mundt, R., & Ray, T. P. 1992, A&A, 262, 229

Prasad, S. 2002, J. Opt. Soc. Am, 19, 1286

Price, S. D., Egan, M. P., Carey, S. J., Mizuno, D. R., & Kuchar, T. A. 2001, AJ, 121, 2819

Redman, R. O., Feldman, P. A., Wyrowski, F., Côté, S., Carey, S. J., & Egan, M. P. 2003, ApJ, 586, 1127

Reid, M. A., Wadsley, J., Petitclerc, N., & Sills, A. 2010, ApJ, 719, 561

Reid, M. A. & Wilson, C. D. 2005, ApJ, 625, 891

Reipurth, B. & Schneider, N. Star Formation and Young Clusters in Cygnus, ed. Reipurth, B., 36–+

Richardson, W. H. 1972, Journal of the Optical Society of America (1917-1983), 62, 55

Rivera-Ingraham, A., Ade, P. A. R., Bock, J. J., Chapin, E. L., Devlin, M. J., Dicker, S. R., Griffin, M., Gundersen, J. O., Halpern, M., Hargrave, P. C., Hughes, D. H., Klein, J., Marsden, G., Martin, P. G., Mauskopf, P., Netterfield, C. B., Olmi, L., Patanchon, G., Rex, M., Scott, D., Semisch, C., Truch, M. D. P., Tucker, C., Tucker, G. S., Viero, M. P., & Wiebe, D. V. 2010, ApJ, 723, 915

Roy, A., Ade, P. A. R., Bock, J. J., Brunt, C. M., Chapin, E. L., Devlin, M. J., Dicker, S. R., France, K., Gibb, A. G., Griffin, M., Gundersen, J. O., Halpern, M., Hargrave, P. C., Hughes, D. H., Klein, J., Marsden, G., Martin, P. G., Mauskopf, P., Netterfield, C. B., Olmi, L., Patanchon, G., Rex, M., Scott, D., Semisch, C., Truch, M. D. P., Tucker, C., Tucker, G. S., Viero, M. P., & Wiebe, D. V. 2011a, ApJ, 730, in press

Roy, A., Ade, P. A. R., Bock, J. J., Chapin, E. L., Devlin, M. J., Dicker, S. R., France, K., Gibb, A. G., Griffin, M., Gundersen, J. O., Halpern, M., Hargrave, P. C., Hughes, D. H., Klein, J., Marsden, G., Martin, P. G., Mauskopf, P., Netterfield, J. L. M. O. C. B., Noriega-Crespo, A., Olmi, L., Patanchon, G., Rex, M., Scott, D., Semisch, C., Truch, M. D. P., Tucker, C., Tucker, G. S., Viero, M. P., & Wiebe, D. V. 2011b, ApJ, 727, 114

Roy, A., Ade, P. A. R., Bock, J. J., Chapin, E. L., Devlin, M. J., Dicker, S. R., Griffin, M., Gundersen, J. O., Halpern, M., Hargrave, P. C., Hughes, D. H., Klein, J., Marsden, G., Martin, P. G., Mauskopf, P., Miville-Deschênes, M., Netterfield, C. B., Olmi, L., Patanchon, G., Rex, M., Scott, D., Semisch, C., Truch, M. D. P., Tucker, C., Tucker, G. S., Viero, M. P., & Wiebe, D. V. 2010, ApJ, 708, 1611

Salpeter, E. E. 1955, ApJ, 121, 161

Samal, M. R., Pandey, A. K., Ojha, D. K., Ghosh, S. K., Kulkarni, V. K., Kusakabe, N., Tamura, M., Bhatt, B. C., Thompson, M. A., & Sagar, R. 2010, ApJ, 714, 1015

Schaerer, D. & de Koter, A. 1997, A&A, 322, 598

Schlegel, D. J., Finkbeiner, D. P., & Davis, M. 1998, ApJ, 500, 525

Schneider, N., Bontemps, S., Simon, R., Jakob, H., Motte, F., Miller, M., Kramer, C., & Stutzki, J. 2006a, A&A, 458, 855

—. 2006b, A&A, 458, 855

Sebring, T. 2010, in Society of Photo-Optical Instrumentation Engineers (SPIE) Conference Series, Vol. 7733, Society of Photo-Optical Instrumentation Engineers (SPIE) Conference Series

Shu, F. H., Adams, F. C., & Lizano, S. 1987, ARA&A, 25, 23

Sibthorpe, B., Ade, P. A. R., Bock, J. J., Chapin, E. L., Devlin, M. J., Dicker, S., Griffin, M., Gundersen, J. O., Halpern, M., Hargrave, P. C., Hughes, D. H., Jeong, W., Kaneda, H., Klein, J., Koo, B., Lee, H., Marsden, G., Martin, P. G., Mauskopf, P., Moon, D., Netterfield, C. B., Olmi, L., Pascale, E., Patanchon, G., Rex, M., Roy, A., Scott, D., Semisch, C., Truch, M. D. P., Tucker, C., Tucker, G. S., Viero, M. P., & Wiebe, D. V. 2010, ApJ, 719, 1553

Simon, R., Rathborne, J. M., Shah, R. Y., Jackson, J. M., & Chambers, E. T. 2006, ApJ, 653, 1325

Smith, R. J., Longmore, S., & Bonnell, I. 2009, MNRAS, 400, 1775

Solomon, P. M., Sanders, D. B., & Rivolo, A. R. 1985, ApJ, 292, L19

Sridharan, T. K., Beuther, H., Saito, M., Wyrowski, F., & Schilke, P. 2005, ApJ, 634, L57

Stahler, S. W. & Palla, F. 2005, The Formation of Stars, ed. Stahler, S. W. & Palla, F.

Stutzki, J. & Guesten, R. 1990, ApJ, 356, 513

Taylor, A. R., Gibson, S. J., Peracaula, M., Martin, P. G., Landecker, T. L., Brunt, C. M., Dewdney, P. E., Dougherty, S. M., Gray, A. D., Higgs, L. A., Kerton, C. R., Knee, L. B. G., Kothes, R., Purton, C. R., Uyaniker, B., Wallace, B. J., Willis, A. G., & Durand, D. 2003, AJ, 125, 3145

Thompson, M. A., Hatchell, J., Walsh, A. J., MacDonald, G. H., & Millar, T. J. 2006, A&A, 453, 1003

Truch, M. D. P., Ade, P. A. R., Bock, J. J., Chapin, E. L., Devlin, M. J., Dicker, S., Griffin, M., Gundersen, J. O., Halpern, M., Hargrave, P. C., Hughes, D. H., Klein, J., Marsden, G., Martin, P. G., Mauskopf, P., Netterfield, C. B., Olmi, L., Pascale, E., Patanchon, G., Rex, M., Scott, D., Semisch, C., Tucker, C., Tucker, G. S., Viero, M. P., & Wiebe, D. V. 2008, ApJ, 681, 415

Truch, M. D. P., Ade, P. A. R., Bock, J. J., Chapin, E. L., Devlin, M. J., Dicker, S. R., Griffin, M., Gundersen, J. O., Halpern, M., Hargrave, P. C., Hughes, D. H., Klein, J., Marsden, G., Martin, P. G., Mauskopf, P., Moncelsi, L., Netterfield, C. B., Olmi, L., Pascale, E., Patanchon, G., Rex, M., Scott, D., Semisch, C., Thomas, N. E., Tucker, C., Tucker, G. S., Viero, M. P., & Wiebe, D. V. 2009, ApJ, in press

Tsumuraya, F., Miura, N., & Baba, N. 1994, A&A, 282, 699

Uyanıker, B., Fürst, E., Reich, W., Aschenbach, B., & Wielebinski, R. 2001, A&A, 371, 675

Van der Tak, F. F. S. & Menten, K. M. 2005, A&A, 437, 947

Varosi, F. & Landsman, W. B. 1993, in Astronomical Society of the Pacific Conference Series, Vol. 52, Astronomical Data Analysis Software and Systems II, ed. R. J. Hanisch, R. J. V. Brissenden, & J. Barnes, 515–+

Velusamy, T., Marsh, K. A., Beichman, C. A., Backus, C. R., & Thompson, T. J. 2008, AJ, 136, 197

Viero, M. P., Ade, P. A. R., Bock, J. J., Chapin, E. L., Devlin, M. J., Griffin, M., Gundersen, J. O., Halpern, M., Hargrave, P. C., Hughes, D. H., Klein, J., MacTavish, C. J., Marsden, G., Martin, P. G., Mauskopf, P., Moncelsi, L., Negrello, M., Netterfield, C. B., Olmi, L., Pascale, E., Patanchon, G., Rex, M., Scott, D., Semisch, C., Thomas, N., Truch, M. D. P., Tucker, C., Tucker, G. S., & Wiebe, D. V. 2009, ApJ, 707, 1766

Waller, W. H. & Boulanger, F. 1994, in Astronomical Society of the Pacific Conference Series, Vol. 58, The First Symposium on the Infrared Cirrus and Diffuse Interstellar Clouds, ed. R. M. Cutri & W. B. Latter, 129

Wang, P., Li, Z., Abel, T., & Nakamura, F. 2010, ApJ, 709, 27

Wendker, H. J., Higgs, L. A., & Landecker, T. L. 1991, A&A, 241, 551

Werner, M. W., Roellig, T. L., Low, F. J., Rieke, G. H., Rieke, M., Hoffmann, W. F., Young, E., Houck, J. R., Brandl, B., Fazio, G. G., Hora, J. L., Gehrz, R. D., Helou, G., Soifer, B. T., Stauffer, J., Keene, J., Eisenhardt, P., Gallagher, D., Gautier, T. N., Irace, W., Lawrence, C. R., Simmons, L., Van Cleve, J. E., Jura, M., Wright, E. L., & Cruikshank, D. P. 2004, ApJS, 154, 1

Westerhout, G. 1958, Bull. Astron. Inst. Netherlands, 14, 215

Wilcock, L. A., Kirk, J. M., Stamatellos, D., Ward-Thompson, D., Whitworth, A., Battersby, C., Brunt, C., Fuller, G. A., Griffin, M., Molinari, S., Martin, P., Mottram, J. C., Peretto, N., Plume, R., Smith, H. A., & Thompson, M. A. 2011, A&A, 526, A159+

Williams, J. P., de Geus, E. J., & Blitz, L. 1994, ApJ, 428, 693

Wood, D. O. S. & Churchwell, E. 1989a, ApJ, 340, 265

—. 1989b, ApJS, 69, 831

Wu, L.-X. & Yang, J. 2005, Chinese Astronomy and Astrophysics, 29, 370

Young, K. E., Lee, J., Evans, II, N. J., Goldsmith, P. F., & Doty, S. D. 2004, ApJ, 614, 252

Zinnecker, H. & Yorke, H. W. 2007, ARA&A, 45, 481